Perovskite chromite-based fuel electrode for solid oxide cells (SOCs): towards the understanding of the electrochemical performance

Von der Fakultät Energie-, Verfahrens- und Biotechnik der Universität Stuttgart
zur Erlangung der Würde eines Doktors der
Ingenieurwissenschaften (Dr.-Ing.) genehmigte Abhandlung

Vorgelegt von
M. Sc. **Diana María Amaya Dueñas**
aus Bogotá, Kolumbien

Hauptberichter: Prof. Dr. rer.nat. K. Andreas Friedrich
Mitberichter: Univ.-Prof. Dr. Jürgen Fleig
Prüfungsvorsitzender: Prof. Dr. rer. nat. habil. André Thess

Tag der mündlichen Prüfung: 19.01.2023

Institut für Gebäudeenergetik, Thermotechnik und Energiespeicherung
der Universität Stuttgart
2023

“We must believe in ourselves or no one else will believe in us; we must match our aspirations with the competence, courage and determination to succeed; and we must feel a personal responsibility to ease the path for those who come afterwards. The world cannot afford the loss of the talents of half its people if we are to solve the many problems which beset us.*”*

Rosalyn Yalow’s speech at the Nobel Banquet, December 10th 1977

Acknowledgments

I would like to express my gratitude to Prof. K. Andreas Friedrich for providing me the opportunity of pursing my PhD in the department of Electrochemical Energy Technology from the Institute of Engineering Thermodynamics at DLR in Stuttgart. For this opportunity, I am very thankful.

My sincere gratitude to my co-supervisor Dr. Rémi Costa. Thank you because you always encouraged me to move forward. Your constant guidance and support helped me to become a better scientist.

Specials thanks to my office colleagues Dr. Matthias Riegraf and Haoyu Zheng for your daily basis support. To Matthias, thank you for all the fruitful discussions but most important for your constant support and your scientific curiosity. I would also like to thank my colleagues Dr. Noriko Sata, Dr. Indro Biswas and Dr. Feng Han for your advice and constant support. I would like to extend this also to Ina Plock, Dr. Robert Ruckdäschel, Thomas Lorscheider and Günter Roth for their technical support.

Sincere thanks to my PhD colleagues Fabian Bienen, Srikanth Santhanam, Joachim Häcker, Christina Schmitt, Patrick Sarkezi-Selsky, Marius Tomberg, Marc Riedel, Li Wang, Sanchit Gupta, and Maximilian Groß for always being open to help, for fruitful scientific discussions and for listening whenever I needed support. I would also like to thank Dr. Andrea Gutiérrez for always having an open door for discussion and for motivating me.

Beyond DLR, I would like to express my gratitude to Dr. Andreas Nenning, Dr. Alexander Opitz and Prof. Jürgen Fleig for providing me with the opportunity to conduct a research stay at TU Wien, Institute for Chemical Technologies and Analytics.

To my family, I could not express how grateful I am for your support in this pursuit of my Doctorate (*porque adentro es oscuro*). To my mother Clara, my father Humberto and my brother Camilo I will always be thankful for having you as my lovely family. You inspired and motivated me every day during this process.

And last but not least, I would like to thank my dear husband Jakob for always motivating me and for your unconditional support in this journey. Thank you for brightening my world in difficult moments.

Declaration

I certify that the dissertation entitled:

„ Perovskite chromite-based fuel electrode for solid oxide cells (SOCs): towards the understanding of the electrochemical performance “

is entirely my own work. Passages and ideas from other sources have been clearly marked.

Erklärung

Ich versichere, dass ich die vorliegende Dissertation mit dem Titel:

„ Perovskite chromite-based fuel electrode for solid oxide cells (SOCs): towards the understanding of the electrochemical performance “

selbständig verfasst und keine anderen als die angegebenen Quellen und Hilfsmittel benutzt habe. Passagen und Gedanken aus fremden Quellen sind als solche kenntlich gemacht.

Diana María Amaya Dueñas

Stuttgart, 11.02.2023

Abstract

The current energy transition is a key driver for the continuous development of fuel cells and electrolyzers due to the rapid growth of the clean energy demand and the need to overcome the intermittency of the power supply of renewable energy sources, such as wind and solar energy. In this regard, solid oxide cells (SOC) are promising systems that allow to overcome such fluctuations: they convert renewable electrical energy into chemical energy in the form of hydrogen and valuable fuels and chemicals, while they can also repower the grid by converting fuels and hydrogen into electrical power. This feature in reversibility has attracted the interest among Power-to-X technologies, which can be exploited by operating SOCs in fuel cell (SOFC), electrolysis (SOEL) and reversible (rSOC) modes. Nevertheless, SOCs are not yet a mature technology due to limitations on the performance of their electrolyte and electrodes. Typical fuel electrodes made of Ni-based cermets are in contact not only with hydrogen, but also with reactants such as natural gas, biogas, steam and carbon dioxide, leading to important operation issues related to high temperatures and poisoning tolerance, which significantly detriment the performance of these systems.

Due to the urgent need for the development of sustainable SOC systems in clean energy scenarios, this thesis aims to cover the Ni cermets issues related to SOCs operation, such as nickel agglomeration, nickel migration, structural cell damage and carbon deposition. Therefore, with the motivation to propose alternative fuel electrode materials to the state-of-the-art Ni cermets, formulations of perovskite chromite-based fuel electrodes were investigated in different SOC operating conditions.

Firstly, different perovskite compositions were investigated by X-ray diffraction (XRD) to ensure the desired phase. With these crystal structure characterizations, the lanthanum-chromite perovskite with Ni doping (LSCrN) was selected as candidate fuel electrode material with the compositions $La_{0.7}Sr_{0.3}Cr_{0.85}Ni_{0.15}O_{3-\delta}$ (L70SCrN) and $La_{0.65}Sr_{0.3}Cr_{0.85}Ni_{0.15}O_{3-\delta}$ (L65SCrN). These materials were synthetized by the glycine-nitrate combustion method and ceramic powder morphology was characterized by scanning electron microscopy (SEM). An experimental protocol for the cell manufacturing process was designed and the electrolyte-supported-cells (ESCs) were produced by screen-printing, drying and sintering processes. ESCs were tested in different operating SOC modes: fuel cell (SOFC), steam electrolysis (SOEL), steam and carbon dioxide co-electrolysis (co-SOEL), as well as in reversible mode (rSOC) and even in dry carbon dioxide electrolysis operation. *In situ* electrochemical characterizations were performed by evaluating the voltage – current response and the electrochemical impedance spectroscopy (EIS). In parallel, the exsolution of nickel particles from the produced LSCrN ceramic powders was investigated by means of temperature programmed reduction (TPR), X-ray spectroscopy (XPS) and XRD techniques. It was shown that the introduction of A-site deficiency promoted the reduction of metallic nickel particles on the perovskite surface. The particle distribution was found to be dependent on the temperature, the atmosphere and the overpotential. In co-SOEL operation, cells with the developed L65SCrN electrode showed a comparable performance to the ones with state-of-the-art Ni cermets, e.g. – 0.8 A·cm^{-2} at 1.32 V and 860 °C.

The long-term stability (~ 1000 hours) suggested that under strongly reducing atmospheres, such as in SOEL at 860 °C, the L65SCrN electrode suffered from accelerated performance degradation due to an alteration of the transport properties. Nonetheless, it was found that a decrease in operating temperature (below 830 °C) could be a suitable strategy to mitigate this durability issue. These findings are related to a gain in performance of the perovskite electrodes against the state-of-the-art Ni electrodes at temperatures between 770 °C and 830 °C, possibly due to lower reaction energy barriers. These outcomes were used as basis for a scale-up analysis from the cell level up to the system level, i.e. up to the MW scale, by analyzing a real case application of SOEL-based systems for hydrogen production. This analysis suggested that the implementation of perovskite electrodes in SOEL systems, together with a decrease of the system operating temperature, would lead to a significant reduction of the number of cells in the stacks and hence of the system components, simplifying the system layout. Additionally, the required amount of Ni raw material would also be significantly decreased, which would mitigate future supply chain issues that the mineral market may experience in the upcoming years. This study paves the way for future alternative electrode development for SOC applications while suggesting potential benefits at the system scale.

Zusammenfassung

Die derzeitige Energiewende ist aufgrund des raschen Anstiegs der Nachfrage nach sauberer Energie und der Notwendigkeit, die Schwankungen der Stromversorgung aus erneuerbaren Energiequellen wie Wind- und Sonnenenergie zu überwinden, ein wichtiger Motor für die kontinuierliche Entwicklung von Brennstoffzellen und Elektrolyseuren. In dieser Hinsicht sind Festoxidzellen (SOC) vielversprechende Systeme, die es ermöglichen solche Schwankungen zu überwinden: Sie wandeln erneuerbare elektrische Energie in chemische Energie in Form von Wasserstoff oder Synthesegase (Wasserstoff zusammen mit Kohlenmonoxid) um, die Ausgangsstoffe für die Herstellung von Brennstoffen sowie Chemikalien sind. Gleichzeitig können sie das Netz durch die Umwandlung von Brennstoffen und Wasserstoff in elektrische Energie wieder mit Strom versorgen. Diese Eigenschaft der Reversibilität hat das Interesse für die Anwendung als P2X-Technolgie geweckt, wobei SOCs im Brennstoffzellen- (SOFC), Elektrolyse- (SOEL) und reversiblen (rSOC) Modi genutzt werden können. Dennoch sind SOCs bisher noch keine ausgereifte Technologie, da die Leistungsfähigkeit ihrer Elektrolyte und Elektroden begrenzt ist. Typische Brenngaselektroden aus Ni-Cermets kommen nicht nur mit Wasserstoff, sondern auch mit Reaktanten wie Erdgas, Wasserdampf und Kohlendioxid in Kontakt. Dies führt zu erheblichen Problemen beim Betrieb im Zusammenhang mit hohen Temperaturen und Vergiftungstoleranzen, was die Leistung dieser Systeme erheblich beeinträchtigt.

Aufgrund des dringenden Bedarfs an der Entwicklung nachhaltiger SOC-Systeme in sauberen Energieszenarien, zielt diese Dissertation darauf ab die Probleme von Ni-Cermets im Zusammenhang mit dem Betrieb von SOCs zu behandeln, wie z. B. Nickelagglomeration, Nickelmigration, strukturelle Zellschäden und Kohlenstoffablagerungen. Mit dem Ziel alternative Brenngaselektrodenmaterialien zu den hochmodernen Ni-Cermets vorzuschlagen wurden daher Zusammensetzungen von Brenngaselektroden auf Perowskit-Chromit-Basis in verschiedenen SOC-Betriebsbedingungen untersucht.

Zunächst wurden verschiedene Perowskit-Zusammensetzungen mittels Röntgenbeugung (XRD) untersucht, um die gewünschte Phase sicherzustellen. Anhand dieser Kristallstrukturcharakterisierungen wurde der Lanthan-Chromit-Perowskit mit Ni-Dotierung (LSCrN) mit den Zusammensetzungen $La_{0.7}Sr_{0.3}Cr_{0.85}Ni_{0.15}O_{3-\delta}$ (L70SCrN) und $La_{0.65}Sr_{0.3}Cr_{0.85}Ni_{0.15}O_{3-\delta}$ (L65SCrN) als Brennstoff-Elektrodenmaterial ausgewählt. Diese

Materialien wurden durch die Glycin-Nitrat-Verbrennungsmethode synthetisiert und die Morphologie des Keramikpulvers wurde durch Rasterelektronenmikroskopie (REM) charakterisiert. Ein Versuchsprotokoll für den Zellherstellungsprozess wurde entworfen und die Elektrolyt-gestützten Zellen (ESCs) wurden durch Siebdruck-, Trocknungs- und Sinterungsprozesse hergestellt. Die ESCs wurden in verschiedenen SOC-Betriebsmodi getestet: SOFC, (SOEL, Dampf- und Kohlendioxid-Ko-elektrolyse (ko-SOEL) sowie im rSOC und sogar im Trockenelektrolyse-Betrieb mit Kohlendioxid. In-situ elektrochemische Charakterisierungen wurden durch Auswertung des Spannungs-/Stromverhaltens und der elektrochemischen Impedanzspektroskopie (EIS) durchgeführt. Parallel dazu wurde die Herauslösung von Nickelpartikeln aus den hergestellten LSCrN-Keramikpulvern mittels Temperaturprogrammierter Reduktion (TPR), Röntgenspektroskopie (XPS) und XRD-Techniken untersucht. Es zeigte sich, dass die Einführung von A-Leerstellen die Reduktion von metallischen Nickelpartikeln auf der Perowskit-Oberfläche fördert. Dabei wurde festgestellt, dass die Partikelverteilung von der Temperatur, der Atmosphäre und der Überspannung abhängig ist. Bei nominaler Betriebstemperatur (~ 860 °C) war die elektrochemische Leistung der entwickelten L65SCrN-Elektroden vergleichbar mit den modernen Ni-Cermet Elektroden, d.h. – 0.8 A·cm^{-2} bei 1.32 V.

Die Langzeitstabilität (~ 1000 Stunden) deutet darauf hin, dass die L65SCrN-Elektrode unter stark reduzierenden Atmosphären, wie z. B. in SOEL bei 860 °C, unter einer beschleunigten Leistungsverschlechterung aufgrund einer Veränderung der Transporteigenschaften leidet. Es wurde jedoch festgestellt, dass eine Senkung der Betriebstemperatur (unter 830 °C) eine geeignete Strategie sein könnte, um dieses Problem der Lebensdauer abzumildern. Diese Ergebnisse stehen im Zusammenhang mit einem Leistungsgewinn der Perowskit-Elektroden gegenüber den modernen Ni-Elektroden bei Temperaturen zwischen 770 °C und 830 °C. Dies ist möglicherweise auf niedrigere Reaktionsenergiebarrieren zurückzuführen. Diese Erkenntnisse wurden als Grundlage für eine Scale-up-Analyse von der Zellebene bis zur Systemebene, d. h. bis zum MW-Maßstab, verwendet, indem ein realer Anwendungsfall von SOEL-basierten Systemen für die Wasserstofferzeugung analysiert wurde. Diese Analyse ergab, dass der Einsatz von Perowskit-Elektroden in SOEL-Systemen, zusammen mit einer Senkung der Betriebstemperatur des Systems, zu einer erheblichen Verringerung der Anzahl der Zellen in den Stacks und damit der Systemkomponenten führen würde. Darüber hinaus würde auch die benötigte Menge an Ni-Rohstoff deutlich sinken, was künftige Probleme in der Versorgungskette, mit denen der Mineralienmarkt in den kommenden Jahren konfrontiert sein könnte, entschärfen würde. Diese Dissertation ebnet den Weg für die künftige Entwicklung alternativer Elektroden für SOC-Anwendungen und weist gleichzeitig auf potenzielle Vorteile im Systemmaßstab hin.

List of publications

This cumulative doctoral thesis is based mainly on three articles that were published after a peer-review process, from which the original texts are included in Chapter 12.

Article I: Diana-María Amaya-Dueñas, Guoxing Chen, Anke Weidenkaff, Noriko Sata, Feng Han, Indro Biswas, Rémi Costa and K. Andreas Friedrich, "A-site deficient chromite with in situ Ni exsolution as a fuel electrode for solid oxide cells (SOCs)" *J. Mater. Chem. A*, vol. 9, pp. 5685-5701, 2021.

Contribution Diana-María Amaya-Dueñas: Material synthesis, characterization (except XPS), cell manufacturing and cell electrochemical testing, as well as writing, evaluation, submission and review process.

Article II: Matthias Riegraf, Diana M. Amaya-Dueñas, Noriko Sata, K. Andreas Friedrich and R. Costa, "Performance and Limitations of Nickel-Doped Chromite Anodes in Electrolyte-Supported Solid Oxide Fuel Cells" *ChemSusChem*, vol. 14, pp. 2401-2413, 2021.

Contribution Diana-María Amaya-Dueñas: Material synthesis, characterization (except XRD), cell manufacturing and cell electrochemical testing (except sulfur tolerance experiments), as well as writing, evaluation and review process.

Article III: D. M. Amaya-Dueñas, M. Riegraf, A. Nenning, A. K. Opitz, R. Costa, and K. A. Friedrich, "Operational Aspects of a Perovskite Chromite-Based Fuel Electrode in Solid Oxide Electrolysis Cells (SOEC)," *ACS Applied Energy Materials*, 2022/07/08 2022, doi: 10.1021/acsaem.2c00680.

Contribution Diana-María Amaya-Dueñas: Material synthesis, characterization (except Van der Pauw measurements), cell manufacturing and cell electrochemical testing, as well as writing, evaluation, submission and review process.

Scientific results from additional publications are also presented in Chapters 11 and 12.

Table of contents

List of abbreviations

AEL	Alkaline electrolysis
ASC	Anode-supported cell
ASR	Area specific resistance
BSE	Back-scattered electrons
CGO	Gadolinium-doped ceria
CHP	Combined heat and power
CPE	Constant phase elements
CTE	Coefficient of thermal expansion
DPB	Double phase boundary
DRT	Distribution of relaxation times
ECM	Equivalent circuit model
EDX	Energy dispersive X-ray spectroscopy
EIS	Electrochemical impedance spectroscopy
ESC	Electrolyte-supported cell
IKTS	Fraunhofer Institute for Ceramic Technologies and Systems
KIT	Karlsruhe Institute of Technology
LF	Low frequency
LSCrN	Lanthanum strontium nickel chromite
LSCF	Lanthanum strontium cobalt ferrite
LSM	Lanthanum strontium manganite
HER	hydrogen evolution reaction
OER	oxygen evolution reaction
MIEC	Mixed ionic-electronic conductor

MF	Middle frequency
MSC	Metal-supported cell
OCV	Open circuit voltage
PEMFC	Polymer electrolyte membrane fuel cell
PEMEL	Polymer electrolyte membrane electrolysis
RWGS	Reverse water gas shift reaction
S/C	Steam-to-carbon
ScSZ	Scandia-stabilized zirconia
SE	Secondary electrons
SEM	Scanning electron microscopy
SOEC	Solid oxide electrolysis cell
SOEL	Solid oxide electrolysis
SOFC	Solid oxide fuel cell
TPB	Triple phase boundary
WGS	Water gas shift reaction
YSZ	Yttria-stabilized zirconia
3YSZ	$(Y_2O_3)_{0.03}(ZrO_2)_{0.97}$
8YSZ	$(Y_2O_3)_{0.08}(ZrO_2)_{0.92}$
XPS	X-ray photoelectron spectroscopy
XRD	X-ray diffraction

List of symbols

Symbol	Description	Unit
z	number of moles of electrons	-
$E°$	standard cell potential	V
E_{rev}	reversible cell potential	V
T	temperature	°C
a_i	activity of species *i*	-
v_i	stoichiometric coefficient of species *i*	-
$\Delta G_r^{T,P}$	change in Gibbs free energy of reaction	$kJ \cdot mol^{-1}$
$\Delta H_r^{T,P}$	change in enthalpy of reaction	$kJ \cdot mol^{-1}$
ΔS_r	change in entropy of reaction	$kJ \cdot mol^{-1}$
P	total pressure	Pa
$T \Delta S_r$	reversible heat of reaction	$kJ \cdot mol^{-1}$
V_{th}	thermoneutral cell voltage	V
V_{rev}	reversible cell voltage	V
ϵ_{el}	electrical efficiency	-
V_{cell}	cell voltage	V
η_{act}	activation losses overpotential	V
η_{ohmic}	ohmic losses overpotential	V
η_{conc}	concentration losses overpotential	V
ASR_{total}	total area specific resistance	$\Omega \cdot cm^2$
J	current density	$A \cdot cm^{-2}$
A	cell area	cm^2
r	area-normalized reaction rate	$mol \cdot cm^{-2} \cdot s^{-1}$
$\epsilon_{Faradaic}$	Faradaic efficiency	-
P_{cell}	cell power	W
I	current	A
$\frac{\dot{m}}{A}$	normalized hydrogen production	$kg\ H_2 \cdot cm^{-2} \cdot h^{-1}$
r_A	ionic radii of the atoms A	Å

t	tolerance factor	-
λ	wavelength of the incident beam	nm
d_{hkl}	lattice spacing	nm
θ	diffraction angle	°
ω	angular frequency	rad·s^{-1}
Z'	real impedance	Ω
Z"	imaginary impedance	Ω
R_{ohmic}	ohmic resistance	Ω
R_{pol}	polarization resistance	Ω
σ_{ion}	ionic conductivity	S·cm^{-1}
σ_{el}	electrical conductivity	S·cm^{-1}
ρ	resistivity	cm·S^{-1}
$P_s{}^i$	survival probability	-
σ_o	characteristic strength	Pa
m	Weibull modulus	-
$\varepsilon_{output/year}$	yearly energy output	GWh
$\frac{P_{system}}{\dot{m}_{H_{2-required}}}$	specific energy consumption	kWh·kg H$_2$$^{-1}$
$t_{operation/year}$	nominal operation of electrolyzers in a year	h
$\theta^{Ni}_{GWh/year}$	amount of Ni per energy output in a year	kg Ni·GWh^{-1}

List of constants

Symbol	Description	Value	Unit
F	Faraday constant	96.485	C·mol^{-1}
j	imaginary unit	$\sqrt{-1}$	-
R	ideal gas constant	8.314	J·K^{-1} mol^{-1}

1 Introduction

The Intergovernmental panel on climate change (IPCC) reported that between the years 1880 and 2012 the global average surface temperature has increased 0.85 °C. Until today, human and natural systems have been significantly altered with extreme weather phenomena, such as droughts, floods and sea level rise, as well as with biodiversity loss. All in all, these changes are producing unprecedent risks for human populations. The increase of fossil-fuel-based materials consumption and the dynamic changing lifestyles are major drivers of the rising of greenhouse gases emissions. For instance, the global carbon dioxide (CO_2) concentration has risen since year 2000 for about 20 ppm per decade, which is up to 10 times faster than any rise in CO_2 during the past 800.000 years [1].

The secondary-energy sector, i.e. electricity and heat generation as well as petroleum products and synthetic fuel production [2], represents three-quarters of the current greenhouse gas emissions and holds the key to avoid devastating effects on climate change. This great challenge that human kind is facing, is consistent with the significant reduction of CO_2 emissions to net zero by 2050. With this, the long-term increase in the average global temperature to 1.5 °C could be limited, which will require a complete transformation of the energy sector in terms of how we produce, transport and consume energy [3]. To address this problem, a considerable deployment of clean and efficient energy technologies is required. Scale-up of solar and wind energy sources would definitely contribute to the solution [3]. However, they are location-specific and intermittent energy sources and for this reason, energy storage is a vital aspect for the supply and demand in future renewable energy scenarios [4]. For instance, seasonal storage would be very relevant if the set of energy storage technologies would be broader and therefore would support the stability of power grids [3].

In vision of this and the Paris Agreement, the European Union launched the Hydrogen Strategy for a climate-neutral Europe in July 2020, with the main purpose to efficiently use hydrogen as energy carrier for power generation and energy storage, as well as on plenty of applications in the industry, transport, mobility and building sectors [5] [6] [7]. Also, other countries such as Chile [8] and Colombia [9] have published their hydrogen roadmaps in 2020 and 2021, respectively.

A key aspect of the green hydrogen production via water electrolysis is that disregarding the electrolysis technology, the required input of electricity derives from low CO_2 (renewable) sources [10], making it essential to reach the carbon neutrality by 2050 [5]. Hydrogen plays a vital role in the energy transition since it serves as energy carrier allowing renewable energy to be stored in a flexible way, while supporting the balance in energy supply and demand [10]. In the frame of current energy transition, fuel cells and electrolyzers are gaining significant interest due to their potential to generate power and also to store electrical energy in the form of valuable chemicals via electrolysis operation.

Fuel cells, for instance, are devices that convert chemical energy stored in fuels into electrical energy via redox reactions. An analogy with continuous stirring chemical reactors could be applied for fuel cells, because they will continue to yield a product (in this case electricity) as long as the raw material (fuel) is continuously supplied. This is the main difference between fuel cells and batteries, since the fuel cell is not consumed when electricity is produced [11]. A fuel cell consists of two electrodes that are spatially separated by an electrolyte. Their underlying operation principle can be explained with the following steps [11], as sketched in Figure 1:

1. Flow of reactants (fuel and air) into the fuel cell through the two porous electrodes which are isolated and spatially separated by the electrolyte.
2. Electrochemical reactions.
3. Ionic conduction (cations or anions) through the electrolyte – electronic conduction through an external circuit.
4. Products removal from the fuel cell (exhaust from each electrode compartment).

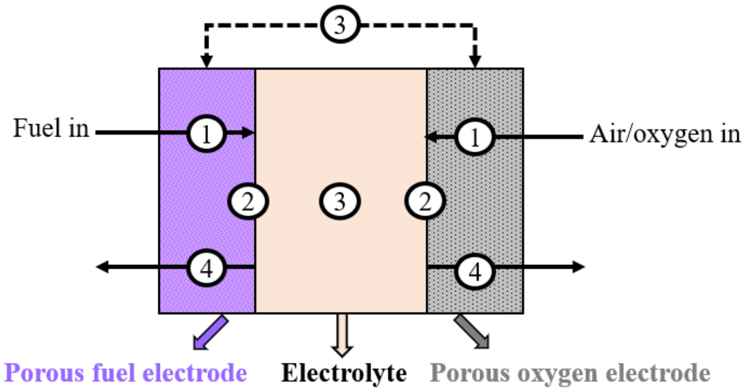

Figure 1 Electrochemical cell operating in power generation mode: (1) reactants transport, (2) electrochemical reaction interfaces, (3) ionic and electronic conduction and (4) products removal. Adapted from [11].

Based on the same fundamental principles, there are different types of electrochemical cells, depending on the type of fuel, materials components and operating temperature. Among them, there are five main types which are classified by the nature of their electrolyte's materials: phosphoric acid fuel cell (PAFC), polymer electrolyte membrane fuel cell (PEMFC), alkaline fuel cell (AFC), molten carbonate fuel cell (MCFC) and solid oxide fuel cell (SOFC) [11]. In this regard, the polymer electrolyte- and the alkaline-based cells, as well as the solid oxide cells (SOC) are technologies that currently are gaining more attention due to the possibility to also operate in electrolysis modes. Their broad range of operating temperatures starts from ~ 60 °C (for the alkaline systems) and from 80 °C up to ~ 200 °C for the polymer-based, and jumping to 600 up to 900 °C for SOC [11]. For the electrolysis operation, PEMEL stands for polymer electrolyte membrane electrolysis cells and AEL for alkaline electrolysis cells. For the case of SOFC another more general convention is used as solid oxide cells SOC, meaning that when these cells operate in electrolysis mode they are mostly known as SOEC, solid oxide electrolysis cells. However, it is important to note that SOC have the unique feature to operate in both modes with the same material configurations. For this reversibility in operation between fuel cell and electrolysis modes, these cells are mostly known as rSOC – reversible solid oxide cells.

In the frame of the energy transition and the importance of overcoming the peaks of energy demand with sustainable technologies, fuel cells and electrolyzers play a very important role due to their availability to generate power and to store energy in the form of valuable chemicals. In this sense, the concept of Power-to-X (P2X) technologies entails the conversion of renewable electrical energy in the form of fuels and chemicals [12]. Also, terms known as Power-to-gas and Power-to-heat are part of these technologies. Power-to-chemicals is related to the production of relevant raw materials for important industrial processes, such as carbon monoxide, formate/formic acid, ethylene or methanol [13] [14]. Power-to-fuel or also Power-to-liquid refer to the production of synthetic fuels, such as aircraft and freight fuels, by using carbon dioxide captured from the atmosphere or from industrial processes, such as steel and cement production, as well as industrial waste from coal power plants. Among the electrolysis technologies, solid oxide electrolysis (SOEL) benefit from kinetic and thermodynamic efficiencies by converting steam into hydrogen at high temperatures typically between 700°C and 900°C, in comparison to the low temperature technologies, such as AEL and PEMEL (< 200°C) [15]. Beyond electrolysis operation, importance should be given also to the co-electrolysis of H_2O and CO_2 at high temperature in order to produce syngas (H_2 + CO), which is considered a key feedstock that can be used as raw material for the Fischer-Tropsch (F-T) process for liquid fuels production [14] [16]. Due to the hydrocarbon-rich mixtures that are present in reactants and products streams in SOCs, substantial efforts on Research &

Development (R&D) are being made with the main purpose to improve the performance and availability of these systems on the long-term for plenty of P2X applications.

A primary concern of the R&D in SOC is the fuel electrode performance due to the variety of fuel and exhaust gases. Ni-based fuel electrodes have been widely studied and implemented at industrial scales due to the good catalytic activity for SOC operation, making them crucial for the performance, efficiency and durability of the SOC-based systems. However, SOC fuel electrodes are prone to irreversible microstructural alterations in atmospheres oscillating between reducing and oxidizing conditions [17], and also susceptible to sulfur poisoning and carbon deposition [18, 19] [20]. Other poisoning mechanisms that not only involve the fuel electrode, but also the oxygen electrode are chromia and silica poisoning [21].

This thesis focuses on the development and evaluation of a perovskite chromite-based fuel electrode for SOCs as alternative to replace the Ni cermet fuel electrodes on different SOC operating modes. The stability in dual atmospheres (i.e. oxidative and reducing) was evaluated, as well as in long-term experiments. The electrochemical performance was compared to the state-of-the-art fuel electrodes, for which comparable results were achieved. Among the first chapters of this thesis (Chapters 2 – 5), the fundamentals, the motivation and scientific approach, the materials and methods and the characterization techniques implemented are detailed and explained. In Chapter 6 a general discussion about the scientific context of SOCs and the role of perovskite fuel electrodes is thoroughly discussed, in which advantages, disadvantages and key aspects for further up-scaling of are addressed. As closure, the key results and the conclusions of this thesis are summarized in Chapter 7, followed by Chapter 8 with the perspectives and follow-up research activities.

2 Fundamentals

In this chapter, the fundamentals of thermodynamics in high temperature fuel and electrolysis cells are explained. Theoretical concepts of the electrode kinetics, as well as a description of the different types of SOC architectures and typically used materials are also presented. Figures of merit that relate the thermodynamic properties with the electrochemical performances of these high temperature cells are also detailed.

2.1 High temperature electrochemical cells

The following sketch explains these two types of operating modes: fuel cell (power generation) and electrolysis (energy storage), as depicted in Figure 2.

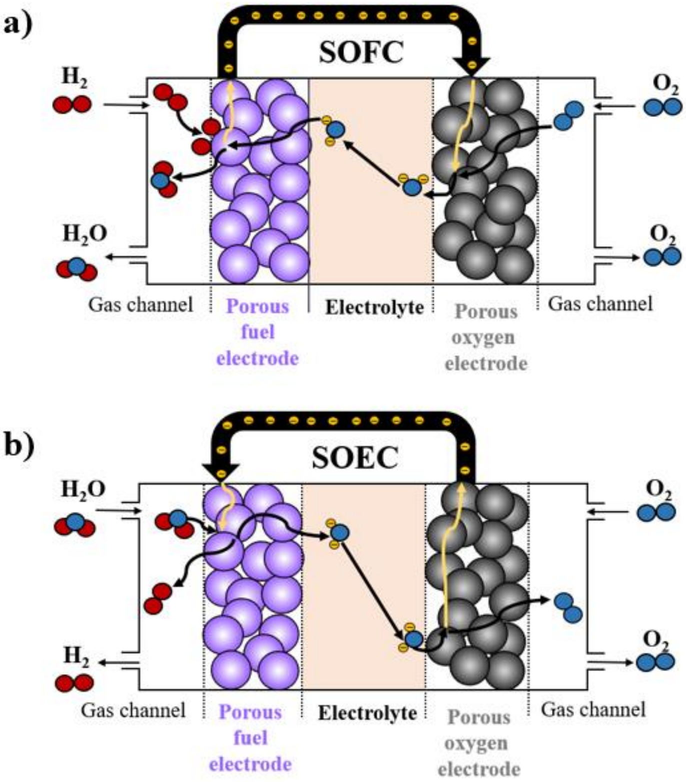

Figure 2 a) Fuel cell mode SOFC (power generation). b) Electrolyzer cell SOEC in electrolysis mode SOEL (energy storage).

In SOFC operation, porous fuel electrodes host the electrochemical oxidation of fuels, such as H_2, depleting oxygen anions O^{2-} and providing a significant concentration gradient of oxygen. This gradient is the driving force (or chemical potential) that is converted to electric potential to drive the electron flow from the fuel electrode to the oxygen electrode via an external circuit [22], as shown in Figure 2a.

On the contrary in SOEL operation, the porous fuel electrode hosts the water (steam) and/or CO_2 splitting reactions by electrolyzing these gases with (renewable) electrical energy, with the aim to yield H_2 and/or CO, providing an oxygen gradient concentration, leading to transport of O^{2-} anions from the fuel electrode through the electrolyte towards the oxygen electrode (Figure 2b). Oxygen electrodes are responsible for the electrochemical reduction of O_2 to O^{2-}, which are transported through the electrolyte between the electrodes in both SOFC and SOEL operating modes [22].

In the following section, the thermodynamic and kinetics theories applied to the various SOC operating modes are explained and discussed.

2.2 Thermodynamics

The performance of an electrochemical cell is mainly described by thermodynamic and electrochemistry principles. The kinetics of redox reactions as well as the mass and energy transport phenomena within these cells determine their extent of operation and applications. These aspects are strongly influenced by operating parameters such as the pressure, temperature and gas compositions [23]. By taking an electrochemical cell as a control volume, the enthalpies of the reactants are equivalent to the sum of the enthalpies of the products, the net generated or consumed heat (including heat losses from the surroundings), as well as the DC power input/output [23].

2.3 Nernst potential on electrochemical cells

From a thermodynamic perspective, the maximum electrical work output is related to the free-energy change of a half-cell reaction at a constant temperature and pressure. The free energy change of such reaction is indicated by equation (1) [23]:

$$\Delta G = -zFE_{rev} \qquad (1)$$

Where ΔG is the change in the free energy at a given temperature and pressure (also known as the chemical potential), z the number of moles of electrons involved in the reaction, E_{rev} the ideal cell potential and F the Faraday's constant [23]. The Nernst equation gives the relationship between the ideal cell potential at standard conditions E° and the ideal equilibrium cell potential E_{rev} at different temperatures and pressures. For a system with an arbitrary number of reactants and products, the Nernst equation (2) takes the following form:

$$E_{rev} = E^{\circ} - \frac{RT}{zF} ln \frac{\prod a_{products}^{v_i}}{\prod a_{reactants}^{v_i}} \tag{2}$$

Where the R is the universal gas constant, T the cell temperature and a the activity of each species with their corresponding stoichiometric coefficient v_i [11]. On an electrochemical cell, the Nernst equation describes the electrode potential, and the difference between both electrodes' potential, when no electric current flows through the cell, is known as reversible voltage (V_{rev}) or open circuit voltage OCV.

2.4 High temperature fuel cells

In fuel cell operation the following half-reactions in equations (3) and (4) are considered:

$$Fuel\ electrode: H_2 + O^{2-} \leftrightarrow H_2O + 2e^- \tag{3}$$

$$Oxygen\ electrode: \frac{1}{2}O_2 + 2e^- \leftrightarrow O^{2-} \tag{4}$$

Due to the high operating temperatures, educts and products are gaseous species and may be considered as ideal gases. Their activity coefficients are thus equivalent to their partial pressures, turning Nernst equation for the SOFC case as:

$$V_{rev,SOFC} = \frac{\Delta G^{\circ}}{zF} - \frac{RT}{zF} ln \frac{p_{H_2O}}{p_{H_2} p_{O_2}^{1/2}} \tag{5}$$

2.5 High temperature steam electrolysis cells

In SOEL operation, the Nernst equation may be applied with the corresponding partial pressures, but having in mind the sign of the equation terms, since electrolysis operation implies input of electrical energy. The fuel and oxygen electrodes corresponding half-reactions are described by equations (6) and (7) respectively:

$$Fuel\ electrode: H_2O + 2e^- \leftrightarrow\ H_2 + O^{2-} \tag{6}$$

$$Oxygen\ electrode: O^{2-} \leftrightarrow \frac{1}{2}O_2 + 2e^- \tag{7}$$

In this case the $V_{rev,SOEC}$ is given by equation (8) [24]:

$$V_{rev,SOEC} = -\frac{\Delta G^{\circ}}{zF} + \frac{RT}{zF} ln \frac{p_{H_2} p_{O_2}^{1/2}}{p_{H_2O}} \tag{8}$$

For electrolysis operation, $\Delta G_r^{T,P}$ is also considered as the minimum electric energy supply required for the water electrolysis reaction, which is related to the change in reaction enthalpy $\Delta H_r^{T,P}$ and reaction entropy $\Delta S_r^{T,P}$ at a given temperature T and total pressure P [23] [25] [26]:

$$\Delta G_r^{T,P} = \Delta H_r^{T,P} - T\Delta S_r^{T,P} \tag{9}$$

The relation between these thermodynamic parameters in a broad range of temperature is shown in Figure 3 for the steam electrolysis reaction. This plot shows that the electric demand ($\Delta G_r^{T,P}$) decreases while the heat energy demand ($T\Delta S_r$) increases with temperature increment [25].

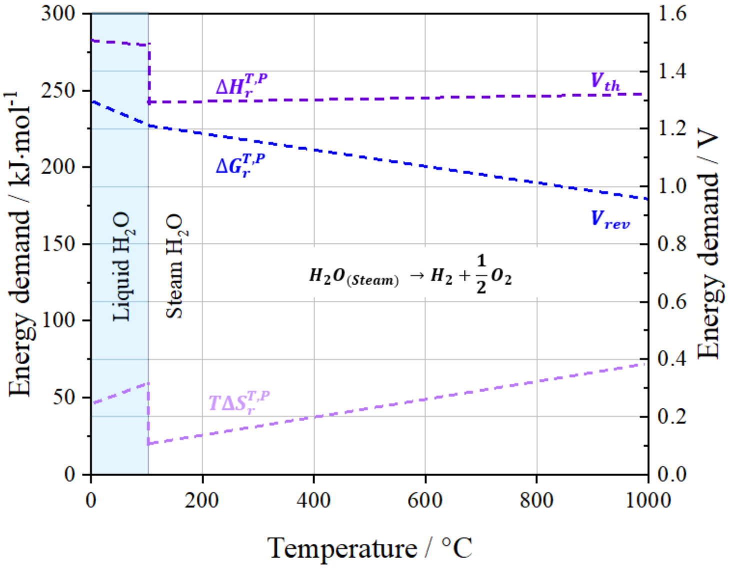

Figure 3 Thermodynamic properties and corresponding voltages for water electrolysis as a function of the temperature. Adapted from [27].

Other important cell voltages can be calculated from these relations: the thermoneutral cell voltage V_{th} and the reversible cell potential V_{rev} [27], as shown in equations (10) and (11):

$$V_{th} = \frac{\Delta H_r^{T,P}}{zF} \tag{10}$$

$$V_{rev} = \frac{\Delta G_r^{T,P}}{zF} \tag{11}$$

Where V_{th} corresponds to the required voltage for adiabatically operation, where no heat is lost or added to the cell. V_{rev} corresponds to the minimum cell voltage required for a reversible process when heat is provided by the surroundings [27]. For SOEL for instance at 860 °C and atmospheric pressure as in equation (12), the enthalpy of reaction $\Delta H_{r,SOEC}^{T=860\,°C,1\,bar}$ is 249 kJ/mol. So by applying this value in equation (10), the thermoneutral voltage for steam electrolysis is 1.29 V [28].

$$H_2O_{(Steam)} \rightarrow H_2 + \frac{1}{2}O_2\,, \qquad \Delta H_r^{860°C,1\,bar} = 249\,\frac{kJ}{mol} \tag{12}$$

At the typical SOEL operating temperatures, V_{th} remains relatively constant. Only below the boiling point of water would result in significantly different values [27], as shown with the blue-area in Figure 3. At the thermoneutral voltage the cell can be operated at thermal equilibrium with an electrical efficiency ϵ_{el} of 100%. The operation below this voltage corresponds to an endothermic regime where the electric energy is lower than the enthalpy of reaction and the heat must be supplied. Above the thermoneutral voltage, exothermic mode is achieved, where electrical efficiencies below 100% are obtained [25]. The electrolysis electrical efficiency is defined as the thermoneutral voltage divided by the measured cell voltage V_{cell} [27]:

$$\epsilon_{el} = \frac{V_{th}}{V_{cell}} \tag{13}$$

The applied cell voltage required for water electrolysis is not only a function of thermodynamic parameters, but also of additional overpotentials that are related to different losses within the cell, that could also affect the cell performance [27].

2.6 High temperature CO_2 electrolysis cells

Besides the electrochemical reactions that take place within a SOC in operation, important factors such as parallel thermodynamic reactions should be considered. Due to the fuel flexibility on both SOFC and SOEL operation, specifically with hydrocarbon-based fuels, carbonaceous species could lead to the formation of solid clusters of carbon within the fuel electrodes. In SOECs, carbon dioxide could also be electrolyzed to produce oxygen and carbon monoxide, which is an important raw material for a wide range of industrial applications, e.g., for the production of commodity and specialty chemicals [29]. The oxygen electrode half-reaction is the same as for steam electrolysis - as shown in equation (15). On the fuel electrode, the carbon dioxide electrolysis takes place as described by equation (14) [29]:

$$Fuel\ electrode: CO_2 + 2e^- \leftrightarrow\ CO + O^{2-} \tag{14}$$

$$Oxygen\ electrode: O^{2-} \leftrightarrow \frac{1}{2}O_2 + 2e^- \qquad (15)$$

Hence, in this case the Nernst equation is as follow (16):

$$V_{rev,CO_2SOEC} = -\frac{\Delta G^{\circ}}{zF} + \frac{RT}{zF} ln \frac{p_{CO} p_{O_2}^{1/2}}{p_{CO_2}} \qquad (16)$$

Similarly to water electrolysis, the evolution of the thermodynamic properties as a function of temperature is depicted for CO_2 electrolysis in Figure 4. This plot also shows how the electric demand decreases as the heat energy demand increases, while increasing the temperature. For instance, at 860 °C the enthalpy of reaction for CO_2 electrolysis $\Delta H_{r,CO_2SOEC}^{T=860\,°C,1\,bar}$ is ~ 283 kJ/mol (equation (17)), which does not change significantly in the broad range of temperatures.

$$CO_2 \rightarrow CO + \frac{1}{2}O_2\,, \qquad \Delta H_r^{860°C,1\,bar} = 283\,\frac{kJ}{mol} \qquad (17)$$

From equation (10) the thermoneutral voltage is calculated as ~ 1.47 V, which can also be observed as the $\Delta H_r^{T,P}$ data in Figure 4 (right axis).

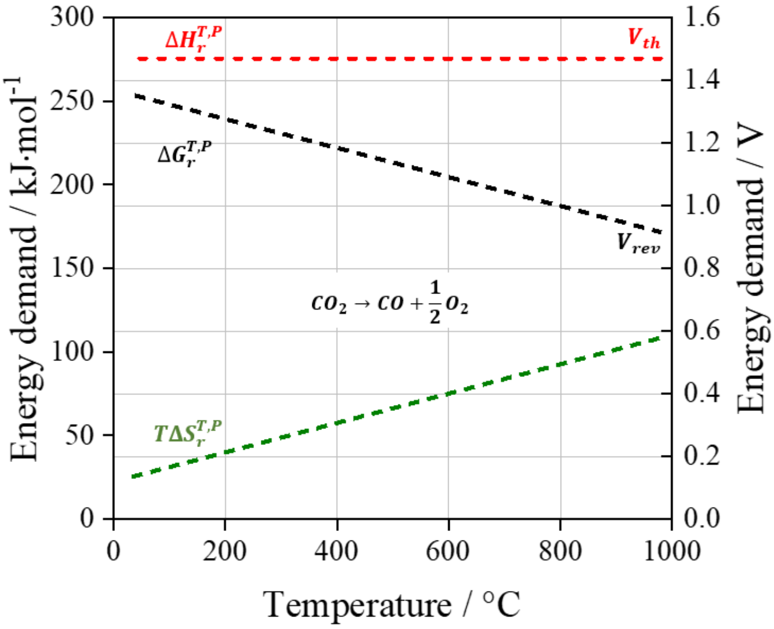

Figure 4 Thermodynamics and corresponding voltages of the CO_2 electrolysis reaction as a function of the temperature. Adapted from [29].

2.7 High temperature H_2O - CO_2 co-electrolysis cells

In regard to H_2O and CO_2 co-electrolysis operation at high temperature, both endothermic reactions, equations (6) and (14) take place simultaneously at the fuel electrode, resulting in equation (18) .

$$H_2O_{(Steam)} + CO_2 \rightarrow H_2 + CO + O_2 \tag{18}$$

Furthermore, this electrochemical reduction reaction is linked to the reverse water gas shift reactions (RWGS) shown in equation (19), which is also endothermic [28]. The production of oxygen takes place at the oxygen electrode [26], as depicted in equation (20).

$$RWGS: H_2 + CO_2 \rightarrow H_2O_{(Steam)} + CO, \qquad \Delta H_r^{860°C,1\,bar} = 34\frac{kJ}{mol} \tag{19}$$

$$Oxygen\ electrode: 2O^{2-} \leftrightarrow O_2 + 4e^- \tag{20}$$

The estimation of the Nernst voltage for H_2O and CO_2 co-electrolysis from the products and reactants at the fuel electrode results difficult if the gas composition is not at equilibrium, given the influence of the RWGS - WGS reactions. Due to the presence of the RWGS reaction on the fuel electrode, it is still not completely clear if this reaction contributes to the CO production [26]. However, Stempien et al. reported that the direction of this reaction depends mainly on the temperature of the steam and carbon dioxide mixture: below 827 °C the water gas shift reaction (WGS) will take place, favoring the production of hydrogen and carbon dioxide [30]. Additionally, the authors also calculated an equilibrium potential for high temperature H_2O and CO_2 co-electrolysis, by combining the Nernst equations for both H_2O electrolysis and CO_2 electrolysis reactions as a function of the coverage of each species [31]. The authors assumed an adsorption process that follows the Langmuir isotherm, in which the number of active sites available for adsorption on the fuel electrode is required [31].

Due to the lack of data about such constants in lanthanum-chromites with doping of nickel on the B-site, this approach was not considered in this thesis. Nevertheless, the Nernst voltage could also be calculated as a function of the oxygen species. Such voltage is simplified because operating parameters such as temperature, pressure and species do not vary, i.e. there is no chemical potential difference ($\Delta G^{\circ} \sim 0$). Hence, the Nernst voltage could be calculated with the partial pressure of oxygen on both sides of the cell, as [31]:

$$V_{rev,O_2 co-SOEC} = \frac{RT}{zF} ln \frac{p_{O_2 fuel\ electrode}}{p_{O_2 oxygen\ electrode}} \tag{21}$$

In this thesis, the thermodynamic tool and database Cantera [32] was used to calculate the values of the thermodynamic properties in equilibrium (*G*, *H* and *S*) of the gases in the fuel electrode and oxygen electrodes, depending on a specific fuel gas mixture, as well as including the air. At equilibrium, the gas compositions and thus the partial pressures were also calculated for both electrodes. From those results, the oxygen partial pressures at the fuel and oxygen electrodes were taken at a specific temperature and absolute pressure, which allowed to calculate the Nernst voltage for co-electrolysis operation, as in equation (21). Important to note is that for this Nernst calculation, the number of electrons *z* corresponds to 4 instead of 2, as equation (20). This is explained by combining the electrolysis reactions on the fuel electrode (6) and (14) with the reaction on the oxygen electrode (20).

This approach was also corroborated by calculating the Nernst voltage for each electrolysis reaction separately by 3 ways:

(i) with the Nernst voltage for steam electrolysis reaction in equation (8),
(ii) for carbon dioxide electrolysis reaction in equation (16) and
(iii) with the oxygen production in equation (21).

These 3 equations resulted in the same values for the Nernst voltage in co-electrolysis operation, which is expected from Hess law.

In general, the thermoneutral voltage assumes that the gases are in thermodynamic equilibrium. The relation of the thermodynamic properties in co-electrolysis operation can be also observed in a wide range of temperature as shown in Figure 5. In this thesis, the enthalpy values used for this calculation were also calculated from Cantera [32].

Similarly, to the other electrolysis operating modes, the thermoneutral voltage can be calculated by applying equation (10) as following:

$$V_{th_{co}-SOEC} = \frac{\Delta H_r^{T,P}}{zF} = \frac{(H_{H_2}^{T,P} + H_{CO}^{T,P} + 0.21 * H_{O_2}^{T,P} - H_{CO_2}^{T,P} - H_{H_2O}^{T,P})}{4F} = \sim 1.32\ V \tag{22}$$

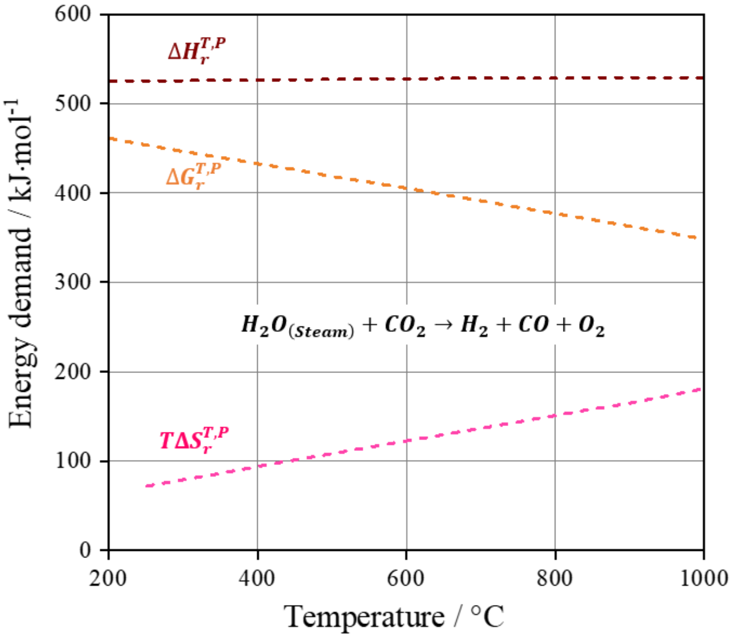

Figure 5 Thermodynamic properties of H_2O and CO_2 co-electrolysis reaction as a function of the temperature. Adapted from [28].

However, an important challenge during co-electrolysis operation is to avoid the risk given by carbon deposition in the fuel electrode via the Boudouard equilibrium reaction, in equation (23):

$$Boudouard: 2CO \leftrightarrow CO_2 + C_{(s)}\ , \qquad \Delta H_r^{860°C, 1\ bar} = -169\,\frac{kJ}{mol} \tag{23}$$

This reaction could lead to the formation of carbon, sometimes in the form of nanotubes or whiskers on the Ni surface, causing fatal failure of the SOC. The evolution of the reaction towards solid carbon is favored at lower temperatures and is catalyzed by metallic nickel. Owing the fast reaction rates of reforming reactions, it is possible to assume that the carbon formation regime is governed by the thermodynamic equilibrium of the C-H-O mixtures as a function of the composition, pressure and temperature [28], as shown in the ternary equilibrium diagram of C-H-O mixtures (Figure 6). Hence, careful selection of the operating conditions is essential to avoid *operando* carbon deposition on the fuel electrode [28].

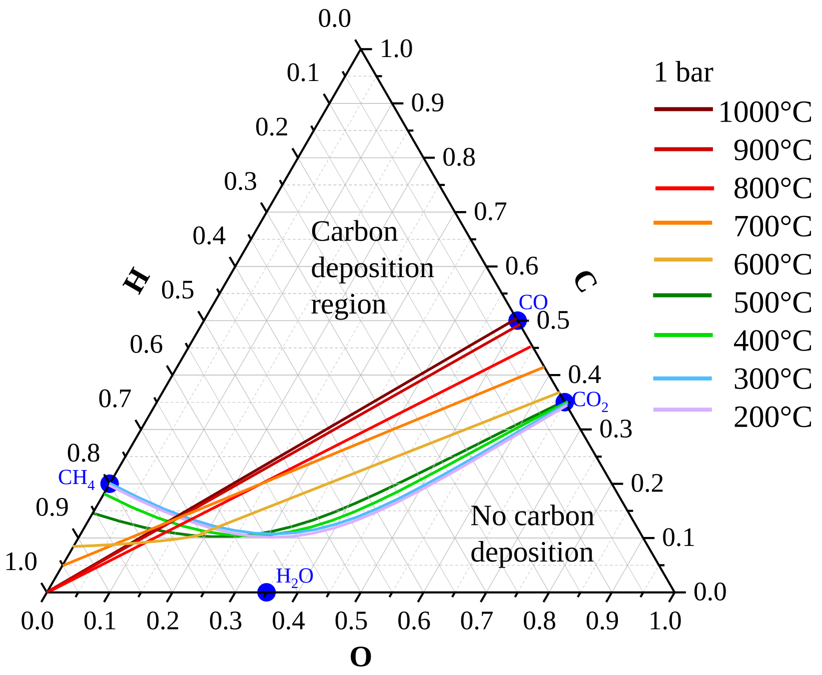

Figure 6 C-H-O ternary diagram with equilibrium compositions. Temperature profiles were adapted from [33].

Beyond thermodynamic properties, the cell performance is governed by the kinetics of the electrochemical reactions that take place within the electrodes, which are typically represented as voltage losses. These concepts are explained in the next section, starting with the current-voltage *i*-*V* characteristic theoretical concepts.

2.8 Kinetics

2.8.1 Current-voltage (*i*-*V*) characteristics

The performance of an electrochemical cell can be evaluated with the current-voltage (*i*-*V*) characteristics curve (Figure 7). Typically, these curves are plotted in terms of the current density at a given voltage [11]. Ideally, an electrochemical cell would supply/consume a constant amount of current while maintaining a constant voltage defined by thermodynamics. However, the more current is supplied/consumed by the cell, the greater these losses. The three main type of losses are [11]:

- Activation losses η_{act}: due to the electrochemical reaction kinetics on the fuel electrode and oxygen electrode.

- Ohmic losses η_{ohmic}: due to ionic conduction on the electrolyte, electronic transport in the electrodes, current collection and interfacial resistances.
- Concentration losses η_{conc}: due to the mass transport limitations.

These losses are commonly referred as overpotentials η, and the sign should be adjusted as a function of the operating mode. If the cell voltage in SOFC mode is calculated, then the overpotentials should be subtracted from the ideal thermodynamic voltage (OCV) and if the cell is operating in SOEC, the overpotentials should be summed to the OCV, as described in equation (24):

$$V_{cell} = V_{rev} \pm \eta_{act} \pm \eta_{ohmic} \pm \eta_{conc} \tag{24}$$

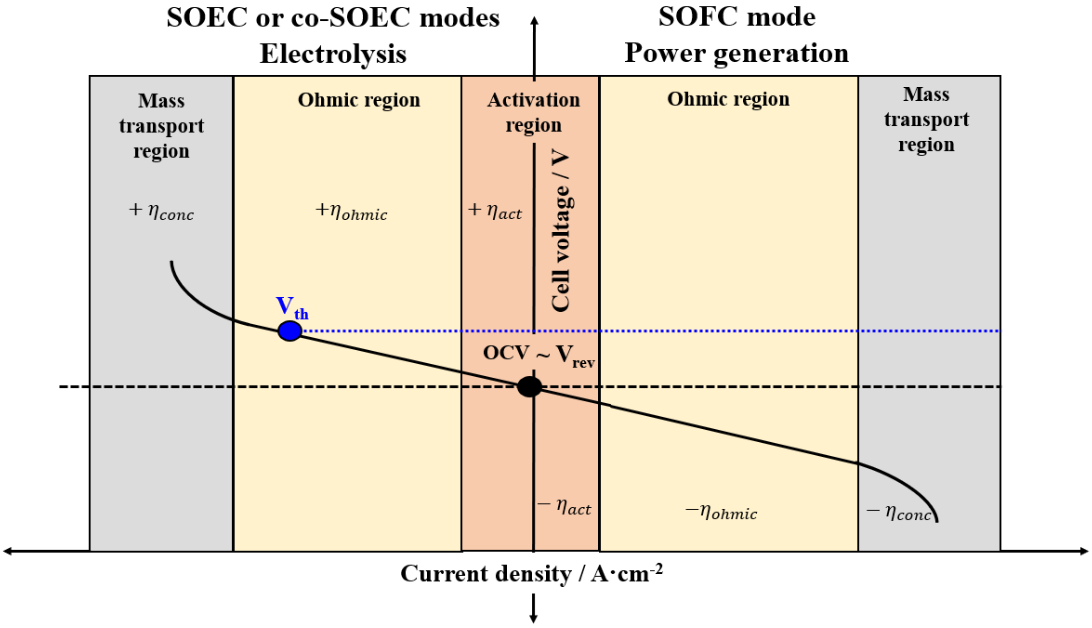

Figure 7 Current-voltage (*i*-*V*) characteristics curve for SOFC and SOEC operating modes. The cell voltage is depicted, as well as the different predominance regions of the overpotentials. Adapted from [11].

In a first approximation, the cell voltage is described by Ohm's law as a function of the OCV, the total area specific resistance ASR_{total} ($\Omega \cdot cm^2$) and the current density J, as stated in equation (25):

$$V_{cell} = V_{rev} \pm ASR_{total} * J \tag{25}$$

Furthermore, the ASR_{total} is also a function of the different overpotentials on the cell, which can be expressed in terms of the corresponding ASR for each overpotential, as described by equations (26) and (27):

$$ASR_{total} = \frac{|\,\eta_{act} + \eta_{ohmic} + \eta_{conc}|}{J} \tag{26}$$

$$ASR_{Total} = (ASR_{act}) + (ASR_{ohmic}) + (ASR_{conc}) \tag{27}$$

These losses could be further deconvoluted in terms of the different electrodes and interfaces on the cell, as shown in equation (28). For instance, the activation area specific resistance ASR_{act} can be deconvoluted as a function of the fuel and oxygen electrode as ASR_{FE} and ASR_{OE} respectively. The ohmic losses ASR_{ohmic} could be written in terms of the area specific resistance of the electrolyte ASR_{E} and the current collection interfaces ASR_{CCI}, and the concentration loss contribution is related to the area specific resistance of the gas diffusion and transport limitations, ASR_{Gas}.

$$ASR_{Total} = (ASR_{FE} + ASR_{OE}) + (ASR_{E} + ASR_{CCI}) + (ASR_{Gas}) \tag{28}$$

Well-designed cells typically give an ASR_{total} between 0.05 and 0.1 $\Omega{\cdot}cm^2$, for which the ASR_{ohmic} term mostly accounts for the electrolyte resistance and thickness. In case the electrolyte thickness cannot be reduced, the ohmic term could be decreased with highly ionic conductors [34].

2.8.2 Kinetic/activation overpotential

The produced/consumed current *i* that corresponds to the amount of electrons involved in the electrochemical reaction per unit of time, depends on the reaction rate, which is a relevant parameter for the cell performance [35]. From Faraday's law, the current can be expressed as equation (29) [35]:

$$i = \frac{dQ}{dt} \tag{29}$$

Where *Q* is the charge (in *C*) and *t* is time. Assuming that each electrochemical reaction is the transfer of *z* electrons, then equation (29) can be written as [35]:

$$i = zF\frac{dN}{dt} \tag{30}$$

Where *dN/dt* is the rate of electrochemical reaction rate (mol/s) and *F* corresponds to the Faraday's constant (96.485 C/mol) [35]. Electrochemical reactions deal with the charge transfer between an electronic conductor and a chemical species. In SOCs, the electrode has to be porous to enable the gaseous chemical species to be in contact with the electronic conductor and the electrolyte [35]. Current density allows to measure the electrochemical reaction rate per interface area J (A·cm^{-2}) as the normalized value of the current by unit area-basis, i.e. by the active cell area A, as shown in equation (31):

$$J = \frac{i}{A} \tag{31}$$

$$r = \frac{1}{A}\frac{dN}{dt} = \frac{i}{AzF} = \frac{J}{zF} \tag{32}$$

The area-normalized reaction rate r (mol/cm^2·s) in terms of the current density could be expressed as in equation (32). However, the produced/consumed current is also limited. Electrochemical reaction rates are finite because an energy barrier (also called activation energy barrier) impedes the conversion of reactants into products [35]. As illustrated in Figure 8, the reactants should overcome a hill in order to be converted into products, in which the probability that the reactants can overcome such barrier determines the rate at which the reaction takes place [35].

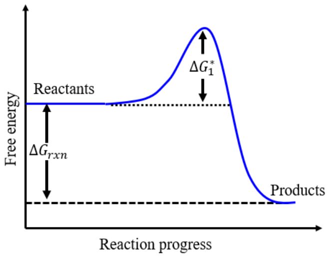

Figure 8 An activation energy barrier (ΔG_1^*) impedes the conversion of reactants to products. Adapted from [35].

Hence, the produced/consumed current by an electrochemical reaction is the variable of outmost interest. Knowing that current density J and reaction rate r are related by equation (32) as $J=zFr$, then the current density in the forward direction and reverse direction could be expressed respectively as equations (33) and (34) [35]:

$$J_1 = zFc_R f_1 e^{-\frac{\Delta G_1^*}{RT}} \tag{33}$$

$$J_2 = zFc_R f_2 e^{-\frac{(\Delta G_1^* - \Delta G_r^*)}{RT}} \tag{34}$$

Under thermodynamic equilibrium conditions, the forward and reverse current densities are balanced $J_1 = J_2 = J_o$, where J_o is also known as the reaction exchange current density [35].

In electrochemical reactions, charged species are present as either reactants or products, where their free energy is a function of the cell voltage. If the cell voltage is modified, the activation energy barrier would be also. When the activation overpotential η_{act} is applied to the cell, the activation energy barrier of the forward reaction is favored by a factor of $\alpha zF\eta_{act}$, while the activation energy barrier of the reverse reaction is decreased by a factor of $(1-\alpha)zF\eta_{act}$ [35]. The coefficient α quantifies how to the change in electrical potential across the reaction interface affects the size of the forward versus reverse activation energy barriers, which for most electrochemical reactions lies between 0.2 and 0.5 [35]. Therefore, including the η_{act} contribution to the current density expression for both forward and reverse reactions, the respectively current densities could be written as [35]:

$$J_1 = J_o e^{\frac{\alpha zF\eta_{act}}{RT}} \tag{35}$$

$$J_2 = J_o e^{\frac{-(1-\alpha)zF\eta_{act}}{RT}} \tag{36}$$

Hence, the net current $J = (J_1 - J_2)$ known as the Butler-Volmer equation corresponds to:

$$J = J_o \left[e^{\frac{\alpha zF\eta_{act}}{RT}} - e^{\frac{-(1-\alpha)zF\eta_{act}}{RT}} \right] \tag{37}$$

This equation is considered as the cornerstone of electrochemical kinetics and it is used as the starting point to describe the relation between current and voltage in fuel cells and electrolyzers. This equation predicts that the exchange current density is proportional to the electrochemical reaction rate at a given activation overpotential, either for the fuel electrode or for the oxygen electrode. Meaning that such electrochemical reactions lead to voltage losses that are represented by η_{act}.The Butler-Volmer equation can be simplified with two approximations for the two extrema of η_{act} [35]:

- For small η_{act} (for η < ~15 mV) an expansion of a Taylor series of the exponential terms can be applied as:

$$J = J_o \frac{nF\eta_{act}}{RT} \tag{38}$$

- For large η_{act} (for η > ~50 - 100 mV), the second exponential term of the Butler-Volmer equation is considered as negligible. Then, the forward reaction dominates, yielding an irreversible reaction process with η_{act} as:

$$\eta_{act} = -\frac{RT}{\alpha nF}\ln(J_o) + \frac{RT}{\alpha nF}\ln(J) \tag{39}$$

Where J_o and α could be estimated by linear fitting of η_{act} versus $ln(J)$ or $log(J)$ yielding the following expression known as Tafel equation, where b is called the Tafel slope [35]:

$$\eta_{act} = a + b\ log(J) \tag{40}$$

In order to improve the kinetic performance on an electrochemical cell, the main parameter to influence (and to increase) would be J_o, which is related to the rate of exchange between reactants and products in their equilibrium states. Three main forms to increase J_o are described as following (for the forward reaction) [35]:

- Increase the reactant concentration c_R.
- Decrease the activation energy barrier ΔG_1^*.
- Increase the temperature T.
- Increase the number of reaction sites: related to the increment of the reaction surface interface.

However, here is important to mention the role of α, which would also be affected by the selected catalyst. The Butler-Volmer equation also predicts that the increment in α would yield a higher current density. Ergo, a catalyst with high α values should be targeted, since the cell performance would significantly improve with higher current densities [35].

Ideally, SOCS electrodes with highly porous 3D structures should guarantee contact sites between: (i) the gas-phase (through the pores), (ii) the electrical conductive phase and (iii) the electrolyte [35]. These reaction sites are known as triple-phase zones or triple-phase boundaries (TPBs), which state that the electrochemical reaction could only occur where the three following phases are in contact: electrolyte particles, gas and electrically connected catalyst (for the case of the cermet-based electrodes). With perovskite electrodes, typically mixed ionic and electronic conductors (MIEC) are used, in which the electrochemical reaction takes place at the double-phase boundaries (DPBs) between gas particles and mixed ionic and electronic conductive particles. A sketch for the TPBs and DPBs is shown in Figure 9, where a cermet fuel electrode and a MIEC-based fuel electrode are depicted. Concerning the materials selection (both on the fuel and oxygen electrodes), relevant characteristics should be considered [35] [36]:

- Dual atmosphere tolerant (oxidative and reducing)
- High porosity
- High catalytic activity (high J_o)
- High electrical conductivity
- Good mechanical strength
- Good manufacturability

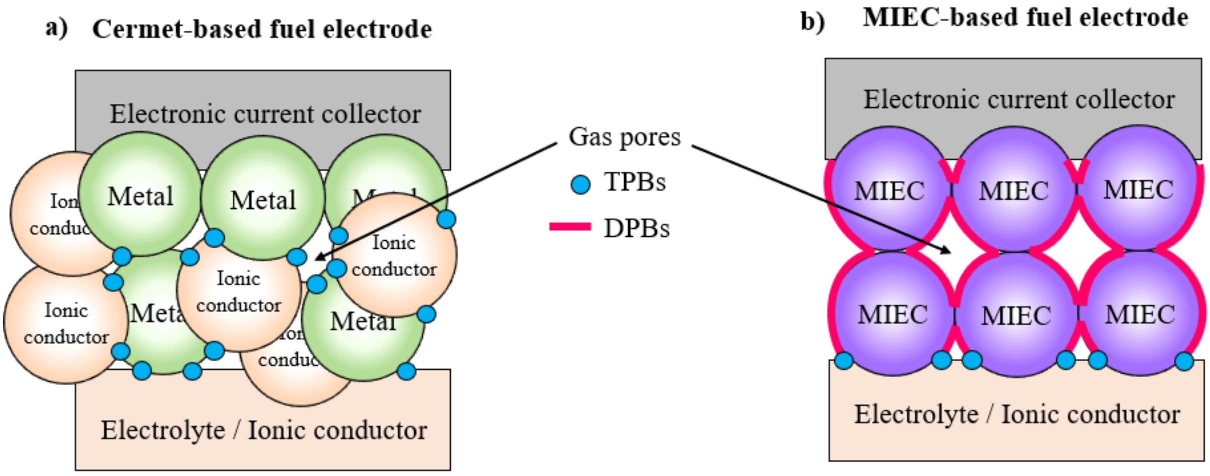

Figure 9 Simplified sketch for the TPBs and DPBs on (a) a cermet-based fuel electrode and (b) a MIEC-based fuel electrode.

Beyond 1D interactions, the catalytic thickness within the electrode is also another relevant parameter. Typically, the thickness of most of the active catalyst layer is comprised between ~10 and 50 µm. On one hand, a thin layer favors the gas diffusion and fuel conversion, and on the other hand thicker layers incorporate higher catalyst loading which yield to more TPBs and therefore a catalyst layer optimization requires a complex balance between mass transport and catalytic activity [35].

2.8.3 Ohmic overpotential

Besides the energy loss that fuel cells need to undergo in order to favor their kinetics, a relevant overpotential is associated to the intrinsic resistance of the cell’s conductors to charge flow. Such loss obeys Ohm’s law and therefore is denoted as Ohmic loss. As mentioned in section 2.8.1, ohmic losses, denoted by η_{ohmic}, are mostly due to ionic conduction in the electrolyte, the current collection (dependent on the electrical conductivity of the collector material) and interfacial resistances. Following the Ohm's law linear behavior of the cell voltage in terms of the current, this conductor resistance R_{ohmic} corresponds to the slope of Ohm's law $V = iR$, which could also be expressed in terms of the conductor length L, cross-sectional area A and conductivity σ as in equation (41). However, this expression could also be written in terms of the electronic R_{elec} and the ionic R_{ionic} resistance contributions as equation (42), where the ionic contribution tends to dominate due to the difficulty of ionic charge transport towards electronic charge transport. The contact resistance $\mathrm{R_{CCI}}$ associated to the interfaces between electrolyte and electrodes should also be considered, as well as the current collection contribution [34].

$$\eta_{ohmic} = iR_{ohmic} = i\left(\frac{L}{A\sigma}\right) \tag{41}$$

$$\eta_{ohmic} = iR_{ohmic} = i(R_{elec} + R_{ionic} + \mathrm{R_{CCI}}) \tag{42}$$

On electrochemical cells, ohmic losses could be minimized by implementing thin electrolytes with high (ionic) conductivity materials [34].

2.8.4 Concentration overpotential

In electrochemical reactions, the concentration losses (η_{conc}) could be represented as the reactants depletion and products accumulation at the catalyst layer within the electrode. This phenomenon can be explained with Figure 10, where the concentration of the reactants c_R^* at the catalyst layer is less than the concentration of reactants c_R^0 (meaning within the gas flow channel): $c_R^* < c_R^0$. Whereas for the products concentration c_P^* at the catalyst layer is greater than the concentration of the products at the flow channel c_P^0: $c_P^* > c_P^0$. Such concentration gradient influences the electrochemical cell performance with the following aspects [37]:

1. Nernstian losses: As described by the Nernst equation, the cell voltage would decrease due to the depletion of reactant concentration at the catalyst layer with respect to the concentration on the gas bulk.
2. Reaction losses: The activation losses related to the electrochemical reaction kinetics would also increase because of the reactant concentration decrement, while the product concentration at the catalyst layer increases, as predicted by the Butler-Volmer equation.

Therefore, the cumulative contribution of these losses is what is typically referred as concentration losses or mass transport losses [37].

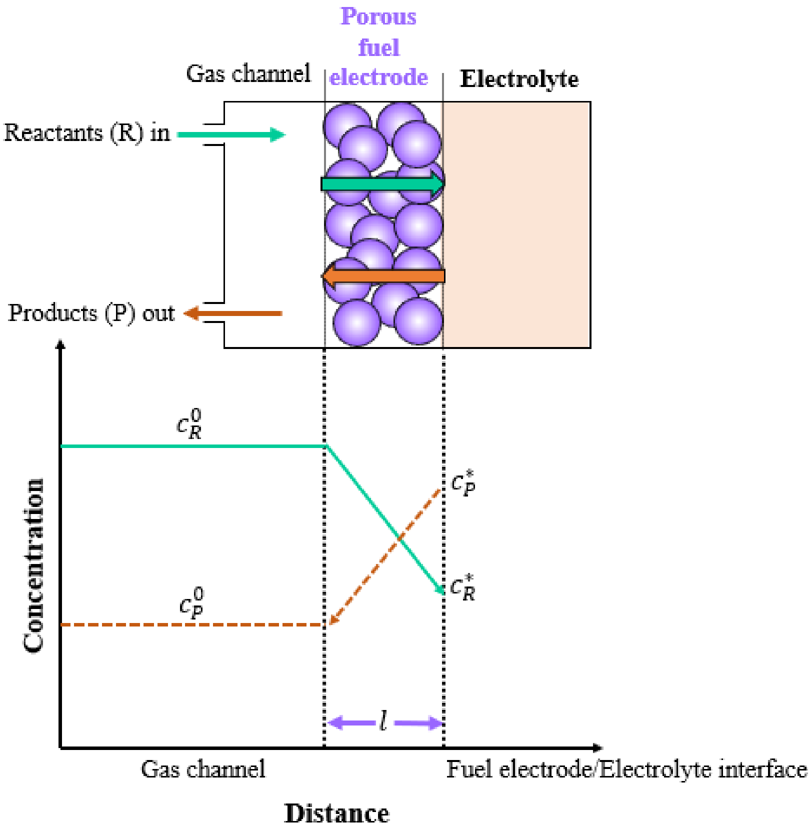

Figure 10 Simplified sketch of the mass transport phenomena within a SOC fuel electrode. Convective flows of reactants and products within the fuel gas channel correspond to the species concentration outside the diffusion layer (electrode), as c_R^0 and c_P^0. Adapted from [37].

Having these contributions in mind, the operating current density of the cell could be written as equation (43):

$$J = zFD^{eff}\frac{c_R^* - c_R^0}{l} \quad (43)$$

Where D^{eff} (cm^2/s) is the effective reactant diffusivity within the catalyst layer (also dependent on the electrode porosity and tortuosity) and l is the electrode thickness, which in this case is assumed to be the diffusion layer thickness. However, a situation in which the cell performance could considerably decrease, would be when the reactant concentration at the active sites drops to zero, which corresponds to the limiting case for mass transport. In such situation, the fuel cell could not stand a higher current density than the one that causes this reactant starvation. Such current density is denoted as the limiting current density J_L which can be calculated as equation (44), when $c_R^* = 0$ [37]:

$$J_L = zFD^{eff}\frac{c_R^0}{l} \tag{44}$$

With these parameters, the concentration overpotential could be expressed in terms of the Nernstian and reactions losses, as:

$$\eta_{conc} = \eta_{conc,Nernst} + \eta_{conc,BV} \tag{45}$$

The Nernstian losses can be written as equation (46):

$$\eta_{conc,Nernst} = \frac{RT}{zF} ln\frac{J_L}{J_L - J} \tag{46}$$

Analogous to the Nernst equation, the reaction losses can be expressed as:

$$\eta_{conc,BV} = \frac{RT}{\alpha zF} ln\frac{J_L}{J_L - J} \tag{47}$$

Hence, the total concentration overpotential yields:

$$\eta_{conc} = \frac{RT}{zF}\left(\frac{\alpha + 1}{\alpha}\right) ln\frac{J_L}{J_L - J} \tag{48}$$

In SOCs not only mass (concentration) losses take place, but other transport mechanisms are also relevant, such as the gas convective transport along the flow channels that are adjacent to the porous electrode. Such mass transport loss is a function of: (i) the viscosity of the gas mixture within the channels (also function of pressure, temperature and compositions), (ii) the pressure drop along the channels, (iii) the velocity of the gas flow, (iv) and the geometry of the gas channels [37]. The nature of the gas flow distribution may differ significantly on different cell architectures. The fuel gas flow distributes perpendicular to the surface of the fuel electrode (diffusive mass transport), but also parallel along the gas channels (from inlet to outlet). Regardless the flow distribution on the gas channels, the perpendicular gas flow may exhibit a higher resistance on anode-supported-cells (ASC) than on electrolyte-supported-cells, just because the electrode (diffusive) layer is significantly larger, meaning that the gas flow should diffuse across a larger path. Cross-section and side views of the fuel gas flow distribution on these cell architectures are depicted in Figure 11. Details about the different cell architectures employed in SOCs are explained in the following section.

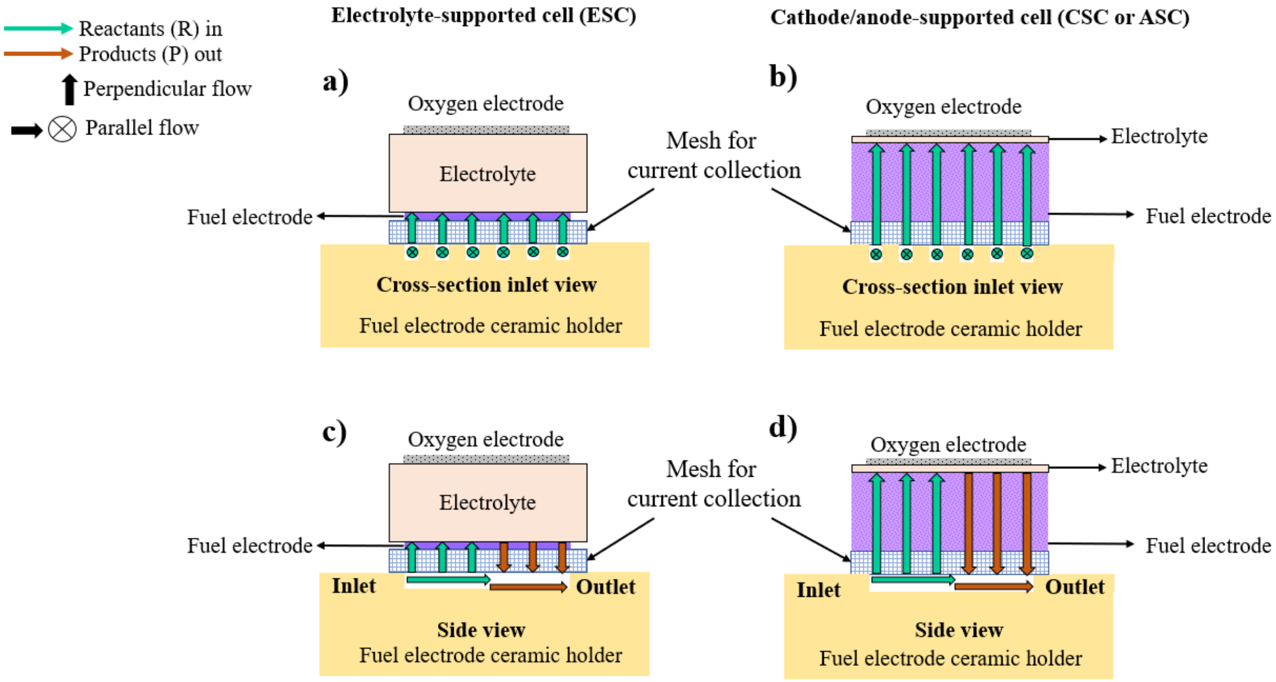

Figure 11 Simplified fuel gas flow distribution for electrolyte-supported cells (a and c) and for cathode/anode-supported cells (b and d).

Hence, it is possible to assume that while convective gas transport dominates in the flow channel, the diffusive mass transport dominates in the diffusion layer (within the porous electrode), where only the perpendicular direction of diffusion is considered. The convective contribution to η_{conc} could be minimized by careful selection of the gas channels geometry. Parallel-flow designs provide an overall low pressure drop between the gas inlet and outlet [37]. However, such contribution is not considered in equation (48).

Despite the different contributions to the voltage losses, different performance indicators are typically used to compare technologies, e. g. between high and low temperature electrolysis technologies, with the aim to evaluate the performance at a specific operating point. Hence, the following figures of merit were used within this thesis, mainly for the case of the electrolyzers.

2.9 Performance figures of merit

Typical figures of merit (FOM) for electrolyzers, such as the specific energy consumption [38] and the normalized hydrogen production are commonly calculated at the thermoneutral voltage. The specific energy consumption can be calculated with the consumed cell power P_{cell} and the produced hydrogen mass flow $\dot{m}$ in terms of the cell voltage and the faradaic efficiency, assuming $\epsilon_{Faradaic}$ of ~1 for SOEL [29]. The latter term is calculated with the measured charge to yield the product $q_{product}$, and with the total theoretical charge q [38] [39]:

$$\epsilon_{Faradaic} = \frac{q_{product}}{q} \tag{49}$$

Then, the specific energy consumption is expressed as [38]:

$$\frac{P_{cell}}{\dot{m}} = \frac{-zFV_{cell}}{\epsilon_{Faradaic}M} \tag{50}$$

, and the normalized hydrogen production $\frac{\dot{m}}{A}$ (kg H_2/cm^2·h) calculated at thermoneutral voltage is expressed by equation (51), where M and $\dot{n}$ stand for hydrogen molecular weight and hydrogen molar flow, respectively.

$$\frac{\dot{m}}{A} = \dot{n}M \frac{I}{zFA} = \frac{\dot{n}MJ}{zF} \tag{51}$$

Another relevant FOM for the performance of an electrolyzer is the specific energy requirement (kWh/kg H_2). In SOEL, this is calculated as the ratio between the consumed power P_{cell} and the produced hydrogen mass flow $\dot{m}$, with $\epsilon_{Faradaic}$ ~1. An analytical expression to obtain this FOM from the current, cell voltage and power consumption is described with equations (52) to (57):

$$P_{cell} = V_{cell} * I \tag{52}$$

$$V_{cell} = V_{rev} + (ASR_{Total}) * \frac{I}{A} \tag{53}$$

$$P_{cell} = \left(V_{rev} + (ASR_{Total}) * \frac{I}{A}\right) * I\,, \quad I = \dot{n}zF \tag{54}$$

$$P_{cell} = V_{rev} * \dot{n}zF + \frac{(ASR_{Total})}{A} * (\dot{n}zF)^2, \;\; \dot{n} = \frac{\dot{m}}{M} \tag{55}$$

$$P_{cell} = \frac{\dot{m}}{M} * \left[V_{rev} * zF + \frac{(ASR_{Total})}{A} * \frac{\dot{m}}{M}(zF)^2\right] \tag{56}$$

$$\frac{P_{cell}}{\dot{m}} = V_{rev} * \frac{zF}{M} + \frac{\dot{m}}{A} * (ASR_{Total}) * \left(\frac{zF}{M}\right)^2 \tag{57}$$

Typical values of $\frac{P_{cell}}{\dot{m}}$ for SOEL are around 37 kWh/kg H_2 at cell level while it can be as high as 40 – 44 kWh/kg H_2 at the stack level [40] [41].

The cell performance is not only related to the thermodynamic characteristics of the different operating modes, but also to the cell architecture. The ohmic and the concentration overpotentials are significantly affected by the thickness and morphology of the electrolyte and the electrodes. Following, different SOC architectures are detailed.

2.10 SOC cell architectures

SOCs have been developed in tubular and planar architectures since the decade of 1960s. The SOFC system coupled to a gas turbine from Siemens Westinghouse, was based on a tubular design, having promising results for that time. However, the planar architectures have received more attention during the last decade due to their performance approximately twice as high as for tubular structures [39]. Different planar cell architectures have been classified in terms of their mechanical support: electrolyte-supported cells (ESC), cathode/anode-supported cells (ASC) and metal-supported cells (MSC) [42], as depicted in Figure 12. The ESCs operate with a thick electrolyte layer (100 µm – 1 mm) that provides the mechanical strength with thin porous electrodes. Due to the high ohmic contribution from the electrolyte, these ESCs are operated at high temperatures (850 °C – 1000 °C) to favor the electrolyte's ionic conductivity. On the ASC designs the operating temperature is reduced to ~ 800 °C or below due to the thin electrolyte layer (typically ~50 µm).

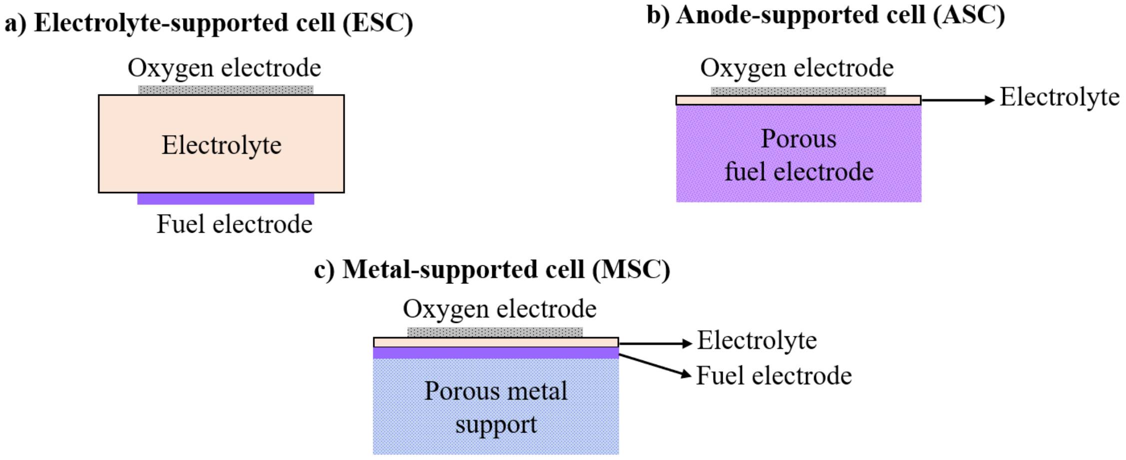

Figure 12 Electrochemical cell architectures. a) Electrolyte-supported cell (ESC). b) Anode-supported cell (ASC). c) Metal-supported cell (MSC).

Nevertheless, the ESC and ASC present an important drawback due to their brittle mechanical support, which are made of ceramic materials, as well as of composites between ceramic and metal – cermets [42]. By contrast, MSC designs consist of thin ceramic layers for the electrochemical reactions (electrodes and electrolyte), but with an additional mechanical porous support, typically made of robust metallic materials [42]. In the frame of this thesis, electrochemical characterizations were performed in ESC architecture, from which their typical materials are discussed in the following section.

2.11 Typical materials for ESC

2.11.1 Electrolyte

Crystalline oxide ceramic electrolytes conduct oxygen ions by defect hopping mechanisms that take place at high temperatures. Yttria-stabilized zirconia (ZrO_2), samaria- and gadolinia-doped ceria (CeO_2), known as YSZ, SDC and GDC/CGO respectively, are ceramic oxides, with crystalline fluorite structure, that are widely used as electrolytes in SOC [43].

YSZ is so far the state of the art electrolyte material for SOCs [43] [44]. YSZ stands for the doped ZrO_2 with a certain amount of Y_2O_3, typically with 3 or 8 mol %, corresponding to 3YSZ and 8YSZ, respectively. Despite the lower oxide ion conductivity of 3YSZ, this choice is advantageous due to its outstanding mechanical stability [44], which is required for instance on ESC architectures. By contrast, SDC and CGO electrolytes offer higher ionic conductivity than YSZ, but in reducing conditions they also present electronic conduction (above ~ 600 °C), which could cause an electronic current leakage through the electrolyte under operation [44]. The optimal dopant concentrations for SDC and CGO are typically around 10 and 20 %. A commonly used formulation is $Ce_{0.9}Gd_{0.1}O_{1.95}$, which is referred as CGO10 [43].

Besides the fluorite structure, perovskite oxides such as lanthanum gallates (LSGM) also exhibit good ionic conductivities. However, they present important issues such as the evaporation of Ga in reducing atmospheres, the poor compatibility with Ni and NiO (present in the typical fuel electrodes), the low mechanical stability and the expensive costs of gallium [44]. Furthermore, other alternative of doping zirconia with scandium instead of yttrium has also been studied with the aim to increase the ionic conductivity. Hence, Sc-doped ZrO_2 (ScSZ) electrolyte are very promising for reducing the operating temperature in SOCs. Nevertheless, the price and availability of scandium are relevant limitations [44].

Nowadays, commercial references of ESCs and stacks implement 3YSZ electrolytes with a CGO barrier layer coating, mainly to avoid chemical reactions between the electrolyte and the oxygen electrode (typically made of iron-doped lanthanum strontium cobaltites) [45]. In this thesis, commercial 3YSZ 90 µm-thick electrolytes with a CGO20 barrier (5 µm) coated in both sides were used (Kerafol GmbH, Eschenbach, Germany).

2.11.2 Perovskite oxides fundamentals

Before introducing the oxygen and fuel electrodes used in SOC, it is relevant to introduce the perovskites oxides in general. SOC electrodes should ideally be porous and both mixed ionic and electronic conductors (MIEC) to allow the electrochemical reactions to occur at the double-phase boundaries (DPB) and triple phase boundaries (TPB), where molecules, ions and electrons gather [36]. In this regard, perovskite oxides present this unique MIEC characteristic, making them very suitable for SOC electrodes. Their properties are strongly depending on their elementary composition ABO_3. For instance, by varying the composition on their A and B sites, significant changes can be tuned in regard to their transport properties, catalytic activity and their stability in oxidizing and reducing conditions [22]. An ideal perovskite structure is depicted in Figure 13. This structure could be seen as the BO_6 octahedron forming a center of a cube with a larger A atom at the corners, or as cube consisting of corner-sharing BO_6 octahedra with A atoms at the center. The coordination number of A and B cations are 12 and 6, respectively. The ideal relation between ionic radii is given by equation (58) [46], where r_A, r_B and r_O represent the ionic radii of the atoms A, B and O respectively:

$$r_A + r_O = \sqrt{2(r_B + r_O)} \qquad (58)$$

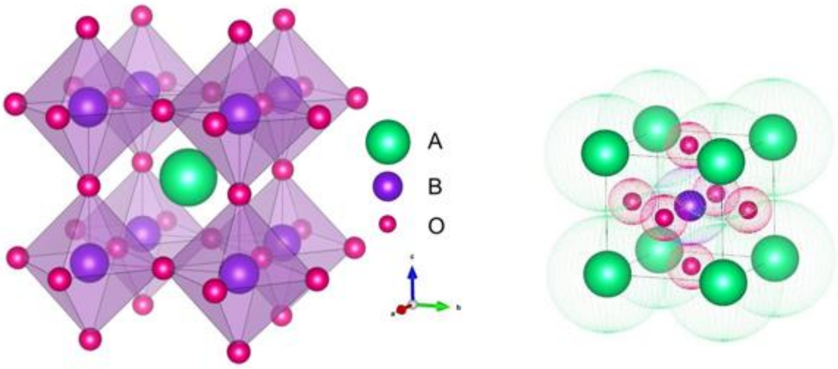

Figure 13 Left: Cubic perovskite crystal structure with A-center surrounded by 8 BO_6 octahedra. Right: Cubic perovskite crystal structure with a BO_6 octahedron center and A atoms on the corners. Crystal structures were generated with software VESTA [47].

However, this ideal cubic structure is rarely maintained. Typical distortions of the ideal cubic crystal structure are represented by orthorhombic and rhombohedral crystal systems, among less common arrangements such as tetragonal, monoclinic and triclinic. Therefore, the tolerance factor *t*, is a measure of the distortion and varies typically between 0.75 and 1 (cubic structure), which can be calculated as follow [46]:

$$t = \frac{r_A + r_O}{\sqrt{2(r_B + r_O)}} \tag{59}$$

2.11.3 Electrodes

In general, the electrochemical reactions take place on the TPBs (as mentioned in section 2.8.2) and DPBs (for MIEC electrodes), which constitute catalytic active sites (or regions) where electrons, gaseous reactants and O^{2-} react. Preferably, the electrodes present a porous structure with the following properties [43] [22]:

- Oxygen anion conductivity
- Electrical conductivity
- Chemical stability and compatibility
- High temperature compatibility with the electrolyte and interconnect materials (thermal expansion matching with limited reactivity)
- Durability at high temperatures and under thermal cycling
- Mechanical strength (trade between porosity and mechanical support)
- Catalytic activity
- For the fuel electrode: fuel flexibility and tolerance to impurities and coking in operation with hydrocarbon fuels (in SOFC and CO_2 electrolysis in SOEL), as well as with high contents of steam (silica impurities) in SOEL operation
- Low costs

2.11.4 Oxygen electrode

The oxygen electrode should provide high electrochemical activity for the reduction of oxygen. MIEC materials are great candidates for these electrodes, providing DPB regions and regions for this reaction to take place [43]. Such mixed conducting properties could be achieved with a cermet composite, where the metallic phase contributes with the high electronic conduction. However, due to the oxidizing conditions of the oxygen electrodes, the cermets are not adequate for SOC oxygen electrodes. Only ceramic materials that are stable at high temperatures and high pO_2 atmospheres may be considered.

Because of this, perovskites oxides such as strontium-doped $LaMnO_3$ (LSM) have been implemented as oxygen electrode due to their good physical and chemical stability, as well as good electrical conductivity, but with an important drawback, which is its lower oxygen ion conductivity [43]. Namely, iron-doped lanthanum cobaltites have been actively investigated because the incorporation of Fe on the $LaCoO_3$ avoids chemical interaction with the YSZ electrolyte, which could lead to the formation of insulating phases such as $La_2Zr_2O_7$ and CoO [43]. $La_{1-x}Sr_xCo_{1-y}Fe_yO_{3-\delta}$ (LSCF) - typically with a concentration of Fe ~80% - is a state-of-the-art material for SOC operation due to its good MIEC properties at high temperatures. For instance, at 800 °C its electrical conductivity is ~ 100 S/cm and its ionic conductivity relatively high, with values from 0.01 up to 1 S/cm. These conductivities may vary in function of the Sr and Fe concentrations [43]. In this thesis, the oxygen electrode composition that was used in the electrochemical tests corresponds to the commercial reference from Heraeus: $La_{0.58}Sr_{0.4}Fe_{0.8}Co_{0.2}O_{3-\delta}$ (LSCF).

2.11.5 Fuel electrode

Ni-YSZ cermet have been widely studied as fuel electrodes in ASC architectures for SOFC operation. These materials have provided satisfactory performances in the temperature range of 800 °C and 1000 °C [22]. They are typically prepared by sintering NiO and YSZ powders together, yielding a NiO/YSZ composite. Upon exposure to reducing atmospheres, the NiO phase is reduced to Ni, resulting in a porous Ni-YSZ fuel electrode [43]. Ni provides electrical conductivity and catalytic activity, while the YSZ phase provides ionic conductivity, as well as the structural framework of the electrode, acting also as inhibitor for the coarsening of Ni during preparation and operation [43]. However, these cermets present several disadvantages that are mostly related to Ni coarsening, agglomeration and re-oxidation, leading to a reduction of the TPB lengths and hence also a decrement on the electrical conductivity. Furthermore, important issues by fueling the cells with reformates, include low tolerance to sulfur impurities and propensity to carbon deposition. In the case of sulfur poisoning, the TPB lengths are substantially reduced due to the absorption of H_2S on the active sites of the nickel.

As for carbon deposition, the high catalytic activity of nickel towards the carbon-carbon bond favors the formation of carbon deposits, blocking the electrochemical reactions on the fuel electrode. If large amounts of steam are added to the fuel gases in SOFC operation on a steam to carbon ratio (S/C) of ~2-3, this issue could be mitigated. However, the OCV would decrease, as well as the power density [48]. Nevertheless, high amounts of steam could also accelerate Ni agglomeration and reduce the performance due to fuel dilution [43], but also due to loss of electrical percolation and diminution of the triple-phase-boundary (TPB) length [49] [17]. Additionally, there are other known phenomena from SOEL operation such as the enhanced evaporation of $Ni(OH)_2$ [49] [17] [50] and silicon poisoning of the fuel electrode, both due to higher H_2O contents (~ 10% - 90%) in the fuel gas, supplied with a non-extra pure steam feed [50] [51]. In SOEL operation, degradation phenomena have been observed mainly because of the larger pO_2 gradient across the electrolyte, resulting in a dominant driving force of different diffusion processes, causing Ni depletion near to the electrolyte [17].

In contrast, CGO-based fuel electrodes – commonly in ESC architectures – have been recently studied due to their MIEC properties, but also due to their ability to suppress carbon deposition [43] [52]. Their performance could be significantly improved by adding Ni, Co or also noble metals to the CGO ceramic phase, resulting in a cermet composite. For instance, even with pure hydrogen, Ni-CGO cermets outperform Ni-YSZ [43], and due to its coke tolerance, they outperform also in in H_2O-CO_2 co-electrolysis and dry CO_2 electrolysis operation. However, by reason of the large content of metallic Ni, such Ni-CGO composites are also sensitive to microstructure variations caused by grain coarsening upon redox cycling, which detriments their electrical conductivity [53]. Hence, redox cycling is still challenging on conventional Ni-CGO electrodes, due to the dimensional expansion of Ni/NiO upon oxidation, leading also to Ni grain coarsening, as well as electrode delamination [54]. With the aim to improve its dimensional stability, Ni nanoparticles infiltration into the ceramic backbone has shown an initial good performance, unfortunately also with a rapid Ni coarsening at high temperatures, leading to high degradation rates [54, 55].

Therefore, a key aspect of the cell performance is the optimization of the fuel electrode in the operation window of the SOCs. Kinetic and thermodynamic behaviors depend on how suitable is the fuel electrode for operating with the different typical gas mixtures in SOC. Besides of having a good catalytic activity towards electrolysis and oxidation reactions, tolerance against sulfur poisoning and carbon depositions, as well as stability in dual atmospheres (i.e. oxidative and reducing), are key aspects that could be optimized in the fuel electrodes.

2.11.6 Perovskites as target for Ni exsolution on SOC fuel electrodes

Alternative fuel electrode materials for the Ni cermets on ESC are the perovskite-based oxides (ABO_3). They have been explored due to their remarkable stability in redox conditions and their promising catalytic properties on a wide range of compositions. This has been achieved by doping their A-sites with lanthanides and alkaline-earth metals and their B-sites with transition metals, such as Mn, Co, Fe, Ni, Cr and Ti [56]. Outstanding performance has been shown in H_2O electrolysis with strontium titanates fuel electrodes with B-site doping of Ni and Fe by the exsolution method.

The exsolution of metallic nanoparticles takes place when catalytically active metals are embedded on the perovskite lattice under oxidizing conditions and then released as nanoparticles on the surface in reducing conditions [57] [58] [59] [60], as shown in Figure 14:

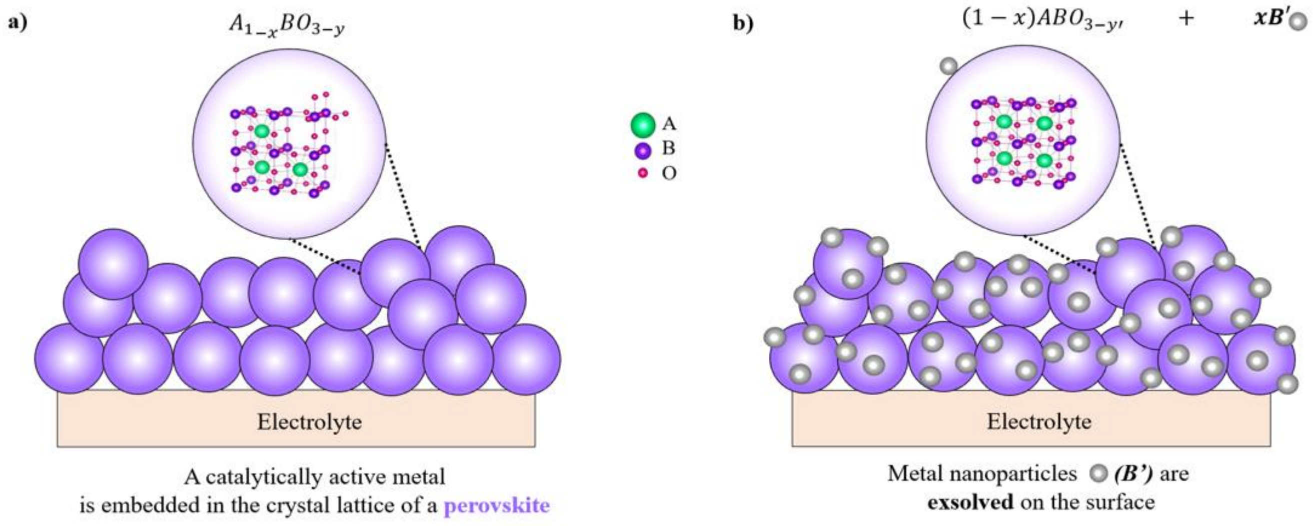

Figure 14 a) A-site deficient perovskite-based fuel electrode. b) Exsolution of metal B nanoparticles on the perovskite surface after exposure to reducing atmosphere at high temperatures and/or cathodic overpotential. Perovskite networks were generated with the software VESTA [47].

Exsolution is favored upon A-site deficiency because when the oxygen vacancy concentration is high enough, the perovskite lattice partially destabilizes due to the high deficiency on A- and O-sites. Hence, metal particles from the B-site exsolve while charge balance of the lattice is maintained [61] [62]. Recently Neagu et al. investigated Ni exsolution on A-site deficient lanthanum-calcium doped titanates and lanthanum-cerium doped titanates by *in situ* observation with environmental transmission microscopy (ETEM). They found that the exsolution phenomena and thus the shape of the resulting nanoparticle are significantly affected by the temperature and the oxygen partial pressure (pO_2), [62] being important operating parameters for SOC systems [57]. Nevertheless, such titanate electrodes with Ni exsolution have mainly been investigated at the button cell scale (~1 cm^2 of active cell area) and not yet been compared to state of the art Ni- based cermet electrodes in operation with equivalent boundary conditions [54].

Besides titanates, other perovskite families, such as lanthanum chromites have been also considered as fuel electrodes in SOC. On one hand, $LaCrO_3$-based oxides have been studied as interconnect materials for SOFCs due to their high electrical conductivity and stability in both reducing and oxidizing conditions at high temperatures, as well as their low activity toward carbon deposition [54] [63] [64]. On the other hand, lanthanum chromites can also host B cations and exsolved them as metallic nanoparticle on their surface, just as $(La,Sr)(Cr,M)O_3$ perovskites (M= Mn, Fe, Co and Ni) [57]. Among them, Ni was identified as very promising B-site dopant with good (electro)catalytic activity [64] [65]. Stoichiometric and A-site deficient formulations of these chromites have been recently investigated in H_2O electrolysis, CO_2 electrolysis and co-electrolysis [57] [59] [66] [67] [68] [69]. Sun et al. investigated A-site deficient Ni-doped lanthanum chromites and their application in SOFC in small button cells at 800 °C. They reported an increased performance of an A-site deficient chromite $La_{0.6}Sr_{0.3}Cr_{0.85}Ni_{0.15}O_{3-\delta}$ fuel electrode in comparison to the stoichiometric formulation ($La_{0.7}Sr_{0.3}Cr_{0.85}Ni_{0.15}O_{3-\delta}$) [70]. However, they also observed a significant performance degradation within the first 24 hours of operation, which was related to Ni particle coarsening, but redox cycling showed to fully recover the performance [54] [70]. Nevertheless, Ni exsolution behavior on lanthanum chromites upon temperature and pO_2 variation, as well as their electrochemical reactions in SOC operating modes are not yet fully understood.

In the following chapter, the motivation to investigate alternative perovskite fuel electrode in SOCs is presented, as well as the scientific approach that was followed for the completion of this thesis. The pertinent research questions are also addressed.

3 Motivation & scientific research approach

SOC technologies are by far one of the most promising alternatives for low-emission-power generation and -energy storage. However, these technologies are not yet completely mature and are currently competing with the low temperature technologies [15].

The scientific research and development in the SOCs materials field is strongly dominated by the Ni cermets fuel electrodes and hence meaningful knowledge has been acquired in the last 40 years. Despite the promising catalytic properties of these Ni cermets for the most of the SOCs applications, these materials exhibit important issues during operation that endanger the performance of the SOC-based systems [17, 43, 49, 50, 52-55].

Furthermore, their main raw material, nickel (and hence nickel oxide) is considered by the International Energy Agency (IEA) as a critical mineral for the energy transition [71], not only due to possible shortage supply in the next 20 – 30 years, but also due to social and environmental aspects that are correlated to its toxicity. Therefore, the motivation to replace this material, or to decrease significantly its use, is an important driver for the SOCs technologies deployment on the current energy transition.

Having these aspects in mind, the main motivation of this thesis is to develop and evaluate an alternative fuel electrode material for SOCs. For this, a perovskite-based fuel electrode is proposed with the aim to achieve a catalytical performance as good as the Ni cermets, as well as a stable operation and durability in the different SOC operating modes. Also, an important feature would be to evaluate if the implementation of such perovskite-based fuel electrode would require significantly lower amounts of Ni/NiO raw material than the state-of-the-art cermets. This would also be a relevant outcome for the deployment at larger scales (~ MW) of power generation and energy storage SOC-based systems.

In this thesis, the main focus is given to the formulation and implementation of a Ni-doped lanthanum strontium chromite decorated with Ni exsolution as fuel electrode on ESC architecture. Namely, with the purpose to electrochemically evaluate this fuel electrode in different SOC operating modes with respect to the typical Ni cermets fuel electrodes.

Taking as a reference the study by Sun et al. with a Ni partial substitution on the B site of 15% [70], and going beyond SOFC operation, in this thesis the nominal A-site deficiency was considered only on the Lanthanum content. The Sr concentration was kept constant in 30% because of the following reports:

- For stoichiometric lanthanum chromites, Sr was found to increase the electrical conductivity [64] [65], where optimal values were reported with 30-40 % Sr content on the A-site [72].
- Sujatha Devi and Subba Rao reported in $La_{1-x}Sr_xCrO_3$ formulations increments in the conductivity up to a Sr-doping level of $x \leq 0.3$, which were attributed to the formation of Cr^{4+} ions as a result of charge compensation and conduction. However, they also found that further increase in the Sr content, i.e. for x beyond 0.35, led to a decrement in the conductivity [73].

Considering the above, this thesis focused on the formulations of $La_xSr_{0.3}Cr_{0.85}Ni_{0.15}O_{3-\delta}$ (LSCrN) with lanthanum contents between $0.50 \leq x \leq 0.70$.

3.1 Scientific questions

The research questions that are addressed by this thesis are:

i) How can a perovskite-based fuel electrode compete with the state-of-the-art Ni-cermets in the different SOC operating modes?
ii) What could be the benefits to operate SOCs with this perovskite-based fuel electrode over the state-of-the-art Ni cermets?

With the aim to address and answer the above proposed research questions, a four stages-scientific approach was considered, as detailed in Figure 15. These stages encompass different facets of materials science and engineering in order to select, formulate, synthesize and characterize a reliable perovskite-based fuel electrode for SOC. The scientific results obtained during all the stages of this thesis are presented in three main publications labelled as Articles I, II and III. Additional publications are also mentioned across this thesis (see Chapter 11 and Chapter 12).

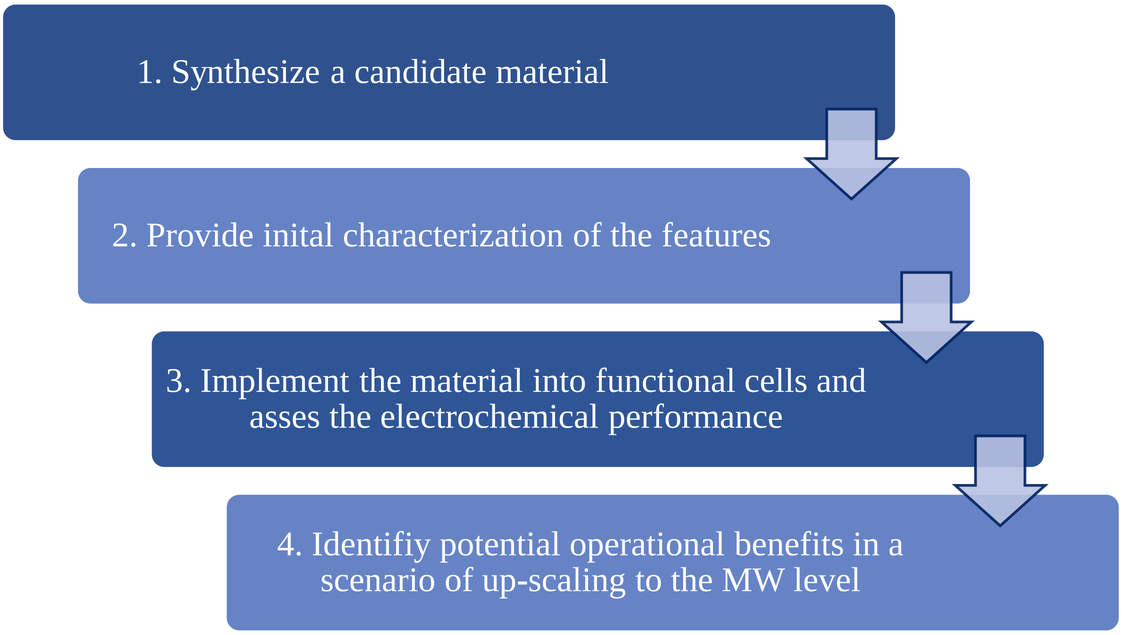

Figure 15 Sketch of the different stages of the proposed scientific approach.

The different stages of the proposed scientific approach are detailed as following:

- **First and second stages – Synthesis and characterization of candidate material**
  In these stages, different $La_xSr_{0.3}Cr_{0.85}Ni_{0.15}O_{3-\delta}$ formulations with $0.50 \leq x \leq 0.70$ were investigated. Characterization techniques allowed to define to which extent the proposed formulations were chemically stable. Thermal behavior was also evaluated with the aim to design and propose the most relevant parameters for the cells manufacturing processes. Once the perovskite formulations were defined, commercial purchase of the proposed formulations (~ 1 kg) were inquired in order to implement a manufacturing process protocol with enough stock of raw materials (**Article I** and **Article II**).
- **Third stage - Implement the selected material into functional solid oxide cells and asses the electrochemical performance**
  With the commercial raw perovskite materials, relevant manufacturing processes and methods were performed: ceramic ink preparation, electrode screen-printing and sintering. Important parameters such as electrode thickness and sintering temperatures were varied, as well as different contacting materials. The cell performance was evaluated and compared with state-of-the-art cells, for which the best combination of processing parameters for the manufactured perovskite-based cells was identified. (**Article I,** and **Article II**). The manufactured cells were tested in different operation

modes characteristic from SOC systems. For all of them, the cell performance at different temperatures and gas compositions was evaluated. Electrochemical characterization techniques gave insights about the performance and limitations of the proposed perovskite-based electrode under different operating conditions. Redox and long-term stability were also evaluated. It was important to note in this stage, that there was a synergy of different characterizations techniques and the electrochemical testing of these cells, which allowed to build a comprehensive understanding of the behavior and the performance of these perovskite electrodes (**Article I, Article II** and **Article III**).

- **Fourth stage – Identification of potential operational benefits in a scenario of up-scaling to the MW level**

  In this final stage, feasible aspects for the scale-up were evaluated with the performance results at the cell level reported on [74]. Advantages and disadvantages in regard to the further use of these electrodes were identified. Alternative pathways and different approaches in regard to the identified limitations were proposed for the scale-up of perovskite electrodes to the MW scale.

The main publications of this thesis could also be graphically described with the diagram in Figure 16. Different SOC operating modes were evaluated within these publications, by presenting the evaluation of the proposed perovskite-based fuel electrode, also with the benchmarking of the state-of-the-art fuel electrodes.

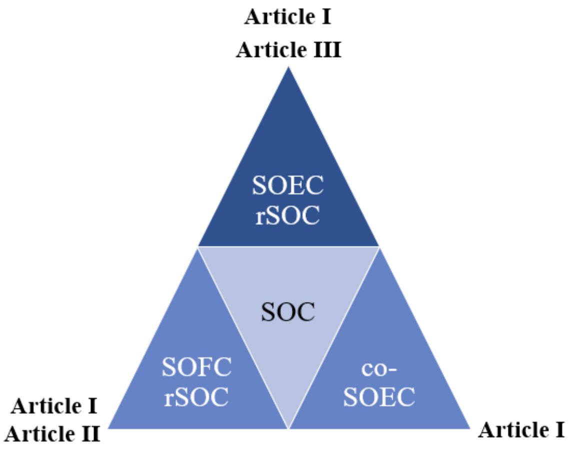

Figure 16 Sketch of the different operating SOC modes that were addressed in the frame of this thesis with the three main publications (**Article I, Article II** and **Article III**).

4 Materials & methods

In this chapter, the experimental methods and procedures performed in this thesis are described. Starting with the perovskite ceramic powder synthesis, the respective ceramic ink preparation and with the following experimental procedures, such as screen-printing and sintering, which all in all encompass the cells manufacturing process. Different types of samples were produced and characterized along this thesis:

i) perovskite powders in oxidized and reduced form
ii) symmetrical-button cells (2 cm diameter)
iii) square electrolyte-supported cells (5 cm x 5 cm)

4.1 Powder synthesis

The glycine nitrate combustion method was implemented for the synthesis of the ceramic precursors LSCrN, as explained in [70] [57]. Once the stoichiometry was fixed, only the content of La was varied and four different compositions were prepared as shown in Table 1:

Table 1 LSCrN powder formulations with different La deficiency on A-site.

Abbreviation	La deficiency (%)	A - site deficiency (%)	Formulation
L70SCrN	-	-	$La_{0.7}Sr_{0.3}Cr_{0.85}Ni_{0.15}O_{3-\delta}$
L65SCrN	7	5	$La_{0.65}Sr_{0.3}Cr_{0.85}Ni_{0.15}O_{3-\delta}$
L60SCrN	14	10	$La_{0.6}Sr_{0.3}Cr_{0.85}Ni_{0.15}O_{3-\delta}$
L50SCrN	29	20	$La_{0.5}Sr_{0.3}Cr_{0.85}Ni_{0.15}O_{3-\delta}$

For the preparation of these powder formulations, stoichiometric amounts of the nitrate precursors were weighed and dissolved in deionized water and further mixed with glycine (J.T.Baker™), with a molar ratio of 2:1 with respect to the total content of metal cations). Then, these mixtures were stirred and heated at 80°C on a hot plate until a dark-green colored gel was formed, as shown in Figure 17:

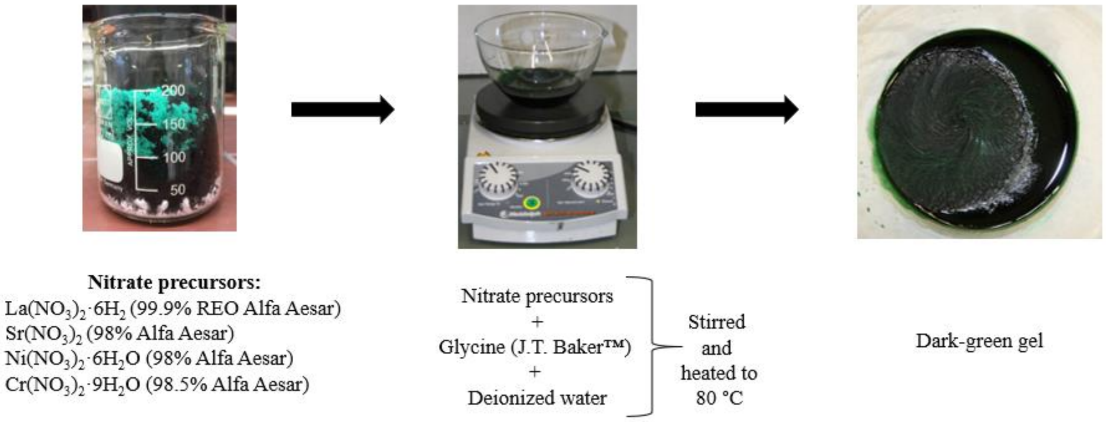

Figure 17 Steps for the glycine nitrate combustion method for the preparation of LSCrN precursors.

However, in order to determine the temperature in which the self-combustion was taking place, thermogravimetric measurements in synthetic air were performed on these gels, indicating that the exothermic self-combustion reaction was taking place at 220°C. (These measurements are explained in section 5.3). Therefore, once the gel was formed, it was heated up to 220 °C in an oil-bath configuration, as shown in Figure 18:

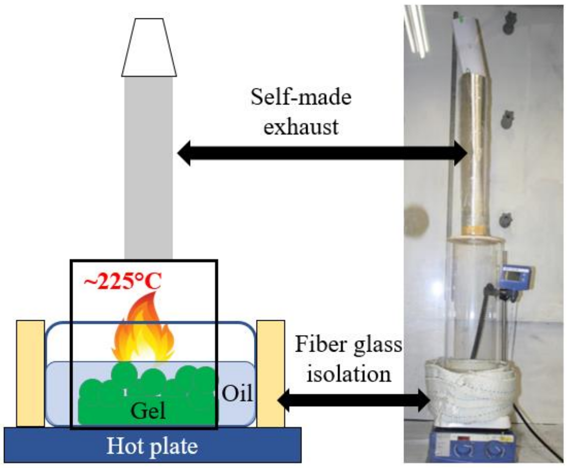

Figure 18 Setup for the production of LSCrN ceramic precursor from the self-combustion reaction of the formed gel at ~ 220°C under stirring in an oil bath.

After the self-combustion reaction occurred, the resulting ceramic precursor was calcined in air with a heating ramp of 3 °C/min up to 1400 °C with a holding time of 1 hour. This temperature was selected because it was the minimal point at which the perovskite phase was achieved [75], consistent also with other studies on lanthanum chromites [76]. The obtained perovskite powder LSCrN is shown in Figure 19:

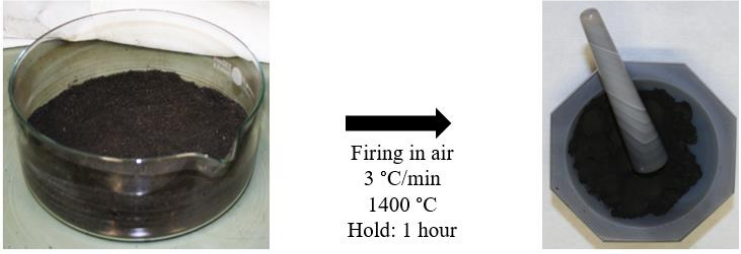

Ceramic precursor

LSCrN ceramic powder

Figure 19 Left: Ceramic precursor after self-combustion reaction. Right: After firing in air at 1400 °C for 1 hour, the LSCrN ceramic powder was obtained.

The self-made L65SCrN and L70SCrN powders were mainly composed of a LSC perovskite phase and a secondary phase of NiO (corresponding ca. to the targeted nominal A-site deficiency) , as verified by XRD in [57]). Customized synthesis of large quantities was made by the company Marion Technologies for the two powder compositions L65SCrN and L70SCrN. For each composition, 1 kg of powder was manufactured. The LSCrN-powder samples that were herein produced were further characterized by different techniques, which are explained and detailed in chapter 5.

4.2 Ceramic ink preparation

Ceramic inks of the L65SCrN and L70SCrN powders were prepared at a powder-to-solution proportion of 2:1, starting with a solution of α-Terpinol (94 wt %) and ethyl cellulose (6 wt %). The ceramic powder was then slowly added into the vehicle ink and mixed by hand. Then, such ceramic suspensions were mixed with the 3-roll milling machine EXAKT 80E EL (Figure 20) with the parameters depicted in Table 2 (starting with the mode 1):

Table 2 Experimental parameters for preparing the LSCrN ceramic inks on the 3-roll milling machine EXAKT 80E EL.

Gaps between rolls	**Distance between rolls (μm)**		
Mode	Mode 1	Mode 2	Mode 3
First Gap	45	30	15
Second Gap	15	10	5
# of repetitions	4	2	2

After passing the ink through the 3 rolls, fixing the distance between rolls for each mode (mode 1 to 3), the mixing process finalized by applying the “Force Mode” and passing the ink just one more time through the rolls. The force mode allows to break the smallest agglomerate more efficiently, making the mixing of the solvent and powder more homogenous, and resulting in the targeted ceramic ink.

Figure 20 3-roll milling machine EXAKT 80E EL.

4.3 Screen printing

In this thesis, electrolyte-supported-cells were manufactured and further used for the different electrochemical characterizations and durability tests. Two different configurations were investigated: symmetrical button cells and square full cells, both implementing the perovskite fuel electrode L65SCrN.

Figure 21 Screen printer machine Aurel model 900 (Aurel automation s.p.a, Italy).

4.4 Symmetrical button cells

Symmetrical button cells were prepared by screen printing round shape electrodes of 10 mm-diameter with the prepared L65SCrN ink on either side of a 20 mm-diameter commercial 90 µm-thick 3YSZ electrolytes sandwiched between two 5 µm-thick CGO20 barrier layers, from Kerafol GmbH (Eschenbach, Germany). The screen-printing was performed with the printing machine Aurel model 900 (Aurel automation s.p.a, Italy) shown in Figure 21, with configuration “Print + Print”. Then, the half-cell was dried at 60 °C until the ink solvents evaporated (~ after 30 minutes). Afterwards, the printing and drying processes were repeated for the other side. Next, the cells were heated up at 3 °C/min to 1200 °C in air and fired for one hour. Platinum paste (Heraeus) was used as current collector and hand-brushed on both electrode surfaces. Following, the cells were heated up at 3 °C/min to 1050 °C in air and held also for one hour. The active electrode area was 0.785 cm^2 as shown in Figure 22:

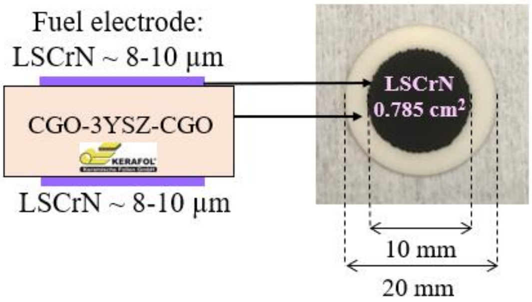

Figure 22 Left: Sketch of symmetrical button ESC with LSCrN fuel electrode. Right: Upper view of the prepared symmetrical button cell after sintering.

4.5 Square full cells

Square full cells were prepared with commercial references from the electrolyte and the oxygen electrode, with the main purpose to only vary the fuel electrode composition: L65SCrN and L70SCrN. The prepared ceramic inks of the L65SCrN and L70SCrN powders were screen printed on one side of the electrolyte-substrates also supplied by Kerafol GmbH Germany. These substrates were 90 µm-thick squares (5 cm x 5 cm) of 3YSZ double side coated with a 5 µm-thick (centered square of 4 cm x 4cm) of $Ce_{0.8}Gd_{0.2}O_{2-\delta}$: CGO20-3YSZ-CGO20. The screen-printing of the fuel electrode was performed, following the same printing and drying parameters as used for the symmetrical button cells, but by using a printing mesh with a square window of 4 cm x 4 cm and centering this printing area over the CGO20 area of the electrolyte. Then, the fuel electrode on the half-cell was fired in air at temperatures between 1100 °C and 1200 °C, with a heating rate of 3 °C/min and holding time of one hour. Regarding the oxygen electrode, the commercial ink of $La_{0.58}Sr_{0.4}Fe_{0.8}Co_{0.2}O_{3-\delta}$ (LSCF) from Heraeus was printed on the other side of the fired half-cell, using the same printing and drying parameters as for the fuel electrode, but with another mesh in order to avoid materials cross contamination between LSCrN and LSCF inks. Further to the drying process of the LSCF, an area of platinum paste (Heraeus) of 4 cm x 4 cm was hand-brushed over the fuel electrode and further dried at 60 °C until solvent evaporation took place. This platinum paste was used as current collector layer for the fuel electrode. Finally, the platinum and LSCF were co-fired in air up to 1050 °C and held for one hour. Nominal heating rate was used as well for this thermal process. The printed area for both electrodes was 16 cm^2 as shown in Figure 23:

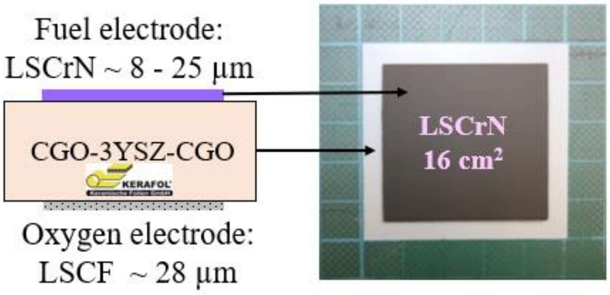

Figure 23 Left: Sketch of full cell ESC 5 cm x 5 cm with LSCrN fuel electrode and LSCF oxygen electrode. Right: Upper view of the prepared full cell after sintering where the LSCrN fuel electrode is observed from the top.

The symmetrical button cells and full square electrolyte-supported-cells produced in this thesis were further investigated by means of microscopy, diffraction and electrochemical characterization techniques, that are detailed in chapter 5.

5 Characterization techniques

In this chapter, the different characterization techniques that were used in this doctoral thesis are described. Among them, features of the powder morphology, crystal structure and surface chemistry were characterized by scanning electron microscopy (coupled with energy dispersive X – ray spectroscopy), X-ray diffraction and X-ray photoelectron spectroscopy respectively. Powder thermal properties in oxidizing and reducing conditions were investigated by thermogravimetric analyses and temperature-programmed reduction. Regarding *in situ* electrochemical characterizations, the different test benches and setups used in this thesis are detailed, where *i-V* characteristics, electrochemical impedance spectroscopy and chronopotentiometry/chronoamperometry characterizations were performed. With these techniques, equivalent circuit modelling and distribution of relaxations times provided a first glance about the perovskite fuel electrode kinetics. Finally, the Van der Pauw method is also explained, which allowed to measure the electronic conductivity of the perovskite fuel electrode.

5.1 Scanning electron microscopy

Scanning electron microscopes (SEM) are instruments that create magnified images that reveal information about the size, shape and composition of a specimen at the microscopic scale. Its operation principle involves a finely focused electron beam emitted by an electron source. The energy of these electrons in the beam corresponds to E_0. During emission, the electrons are accelerated with an energy typically in the range from $E_0 = 0.1$ and 30 keV [77] [78].

Once emitted, the primary electrons are focused by condenser lenses and electromagnetic coils, which narrow the beam in a raster (x-y) pattern and place it in discrete locations on the specimen [77]. The interaction of the electron beam with these locations can lead to the emission of back-scattered electrons (BSEs) and secondary electrons (SEs) [78], as shown in Figure 24. At all the discrete beam locations, the electron signals are measured by one or more electron detectors, from which their name is related to the type of electrons that they are sensitive to: either BSE or SE secondary detectors [77]. For each detector, the electron signal is measured at each individual raster location on the specimen, then it is scanned, digitalized and recorded into computer memory, and subsequently used in order to determine the topography in different levels of gray at each x-y location. Then, such coordinates are displayed in the computer screen, forming all together a single image element (or pixel) [77].

Inelastic scattering events of the electrons with the valence electrons of the sample generates electrons with kinetic energies lower than 50 eV, which correspond to the SEs with information depths of ~ 5 – 50 nm, revealing topographic features and characteristics [79]. BSEs originate from elastic interactions of the electrons with the atoms nuclei, being proportional to the atomic number of the sample, where information depths range from 50 up to 300 nm [79]. For different atomic numbers, different gray levels can be observed on the formed image, providing information about chemical variations on the sample.

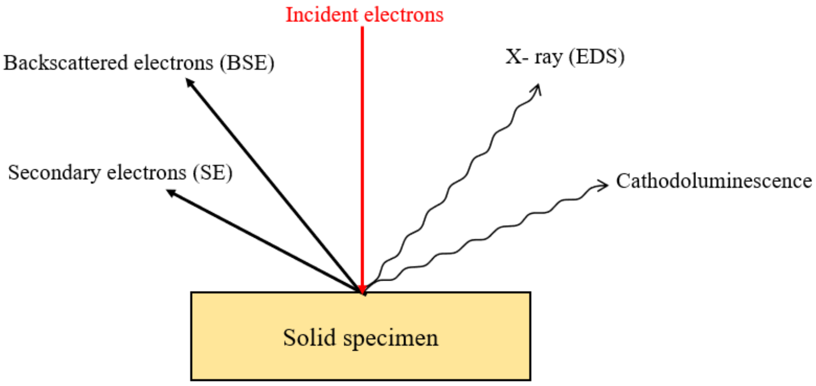

Figure 24 Schematic drawing of signals generated by electron emissions when an incident electron beam interacts with a solid specimen. Adapted from [78] [80].

In conventional SEMs, the electron column and the specimen chamber and detectors must be operated under high vacuum conditions ($<10^{-4}$ Pa), in order to minimize undesired scattering of the electron beam, which could take place due to interactions of atoms and molecules with atmospheric gases [77]. For the characterization of different microstructural features, a flat specimen surface is required. Typically, sample preparation is performed by careful grinding and polishing protocols according to standard metallographic methods [81] [78].

In this thesis, morphology and microstructural characterizations were performed by using the scanning electron microscope Zeiss ULTRA PLUS SEM (Carl Zeiss AG, Germany). equipped with a fuel emission gun (FEG). Features of the LSCrN powder samples (as prepared and after reduction thermal treatments) were investigated, mainly with the SE detector (Figure 25 a and b respectively). Also, the electrolyte-supported cells after electrochemical operation (Figure 25 c) were investigated with both SE and BSE detectors.

For the analysis on the cells' cross-section, the samples were embedded into a suitable resin and after mirror polishing, they were metallized with a thin sputtered metallic layer. Areas of non-interest were coated with a silver paste in order to avoid charging effects due to the insulating nature of the resin and the electrolyte material.

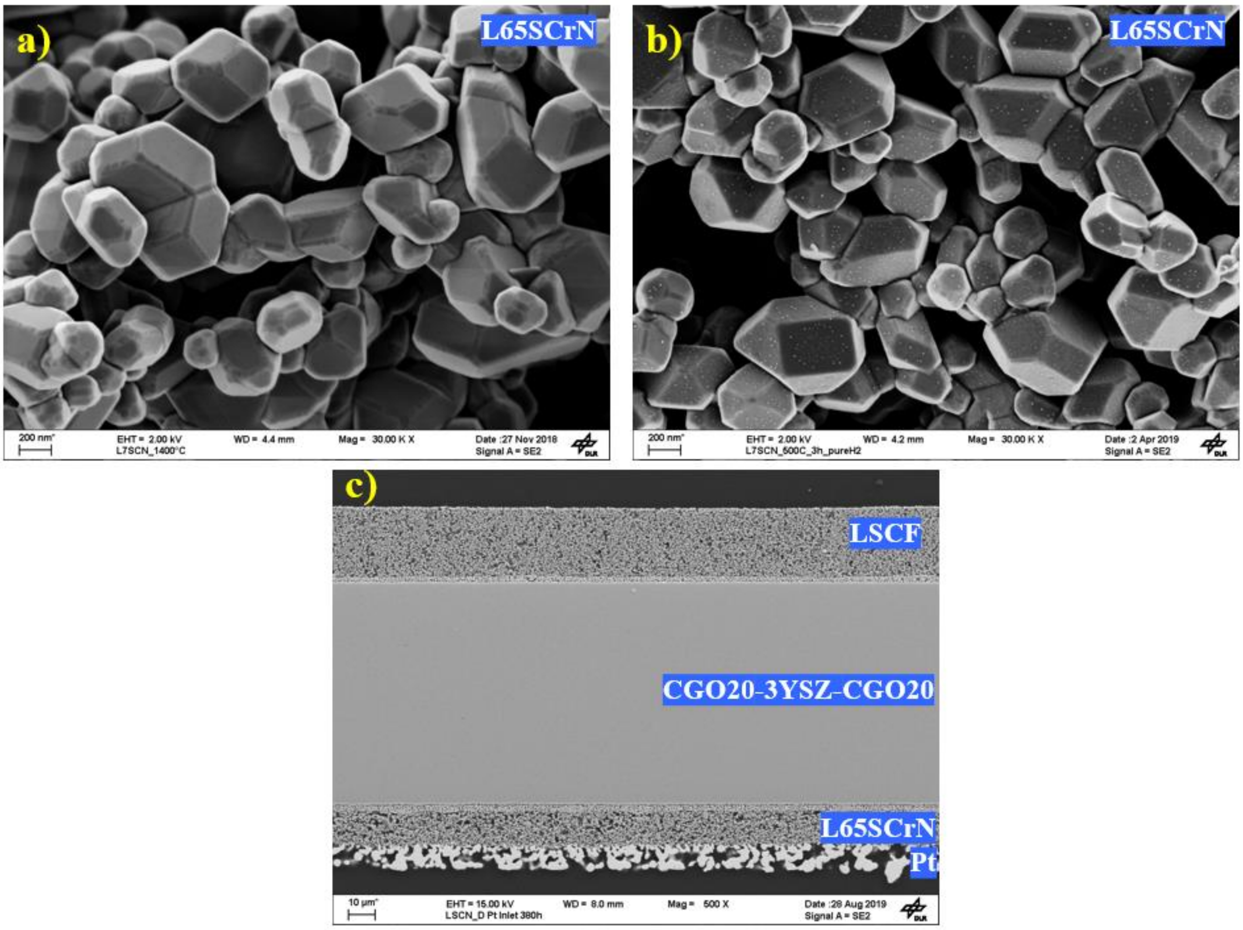

Figure 25 SEM images of: a) LS65SCrN ceramic powder as prepared, b) L65SCrN ceramic powder after reduction with hydrogen at 500 °C, where nickel nanoparticles are observable and c) cross-section view of electrochemical cell with L65SCrN fuel electrode after rSOC operation at 860 °C (image adapted from [57]).

5.2 Energy dispersive X – ray spectroscopy

Typical SEM setups also include energy dispersive X – ray spectroscopy (EDS). By performing SEM analyses, it is possible to reduce the composition search on a microscopic area, based on the elementary composition that could be obtained by EDS. With it, the area of interest could be analyzed and matched with an indexed element database [79]. The EDS detector collects the signals of characteristic X-rays from a wide range of elements in a sample. Common resolution values are between 150 – 200 eV. Typically Si(Li) detectors are used, which consist of a small cylinder of silicon and lithium in the form of diode. The X-ray photons collected by the detector generate a specific number of electron-hole pairs. EDS spectra are plotted as the intensity of characteristic X-rays versus the X-ray range.

As a complement to the SEM analyses on the cross-section of the tested cells, EDS was also performed with the aim to study the chemical compositions between the different cell components. For this purpose, the Bruker XFlash 5010 detector supported with the software Quantax 400 was used in combination with the Zeiss ULTRA PLUS SEM. Insights about contaminants on the catalytic layers or formation of new phases were also analyzed.

5.3 Thermogravimetric analysis

Thermal analysis techniques allow to measure materials properties upon temperature changes, with respect to dimensions, mass, phase and mechanical behavior. Among the most typically used thermal characterization techniques, thermogravimetry (TG) allows to examine the decomposition of materials by monitoring mass changes as a function of the temperature upon a scanning mode [82]. TG plots indicate the mass change (in %) versus the increasing temperature. TG setups mainly include a microbalance, furnace, temperature programmer and computer, where the key component is the microbalance. It measures mass change of +/- 1 µg with a maximum mass of 100 mg. TG can be performed in either reactive (with corrosive, oxidizing and reducing gases) or nonreactive (inert) atmosphere. Typical gas flows of 15 – 25 mL/min are used for a sample mass between 2 and 10 mg [82]. Heating rates of 5 – 10 °C/min are recommended. For high-resolution, the heating rates can be reduced to 1 °C/min.

The TG curves performed in this thesis were analyzed in different atmospheres:

i. The dark-green gel that was synthesized during the nitrate combustion method described in section 4.1, was analyzed by TG with the analyzer Netzsch Jupiter 449C in synthetic air at a nominal heating ramp of 3 °C/min from 25 °C up to 1100 °C [75], with the aim to determine at which temperature the solvent evaporation was taking place, as well as the self-combustion reaction. The latter temperature was crucial for the powder processing: without knowing this temperature low yields were achieved since on the first experimental trials the dark-green gel was placed directly on the oven and taken out after thermal treatment at ~ 1400 °C. Therefore, the setup from Figure 18 was used to re-collect the ceramic precursor after self-combustion reaction. Afterwards, the ceramic precursor (Figure 19) was placed in the oven for further calcination up to 1400 °C. It is important to point out that during these analyses, it was challenging to keep constant the amount of sample (approximately between 6 – 12 mg of gel), due to the high viscosity and complex sticky behavior. Despite this issue, the results indicated reproducible values as shown in Figure 26:

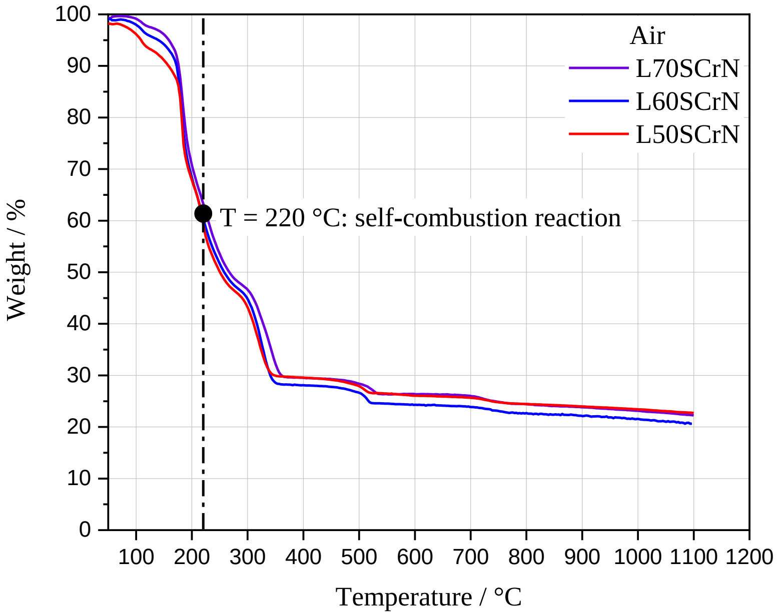

Figure 26 TGA of L70SCrN, L60SCrN and L50SCrN gels in air up to 1100 °C with a heating rate of 3 ° C/min, where the temperature of self-combustion reaction is specified, corresponding to ~ 220 °C for the three measured gel samples. Plot adapted from [75].

Once the L65SCrN and L70SCrN ceramic powders were synthetized, TG analyses were performed under reducing atmosphere (2 mL/min of 5% H_2–Ar) with the same device and heating rate as previously described, but from 25 °C up to 1200 °C [57]. The sample mass for both powders was kept at ~ 22 mg. This time, the main purpose of these analyses was to compare the reducibility of these two powders i.e., to create oxygen vacancies – and thus to exsolve metallic Ni nanoparticles. These results are depicted in Figure 27:

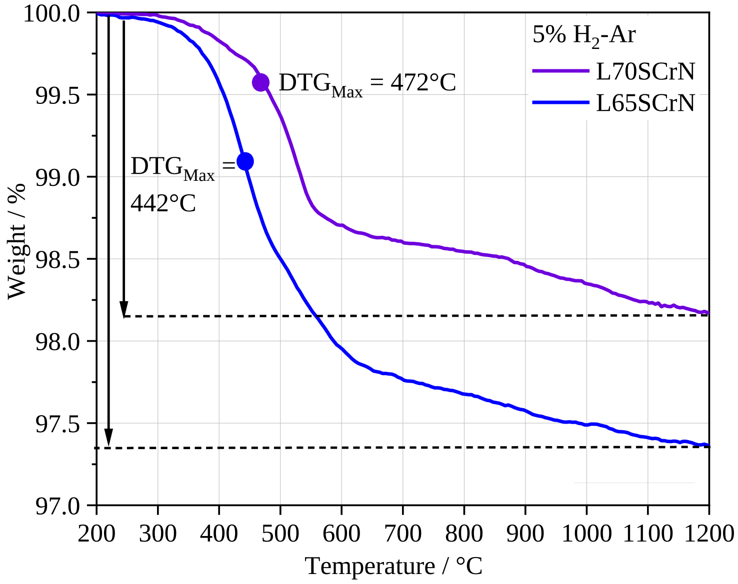

Figure 27 TGA of L70SCrN and L65SCrN powders in 5% H2-Ar up to 1200 °C with a heating rate of 3 ° C/min, where the temperature value at the highest slope (DTG) is specified, corresponding to the fastest mass loss. Plots adapted from [57].

5.4 Temperature-programmed reduction

The reducibility analyses performed by means of TG were complemented with temperature-programmed reduction (TPR). This technique allows to characterize the oxido-reduction properties of bulk and supported catalysts. Typically, a gas flow of H_2 or CO sweeps through a bed of solid specimens placed inside a quartz tube, typically of 20 mm diameter. A thermocouple placed inside the tube monitors the temperature while the furnace increases the temperature with a heating ramp between 1 – 20 °C / min. A thermal conductivity detector (TCD) continuously monitors the effluent gas concentration and in case of changes due to a reduction reaction, the signal response changes according to a change in the oxidation state of the sample. Hence, TPR identifies the temperature required to activate a metallic phase [83], i.e. when complex oxides, such as LSCrN samples, are being analyzed. The characteristic reduction temperature of the sample corresponds to the maximum of the TCD peak. Such peak could also be affected by the amount of sample load, which could alter the thermogram [83]. For reproducibility purposes, it is important to perform various measurements with a nominal amount of sample. In the pre-conditioning stage, inert gases as Ar or He, flush out the residual air and moisture from the solid sample. Then, the main parameters such as the, gas flow, heating ramp and final temperature, with its corresponding holding time are selected. Gas flowrates and heating ramps are also important values that should be optimized for every type of sample: each catalyst requires specific conditions in order to achieve a reproducible characterization [83].

In this thesis, TPR measurements were performed on L65SCrN and L70SCrN powder samples, for which prior measurements were done in order to find optimal parameters shown in Table 3, where mass catalyst was kept constant at ~ 0.05 g.

Table 3 Experimental parameters for TPR measurements on LSCrN ceramic powders.

TPR parameters	**Gas flowrate**	**Temperature range**	**Heating ramp**	**Holding time**
Pre-treatment (Ar)	20 sccm	30 °C – 150 °C	10 °C/min	60 min @ 150 °C
Analysis treatment (5% H_2–Ar)	20 sccm	30 °C – 1100 °C	5 °C/min	60 min @ 1100 °C
Cooling-down (Ar)	20 sccm	1100 °C – 60 °C	-20 °C/min	-

These analyses were performed on the flow-through quartz reactor TPDRO 1100 from Thermo Scientific, Italy. The L65SCrN and L70SCrN powder samples were introduced using quartz glass wool. For monitoring the sample temperature, a thermocouple (type K) was placed in a thin quartz glass tube, within the reactor tube. By using the parameters described in Table 3, it was also found that the offset between the sample and furnace temperature was of about 100 °C, meaning that under these conditions, the sample temperature was ~ 1000 °C [57]. The resulting TPR diagrams are depicted in Figure 28:

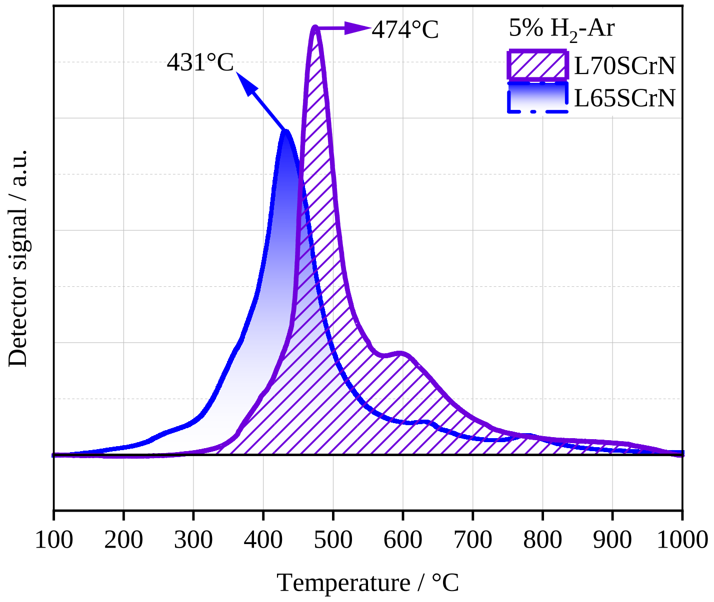

Figure 28 TPR of L70SCrN and L65SCrN powders in 5% H2-Ar up to 1000 °C with a heating rate of 3 ° C/min. The temperature value at the highest detector signal is specified, which complement the TGA measurements. Plots adapted from [57].

5.5 X-ray diffraction

X-ray diffraction is one of the most effective techniques for determining the crystal structure of materials. Different compounds or phases could be identified within the crystal structure, even if they present the same chemical composition [84]. X-rays are high-energy beams of electromagnetic radiation with a characteristic wavelength. They are produced by electrons at high speeds accelerated by a high-voltage field which then collide with a metal target. For this, an X-ray tube with a source of electrons is required, as well as two metal electrodes within a vacuum tube. Typical electron sources include a single-wavelength (monochromatic) X-ray diffraction [84]. The principle of this characterization technique is based on the diffraction of X-rays by periodic atomic planes at a specific angle and wavelengths (Figure 29). The geometrical interpretation of this phenomenon was given by W.L. Bragg with the following expression denoted as Bragg’s law in equation (60) [85]:

$$n\lambda = 2d_{hkl}sin\theta \tag{60}$$

Where n is the order of diffraction, λ the wavelength of the incident beam (in nm), d_{hkl} is the lattice spacing also in nm and θ the angle of the diffracted beam, as shown in Figure 29:

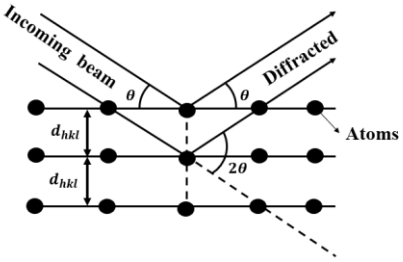

Figure 29 Geometry for diffraction from lattice planes with Bragg's law. Adapted from [85].

The total intensity diffracted by a unit cell is described by the sum of the scattered intensity from the individual atoms. The diffracted intensities I_{hkl} are characteristic of each phase from which structural parameters can be obtained, such as the lattice structure, space group, lattice parameters and indexation indices (Miller's indices h, k *and* l), corresponding to the family of *hkl* planes that are phase-characteristic. Typically, Bragg-Brentano geometry configuration is used during the measurement, which states that the distance between the sample and the detector is constant for all θ angles [85]. Commonly, diffraction patterns are plotted as the intensity distribution versus 2θ, as shown in Figure 30. Once the background is subtracted, the maximum peak intensity I_{max} can be defined as the integrated intensity I_{int}. The peak width is generally characterized by the full width at half maximum (FWHM), which corresponds to the peak breadth at half of the maximum intensity $\frac{I_{max}}{2}$ [85].

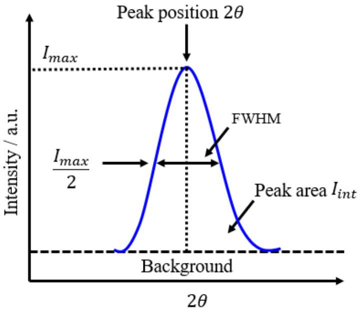

Figure 30 Diffraction peak and information extracted from XRD pattern. Adapted from [85].

With the aim to perform a qualitative analysis on a specific sample, a diffraction pattern over a wide 2θ range (typically from 20°-80°) has to be measured recording as much diffraction peaks as possible, for which each phase produces a characteristic diffraction pattern that allows its identification. After performing the XRD measurement, the different phases within the sample could be identified by comparing the diffraction peaks with known database entries. The main available database is provided by the International Center for Diffraction Data (ICDD) [85].

In this thesis, crystalline structures and phases were characterized by identifying the peak positions on the experimental intensity profiles and matching them with database entries. Once the phases were identified, the database matched-entries allowed to perform a first estimation of the lattice parameters. After redox treatments, for instance after LSCN powder reduction, the new experimental profile allowed to identify lattice changes with the peak shifts to lower diffraction angles, as reported in [57]. Expansion of the lattice after reduction treatment was assessed by the Rietveld method, which also allowed to quantify the phases[57]. Details about this method are explained in section 5.5.1.

These characterizations were performed with a RIGAKU diffractometer operating at 40 kV and 30 mA with a Cu radiation source and a Bragg–Brentano configuration in the range of 2θ from 20° to 80°. Crystalline phases were identified with ICDD database using the software Match [57]. Additional XRD measurements were performed with the diffractometer Bruker AXS equipped with a VÅNTEC-2000 area detector (D8 Discover GADDS) [54].

5.5.1 Quantitative phase analysis by the Rietveld method

Once the phases are identified, different methods for phase quantification are known: method with external standard, method with internal standard, method of intensity ratio and the Rietveld method [85]. Among them, the latter was used in this thesis with the purpose to quantify the elemental composition of the perovskite phase of the LSCrN ceramic powder. Analyses were performed for the powder samples “as-prepared” and “after reduction” with the purpose to quantify, besides the perovskite phase, also the metallic nickel content after exsolution and other impurity phases.

The Rietveld method allows to simultaneously analyze several peaks of a whole XRD pattern. For this, the whole measured pattern is refined with a calculated pattern that considers various structural and microstructural features, as well as experimental parameters. Such refinement is performed by minimization of the function S in equation (61) [85]:

$$S = \sum_i u_i |y_i obs - y_i calc|^2 \tag{61}$$

Where $y_i obs$ corresponds to the measured intensities and $y_i calc$ to the calculated intensities at each 2θ for position i. The parameter u_i stands for a weighing factor taken from the experimental error margins that are assumed to be proportional to the square root of the count rate $y_i obs$ following Poisson counting statistics [85]. Different factors for each analyzed phase should be considered for the refinement, which are: positions of the atoms in the elementary lattice, temperature factor, occupation factor, space group of the lattice, lattice parameters, crystallite size, macrostrains and phase contents. However, there are various instrumental factors that may not be ignored, such as 2θ shifts (instrument errors), instrument profile, profile asymmetry, background, sample positioning error, absorption and wavelength (emission profile) [85]. The refinement of the pattern is commonly based on the peak description by mathematical functions such as Gaussian, Lorentzian, Voigt and Pseudo-Voigt among others. One advantage of these functions is that they can be applied when the instrumental details are unknown. Nevertheless, such functions are based on mathematical fitting which do not allow the direct extraction of microstructural features from the analyzed patterns, such as crystallite size and macrostrains [85].

In the frame of this thesis, the parameters resulting from Rietveld refinement parameters are detailed in [57] and the observed and calculated patterns are shown in Figure 31, where NiO, Ni and perovskite phases were identified and quantified.

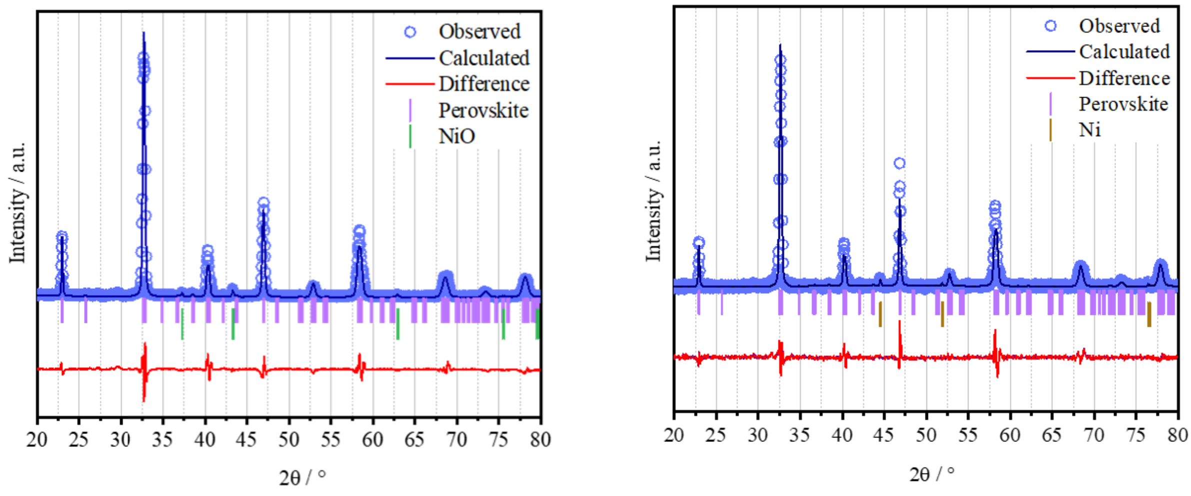

Figure 31 XRD patterns of the as-prepared L65SCrN powder (left) and of the reduced powder in 5% H2-Ar (right). Crystallographic parameters and the concentration of secondary phases were calculated from Rietveld refinement and are detailed in [57]. Plots were adapted from [57].

5.6 X-ray photoelectron spectroscopy

X-ray photoelectron spectroscopy (XPS) is considered as a very powerful technique for the characterization of the surface chemistry of electrocatalysts [67], which in this thesis was the L65SCrN. In principle, an X-ray photon irradiates the surface of a solid sample with an *hv* energy. Then, the sample emits an electron from the inner shell of an atom of the sample by means of the photoelectric effect [86] [87], as shown in Figure 32. However, these photons have limited penetration depth: 1 to 10 nm. Therefore, the detected electrons originate from only few of the top atomic layers, which makes XPS a unique surface-sensitive technique for chemical analyses [87].

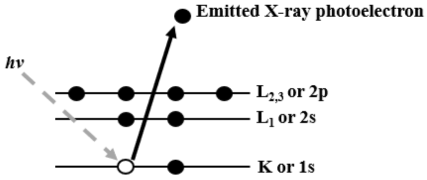

Figure 32 Principle of the XPS emission process for a model atom, where an incoming photon causes the emission of an X-ray photoelectron. Sketch adapted from [86] [87].

With the kinetic energy E_K from the emitted electrons, it is possible to estimate the binding energy E_B of the atomic orbital from which the electron originates [87] with the following relationship in equation (62):

$$E_B = hv - E_k - \phi \tag{62}$$

Where ϕ corresponds to the energy required for an electron to escape the sample's surface (depends on both sample materials and spectrometer), h to the Planck's constant and v to the frequency of the X-ray source [86]. The atomic electrons have characteristic values for their binding energies which allow to identify chemical elements, since photoelectrons are emitted from different electronic shells and subshells from the material's sample [86]. Quantitative analyses can be performed with the peak heights or peak areas. For instance, the chemical states identification is typically done by measuring the peak position [87]. Each binding energy peak is denoted as an element symbol with the shell symbol from where the photoelectron was ejected [86]. For example, Ni 3p, Cr 3s or Cr 2p, as shown in Figure 33.

In regard to the SOC electrode materials, XPS is a valuable characterization technique since it provides insights about their surface chemistry, since electrochemical reactions take place mainly on the surface of these electrocatalysts, without taking into consideration thermodynamic reactions, such as the RWGS when operated in co-electrolysis mode.

In the specific case of the L65SCrN fuel electrode, the main motivation to perform surface analyses by XPS was to evaluate the ratio between Ni and Cr species on the surface of the perovskite in two different states: as-prepared and reduced, and then try to correlate such ratios with the metallic Ni exsolution. The ratio between Cr^{3+} and Cr^{4+} was also of interest because an alteration in this ratio could lead to an expansion or contraction of the lattice, considering that the ionic radii (in an octahedral environment) for Cr^{4+} corresponds to 0.55 Å and 0.615 Å for Cr^{3+} [57] [88]. Besides, the concentration of Cr^{4+} governs the conductivity of this perovskite due to the holes (charge carriers $h^{\bullet}$) that are present on the Cr-sites, such as Cr^{4+} [72, 89], an discussed in [74].

In this thesis, the surface chemistry of L65SCrN powders, as-prepared and reduced (with 5% H_2–Ar from 25 °C to 1200 °C), was investigated by means of XPS (Figure 33). These analyses were carried out on a setup with a base pressure of $2x10^{-10}$ mbar with the hemispherical analyzer ESCALAB250, from ThermoFisher Scientific and a monochromatic Al Kα source with an X-ray energy of 1486.74 eV (XM1000, Scienta Omicron). The peak shape analyses were performed with the software Unifitt 2013, by applying convoluted Gaussian/Lorentzian profiles and a Shirley background function. The surface stoichiometry of the atoms/signals was calculated by using the numerically fitted peak areas [57].

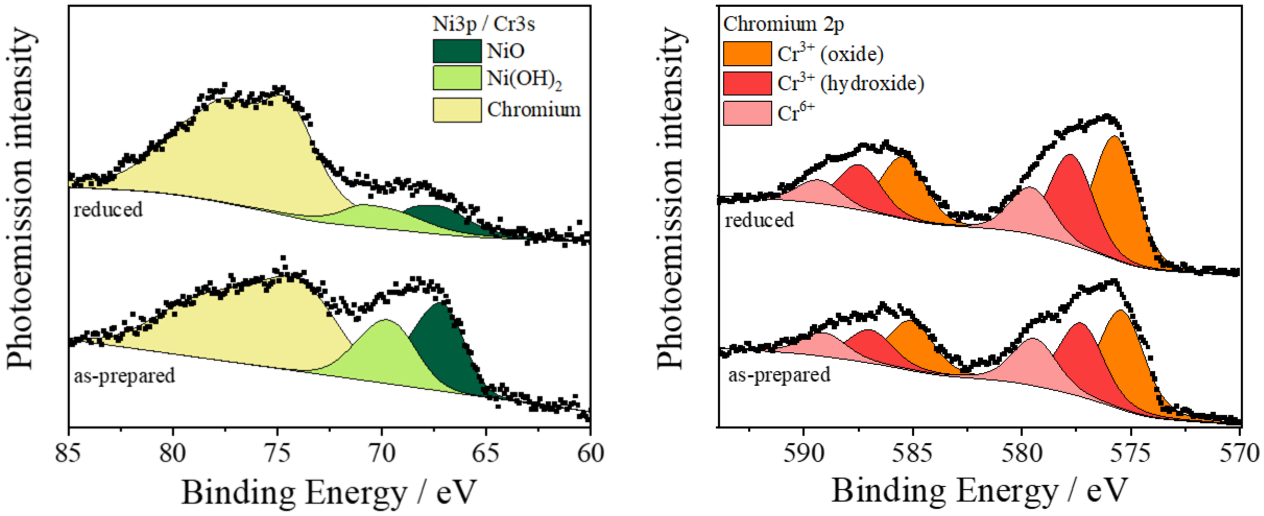

Figure 33 XPS spectra of L65SCrN powders (as-prepared and reduced). Left: Ni 3p / Cr 3s spectra. Right: Chromium 2p spectra. Plots adapted from [57].

5.7 Electrochemical characterization & Analyses

5.7.1 Full cell-test bench description

For the electrochemical characterization of the full square SOCs, a test bench with four parallel test-positions was used, as shown in Figure 34. On each testing site an electrochemical cell can be tested, for which the test rig provides two gas streams: fuel and air/oxygen. These four cell positions are placed on a metallic plate (with a ceramic support). For heating purposes, a furnace is placed over this plate allowing to operate at temperatures up to 900 °C. Cells are typically heated up at a rate of 3°C/min. Namely, for electrolysis conditions, a stainless-steel evaporator (TTI - Technologie-Transfer-Initiative GmbH - Universität Stuttgart) was installed for one cell position (#3). Externally controlled from the test bench, this evaporation system consisted on a module equipped with a mass flow controller (MFC) that pumped water into an evaporator. This evaporator supplied water steam (at ~ 130 °C) within the fuel gas carrier flow that entered the oven and the cell (through the ceramic pipe), as shown in Figure 35 (left image) and Figure 36. The outlet pipe of the evaporator was connected to the ceramic pipe by an assembly of flexible pipes that were heated with an external heating device (HORST - HT30) to a temperature of ~ 130 °C. Like this, it was guaranteed that the possible condensation on the humidified fuel gas was minimized. However, condensation problems could also be present on the fuel outlet pipe, more specifically when leaving the furnace though stainless-steel pipes. Therefore, these outlet pipes (below the metallic plate that supports the oven) were also heated, but up to 90 °C to avoid cooling of the gases below the dew point.

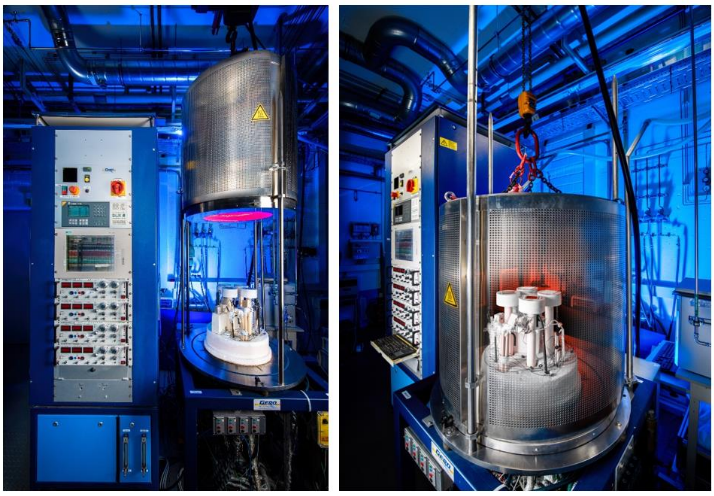

Figure 34 Cell test bench for high temperature electrochemical characterization of solid oxide cells with 4 cell positions and 4 independent electrical loads.

Each cell position is made of a ceramic cell housing, where the fuel inlet and outlet pipes are placed on the bottom and the air/oxygen inlet pipes are feed to the cells from the top with an Inconel pipe (Figure 36). Cell temperatures were monitored with thermocouples type-K, which were placed in designated holes at three positions, where the inlet/outlet of the fuel gas, as well as the air inlet were measured, also with the cell temperature. The latter was sensed by a thermocouple located on a hole 1 mm-deep on the cell housing. On the fuel side, platinum meshes were used for current collection on the perovskite cells. For the Ni cermet cells, nickel meshes were used. On the other side, the oxygen electrode was contacted with a gold mesh.

For ensuring an effective separation between fuel electrode and air electrode compartments, a gold frame was placed on the electrochemical cell with the purpose to isolate both electrodes by softening of the gold at high temperatures (Figure 35 – right image). After placing the cell and the gold frame on the fuel electrode head (fuel electrode facing down the platinum mesh), the cell housing ceramic cover was placed over the fuel electrode head and then the oxygen electrode head was placed over the oxygen electrode surface (facing upwards). The air pipe is placed carefully through a hole on the oxygen electrode head. For further tightness and sealing improvement, five weights (each of 75 g) made of Inconel are placed over the oxygen electrode head, such as depicted in Figure 36.

For the commissioning process and regardless from the type of test, the cells were heated up to 900 °C with a heating rate of 3 °C/min with flow of Nitrogen on the fuel side (1 slpm) and on the oxygen electrode side with an air flow (also of 1 slpm). Then, the fuel electrode was reduced by changing the gas flow from nitrogen by hydrogen (also 1 slpm) and this condition was kept for one hour. After reduction for 1 hour at 900 °C, the operating cell temperature and gas compositions were adjusted, upon desired testing conditions. Appropriate cell tightness was checked by measuring the OCV and comparing it to the theoretical Nernst voltage at the given temperature and gas compositions, calculated by using equations (5), (8), (16) and (21) depending on the operating mode. These thermodynamic calculations were done with the software CANTERA 3.0 [32].

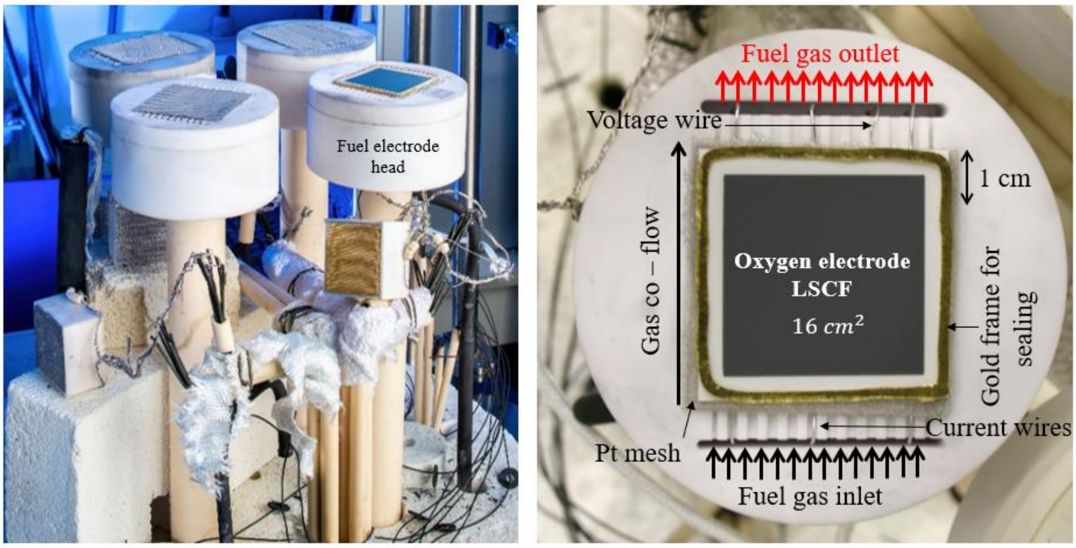

Figure 35 Left: Four cell positions within the oven of the test bench. Right: Electrolyte-supported cell mounted on ceramic holder.

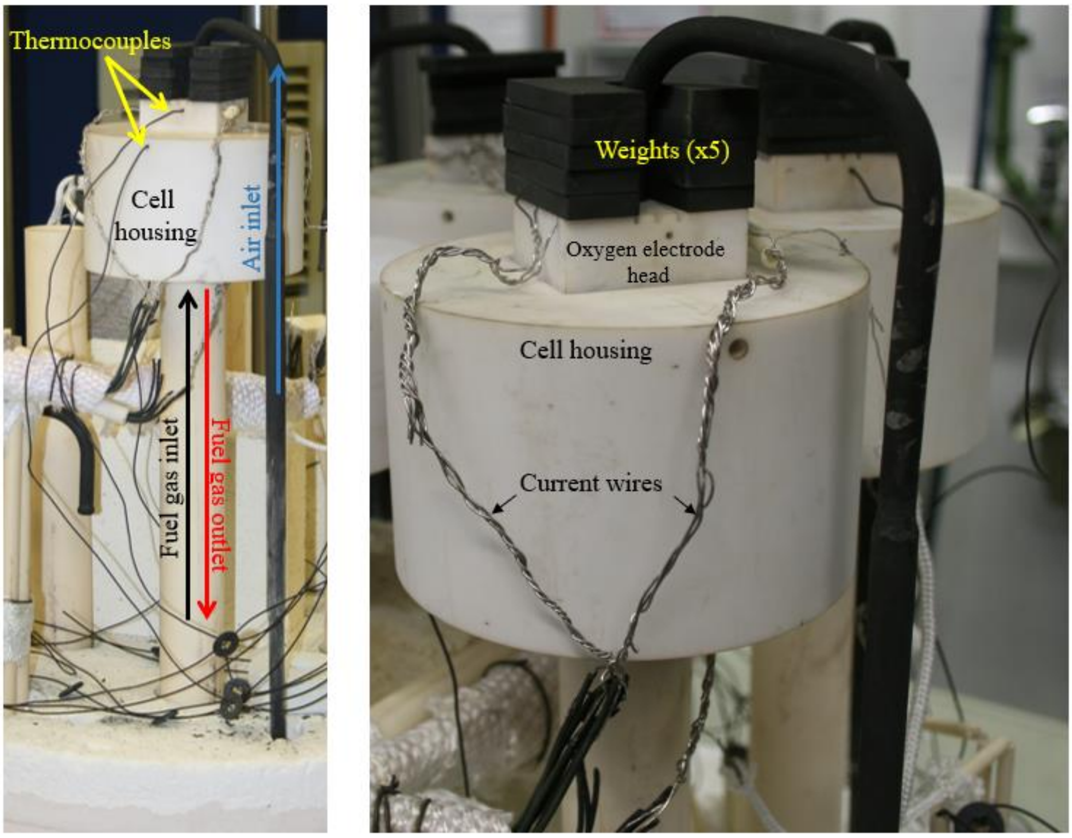

Figure 36 Left: Cell housing setup with fuel pipes (inlet and outlet) and air pipes. Right: Closer view of the cell housing. Both images are complementary since thermocouples, weights and current wires are visible.

5.7.2 *I-V* characteristics

The electrochemical tests were performed with the electronic load implemented on the test rig, for different SOC operating modes. In SOFC operation the polarization curves were measured from OCV down to 0.6 V at a rate of 0.012 A·s^{-1}. In SOEL and co-SOEL modes, polarization curves were performed from OCV up to a maximum cell voltage of 1.5 V, at a rate of - 0.012 A·s^{-1}. In this thesis, different operating modes were characterized (as shown Figure 37) and discussed in the corresponding publications.

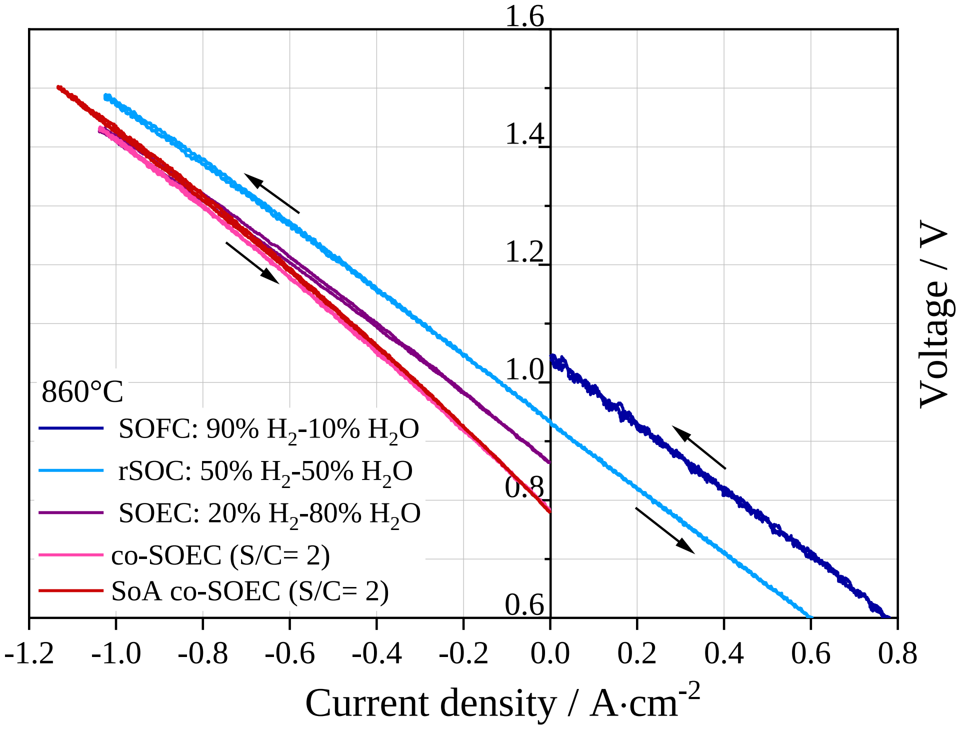

Figure 37 Current-voltage (*i-V*) characteristics recorded at 860 °C of L65SCrN based-fuel electrode ESC in different operating modes: SOFC, rSOC, SOEC and co-SOEC. State-of-the-art (SoA) ESCs were also recorded in co-SOEC mode. Data adapted from [57].

Additionally, an attempt to characterize the L65SCrN fuel electrode under CO_2 electrolysis operation was performed, where voltage was applied to the cell (in steps of 3 minutes) up to 1.9 V and the current density was measured (Figure 38). Unfortunately, further investigations were not continued since it was suspected the presence of impurities on the supplied CO_2 gas, which could be eventually sulfur traces. The influence of those impurities did not allow to differentiate electrochemically between poisoning and consequences of a possible carbon deposition in the cell. At high current densities (~ -0.93 A·cm^{-2}) a strong deactivation of the cell was observed likely due to CO_2 starvation at this condition, for which a reactant utilization

(RU) of 103% was calculated. For such high RU, it was assumed that carbon deposition was possibly taking place on the fuel electrode, likely due to the starvation of CO_2 on the feed gas: the formed CO by electrolysis was further electrochemically reduced to carbon, which potentially was deposited on the electrode surface. Therefore, it was suspected that this phenomenon or carbon deposition may have caused the strong deactivation of the cell, as depicted on the red area in Figure 38 [90]. For most of the electrochemical tests performed in this thesis, the total gas flow on the fuel electrode was kept at 1 slpm. Exceptions were made for the co-SOEC operation, with a total gas flow of 0.84 slpm and for CO_2 electrolysis with 0.1 slpm. The latter low flow rate was chosen with the aim to achieve high current densities. The flow on the oxygen electrode was always adjusted to have the same flow rate that on the fuel electrode.

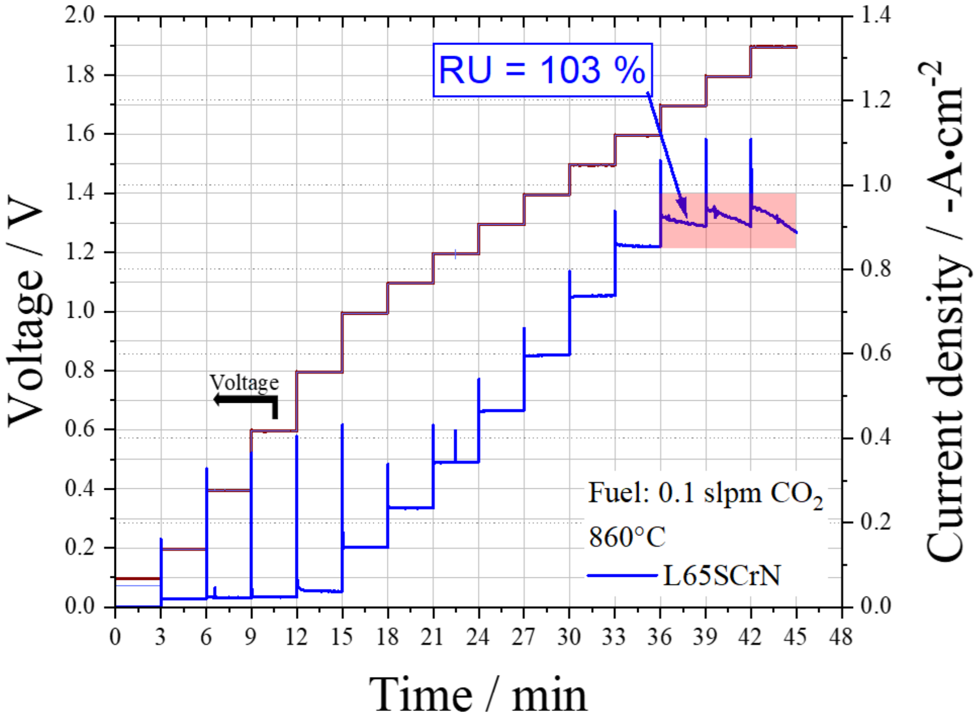

Figure 38 Current-voltage (i-V) characteristics recorded at 860 °C of L65SCrN based-fuel electrode ESC in CO2 electrolysis operation. Voltage was applied in steps of 0.2 V each 3 minutes and current density was measured. Data presented in [90].

Following on Table 4 are the main features and temperature range for the investigated operating modes in this thesis:

Table 4 Temperature ranges and durability times of the different electrochemical tests performed in SOC operating modes.

Operating mode	**Temperature (°C)**	**Tested cells ($16\ cm^2$)**	**Durability tests**	**Reference in this thesis**
SOFC	860	L65SCrN Ni-CGO	~ 170 h	[54], [57]
rSOC	860	L65SCrN	-	[57]
co-SOEC (H_2O- CO_2 electrolysis)	770, 800, 830, 860	L65SCrN Ni-CGO	~ 950 h @ 860 °C	[28] [57]
SOEC	770, 800, 830, 860	L65SCrN Ni-CGO	~1000 h @ 860 °C	[57] [74]
CO_2 electrolysis	860	L65SCrN	~ 96 h	[90]

5.7.3 Electrochemical impedance spectroscopy

As previously explained, the operating voltage of an electrochemical cell experiences significant losses, mainly attributed to ohmic and polarization (kinetics and mass transport) losses. Each of these losses is characterized by a physical process within the cell with a specific time characteristics and frequency response, meaning that there are different rates for these processes: some of them are faster than others [91] [92]. In order to characterize each of these processes, electrochemical impedance spectroscopy (EIS) is the most common technique to characterize the dynamic behavior (or impedance) on electrochemical cells by applying a sinusoidal perturbation (current or voltage) to the cell and measuring the amplitude and phase shift of the response [92]. This method is based on small-signal perturbations, that also reveal the relaxation times from these different processes over a wide range of frequencies f. Overall, the various chemical and physical processes that take place within an electrochemical cell in operation are complex non-linear relationships between voltage and current density, which are characterized by the electrochemical impedance $\underline{Z}$ ($\Omega\cdot cm^2$) [91] [93]. Impedance measurements could be performed near to OCV conditions or under a specified current density, as shown in Figure 39. Taking the example in which a sinusoidal current $i(t) = i_o \sin(\omega t)$ is superposed to a defined range in current I_{load} and applied to the cell, the voltage response is measured as:

$$V(t) = V_o(\omega)\sin[(\omega t + \omega(\phi)] \tag{63}$$

Where $\omega = 2\pi f$ (Hz) corresponds to the angular frequency and $\omega(\phi)$ to the frequency that is a function of the phase shift between current and voltage [92].

From the relation $V(t) = i(t)\underline{Z}(\omega)$, the complex impedance response is calculated as the ratio between the complex solution of the voltage response and current such as:

$$\underline{Z}(\omega) = \frac{V(t)}{i(t)} = \frac{V_o(\omega)}{i_o} e^{j\phi(\omega)} = |Z(\omega)|e^{j\phi(\omega)} = Re\{\underline{Z}(\omega)\} + jIm\{\underline{Z}(\omega)\} = Z' + jZ'' \tag{64}$$

Where Z' corresponds to the real part and Z'' to the imaginary part of the complex impedance, with $j = \sqrt{-1}$. A galvanostatic measurement is employed for describing the sinusoidal applied perturbation as current. In case of an applied voltage perturbation, the measurement is known as potentiostatic [92].

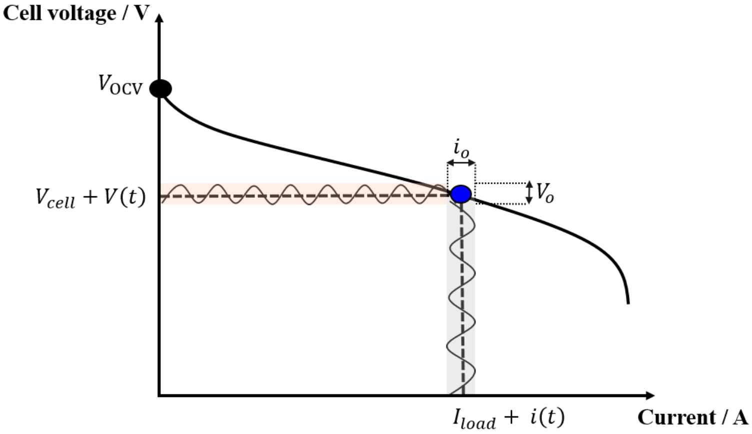

Figure 39 Sketch of the *i*-*V* curve during impedance measurement in SOFC mode: A sinusoidal current of small amplitude $i(t)$ is applied to a defined bias current I_{load} and the voltage response $V(t)$ is measured. Adapted from [92].

Impedance measurements are performed in a discrete range of frequency, for which the impedance response is plotted. Among different plots for reporting complex impedance measurements, the most common are the Nyquist plot ($-Z''$versus Z') and the imaginary impedance plot ($-Z''$versus f), as shown in Figure 40. Typically, both of them are reported since the different electrochemical processes within the cells can be characterized and identified with these variables $Z', Z'',$ and f. However, it is also usual to only report these results with the Nyquist plot. In such a case, the frequency decades should be also depicted on the plot.

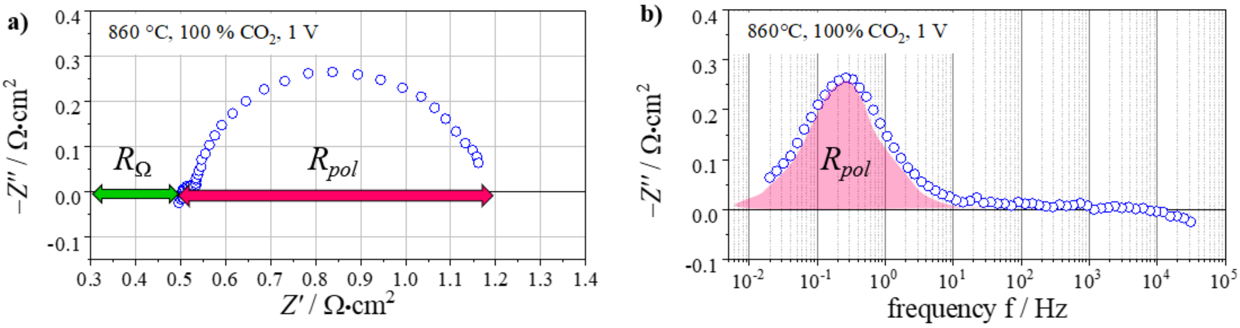

Figure 40 Typical EIS spectrum depicted with the (a) Nyquist plot and with the (b) imaginary impedance plot. Data were recorded for an ESC operated in pure CO_2 electrolysis at 860 °C under cathodic polarization of 1 V. Plots adapted from [90].

Impedance measurements are also complementary to the i-V characteristic measurements. For instance, taking the Nyquist plot, the high frequency intercept ($\omega \rightarrow \infty$) corresponds to the ohmic resistance R_{ohmic}, while the intercept at low frequencies ($\omega \rightarrow 0$) is the resistance value that can be obtained as the instant slope on the i-V characteristic curve at a specific operation point. If the difference between these two intercepts is calculated, the results value corresponds to the polarization resistance R_{pol} [92]. This resistance also corresponds to the sum of the associated-resistance values of the different voltage losses (except for the ohmic losses), as explained in section 2.8.1.

In the frame of this thesis, EIS measurements were performed with different setups. Symmetrical button cells (with active surface area of 0.785 cm^2) were characterized in potentiostatic mode in four-wire mode with a Novocontrol Alpha impedance station in a frequency range from 50 mHz to 100 kHz and amplitude of the voltage stimulus of 50 mV in the symmetrical cell test bench at TU Wien, Research Division Technical Electrochemistry, in Figure 41, right. Equivalent circuit model fitting of the impedance data was performed with the commercially available program ZView® [94].

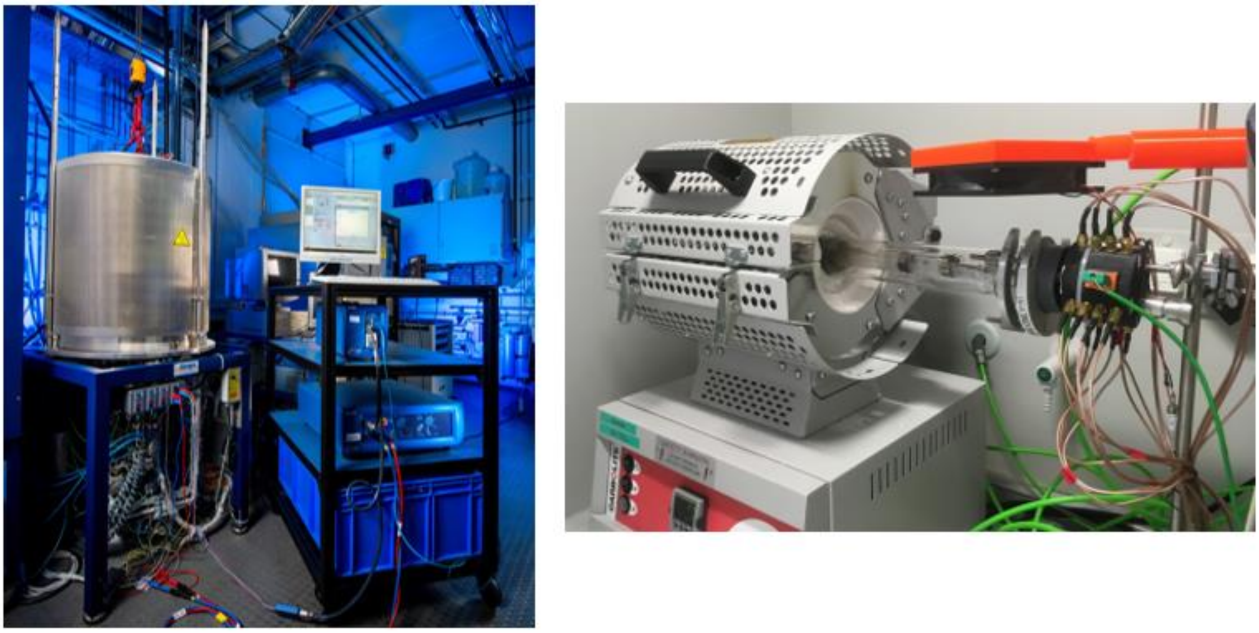

Figure 41 Left: Electrochemical workstation SP-200 from BioLogic Science Instruments at DLR. Right: Setup for symmetrical button cells electrochemical characterization with a Novocontrol Alpha impedance station at TU Wien, Research Division Technical Electrochemistry.

The full electrochemical cells (with active surface area of 16 cm^2) were characterized in galvanostatic mode near to OCV. The workstation Zahner® PP-240 with Thales software) was used in a frequency range from 20 mHz to 100 kHz with 10 points per decade and an AC amplitude of the current stimulus of 500 mA. These parameters were used for the experiments on [54] [57]. During long-term characterizations in co-SOEL and SOEL modes, the electrochemical workstation SP-200 from BioLogic Science Instruments (Figure 41, left) at a frequency range from 50 mHz to 100 kHz and an AC amplitude of 500 mA was used, also close to OCV.

5.7.4 Equivalent circuit models

The various impedance contributions within an electrochemical cell can be evaluated with equivalent circuit models (ECM). Such circuits are typically constituted by different electrical elements, such as inductors, resistors and capacitors [91].

- Inductor: Due to the inductivity present on the wiring in electrical connections on the test bench and also on the impedance device, there is a contribution to the EIS spectrum that is purely complex and positive. This contribution is also considered as a measurement artifact that could be corrected by subtracting its impedance contribution from the EIS curve. However, such artifact could be reduced by twisting the cables [95]. For frequencies $\omega \rightarrow 0$ the inductance L tends to zero, whereas for higher frequencies it is expressed as:

$$\underline{Z}(\omega) = j\omega L \tag{65}$$

- Resistor: The impedance of a resistor is not dependent on the frequencies and therefore it does not present a complex part:

$$\underline{Z}(\omega) = R \tag{66}$$

- Capacitor: On the contrary, the impedance of an ideal capacitor does not present a real part and tends to zero for $\omega \rightarrow \infty$:

$$\underline{Z}(\omega) = \frac{1}{j\omega C} = -j\frac{1}{\omega C} \tag{67}$$

Different series and parallel arrangements of these elements, as well as other more complex combinations between them, describe various electrochemical processes with their respective characteristic frequencies identified by EIS analyses. The simplest configuration of these circuits corresponds to the RQ-element, which is a parallel connection of a resistor with a capacitor, as shown in Figure 42, where the capacitance element can be better described with a constant phase element (CPE), also denoted as Q-element:

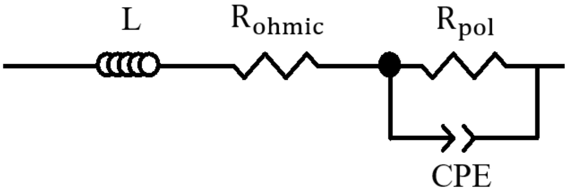

Figure 42 Sketch of equivalent circuit model of an RQ-element: R_{pol} is denoted as R and the capacitor Q as CPE.

The RQ element is also considered as the building block of most of electrochemical systems. Their complex impedance response is expressed as [92] [96]:

$$\underline{Z}_{RQ}(\omega) = \frac{R}{1 + RQ^{-1}} \tag{68}$$

The capacitance of the Q-element can be calculated as [92] [96]:

$$\underline{Z}_{Q}(\omega) = Q(\omega) = \frac{1}{Y_Q(j\omega)^{n_Q}}, 0 \leq n_Q \leq 1 \tag{69}$$

For $n_Q = 1$, $\underline{Z}_Q(\omega)$ behaves as an ideal capacitor with $Y_Q = C$. The characteristic time constant τ_{RQ} as well as the corresponding frequency can be calculated as [92] :

$$\tau_{RQ} = \sqrt[n_Q]{RY_Q} \tag{70}$$

$$f_{max,RQ} = \frac{1}{2\pi\tau_{RQ}} \tag{71}$$

Other more complex elements that describe various diffusion processes in SOCs electrodes, are represented by the Warburg and Gerischer elements [92], which are discussed in more detail in [91] [92].

5.7.5 Distribution of relaxation times

Some of the different processes that take place within an electrochemical cell could have similar relaxation times or range of frequencies, which make more difficult to deconvolute each of them with different combinations of RQ elements. Unfortunately, the selection of a specific ECM is not a straightforward procedure, since some ambiguities or rough assumptions about such processes should be made. Various different ECMs should be proposed until an adequate option that includes all, or most all of the processes contributions is appropriate, which at some end is an indirect assessment of the EIS behavior. An alternative to this issue, is the use of the distribution of relaxation times (DRT) method, which consists of an infinite number of RQ circuits in series representing the total R_{pol}, where the impedance can be expressed in terms of the ohmic resistance R_{ohmic} and the distribution of relaxation times $\gamma(\tau)$ [91] [96], as shown in equation (72):

$$\underline{Z}(\omega) = R_{ohmic} + R_{pol} \int_0^{\infty} \frac{\gamma(\tau)}{1 + j\omega\tau} d\tau \tag{72}$$

Where the term inside the integral includes the contribution of the total polarization resistance and relaxations times between the interval τ and $\tau + d\tau$. The continuous function $\gamma(\tau)$ could be approximated with a discrete expression of N logarithmically distributed RQ elements [97], such as equation (73):

$$\underline{Z}(\omega) = R_{ohmic} + R_{pol} \sum_{n=1}^{N} \frac{\gamma_n}{1 + j\omega\tau_n} \tag{73}$$

For which γ_n corresponds to the contribution to the total R_{pol} of the nth RQ element with relaxation time τ_n [97]. With this assumption, the area under each peak in the DRT resulting curve corresponds to the polarization resistance of the corresponding process, typically reported in ($\Omega\cdot cm^2$) [91]. In this thesis, DRT calculations were performed with the impedance analysis and modelling software ec-idea from [98], as reported in [57].

5.7.6 Chronopotentiometry and chronoamperometry

There are various techniques that allow to monitor the electrochemical cell performance and degradation during a specific period of time. Among them, chronopotentiometry consists on fixing the value of the applied current (or current density for benchmarking purposes) and monitoring the response on the cell voltage (potential). On the contrary, chronoamperometry consists on holding the cell voltage constant and measuring the current variation over time [99]. In the frame of this thesis, both techniques were used.

Chronopotentiometry measurements in co-SOEL and SOEL operating modes were performed. Long-term test in co-electrolysis operation was performed for 950 hours at a fixed electrolysis current density of -0.45 $A\cdot cm^{-2}$ and at a cell temperature of ~ 860 °C [57]. Similarly, 1000 hours-test was performed in SOEL operation at 860 °C with a fixed current density of -0.67 $A\cdot cm^{-2}$ [74]. For both tests, galvanostatic EIS measurements at OCV were performed at regular time interval in order to evaluate the cell performance and degradation. Shorter chronopotentiometry measurements in SOFC were performed for 94 hours at 0.5 $A\cdot cm^{-2}$ at a cell temperature of ~ 860 °C. Afterwards, a series of 4 redox cycles was applied to the cell by purging the fuel electrode with oxygen flow for 45 minutes. Then, EIS measurements were performed in order to characterize the recovery in performance [54]. Chronoamperometry measurements in SOFC mode were performed for ~ 175 hours at a fixed cell voltage of 0.6 V, where the current density was monitored, as reported in [54].

5.7.7 Conductivity measurements

The performance of electrochemical cells is strongly dependent on the electrical conductivity of the electrodes. Despite the challenge to deconvolute the ionic conductivity σ_{ion} from the electrical conductivity σ_{el} in MIEC perovskite-based electrodes, it is possible to assume that $\sigma_{el} \gg \sigma_{ion}$ [100]. In semiconductors, electrons and holes are the charge carriers that move under the influence of an electric field. Such motion generates an electrical current, also known as drift current, which explains the electrical conductivity phenomenon in this type of solids. The magnitude of the current indicates if the solid is good conductor, which is also proportional to the density of the mobile (electrical) charge carriers. Hence, by the general form of Ohm's law, the drift in current $\vec{J}_{drift}$ is proportional to the electric field strength $\vec{E}$, as described in equation (74). This proportionality factor is σ_{el} (S·cm^{-1}). Typically, the conductivity could also be expressed in terms of its inverse value, which is the resistivity ρ [101], as shown in equation (75).

$$\vec{J}_{drift} = \sigma_{el}\vec{E} \tag{74}$$

$$\rho = \frac{1}{\sigma_{el}} \tag{75}$$

With the Van der Pauw method, the σ_{el} can be quantified through estimation of ρ, if the tested material is a flat sheet with known thickness d. By applying a direct voltage to two contact points on a material sheet with the form in Figure 43, the direct current is measured on the other two contact points, for which the resistance value could be estimated [102].

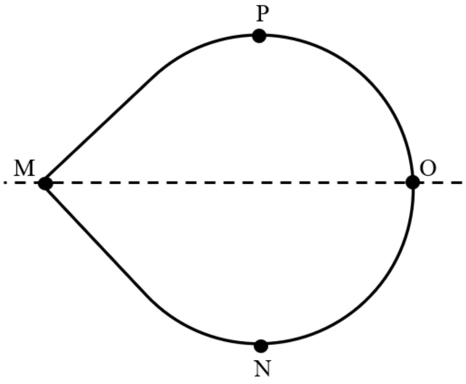

Figure 43 Simplification of the resistivity measurement when the sample has a line of symmetry. If two of the contacts are located on this line and the two others are symmetrically located with respect to the line of symmetry, then one measurement is enough. Adapted from [102].

In the ideal case of a flat lamella, completely free of holes with a line of symmetry, the resistivity can be estimated as [102]:

$$\rho = \frac{\pi d}{\ln(2)} R_{MN,OP} \tag{76}$$

However, for the general case, ρ can be estimated as shown in equation (77), where the factor f is a function of the ratio between $R_{MN,OP}/R_{NO,PM}$, as equation (78) [102]:

$$\rho = \frac{\pi d}{\ln(2)} \frac{R_{MN,OP} + R_{NO,PM}}{2} * f \tag{77}$$

$$cosh\left\{\frac{\left(R_{MN,OP}/R_{NO,PM}\right)-1}{\left(R_{MN,OP}/R_{NO,PM}\right)+1}*\frac{\ln(2)}{f}\right\}=\frac{1}{2}e^{\frac{\ln(2)}{f}} \tag{78}$$

For practical purposes, the plot that describes *cosh* is depicted in [102] and [103], where the values of f can be read as a function of the measured $R_{MN,OP}/R_{NO,PM}$.

In this thesis, the electrical conductivity of the perovskite-based fuel electrode was measured on thin L65SCrN films that were screen printed on inert 1x1 cm Al_2O_3 substrates and fired at 1100 °C. On these samples, Van der Pauw measurements were performed at TU Wien with the purpose to determine the sheet resistance and conductivity, by varying temperatures and gas compositions (with and without humidification). These experiments were performed in a high-temperature chamber set-up which consists of a fused silica tube inside a tubular surface, as described in [103] [104]. The analysis and discussion of these experiments are detailed and reported in [74].

The following chapter entails the general discussion of the results of this doctoral thesis within the current scientific context. Discussions and analyses from the lab-scale up to the system level are presented.

6 General discussion in scientific context

In this chapter, various aspects are discussed with the main purpose of integrating this doctoral thesis in the current scientific context of the different scales of the SOC technologies.

Firstly, a brief historical perspective of the evolution of SOC materials is presented, which explains when and which materials were introduced, focusing on the most commonly used materials for the fuel electrodes and discussing also about the technology readiness level (TRL). Secondly, a comparative assessment of the L65SCrN fuel electrode at the cell level is presented in terms of how these perovskites compete with the state-of-the-art in the different SOC operating modes. Thirdly, the scale-up to larger cell areas is discussed considering the mechanical behavior of ceramic materials subjected to different types of strain-stress states during SOCs typical operation regimes. Finally, to evaluate how this thesis contributes to the scale-up of these perovskite electrodes, a real case will be taken as example, with main parameter the required hydrogen production rate and the required power input. This example case illustrates how these perovskites could be implemented to the macro scale (~MW) electrolyzers and what would be the benefit. Having that in mind, critical raw materials requirements for such macro scales are estimated for the case of state-of-the-art materials and also for L65SCrN-pervoskite electrodes.

6.1 Historical perspective on the evolution of SOC materials

In order to integrate the use of a perovskite-based fuel electrode in SOCs, such as the L65SCrN electrode investigated in this thesis, it is important to start to discuss and analyze its performance within the historical background of SOCs in different industrial applications, as well as at the laboratory scales. This, with the aim to develop an insight on time scales that were required for the introduction of the state-of-the-art materials, with a main focus on the fuel electrode, and also to understand when and why they were implemented.

The history of the electrochemical cells dates back to 1829, when Christian Friedrich Schönbein discovered the operating principle of a fuel cell. In 1838 Sir William Grove developed a wet-cell battery, called “Grove cell” which was based on reversing the electrolysis of water [105].

Focusing on the high temperature applications, the oxide-based materials started to show up on scene. In 1899 Walther Nernst discovered the ceramic material that consisted of 85 % ZrO_2

and 15% Y_2O_3, called “Nernst Mass”, which laid the foundation of the electrolyte material of the solid oxide cells [105] [106]. The first concept of a solid oxide electrochemical cell for power generation (SOFC) was demonstrated in 1937 by Emil Bauer and H. Preis using materials such as zirconium, yttrium, cerium, lanthanum and tungsten oxides operating at 1000 °C [105] [106]. In the 1940s, the Russian O.K. Davtyan added monazite sand to a mixture of sodium carbonate with tungsten trioxide and soda glass, with the purpose to increase the conductivity and mechanical strength of the electrolyte [107]. Other studies began after the pioneering research by Carl Wagner in 1943 since he attributed the electrical conductivity in mixed oxides, such as doped zirconia, to the oxygen vacancies [106].

In 1962, researchers at the Westinghouse Electric Corporation presented a publication with the title “a solid electrolyte fuel cell”, which based the foundation of their ASC tubular SOFC, using zirconium oxide and calcium oxide [105]. They successfully produced and tested various SOFC power systems between 5 and 250 kW between 1980 and 1990 [106], under the name of Siemens Westinghouse Power Corporation (SWPC), where a cermet of Ni-YSZ was used as fuel electrode material [108]. Beyond the power generation mode, high temperature electrolyzers were investigated and developed by Dönitz and Erdle at Dornier GmbH in the 1980s. They developed a commercial SOEC 10-cell stack for hydrogen production based on the concept “Hot Elly” [109], using as fuel electrode a Ni-cermet (likely Ni-YSZ) in tubular architecture [110-112].

At this point, it is noteworthy to stop on the timeline and mention the development of the well-known Ni-YSZ cermet fuel electrode, who was introduced by H. S. Spacil in 1970. Prior to this, early research using single-phase fuel electrodes included graphite, iron oxide, platinum-group metal catalysts (PtGMs) and transition metals [113]. Unfortunately, significant problems were identified with these materials. For instance, graphite was found to be electrochemically corroded, and platinum spalled-off in operation (likely due to water-vapor evolution at the metal-oxide interface). Regarding the transition metals, iron was corroded due to the increment in pO_2, leading to the formation of red-colored iron oxide. Nickel presented a considerable thermal expansion mismatch in comparison to the YSZ-electrolyte, but also presented serious problems of coarsening during operation, obstructing the pores and reducing the TPBs required for the electrochemical reactions [113]. Spacil stated that doping YSZ with a transition metal was the best option to overcome the difference in thermal expansion that would lead to mechanical failure of the cell and the metal-particle coarsening during operation [113] [114]. He also recognized that the role of the ceramic phase was mainly structural, due to the retention of the dispersion of the metal particles, as well as the role of the porosity of the fuel electrode during long-term operation. Spacil also identified that the oxide-ion mobility of the YSZ phase was complementary to the electrical conductivity of the Ni metallic phase, which enhanced significantly the electrocatalytic activity of the fuel electrode and hence the performance [113]. Since then, Ni-YSZ has been the dominant fuel electrode material for which unfortunately, important issues have been also identified mainly in operation with hydrocarbon-based fuels due to carbon deposition in the fuel electrode, as mentioned in section 2.11.5.

Another important stop on the timeline of materials research for SOC applications should be taken on 1989, when CGO-based fuel electrodes where introduced. After noticing the problematic operation with hydrocarbon-based fuels with the Ni-YSZ cermet, as well as the loss of conductivity due to Ni agglomeration and lack of TPBs, researchers proposed the use of MIEC electrodes that could overcome these issues. For this, CGO was a good candidate due to its MIEC properties and also good tolerance against carbon deposition. In this regard, M. Mogensen and J. J. Bentzen reported the use of fuel electrodes based on mixtures between CGO ($Ce_{0.85}Gd_{0.15}O_{1.925}$) and TZ3YA, tetragonal Y_2O_3 doped zirconia ($Zr_{0.945}Y_{0.055}O_{1.973}$) for methane oxidation between 800 - 1000 °C [115]. In their observations, carbon deposition mechanisms were not observed nor identified. However, they reported cracking issues on these electrodes during redox cycling, caused by the expansion of the CeO_2 phase during reduction and contraction during oxidation [115]. Other doped ceria formulations were introduced, such as in 1992 by I. S. Metcalfe et al., who investigated niobia doped ceria fuel electrodes for the oxidation of hydrogen, methane and propene [116] [117]. Further doped-ceria formulations were investigated such as Ce-Zr oxide and Ce-Y-oxide. Other combinations of ceria doped with Cu, Ag, Au, Ni, Mn, Mo, Cr, V, Fe, Co, Ru, Rh, Pd, Pt, Ir, and Os were also studied [118].

Focusing on the Ni-doped ceria fuel electrodes, early research was performed around 1995. At that time, the Japanese company Tokyo Gas reported a patent that describes a method for preparing a fuel electrode for SOFCs based on Ni-Y_2O_3-doped ceria [119]. In 1997, Sulzer Innotec Ltd. reported electrochemical investigations on SOFCs using a fuel electrode based on Ni-CGO [120]. USA researchers investigated in 1999 Ni-CGO fuel electrodes in button CGO-electrolyte-supported cells for hydrogen oxidation between 500 °C and 700 °C [121]. In the same year, Sulzer Innotec and Sulzer Hexis Ltd. reported the performance of a SOFC stack for methane steam reforming at temperatures between 600 °C and 800 °C [122]. Their stack consisted of 63 CGO10-based electrolyte supported cells using LSCF oxygen electrode and Ni-CGO fuel electrode. Each repeating unit was of 120 mm diameter and the active area of each one was 100 cm^2 [122]. Unfortunately, they reported that self-supported CGO cells were not suitable for applications in SOFC for steam reforming nor for operation with natural gas due to the cracking of the ceria under system operating conditions [122]. Besides such cracking issue in Ni-CGO electrodes, researchers in the United Kingdom reported Ni coarsening in these electrodes also under steam reforming conditions [123].

Having in mind the use of these Ni-based cermets, such as Ni-YSZ and Ni-CGO, it is now possible to continue with the timeline. During the 90s-decade, planar SOFC developments were introduced in many corners of the world. In Europe, companies such as Daimler-Benz/Dornier (Friedrichshafen, Germany), Siemens (Erlangen, Germany), Sulzer Hexis (Winthertur, Switzerland) were pioneers. German institutions as Forschungszentrum Jülich (FZJ) and the German Aerospace Center (DLR Stuttgart) developed anode-supported SOFC stacks and metal-supported concepts, respectively [108]. The stack design from FZJ was based on a counter-flow arrangement, which was preferred for operation with natural gas for internal reforming. For this application, they designed a 60-layer stack using Ni-YSZ as fuel electrode, delivering 11.9 kW at 800 °C [108]. This case served as an example for other companies and institutions for the development of anode-supported stacks, such as Global Thermoelectric (Canada), Haldor Topsœ/Risœ (Denmark), Sulzer Hexis (Switzerland), Delphi Automotive Systems, GE, Laurence Livermore and Pacific Northwest National Labs (USA), Nihon Gaishi, Tokyo Gas (Japan) and the Korean Instituter of Energy Research, among others. Several others focused their development also in electrolyte-supported technologies: Risœ (Denmark) until ca. 1995, Fraunhofer IKTS (Germany), Webasto/Staxera (Germany), Cummings/SOFCo (USA), Nippon Shukubai and Toho Gas from Japan, as well as CFCL in Australia, also known an CFC GmbH, who also focused on anode-support technologies. Ceres Power (Great Britain) focused their activities in metal supports (MSC) implementing CGO electrolytes for operation at ~ 550 °C [108].

In the decade of the 2000s, important developments at the cell and stack level were initiated for different applications, such as residential, commercial and power plants [106]. ASC architectures with Ni-YSZ fuel electrodes were continued, mainly known by Haldor Topsœ/ Risœ, SOLIDPower and FZJ. After acquiring CFC GmbH in 2015, the manufacturer of the BlueGEN SOFC system [124], SOLIDPOWER ASC-architectures were implemented within their BlueGEN commercial micro CHP (combined heat and power) system, with 70 planar ASCs with an active area of 80 cm^2 [125] [126]. Metal-supported cell and stack have been developed with the aim to offer system solutions. One example of this is the cooperation between Ceres Power and the Bosch Group: with the SteelCell® technology of metal-supported cell architecture from Ceres Power, they aim to achieve an initial annual production in Germany of around 200 MW of SOFC for 2024 [127]. There are other companies that passively contribute to the SOFC Research & Development (R&D). This is the case of Bloom Energy (USA), one of the biggest SOFC suppliers (~ MW capacity). Unfortunately, the details of the cells architectures and materials are not available for the public [128].

Focusing on ESC architectures, Ni-CGO fuel electrodes were gaining reputation with the stacks and modules from Staxera GmbH [129]. This company was founded in 2005 as a start-up Fraunhofer IKTS, known also as Webasto. They were one of the first SOFC suppliers worldwide to offer off-the-shelf stack modules (ISM) as standardized product [130] [131]. Each of those ISM modules was constituted of two MK200 stacks. Each stack was made of 30 cells with a porous fuel electrode of Ni-CGO, a dense 3YSZ electrolyte and an oxygen electrode of double layered 8YSZ/LSM-LSM. The total thickness of each cell was 160 µm with an active area 127.8 cm^2 [129]. In 2011, the company Sunfire GmbH acquired Webasto/Staxera as nucleus for subsequent electrolyzer developments [132], from which the current standard stack model was the one proposed by Staxera.

Nowadays, Sunfire GmbH is an active partner on the energy transition across Europe. Among various of their projects, it is noteworthy to take the specific example of their consortium on Salzgitter AG for producing green hydrogen. This is the first implementation of a high temperature electrolyzer on the MW range installed at the Salzgitter Flachstahl steel plant. The main purpose is to produce 200 Nm^3/h of hydrogen (18kg H_2/h) at nominal power input of 720 kW with a system of 8 SOEC modules, each with 36 stacks and each stack with 30 ESCs, i. e. with 8640 cells in total [133].

With this historical background on SOCs and focusing on the fuel electrode developments, it is possible to inquire which are the fuel electrode materials in nowadays SOC systems, why they were selected and how much time took their development to come to the current status.

In summary, the state-of-the-art materials for the fuel electrode are mainly Ni-based cermets: Ni-YSZ in ASCs and Ni-CGO in ESCs.

- Starting with the YSZ electrolytes in 1940, the Ni-YSZ from the 1970s was a noteworthy progress due to the high catalytic activity of the Ni and the mechanical support given by the 8YSZ, giving outshining performances at the early 90s in SOFC tubular configurations (~ 250 kW). However, important issues during operation with hydrocarbons exhibited a drawback on these composites. At the same time, the planar architectures were starting to appear. All in all, it took roughly 50 - 60 years to develop this composite and identify promising performances as well as relevant operating issues. Since 2004, ASC-planar systems started to be studied (~ 13 kW) and nowadays modules of ~ 35 kW have been produced with this technology.
- Ni-CGO fuel electrodes have had a more recent history. In 1989, ceria-based electrolytes were firstly introduced already in planar configurations, with the aim to overcome the above-mentioned issues on Ni-YSZ and also due to the ceria MIEC features. However, microstructural mismatches during high temperature operation were identified. In 1992 transition metal doping on ceria oxides was investigated, from which the most promising cermet was Ni-CGO, resulting in a cermet with high catalytic activity as well as better thermal expansion behavior than the ceria electrolytes, confirmed with various studies around 1999. Roughly since 1995, the ESC architecture started to be implemented and from the 2000s larger systems have been produced, achieving SOEL operation in a ~ 90 kW-scale. Hence, for this cermet almost 30 years were required for achieving the current technological status.

Concerning the different SOC operating modes with state-of-the-art electrodes, various technology readiness level (TRL) for these technologies have been reported. Regarding SOFC systems for stationary applications a TRL of ~ 7 - 9 has been reported, due to already field-proven commercial systems. However, SOEL systems present a TRL of ~ 6 (with large scale prototypes). For the reversible operation, a TRL of ~ 4 - 5 has been reported, possibly because of the different mismatches and microstructural alterations that these Ni-based cermets undergo by switching operating modes [134].

From this point, it is relevant to mention recent developments with perovskite-based fuel electrodes. Industry and research have been proposing the use of alternative perovskite-based fuel electrodes to overcome the above-mentioned issues of the Ni cermets in the different operating modes of the SOCs. In 2014, the research group from J. T. S. Irvine (University of St Andrews, United Kingdom) in cooperation with the company Hexis AG (Switzerland), implemented a fuel electrode backbone of a lanthanum and calcium co-doped A-site deficient strontium titanate impregnated with Ni-CGO for a SOFC-stack with ESCs of 100 cm^2 active area [135]. They performed tests on both short stack (5-cell) setup, as well as on the full HEXIS Galileo system (nominal 1 kW). They concluded that the perovskite backbone provided enough electric conductivity to overcome ohmic losses. They reported power densities up to 200 $mA\cdot cm^{-2}$ at 900 °C, which could be compared to the Ni-cermet state-of-the-art fuel electrodes. Redox stability was also confirmed, contrary to the sulfur tolerance, which could not be achieved [135]. Despite those issues, their research is a key starting point for the scale-up of perovskite-based fuel electrodes on ESC architectures, from which many other researchers may learn and improve the identified issues during operation and possibly also during the manufacturing processes of these perovskite-based stacks.

We could question which is the *Status Quo* of the development of perovskite-based fuel electrodes for SOCs. It was just 8 years ago that a perovskite-titanate electrode titanate (impregnated with Ni-CGO) was introduced on an ESC-stack (from 5 to 60 cells) achieving 1 kW of power in SOFC operation, as well as a comparable initial performance to the typical Ni-cermets. Despite of this achievement, it is not possible to place the development of these electrodes in parallel to the Ni-CGO cermets, focusing on ESC architectures. Crucial operational challenges, such as the impurities tolerance (sulfur and coking) should be fully understood and investigated with plenty of different gas compositions in the typical SOC operating modes. Very important would be to perform all of these investigations during significant periods of time (~ 20 000 – 50 000 h for instance) ensuring low degradation rates. Other sources of degradation, e.g. the loss in properties or significant microstructural changes should be addressed. These aspects also count for ASC architectures, in which other relevant features, such as mechanical properties (hardness, fracture strength, yield strength among others) could be more critical than for ESC.

Having these aspects in mind, it could be possible to assign a TRL of ~ 3 – 4 for the actual development and implementation of perovskite electrodes in ESC stacks. Even though there are already good results in performance, issues as the loss of conductivity of the electrode upon long-term operation periods, or as the tolerance against sulfur, should be addressed before upscaling these electrodes to demonstration prototypes or real-life systems (TRL ~ 5 - 7) [136]. However, nowadays the learning curve of the different research institutions is becoming more and more steep, by allowing the share of experiences and issues on the scale-up. Therefore, if the development of the Ni-CGO-based systems took roughly 25 – 30 years, it does not imply that the same time scale would be needed for the perovskite electrodes. With the example of the HEXIS stack, and with the different drivers of replacing or reducing the Ni contents on these systems, it could be possible to believe that the scale-up of perovskite-based SOC systems could take roughly other 10 or 15 years from now, coping also with the objectives for the current energy transition.

All in all, this would also be a function of the further SOC architectures developments, including different cell areas and also of the availability of the different raw materials required for the scale-up of these systems. These aspects will be discussed in the following sections.

6.2 Performance comparison in different SOCs operating modes

Considering how the SOCs materials have evolved, it is possible to locate the L65SCrN fuel electrode with state-of-the-art data on the comparative Table 5. However, since there are no data on the stack level with this perovskite electrode, the comparison is presented at the cell level.

Table 5 Performance comparison of L65SCrN fuel electrode cells with state-of-the-art in SOFC and SOEC operating modes. For the case of ASCs 8YSZ was used as electrolyte while 3YSZ for ESCs.

	Operating mode →			**SOFC**	**SOEC**	
Architecture	**Oxygen electrode**	**Electrolyte**	**Fuel electrode**	**Power generated ($W\cdot cm^{-2}$) @ 0.6 V**	**Produced H_2 ($\times 10^{-5}$ $kg\cdot h^{-1}\cdot cm^{-2}$) @ V_{th} 1.29 V**	**Ref.**
ASC	LSM/YSZ	8YSZ	Ni-YSZ	0.75 @850 °C	~ 3.7 @850 °C	[137]
ESC	LSCF/CGO	3YSZ	Ni-CGO	0.60 @860 °C	~ 2.8 @860 °C	[54][74]
ESC	LSCF/CGO	3YSZ	L65SCrN	0.54 @860 °C	~ 2.8 @860 °C	[54][57]

Regarding co-electrolysis, other perovskite formulations have been investigated but on button cells with smaller active areas, besides the Hexis stack results reported by J.T. Irvine [135]. A comparison of the different performances of these perovskite electrodes, as well as with the state-of-the-art materials is presented in Table 6. The production rate of the syngas is not depicted since such value would need to be calculated with different assumptions for each case. Bypass and/or leakages of the gas flows, as well as tightness and flow quantities, are variables that may affect significantly the rate of gas produced. Also, and more importantly, is the influence of the RWGS reaction, which at some point will compete with the simultaneous electrolysis of H_2O and CO_2. Therefore, the achieved current density at thermoneutral voltage for co-electrolysis (1.32V) could already give an insight about the performance of the different cell configurations:

Table 6 Performance comparison of L65SCrN fuel electrode cells with state-of-the-art in co-SOEC operating mode.

Oxygen electrode	**Electrolyte**	**Fuel electrode**	**Active area**	**S/C ratio in fuel gas**	**Current density @ V_{th} 1.32 V**	**Reference**
LSM/YSZ	8YSZ	Ni-YSZ – support	16 cm^2	S/C=1	~ - 1 $A\cdot cm^{-2}$ @ 850 °C	[20]
LSCF/CGO	3YSZ – support	Ni-CGO	16 cm^2	S/C=2	~ - 0.8 $A\cdot cm^{-2}$ @ 860 °C	[28][57]
LSM/YSZ	ScCeSZ – support	LCT-Ni	0.4 cm^2	S/C=1	~ - 0.52 $A\cdot cm^{-2}$ @ 850 °C	[59]
LSCF/CGO	3YSZ – support	L65SCrN	16 cm^2	S/C=2	~ - 0.8 $A\cdot cm^{-2}$ @ 860 °C	[57]

From both tables, it is clear that the ASC architecture that host the Ni-YSZ cermet is the alternative with the higher values for power generation and hydrogen productions (and in the case of co-electrolysis the one with the highest current density). This feature is mainly attributed to the low ohmic contribution on ASCs. However, it is important here to note that these comparisons are only made at the initial performance of the cells and do not have into consideration the degradation issues on the long-term, which are the main drawback of the Ni-YSZ cermets. What is possible to learn from this architecture is that the low ohmic contribution of the thin electrolyte is an advantage for achieving higher current densities in either mode, due to the lower ASR_{total} that could be achieved. Among the ESC architectures, is possible to observe how the L65SCrN investigated in this thesis could compete with the Ni-CGO. In regard to SOFC operating mode, the Ni-CGO showed slightly better performance, producing 0.6 W·cm^{-2} in comparison to the L65SCrN with 0.54 W·cm^{-2} (both values at 0.6 V and 860 °C). Such difference could be affected by the mounting procedures but also by the thickness of the fuel electrode layer, which at some end will affect the interface resistance (and also the ohmic resistance) and hence the ASR_{total} and the current density achieved at this voltage. In this thesis, such results are detailed in [54]. For steam electrolysis operation, as well as for co-electrolysis operation, the performance among these two fuel electrodes is even more competitive, as described in [57].

On one hand, in co-electrolysis operation at 860 °C, both fuel electrodes presented the same performance behavior, achieving an electrolysis current density of -0.8 A·cm^{-2} at thermoneutral voltage, as shown in Figure 37. In the frame of this thesis, both cells were tested on the same test bench with comparable operating conditions, as detailed in [57]. In regard to the other perovskite-based fuel electrode $La_{0.43}Ca_{0.37}Ni_{0.06}Ti_{0.94}O_3$ (LCT-Ni), performance in co-electrolysis may not be directly compared. Important parameters such as the temperature and the steam to carbon ratio (S/C) influence significantly the cell operation, not to mention the fuel flow rate and flow configuration, which in small button cells of 0.4 cm^2 active area [59] differs significantly than the ones for square geometries with larger areas. Also important is the different electrolyte-support that was employed. Surprisingly, the LCT-Ni cells showed lower performance (- 0.52 A·cm^{-2}) than the L65SCrN despite the better ionic conductivity of their electrolyte support, since it has been reported that scandia-doped zirconia electrolytes present higher ionic conductivities than yttrium-doped zirconia at high temperatures (~ 700 °C) [138]. Therefore, it would be more appropriate to also evaluate the performance of such perovskite with similar operating conditions and cell architecture to the L65SCrN cell in order to isolate external factors to the fuel electrode and evaluate which of them could perform better. On the other hand, the performance in steam electrolysis is very promising. For this operating mode, a more thoroughly temperature screening was performed as shown in Figure 44 a) and explained in detail in [74]. From these results, it is possible to observe that both fuel electrodes present the same performance at higher temperatures (-0.8 A·cm^{-2} at 1.29 V and 860 °C), but while decreasing the operating temperature there is a performance gain for the perovskite L65SCrN fuel electrode. Complementary to this, an estimation of the apparent activation energy barrier for both fuel electrodes was performed in terms of the ASR_{total}, which follows a temperature-dependent Arrhenius-type behavior, as depicted in Figure 44b) – left axis. Such difference indicates that the reaction mechanism of the H_2O electrolysis reaction implicates different surface species, but to determine which mechanism is faster further research and experiments implementing density functional theory (DFT) thermodynamic calculations may be required [139]. Nevertheless, these results allow to calculate the produced hydrogen rate normalized by the area, for which the values are slightly higher for the L65SCrN fuel electrode with temperature decrement, as shown in Figure 44b) and calculated from equation (51).

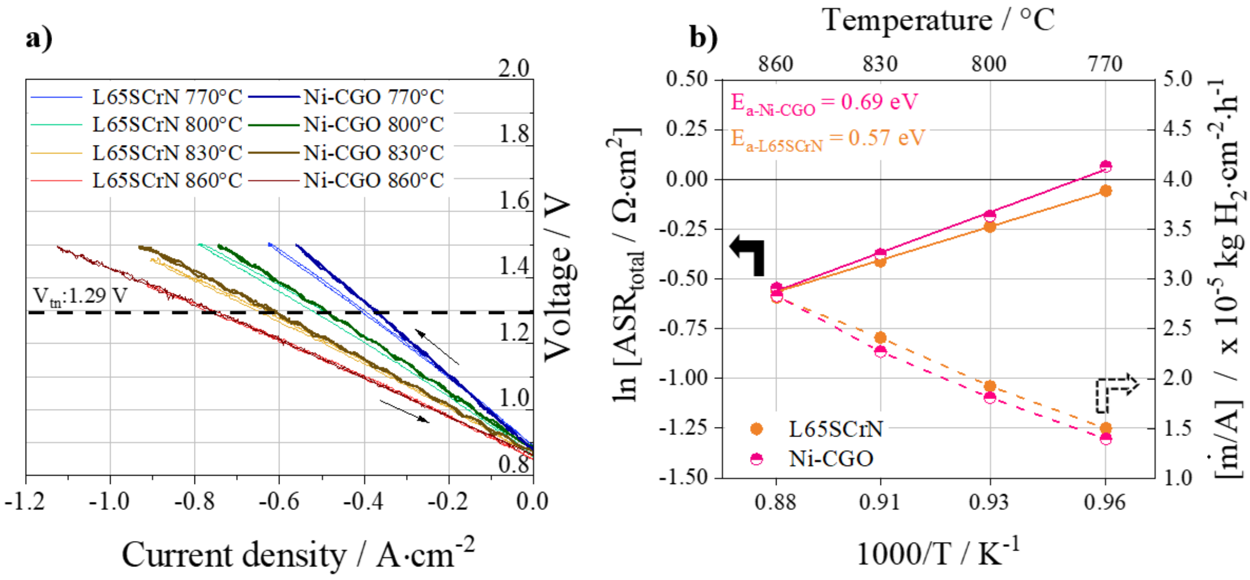

Figure 44 a) Polarization curves of L65SCrN and Ni-CGO fuel electrodes on full ESCs in electrolysis mode with a fuel gas mixture of 80% H_2O - 20% H_2 at 860 °C, 830 °C, 800 °C and 770 °C. Steam electrolysis thermoneutral voltage (1.29 V) is depicted. b) Arrhenius-type plots of the ASR_{total} for the L65SCrN and Ni-CGO cells calculated from (a) on a linear interval close to the thermoneutral point. The corresponding normalized hydrogen production rate is shown on the right axis according to equation (51). Reprinted (adapted) with permission from [74]. Copyright (2023) American Chemical Society.

Certainly, these calculations at larger scales (and possibly also to larger cell areas) would indicate how the perovskite fuel electrode performs and competes with the state-of-the-art Ni-CGO cermet. However, a strong degradation in SOEL operation was observed under such gas composition at 860 °C during ~ 1000 h, corresponding to a voltage increment rate of ~48 mV/1000 h, being almost twice as high as from the Ni-CGO state-of-the-art electrode, with a degradation of 25 mV/1000 h measured in similar conditions [140]. It was assumed that such degradation was originated by an increase in the ohmic resistance, which could be possibly explained with a loss of conductivity during the testing time. Details of this discussion are presented in [74]. From these results, it was also inquired the option of reducing the operating temperature to mitigate such degradation issues.

Therefore, due to all these operating parameters that should still be studied and fully understood, it is possible to consider TRL of ~ 3 – 4 for these perovskite fuel electrodes.

6.3 Scale-up to larger areas

Prior to the scale-up analysis with a real system case, it is worthwhile to inquire about how larger the active cell area might be. The most recent planar stack developments have been designed with areas of 127.8 cm^2, 100 cm^2 and even 80 cm^2 for the Sunfire (Staxera) [129], Hexis [135] and FZJ [125] [126], respectively. Furthermore, since the 2000s decade [108] larger sizes were implemented. Most of the reported cell areas for ESCs lie around 100 cm^2, except for the developments of the companies Chubu Electric Power and Tonen Corporation, with reported cell areas of ~ 400 cm^2 [108] and 729 cm^2 [141] respectively. The joint development between Chubu Electric Power Company and Mitsubishi Heavy Industries (both Japanese) consisted on the mono-block layer (MOLB)-type planar SOFC, operated at 1000 °C with a 40 cells-stack based on a corrugated electrolyte layer architecture. However, they reported performance of about 0.240 $W \cdot cm^{-2}$ at 1000 °C [108]. For the case of the SOFC stack from Tonen Corporation, cell areas up to 729 cm^2 in 65 cells-stack were implemented, achieving power densities of 0.11 $W \cdot cm^{-2}$. However, little further information has been reported because it seems that they stopped SOFC research at the end of the 90s [141].

Beyond these low performance values for larger cell areas and the different operating and manufacturing parameters that could have influenced them, it is important to address why is relevant to keep the reference values and not aiming to design larger areas. This could be explained with fracture mechanics on brittle materials, such as the ceramic components on

SOCs. Ceramic materials and more especially porous ceramics behave as brittle materials and hence they present a statistical strength distribution.

In this regard, the Weibull approach of failure has been widely considered aiming at estimating the risk of rupture of each cell layer in SOCs, i.e. the dense electrolyte and the porous electrodes [142]. According to the Weibull's law of failure, the survival probability ${P_s}^i$ of a structural component *i* (fuel electrode, oxygen electrode or electrolyte), loaded with an applied tensile stress σ corresponds to:

$$ {P_s}^i = \exp\left(-\int V_i \left(\frac{\sigma}{\sigma_o}\right)^m \frac{dV_i}{V_o}\right) \tag{79} $$

, where V_i is the volume of the cell component, σ_o the characteristic strength and the Weibull modulus *m* represents the shape parameters. V_o is taken as a reference volume related to the characteristic strength [142]. With this expression, it is possible to calculate *m*, which correlates how the defect distribution, such as pores and cracks, within a ceramic could lead to fatal failure by rupture, commonly denoted as failure probability. For instance, the higher the *m* value the smaller the spread in the defect size distribution. A higher m-value would especially favor the fracture stresses distribution leading to lower failure probabilities [143].

To introduce how critical would be to increase the active cell area in regards to the mechanical integrity of the cell, the research by Malzbender and Steinbrech from FJZ is very useful because they performed Weibull experiments in ~ 110 µm-thick 6ScSZ and ~ 100 µm-thick 3YSZ electrolytes [143]. They measured the fracture characteristic stresses for both materials and they found that the 6ScSZ was significantly brittle, both at room temperature (RT) and at 800 °C (Table 7).

Table 7 Weibull characterizations on 6ScSZ and 3YSZ electrolytes. Data adapted from [143]: *measured, ** calculated.

Characteristic fracture stress (MPa)	**24x24 mm^2 at RT***	**24x24 mm^2 at 800 °C***	**100x100 mm^2 at RT****	**100x100 mm^2 at 800 °C****	**Weibull modulus *m***
6ScSZ	780 ± 40	430 ± 21	90 ± 40	50 ± 20	5.3 ± 1.0
3YSZ	1300 ± 40	610 ± 20	650 ± 115	170 ± 55	8.7 ± 2.0

An optimal Weibull modulus greater than 10 would be expected in order to have a good reliability and yield of usable components in SOCs [144]. Nevertheless, until now the highest measured modulus corresponds to the Ni-YSZ cermets, as shown in Table 8:

Table 8 Weibull modules at RT and 800 °C for different state-of-the-art ceramic materials used in SOCs. Data adapted from [144].

Material	**Weibull modulus *m* at RT**	**Weibull modulus *m* at 800 °C**
CGO10	3.8	5.7
CGO20	6.0	-
YSZ	5.7	8.6
LSM	6.7	3.7
NiO-YSZ	11.8	-
Y-TZP	3.5	3.9

Other microstructural features, such as the grain size could influence as well the risk of failure. The linear Hall-Petch relationship states that if the grain size is decreased, the strength (also related to hardness) increases, as shown in equation (80) [145]. Meaning that the smaller the grain size, the more grain boundaries the material will have, and the more grain boundaries, the more obstacles for the dislocations. This relationship correlates the yield stress σ with the square root of the grain size d, such as:

$$\sigma = \sigma_o + k\sqrt{d} \tag{80}$$

, in which k is linked to the local yield stress at the grain boundaries and where σ_o is the resistance associated to dislocation movement within the grain [146]. However, below a critical grain size, the hardness would decrease, following the behavior known was inverse Hall-Petch relationship [147] [148] [145]. Therefore, caution should be taken on the selection of the materials synthesis and processing routes, since important parameters such as the solvents, precursors, temperatures and time could all in all influence microstructural features such as the grain size and hence detriment the fracture strength of the ceramic components used in SOC systems. Chemically-induced stresses could also influence the fracture stress states of all cell components. For instance, in ESC architectures the Ni-cermet oxidation could induce a fracture risk on the interface between electrolyte/electrode. As an example, in 10 µm-thick electrodes, an anodic strain lower than 0.3 and 0.35 % is recommended to avoid delamination [142]. In perovskite-based electrodes, such chemically-induced stresses could be even more complex. In MIEC oxides subjected to reducing conditions, additional oxygen vacancies are formed, causing the lattice to expand. This expansion could also be considered as a chemically-induced strain that is highly dependent on the temperature, change in oxygen activity (or change in oxygen vacancy concentration or deviation from stoichiometry), composition, crystal structure and level of doping [144]. For lanthanum-doped chromites, typical strains at 1000 °C under reducing conditions (oxygen activity of ~ 10^{-18}) have been reported to be between 0.2% and 0.4% [144]. However, for the L65SCrN case these values may differ due to the different operating temperatures investigated in this thesis (between 770 °C and 860 °C), as well as the stoichiometry at these conditions (A and O deficiencies) and last but not least, due to the Ni doping on the B-site. All of these defects may contribute differently and uniquely to the strain states on the perovskite lattice. Generally, the resulting chemical strain gradient will create a corresponding stress gradient. Also, the vacancy activity as well as the geometry of the cell components (planar or tubular) will affect the stress distribution across the different cell materials. Therefore, with the aim to avoid mechanical failure from chemically-induced strains, it is necessary to restrict operating conditions to guarantee that these strains remain below ~ 0.1% [144]. The cell's strength may be influenced by the thermal residual stresses, resulting from the difference in thermal expansion coefficients (TEC) of the materials in the different layers. The L65SCrN dilatometry measurements in air allowed to determine a TEC of ~ 11.4 $\times 10^{-6}$ °C^{-1} , which lies between the reported values for YSZ electrolytes and LSM perovskite oxygen electrodes, as shown in Table 9 [142].

Table 9 Young's modulus and TEC values for state-of-the-art ceramic materials used in SOCs. If not specified, table data were adapted from [142]. Additional references are mentioned on the table. *It is assumed that after reduction, the change in volume is almost negligible since the ceramic YSZ network re-accommodates to the new porosity on the Ni cermet, where it is also assumed that the NiO reduces completely to Ni [149].

Material	Young's modulus (GPa)	TEC (x 10^{-6} °C^{-1})
NiO-YSZ	112	~11.9 -12.5 [142] [149]
Ni-YSZ	56.8	~11.9 -12.5 [142] [149] *
YSZ - electrolyte	190	10.8
LSM - oxygen electrode	35.0	11.7
L65SCrN	Values for $La_{0.85}Sr_{0.15}CrO_3$: 93.3 (oxidized) 120.7 (reduced) [150]	11.4 (this thesis)

Additionally, not only reducing atmospheres and high temperatures may affect the cell's strength because of detrimental stress-strain conditions, but also the operation with steam may affect the mechanic of rupture. Large amounts of steam should be considered for SOFC (with the steam produced via hydrogen oxidation at high fuel utilization i.e. at the gas outlet) and for SOEL operating modes (with high contents of steam at low conversion i.e. at the fuel inlet). Water steam may cause a weakening of inter-atomic bonding at the tip of a crack just by chemical reaction with the environment. In this case, the crack advances at a lower applied force, causing a local stress, that is lower than the characteristic fracture stress that may cause an unstable fracture. This phenomenon is denoted as subcritical crack growth, or also environmentally assisted cracking [144] and may not be ignored when operating with SOCs.

In ceramic materials, structural defects as pores and cracks are more relevant in terms of failure. Therefore, if the active cell area is increased, more defects will be present on the ceramic components of the cell, where the number of cracks and pores will significantly increase and the risk of failure would be higher. Taking into consideration the different operating parameters, as well as the different material properties, it is highly recommended to implement fracture analyses with the Weibull method in all the ceramic components of a solid oxide cell, before enlarging their active area size. Segmented planar designs could also be considered, in which for instance, 4 cells could be arranged in 2 x 2, by incrementing the active cell area by 4. Nevertheless, for such cases, mechanical characterizations by the Weibull method would also be relevant, because besides the axial stresses that the cells undergo, it is possible to believe that shear stresses (due to the metallic interfaces of the segmented arrangement) could possibly also modify the stress-state in the cells and deteriorate their fracture toughness.

In the frame of this thesis, a cell-size variation was not taken into consideration for the scale-up analysis due to the different factors that may influence their design, as following:

i) The increment of the cell size would lead to operating challenges caused by the probability of failure among the different cell components and interfaces (L65SCrN or Ni-CGO/CGO/3YSZ/LSCF), where the risk for the ceramic electrodes – both L65SCrN and LSCF – is comparable. Such risk of failure is strongly dependent on the ceramic synthesis processes, as well as on their manufacturing cell processes.

ii) The use of perovskite-based fuel electrodes entails an additional challenge due to the chemical stresses that may be generated by chemical expansion upon reducing atmospheres.

iii) Further engineering would be required for the cell architecture (ESC, ASC, MSC or even new designs), with the aim to maintain the chemical and thermal expansion in an acceptable range, as well as minimizing their mismatch among the different cell components.

The following scale-up analysis would be evaluated mainly in terms of the electrochemical performance as explained in the next section.

6.4 Scale-up from cell level to system level

6.4.1 Example case of high temperature electrolyzers on the MW range installed at the Salzgitter Flachstahl steel plant

As mentioned previously, the case of the consortium at Salzgitter AG steel plant serves as a good example for evaluating the up-scale of perovskite electrodes to the MW scale (Figure 45), based on the results for SOEC operation studied in this thesis. For this, it is important to consider the following system requirements and characteristics [133]:

- Green hydrogen production rate of 200 Nm^3/h (18 kg H_2/h)
- Nominal power (AC) input available: 720 kW
- System composed by: 8 modules
- Each module consists of 36 stacks and each stack of 30 cells → giving 8640 electrolyte supported cells, each cell with an active area of 127.8 cm^2.

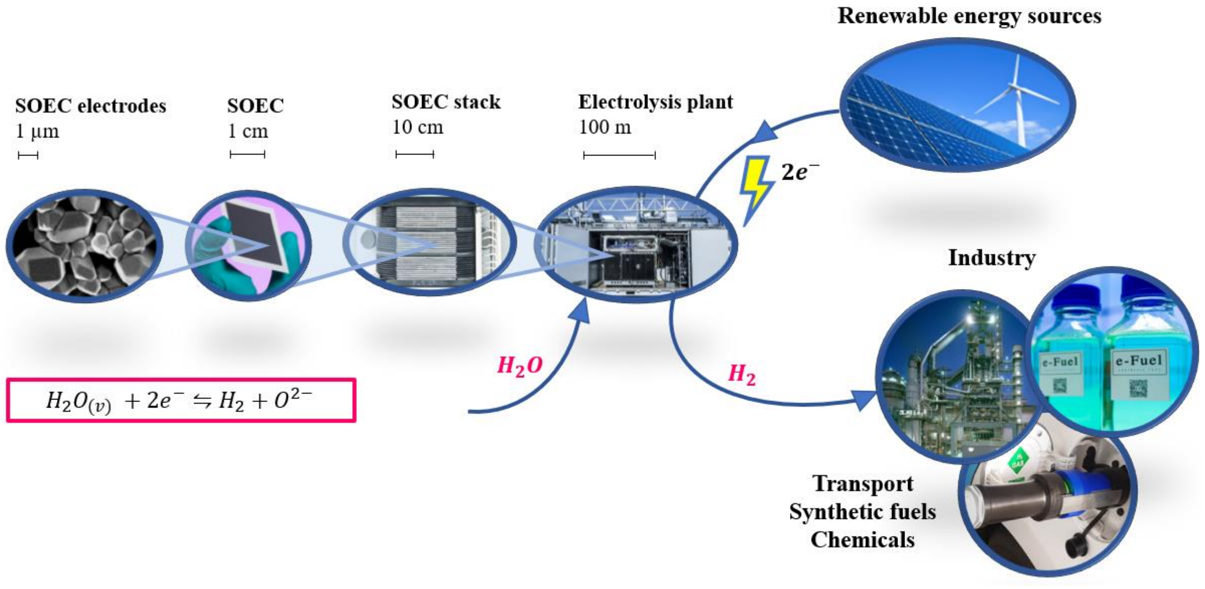

Figure 45 SOECs from the microscale to the macroscale starting from the cell electrodes and single cells that are combined into stacks. Stacks that are arranged into modules. Electrolysis plants that consist of module systems of electrolyzers with the aim to produce green hydrogen at larger scale when electricity from renewable sources (~ MW) is supplied. Adapted from [15].

To evaluate how the perovskite fuel electrode could be implemented at larger scales, it is important to answer the following questions:

i) What is the benefit to use the perovskite fuel electrodes over the state-of-the-art Ni-cermets at the system level?
ii) How could such benefit be exploited?

This thesis aims to answer these questions by correlating the total amount of cells in a system, with the required hydrogen production rate. By using the electrochemical results of ASR_{Total} and current density J at the cell level in thermoneutral operation, from Figure 44, it is possible to estimate the specific energy consumption as a function of the number of cells in the system by arranging the terms in equation (54), as following:

$$P_{cell} = \left(V_{rev} * J * (A_{cell-stack}) + (ASR_{Total}) * \frac{(\dot{n}_{H_2-produced} zF)^2}{A_{cell-stack}}\right) \tag{81}$$

$$\frac{P_{system}}{\dot{m}_{H_2-required}} = \left(V_{rev} * J * (A_{\text{cell-stack}}) + (ASR_{Total}) * \frac{(\dot{n}_{\text{H}_2-produced} zF)^2}{A_{\text{cell-stack}}}\right) * N_{total\ stack-cells} \tag{82}$$

With the expression in equation (82), the following data in Figure 46 could be plotted and the main outcomes are summarized in Table 10.

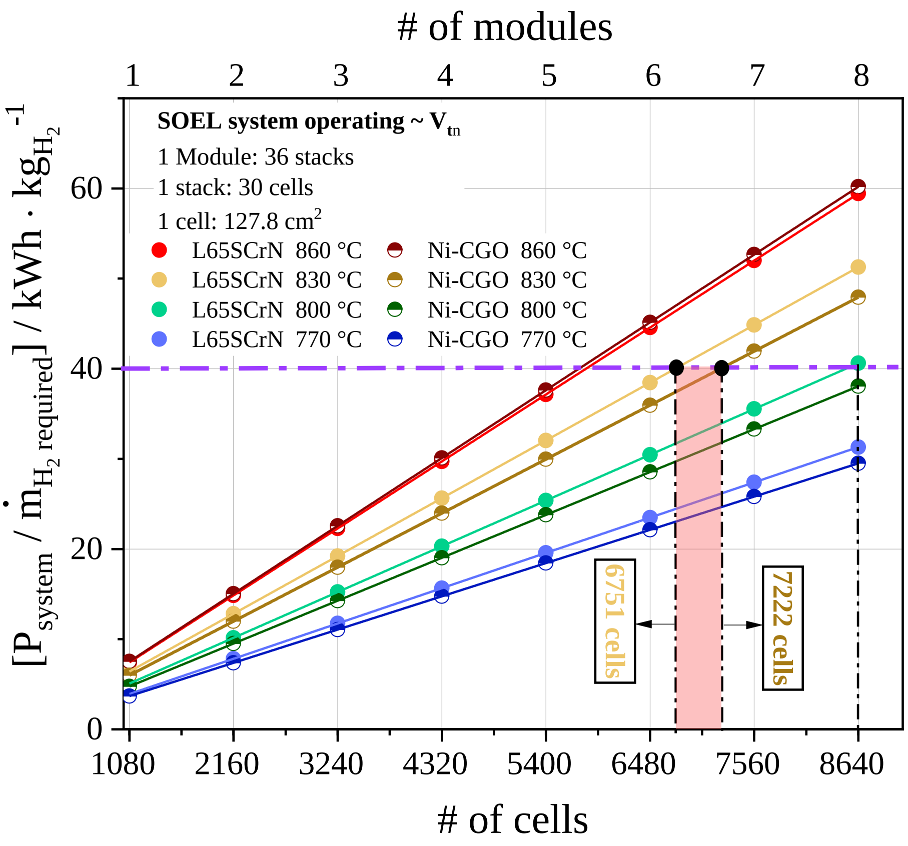

Figure 46 Scale-up estimation of the specific energy requirement vs. the number of cells in a SOL system, related also to the number of modules (1 module = 1080 cells). Results from this thesis at the cell level were used in equation (82) for L65SCrN fuel electrode cells and Ni-CGO fuel electrode cells.

From this plot, it could be observed that by increasing the operating temperature to 860 °C the system would require less cells (ca. 5743) and hence 2 modules less. The drawback of this operating condition, is that it would exceed the maximum operating temperature that is recommended by the module supplier (Sunfire GmbH), which is ~ 850 °C [151]. However, observing the other temperatures, it is possible to extract the following information for thermoneutral operation of the perovskite electrodes against the Ni-CGO fuel electrodes:

- If the system operates at an average temperature of 800 °C, for both type of electrodes, an 8-module system would be required, meaning 8640 cells are required.
- If the system operates at an average temperature of 830 °C the number of cells could be reduced to ~ 6751 for the perovskite electrodes and to ~ 7222 cells for the Ni-CGO fuel electrode-modules. Even though these calculations yield 7 modules regardless the fuel electrode, it is worthwhile to highlight that the use of the perovskite would reduce the manufacturing costs, since ~ 471 cells less would be required. And by assuming

that the costs between Ni-CGO and the perovskite electrodes do not differ significantly, then such reduction on the number of cells would imply a reduction in manufacturing costs.

On larger systems, where the use of perovskite electrodes could imply a more significant reduction of the cells and stacks, the estimations presented on this thesis could be of interest to the industry due to the simplification in relevant aspects such as: stacks and modules manufacturing processes and simplification on the hardware and software interfaces (less sensors and hence less variables to control) [152].

Table 10 Estimation of the number of cells and stacks required for each type of electrode (L65SCrN and Ni-CGO) for an average temperature operation of 830 °C and 800 °C. Results were taken from Figure 46.

Average system temperature	**830 °C**		**800 °C**	
Fuel electrode	**L65SCrN**	**Ni-CGO**	**L65SCrN**	**Ni-CGO**
# of cells (each 127.8 cm^2)	6751	7222	8640	8640
# of modules (each 1080 cells)	6.3 ~ 7	6.7 ~ 7	8	8

6.4.2 Critical raw materials required for electrolysis systems

Besides the hardware simplifications, the use of perovskite electrodes entails an important factor for the SOEL-systems deployment in a sustainable development scenario (SDS), which is the critical raw materials availability.

The International Energy Agency (IEA) has stated that nickel - in mineral form nickel oxide - belong to the most critical raw materials for the energy transition [71]. A wide range of minerals are required for clean energy technologies, such as wind turbines, electric vehicles (EV), batteries, fuel cells and electrolyzers among others. These minerals correspond to oxides of Nickel, Copper, Cobalt, Lithium, Chromium, Zinc, Aluminum, as well as rare earth elements (REEs) and Platinum-group metal catalysts (PtGMs). The IEA classified the relative importance of these materials for a particular clean energy technology between high, moderate and low importance. Within this assessment of the IEA, the overall mineral demand was calculated with four variables: (i) clean energy deployment trends under stated policies scenarios (SETPS) and SDS, (ii) sub-technology shares on each technology area, (ii) mineral intensity of each sub-technology and (iv) mineral intensity improvements. Regarding hydrogen clean technologies, i.e. electrolyzers and fuel cells, nickel and the PtGMs are classified with a high relative importance [71]. Significant efforts to reach the climate carbon-neutrality would be required: the mineral demand would need to be quadrupled for these technologies by 2040. For a faster transition, i.e. net carbon-zero climate by 2050, a sixfold mineral input in comparison to the current one would be required for 2040. In this frame, the fast-increased interest of hydrogen as energy carrier entails a steep growth in demand for nickel [71].

Batteries for energy storage cannot be neglected, especially when it comes to the need in materials. The IEA estimates that in SDS, the battery storage demand would increase by 11 times between 2020 (from 37 GWh) and 2040 (420 GWh), for which the largest relative mineral growth would be for the nickel by 140 times: from 0.4 kilotons (kt) in 2020 up to 57 kt in 2040 [71]. With this, higher mineral prices could also affect the pace on which the industry achieves ambitious goals on SDS. As an example, if the lithium and nickel prices double, the battery costs could increase a 6% [153]. In the case of the electrolyzers, the mineral demand has a significant cost component. Therefore, if the mineral prices for the battery sector increase in respond to the higher demand, the competitiveness among clean energy technologies could be affected, as well as among the different types of electrolyzers. Besides the electrolysis technologies, solar panels, EVs and wind turbines are being deployed on larger scales, for which the mineral market could undergo supply disruptions and volatility [153]. This provides an additional driver for R&D on alternative solutions to reduce the use of critical materials, being crucial for an economically viable and sustainable hydrogen energy matrix.

Nevertheless, global commodities markets are namely exposed to economic and geopolitical hazards. This makes strategic minerals, such as nickel, prone to supply chain disruptions, which may be intensified with the increasing demand as a consequence of the ongoing decarbonization economies and policies. Hence, seeing that nickel turns out to be a critical material for the energy transition within these clean technologies, an estimation of how much nickel could be saved, with the implementation of the perovskite fuel electrodes in SOEL-systems is pertinent.

6.4.3 Estimation of the Ni load per electrolysis energy output

In this section, the Ni requirement for the manufacturing of an SOEL-system in terms of the energy output is calculated. Firstly, an estimation of the NiO load normalized by the area was calculated for cells with 16 cm^2 of active area. For the case of the L65SCrN fuel electrode, in this thesis the half-cells were weighted in two different states: after printing the ceramic ink on the electrolyte substrates (dried at 60°C) and after sintering at high temperature. The difference between these two mass values yielded the mass of the perovskite required for an active area of 16 cm^2. Then, from the sol-gel calculations the NiO mass was estimated. For the case of the state-of-the-art cells, an estimation of the required NiO raw powder per cm^2 was given by Kerafol GmbH, as presented in Table 11:

Table 11 NiO load normalized by the cell area for L65SCrN and Ni-CGO cells.

Fuel electrode	**L65SCrN**	**Ni-CGO**
NiO raw powders required (g/cm^2)	2.35×10^{-5}	6.56×10^{-3}

Secondly, considering that the system operates at an average temperature of 830 °C and 800 °C, the corresponding cumulative area ($A_{cumulative}$) is calculated by multiplying the number of cells for each case (estimated from Figure 46) by the active area of a single cell, which is 127.8 cm^2 (for the cells on the stacks used in this case of study). Then, the required amount of NiO as raw material is calculated in kg for each fuel electrode, by multiplying the estimated $A_{cumulative}$ by the NiO normalized load for each electrode from Table 11:

$$A_{cumulative} = A_{cell-stack} * N_{total\ stack-cells} \tag{83}$$

$$NiO_{required} = \left(\frac{kg\ NiO}{cm^2} \bigg|_{Table\ 11} \right) * A_{cumulative} \tag{84}$$

Thirdly, given the SOEL-system from the Salzgitter consortium as a reference, the yearly energy output $\varepsilon_{output/year}$ is calculated as a function of the specific energy consumption $\frac{P_{system}}{\dot{m}_{H_{2-required}}}$ and the required hydrogen production in a year $\dot{m}_{H_{2/year}}$, as shown in equation (85). For this case, the specific energy consumption is calculated with equation (86).

$$\varepsilon_{output/year} = \frac{P_{system}}{\dot{m}_{H_{2-required}}} * \dot{m}_{H_{2/year}} \tag{85}$$

$$\frac{P_{system-\text{Salzgitter}}}{\dot{m}_{H_{2-required}}} = \frac{720\ kW_{Nominal\ AC\ power}}{\frac{18\ kg\ H_2}{h}} = 40 \frac{kWh}{kg\ H_2} \tag{86}$$

, where $\dot{m}_{H_{2/year}}$ is calculated by multiplying the required production of hydrogen $\dot{m}_{H_{2-required}}$ (in kg per hour), with the operation hours in a year:

$$\dot{m}_{H_2/year} = \dot{m}_{H_2-required} * t_{operation/year} \tag{87}$$

For which $t_{operation-year}$ is considered as 5000 yearly-hours of normal operation, following the standards from the IEA [71]. Then, for comparison purposes, it is possible to estimate the amount of Ni (in the form of NiO for the cells manufacturing) per energy output in a year, denoted as $\theta^{Ni}_{GWh/year}$ for a specific SOEL-system, such as equation (88). The results of these calculations for both fuel electrodes are depicted in Table 12.

$$\theta^{Ni}_{GWh/year} = \frac{NiO_{required}}{\varepsilon_{output/year}} \tag{88}$$

Table 12 Normalized amount of Ni by the GWh energy output for a SOEL-system implementing the L65SCrN and Ni-CGO fuel electrodes at an average operating temperature of 830 °C and 800 °C.

Average system temperature	**830 °C**		**800 °C**	
Fuel electrode	**L65SCrN**	**Ni-CGO**	**L65SCrN**	**Ni-CGO**
$\boldsymbol{N_{total\ stack-cells}}$ (each 127.8 cm^2)	6751	7222	8640	8640
$\boldsymbol{A_{cumulative}}$ (cm^2)	8.6 x 10^5	9.2 x 10^5	1.1 x 10^6	1.1 x 10^6
NiO required (kg)	0.02	6.06	0.03	7.25
$\boldsymbol{\theta^{Ni}_{GWh/year}}$ (kg Ni / GWh year)	**0.01**	**1.68**	**0.01**	**2.01**

For SOEL-systems with perovskite fuel electrodes a requirement of ~ 0.01 kg of Ni/GWh was calculated for both operating temperatures. In contrast, the systems with the traditional Ni-CGO cermets would require ~ 1.7 and 2 kg of Ni/GWh for an average operating temperature of 830 °C and 800 °C respectively.

For a better overview among the different electrolysis technologies, these calculations were plotted together with the estimation from the IEA on the actual levelized demand for selected minerals in electrolyzers (~ 10 – 20 MW) [71], as shown in Figure 47.

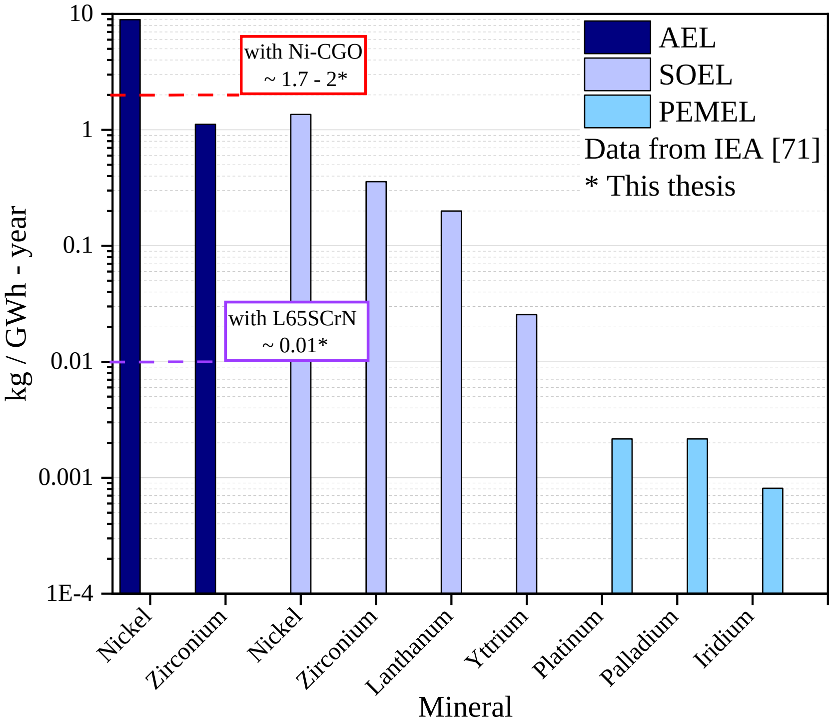

Figure 47 Today-estimated levelized demand (in kg per GWh in a year) for selected minerals in electrolyzers in log scale. Data adapted from IEA [71]. Values calculated for Ni within this thesis are also depicted for SOEL-systems with perovskite fuel electrodes (~ 0.01 kg of Ni/GWh) and with traditional Ni-CGO cermets (~ 1.7 – 2 kg of Ni/GWh).

Regarding the nickel demand, it is possible to observe on this plot that AEL-systems require almost 10 times more amount of Ni compared to SOEL-based systems. On the contrary, PEMEL-systems mineral demand would rely mainly on platinum, palladium and Iridium, without considering nickel as a critical material for this technology. However, as a general remark, the IEA estimates that in the frame of the energy transition and the role of electrolyzers on sustainable development scenarios, the demand of nickel for 2040 would increase on 15.000 tons [71], being like this the most critical materials among zirconium, lanthanum, yttrium, PtGMs, as well as steel and aluminum for the infrastructure.

These findings have important implications for developing perovskite electrodes up to the system level. For SOEL systems the benefit of using the perovskite electrode instead of the Ni cermet would be to reduce in ~ 200 times the amount of required NiO/Ni raw material, while having similar electrochemical performance to the state-of-the-art. Besides, comparing SOEL and AEL technologies, the use of perovskite fuel electrodes in SOEL systems would represent a more significant reduction (about 1000 times less) of the Ni raw material: ~ 10 kg of Ni/GWh for AEL vs. ~ 0.01 kg of Ni/GWh for SOEL systems (Figure 47).

We cannot exclude that other perovskite raw materials are also considered as critical raw materials (CRMs). The European Commission published in 2020 the list of CRMs in which LREEs (including Lanthanum, Cerium and Gadolinium [154]), HREEs, Strontium, Chromium, Cobalt, and Zirconium are included among others [155], by considering supply risks in nine selected strategic technologies: batteries, fuel cells, wind generators, traction motors, photovoltaic, robotics, drones, 3D printing and digital technologies [155] [156]. Other fields such as concentrating solar power (CSP), geothermal, aerospace, health and construction are also relevant applications for CRMs [71, 156].

Overall, even if Ni has been considered one of the most critical raw materials for electrolysis technologies, important attention should also be given to other elements such as La, Sr, Cr, Co, Zr, Ce and Ga. However, since Ni is the common element between the state-of-the-art Ni-CGO fuel electrodes and the L65SCrN, this thesis is focusing mainly on the Ni requirements for SOEL systems.

At this point, it is important to remark that even though these calculations are performed at the thermoneutral conditions i.e. at rated power, this does not imply that all the cells within the system are operated at this temperature. SOEL-systems may need to operate at higher voltages (above the thermoneutral condition) to overcome heat losses from the piping accessories and heat exchangers.

Before upscaling the perovskite fuel electrodes to the module level, it will be important to evaluate the durability. The scale-up estimations on this thesis are based on the electrochemical performance of the investigated types of electrodes on 5 x 5 cm ESCs. Even though durability characterizations for time periods of ca. 1000 hours were performed, it is still insufficient with respect to the target life-time that is at least of about 20 000 hours [157]. Therefore, further research on the durability assessment on larger scales, i.e. on stacks, would complement the estimation of the long-term performance, and then be extrapolated to modules.

Additionally, important mechanical characterizations of the stacks with the perovskite fuel electrodes should be performed, as well as transient analyses of the distribution of temperature and gas flows across the stacks and the modules.

Therefore, if the use of perovskite fuel electrodes would contribute to decrease this nickel demand, it is worthwhile to make the effort on different areas of science for the scale-up of these materials, i.e. fracture mechanics, thermodynamic simulations and techno-economical assessments, besides materials engineering and electrochemistry. The synergy of all these knowledge areas will contribute significantly to the deployment of SOCs systems for the energy transition in sustainable scenarios, for which the R&D in green hydrogen technologies is pivotal. It is estimated that by 2050 the European demand of green hydrogen would increase to ~ 800 TWh, which is equivalent to ca. 25 millions of tons of this valuable energy carrier [158].

All in all, this scale-up analysis of perovskite electrodes to the SOEL-system level allows to understand that the benefit of using these electrodes over the traditional Ni-cermets is to simplify the system layout by reducing the number of cells and hence the number of modules, without affecting the electrochemical performance, that is comparable to the Ni cermets. This could be exploited in terms of BoP, hardware and software simplifications. Another important benefit consists in the significant decrease of required nickel for these modules. The latter finding is relevant for a foreseeable sustainable development of clean energies in frame of the current energy transition, due to the risk of mineral market volatility and shortage in nickel supplies.

7 Conclusions

In this doctoral thesis, alternative perovskite-based fuel electrodes for SOC applications that potentially replace the traditional Ni cermets fuel electrodes were investigated.

An elaborated investigation of different lanthanum chromite-based perovskite candidates was firstly made. The stability and reliability of different compositions were evaluated by X-ray diffraction, from which two lanthanum-chromite perovskites with Ni doping (LSCrN) were selected: $La_{0.70}Sr_{0.3}Cr_{0.85}Ni_{0.15}O_{3-\delta}$ (L70SCrN) and $La_{0.65}Sr_{0.3}Cr_{0.85}Ni_{0.15}O_{3-\delta}$ (L65SCrN). Further chemical and thermal characterization techniques of these perovskite powders contributed to the understanding of chemical interactions between these materials and the typical atmospheres of SOC operation. Under reducing conditions, it was shown that Ni exsolution takes place, a phenomenon that releases anchored metallic Ni nanoparticles on the perovskite surface. It was found that operating parameters such as the oxygen partial pressure, temperature and time are determining for the size and shape of these Ni nanoparticles. These findings gave insights on how the LSCrN morphology would be *operando*, laying a groundwork for future research into the chemical interactions of these nanoparticles and their detailed role on the different reactions mechanisms that a fuel electrode undergoes in SOC operation.

Electrochemical characterizations of full electrolyte-supported-cells (ESCs) showed promising performance of the L65SCrN fuel electrode, due to the similarity with the traditional Ni cermets in SOFC, SOEC and rSOC modes at ~ 860 °C. Also, steam and carbon dioxide co-electrolysis characterizations shed new light on the fuel electrode electrochemical reactions, from which electrochemical impedance spectroscopy (EIS) allowed to propose an equivalent circuit model. Before this study, evidence of such models in co-electrolysis operation for lanthanum chromites with Ni doping was rarely seen. Moreover, a long-term study during ~ 1000 hours provided a first glance of the stability in co-electrolysis operation of this perovskite fuel electrode, being comparable to the state-of-the-art performance.

However, a strong potential-dependency degradation during 150 hours was identified in SOFC operation, likely related to alterations in the Ni nanoparticles, such as particle coarsening or slow Ni cation diffusion within the perovskite. In spite of this degradation, redox cycling experiments confirmed the recovery of the fuel electrode. By comparing sulfur tolerance studies on the traditional Ni-cermets with the exposure of the LSCrN to hydrogen sulfide, it was possible to discuss that the Ni nanoparticles favor hydrogen dissociation on the investigated temperature range.

Durability test during ~ 1000 hours in SOEL operation showed a strong degradation with a significant ohmic contribution, which was related to the electronic conductivity deterioration under these operating conditions. This outcome raises the question of the long-term stability and the role of the point defect chemistry on the transport properties of this perovskite electrode under such operating conditions. Therefore, it is suggested that further long-term investigations by varying parameters such as temperature, time and oxygen partial pressure would be needed in order to better understand the mechanisms of Ni exsolution and its role on the conductivity of this perovskite, and hence on the cell performance in SOC operating modes. For instance, lowering the operating temperature from 860 °C to 800 °C could be an initial approach to mitigate degradation issues.

Yet, the investigation of the SOEL operation in a temperature range between 860 °C and 770 °C showed a gain in performance of the L65SCrN perovskite fuel electrode in comparison to the typically used Ni-CGO cermet. This behavior was explained with possible differences in the electrode kinetics at 800 °C and below, from which it was possible to propose a reaction mechanism, that analogous to SOFC operation, also suggests that on L65SCrN electrodes the Ni nanoparticles facilitate the steam dissociation to further produce hydrogen. With this finding, this thesis attempts to answer what is the benefit of using these perovskite electrodes, not only at the cell scale but also at the system scale.

Then, an estimation of the electrochemical performance on a larger scale (~ MW) was performed by taking as reference the SOEC results at the cell level for 860 °C, 830 °C, 800 °C and 770 °C, assuming that those would be also the average temperature of a SOEL-system composed by commercial ESC stacks and modules. This study was performed using as reference a real SOEL system, designed for producing 18 kg/h of green hydrogen with an electrolysis input of 720 kW. With this scale-up analysis, it is possible to conclude that the benefit of implementing the perovskite fuel electrodes instead of the Ni cermets in ESC stacks and systems is worthwhile, if the system is operated at an average temperature of ~ 830 °C. This condition would reduce the number of cells, and possibly leading to reduction in manufacturing costs. Also, this goes concomitantly with a significant decrease of nickel as commodity to produce these cells, without compromising the electrochemical performance. This may contribute to make SOEL systems less dependent on possible fluctuations on the nickel market, that is expected to be driven by the large demand for electrical vehicles. Furthermore, geopolitical risks could also disrupt the supply chain of nickel, among other critical raw materials.

Prior to this study, it was difficult to make predictions on the benefit that perovskite fuel electrodes could bring at a system level. This thesis leaves open the question if the use of other cell architectures, such as anode-supported-cells (ASC) or metal-supported-cells (MSC) would provide a better performance, by lowering the ohmic contribution given by the thick electrolyte on ESCs.

With the outcomes of this thesis, the durability and the upscaling to the stack-level were identified as remaining challenges that should be addressed in future investigations on perovskite electrodes for SOC systems. The long-term stability at the cell level could be evaluated for significant periods of time of ~ 20 000 hours with minimized degradation rates, for which mitigation strategies could be proposed and identified. Once the durability is proven, the next step would be to proceed with the implementation of perovskite-based electrodes into stacks, also tuning the different cell architectures and even proposing new designs. Additionally, perovskite-based current collectors would be of great interest with the aim to replace nickel and platinum-based collectors.

Beyond the herein studied lanthanum chromite, further research on other mixed ionic and electronic conductors (MIEC) materials could elucidate interesting findings that account more for the understanding of such fuel electrodes and their properties, that may also influence the performance of different SOC systems.

8 Outlook

The use of perovskite materials may go beyond the conventional SOC operating modes that were discussed within this doctoral thesis. For instance, the use of ammonia (NH_3) as fuel for SOFC operation is also receiving great interest among the energy research and industry community. Even though green hydrogen is pivotal for the clean energy transition, its volumetric energy density is very limited [159]. Chemical derivatives from green hydrogen are promising options for hydrogen transport. For instance, green ammonia is an important hydrogen carrier because it can be stored at ~ - 33 °C under atmospheric pressure, or even at room temperature at ~ 10 bar. Contrary to liquid hydrogen, which would need to be cooled to - 253 °C [159]. Since operating SOFC-systems with ammonia would generate NO_x emissions due to the oxidation of the nitrogen with the oxygen anions that are transported from the oxygen electrode through the electrolyte, research in alternative materials would be of great interest.

Here is where the use of perovskite electrodes and also electrolytes could play an important role on the use of ammonia as fuel. Such perovskite-based materials are the proton conducting ceramics (PCC). Instead of using an O^{2-} anion-conducting solid electrolyte, it would be more convenient to implement a H^+ proton-conducting solid electrolyte. This is why research on PCCs materials, not only for the fuel electrode, but also for the electrolyte, is opening a new research area that is already gaining great interest among the scientific community. Considering the low temperature technologies, perovskite electrodes could also be investigated for PEMEL systems as well as for anion exchange membrane water electrolysis (AEMWE). In the case of PEMEL, the acidic environment limits the choice of electrocatalysts to expensive PtGMs, such as Pt on the cathode and IrO_2 on the anode side. The hydrogen evolution reaction (HER) takes place at the cathode and the oxygen evolution reaction (OER) at the anode. Both electrodes require a catalyst that yield good reaction rates and mild overpotentials. Hence, the investigation and development of PtGMs-free catalysts with good electrochemical performances, low production costs (up to the large -scale) [160], as well as chemical tolerance to acidic environments are crucial drivers for the use of perovskite in these systems.

For the case of AEMWE, promising performances have been achieved with PtGMs-free catalysts, such as transition metals (and their alloys), oxides, nitrides, phosphides, and carbides among other options that catalyze the HER, from which Ni-based catalysts outshine [161]. For the OER, various metals exhibit high catalytic activity and corrosion stability in alkaline environments, being Ni the most promising. However, other metal oxides in different forms, such as perovskites, cobaltites for instance, present also high catalytic activities [161]. Therefore, investigation of perovskites for the HER catalysts in AEMWE systems would also be relevant, aiming at replace Ni-based catalysts.

9 Bibliography

[1] M. R. Allen, O.P. Dube, W. Solecki, F. Aragón-Durand, W. Cramer, S. Humphreys, M. Kainuma, J. Kala, N. Mahowald, Y. Mulugetta, R. Perez, M. Wairiu, and K. Zickfeld, "Global Warming of 1.5°C. An IPCC Special Report on the impacts of global warming of 1.5°C above pre-industrial levels and related global greenhouse gas emission pathways, in the context of strengthening the global response to the threat of climate change, sustainable development, and efforts to eradicate poverty," in "Chapter 1: Framing and Context," 2018. [Online]. Available: https://www.ipcc.ch/sr15/chapter/chapter-1/

[2] E. Papadis and G. Tsatsaronis, "Challenges in the decarbonization of the energy sector," *Energy,* vol. 205, p. 118025, 2020/08/15/ 2020, doi: https://doi.org/10.1016/j.energy.2020.118025.

[3] IEA, "Net Zero by 2050," Paris, 2021. [Online]. Available: https://www.iea.org/reports/net-zero-by-2050

[4] S. Y. Gomez and D. Hotza, "Solid Oxide Electrolysers," *The Royal Society of Chemistry 2020,* no. Energy and Environmental Series Series No. 25, 2020.

[5] "A hydrogen strategy for a climate-neutral Europe," European Comission July 8 2020.

[6] P. D. A. van Wijk and J. Chatzimarkakis, "Green Hydrogen for a European Green Deal A 2x40 GW Initiative," Hydrogen Europe, March 2020.

[7] "Hydrogen Roadmap Europe: A Sustainable Pathway For The European Energy Transition," Fuel Cells and Hydrogen 2, Januray 2019.

[8] "National Green Hydrogen Strategy," Ministry of Energy, Government of Chile, 2020. [Online]. Available: https://energia.gob.cl/sites/default/files/national_green_hydrogen_strategy_-_chile.pdf

[9] "Colombia's Hydrogen Roadmap," Ministry of Mines and Energy, Colombia, 2021. [Online]. Available: https://www.minenergia.gov.co/documents/10192/24309272/Colombia%27s+Hydrogen+Roadmap_2810.pdf

[10] "The National Hydrogen Strategy," Federal Ministry for Economic Affairs and Energy Berlin, June 2020.

[11] R. O'Hayre, S.-W. Cha, W. G. Colella, and F. B. Prinz, "Chapter 1: Introduction," in *Fuel Cell Fundamentals*, Third ed.: Wiley, 2016, pp. 1-24.

[12] "How the Kopernikus project P2X converts renewable electricity into plastics and fuels, gases and heat," Federal Ministry of Education and Research 2018. [Online]. Available: https://www.kopernikus-projekte.de/en/projects/p2x

[13] F. Bienen, D. Kopljar, S. Geiger, N. Wagner, and K. A. Friedrich, "Investigation of CO2 Electrolysis on Tin Foil by Electrochemical Impedance Spectroscopy," *ACS Sustainable Chemistry & Engineering,* vol. 8, no. 13, pp. 5192-5199, 2020/04/06 2020, doi: 10.1021/acssuschemeng.9b07625.

[14] J. W. Yun Zheng, Bo Yu,Wenqiang Zhang,Jing Chen;,inli Qiao,Jiujun Zhang, "A review of high temperature co-electrolysis of H_2O and CO_2 to produce sustainable fuels using solid oxide electrolysis cells (SOECs): advanced materials and technology," *Chem. Soc. Rev,* vol. 46, no. 1427, 2017, doi: 10.1039/c6cs00403b.

[15] A. Hauch *et al.*, "Recent advances in solid oxide cell technology for electrolysis," *Science*, vol. 370, no. 6513, Oct 9 2020, doi: 10.1126/science.aba6118.

[16] B. N. G. Kasiraman, M. Balakrishnan, "Performance, emission and combustion improvements in a direct injection diesel engine using cashew nut shell oil as fuel with camphor oil blending," *Energy,* vol. 47, pp. 116-124, 2012.

[17] M. P. Hoerlein, M. Riegraf, R. Costa, G. Schiller, and K. A. Friedrich, "A parameter study of solid oxide electrolysis cell degradation: Microstructural changes of the fuel electrode," *Electrochimica Acta,* vol. 276, pp. 162-175, 2018/06 2018, doi: 10.1016/j.electacta.2018.04.170.

[18] M. Riegraf, M. P. Hoerlein, R. Costa, G. Schiller, and K. A. Friedrich, "Sulfur Poisoning of Electrochemical Reformate Conversion on Nickel/Gadolinium-Doped Ceria Electrodes," *ACS Catalysis,* vol. 7, no. 11, pp. 7760-7771, 2017/10/17 2017, doi: 10.1021/acscatal.7b02177.

[19] Z. Bian, S. Das, M. H. Wai, P. Hongmanorom, and S. Kawi, "A Review on Bimetallic Nickel-Based Catalysts for CO2 Reforming of Methane," *ChemPhysChem,* vol. 18, no. 22, pp. 3117-3134, 2017, doi: https://doi.org/10.1002/cphc.201700529.

[20] Y. Tao, S. D. Ebbesen, and M. B. Mogensen, "Carbon deposition in solid oxide cells during co-electrolysis of H2O and CO2," *Journal of The Electrochemical Society,* vol. 161, no. 3, p. F337, 2014.

[21] A. Staerz, H. G. Seo, T. Defferriere, and H. L. Tuller, "Silica: ubiquitous poison of metal oxide interfaces," *Journal of Materials Chemistry A,* 10.1039/D1TA08469K vol. 10, no. 6, pp. 2618-2636, 2022, doi: 10.1039/D1TA08469K.

[22] S. S. C. Chuang and L. Zhang, "Perovskites and Related Mixed Oxides for SOFC Applications," in *Perovskites and Related Mixed Oxides,* vol. 2, P. Granger, V. I. Parvulescu, S. Kaliaguine, and W. Prellier Eds.: Wiley-VCH Verlag GmbH & Co. KGaA, 2015, ch. 38, pp. 863-879.

[23] I. Pilatowsky, R. J. Romero, C. A. Isaza, S. A. Gamboa, P. J. Sebastian, and W. Rivera, "Thermodynamics of Fuel Cells," in *Cogeneration Fuel Cell-Sorption Air Conditioning Systems*. London: Springer London, 2011, pp. 25-36.

[24] Y. Tanaka, M. P. Hoerlein, and G. Schiller, "Numerical simulation of steam electrolysis with a solid oxide cell for proper evaluation of cell performances," *International Journal of Hydrogen Energy,* vol. 41, no. 2, pp. 752-763, 2016/01/12/ 2016, doi: https://doi.org/10.1016/j.ijhydene.2015.11.048.

[25] M. A. Laguna-Bercero, "Recent advances in high temperature electrolysis using solid oxide fuel cells: A review," *Journal of Power Sources,* vol. 203, pp. 4-16, 2012/04/01/ 2012, doi: https://doi.org/10.1016/j.jpowsour.2011.12.019.

[26] J. r. m. Aicart, "Modeling and experimental validation of high temperature steam and carbon dioxide co-electrolysis

Modélisation et validation expérimentale d'un co-électrolyseur de la vapeur d'eau et du dioxyde de carbone à haute température," PhD, Université de Grenoble, 2014GRENI095, 2014. [Online]. Available: https://tel.archives-ouvertes.fr/tel-01284476

[27] N. Gallandat, K. Romanowicz, and A. Züttel, "An Analytical Model for the Electrolyser Performance Derived from Materials Parameters," *Journal of Power and Energy Engineering,* vol. 05, no. 10, pp. 34-49, 2017, doi: 10.4236/jpee.2017.510003.

[28] D.-M. Amaya-Dueñas, M. Riedel, M. Riegraf, R. Costa, and K. A. Friedrich, "High Temperature Co-electrolysis for Power-to-X," *Chemie Ingenieur Technik,* vol. 92, no. 1-2, pp. 45-52, 2020/01 2020, doi: 10.1002/cite.201900119.

[29] R. Küngas, "Review—Electrochemical CO2 Reduction for CO Production: Comparison of Low- and High-Temperature Electrolysis Technologies," *Journal of The Electrochemical Society,* vol. 167, no. 4, p. 044508, 2020/02/14 2020, doi: 10.1149/1945-7111/ab7099.

[30] J. P. Stempien, Q. Sun, and S. H. Chan, "Solid Oxide Electrolyzer Cell Modeling: A Review," no. 4, pp. 216-246%V 93, 2013-09-09 2013. [Online]. Available: https://papers.itc.pw.edu.pl/index.php/JPT/article/view/443%J Journal of Power Technologies.

[31] J. P. Stempien, Q. Liu, M. Ni, Q. Sun, and S. H. Chan, "Physical principles for the calculation of equilibrium potential for co-electrolysis of steam and carbon dioxide in a Solid Oxide Electrolyzer Cell (SOEC)," *Electrochimica Acta,* vol. 147, pp. 490-497, 2014/11/20/ 2014, doi: https://doi.org/10.1016/j.electacta.2014.09.144.

[32] D. G. Goodwin, H. Moffat, and R. L. Speth, "Cantera: An Object-oriented Software Toolkit for Chemical Kinetics, Thermodynamics, and Transport Processes. Version 2.2.1," 2016.

[33] Z. Jaworski, B. Zakrzewska, and P. Pianko-Oprych, "On thermodynamic equilibrium of carbon deposition from gaseous C-H-O mixtures: updating for nanotubes %J Reviews in Chemical Engineering," vol. 33, no. 3, pp. 217-235, 2017, doi: doi:10.1515/revce-2016-0022.

[34] R. O'Hayre, S.-W. Cha, W. G. Colella, and F. B. Prinz, "Chapter 4: Fuel Cell Charge Transport," in *Fuel Cell Fundamentals,* 2016, pp. 117-166.

[35] R. O'Hayre, S.-W. Cha, W. G. Colella, and F. B. Prinz, "Chapter 3: Fuel Cell Reaction Kinetics," in *Fuel Cell Fundamentals*, 2016, pp. 77-116.

[36] C. Pirovano, A. Rolle, and R.-N. Vannier, "Perovskite and Derivative Compounds as Mixed Ionic-Electronic Conductors," in *Perovskites and Related Mixed Oxides*: Wiley-VCH Verlag GmbH & Co. KGaA, 2015, pp. 169-188.

[37] R. O'Hayre, S.-W. Cha, W. G. Colella, and F. B. Prinz, "Chapter 5: Fuel Cell Mass Transport," in *Fuel Cell Fundamentals*, 2016, pp. 167-202.

[38] S. C. Perry, C. Ponce de León, and F. C. Walsh, "Review—The Design, Performance and Continuing Development of Electrochemical Reactors for Clean Electrosynthesis," *Journal of The Electrochemical Society,* vol. 167, p. 155525, 2020, doi: 10.1149/1945-7111/abc58e.

[39] S. Srinivasan, *Fuel Cells From Fundamentals to Applications*. Springer, 2006.

[40] Andreas Friedrich *et al.*, "Von der Elektrolyse zur Brenntoffzelle," in *FVEE – Jahrestagung 2019: Energy Research for Future – Forschung für die Herausforderungen der Energiewende*, 2019.

[41] S. GmbH. *Sunfire HyLink*.

[42] M. C. Tucker, "Progress in metal-supported solid oxide fuel cells: A review," *Journal of Power Sources,* vol. 195, no. 15, pp. 4570-4582, 2010/08/01/ 2010, doi: https://doi.org/10.1016/j.jpowsour.2010.02.035.

[43] R. O'Hayre, S.-W. Cha, W. G. Colella, and F. B. Prinz, "Chapter 9: PEMFC and SOFC Materials," in *Fuel Cell Fundamentals*, 2016, pp. 303-346.

[44] E. Ivers-Tiffée, A. Weber, and D. Herbstritt, "Materials and technologies for SOFC-components," *Journal of the European Ceramic Society,* vol. 21, no. 10, pp. 1805-1811, 2001/01/01/ 2001, doi: https://doi.org/10.1016/S0955-2219(01)00120-0.

[45] L. Nie, Z. Liu, M. Liu, L. Yang, Y. Zhang, and M. Liu, "Enhanced Performance of La0.6Sr0.4Co0.2Fe0.8O3-\delta(LSCF) Cathodes with Graded Microstructure Fabricated by Tape Casting," *Journal of Electrochemical Science and Technology,* vol. 1, no. 1, pp. 50-56, 2010, doi: 10.5229/jecst.2010.1.1.050.

[46] M. M. Nair and S. Kaliaguine, "Synthesis and Catalytic Applications of Nanocast Oxide-Type Perovskites," in *Perovskites and Related Mixed Oxides,* vol. 1, P. Granger, V. I. Parvulescu, S. Kaliaguine, and W. Prellier Eds.: Wiley-VCH Verlag GmbH & Co. KGaA, 2015, ch. 3, pp. 47-67.

[47] K. Momma and F. Izumi, "VESTA 3 for three-dimensional visualization of crystal, volumetric and morphology data," *Journal of Applied Crystallography,* vol. 44, no. 6, pp. 1272-1276, 2011, doi: doi:10.1107/S0021889811038970.

[48] J. Mermelstein, M. Millan, and N. Brandon, "The impact of steam and current density on carbon formation from biomass gasification tar on Ni/YSZ, and Ni/CGO solid oxide fuel cell anodes," *Journal of Power Sources,* vol. 195, no. 6, pp. 1657-1666, 2010/03/15/ 2010, doi: https://doi.org/10.1016/j.jpowsour.2009.09.046.

[49] R. Knibbe *et al.*, "Oxidation in ceria infiltrated metal supported SOFCs – A TEM investigation," *Journal of Power Sources,* vol. 228, pp. 75-82, 2013, doi: 10.1016/j.jpowsour.2012.11.051.

[50] F. Tietz, D. Sebold, A. Brisse, and J. Schefold, "Degradation phenomena in a solid oxide electrolysis cell after 9000 h of operation," *Journal of Power Sources,* vol. 223, pp. 129-135, 2013, doi: 10.1016/j.jpowsour.2012.09.061.

[51] L. Holzer *et al.*, "Microstructure degradation of cermet anodes for solid oxide fuel cells: Quantification of nickel grain growth in dry and in humid atmospheres," *Journal of Power Sources,* vol. 196, no. 3, pp. 1279-1294, 2011/02/01/ 2011, doi: https://doi.org/10.1016/j.jpowsour.2010.08.017.

[52] V. Duboviks, R. C. Maher, M. Kishimoto, L. F. Cohen, N. P. Brandon, and G. J. Offer, "A Raman spectroscopic study of the carbon deposition mechanism on Ni/CGO electrodes during CO/CO2 electrolysis," *Phys. Chem. Chem. Phys.,* vol. 16, no. 26, pp. 13063-13068, 2014, doi: 10.1039/c4cp01503g.

[53] A. Faes, A. Hessler-Wyser, A. Zryd, and J. Van Herle, "A Review of RedOx Cycling of Solid Oxide Fuel Cells Anode," (in eng), *Membranes (Basel),* vol. 2, no. 3, pp. 585-664, 2012, doi: 10.3390/membranes2030585.

[54] Matthias Riegraf, Diana M. Amaya-Dueñas, Noriko Sata, K. Andreas Friedrich, and R. Costa, "Performance and Limitations of Nickel-Doped Chromite Anodes in Electrolyte-Supported Solid Oxide Fuel Cells," *ChemSusChem,* vol. 14, pp. 2401-2413, 2021.

[55] M. C. Tucker, "Durability of symmetric-structured metal-supported solid oxide fuel cells," *Journal of Power Sources,* vol. 369, pp. 6-12, 2017/11/30/ 2017, doi: https://doi.org/10.1016/j.jpowsour.2017.09.075.

[56] H. Zhu, P. Zhang, and S. Dai, "Recent Advances of Lanthanum-Based Perovskite Oxides for Catalysis," *ACS Catalysis,* vol. 5, no. 11, pp. 6370-6385, 2015/09/30 2015, doi: 10.1021/acscatal.5b01667.

[57] D.-M. Amaya-Dueñas *et al.*, "A-site deficient chromite with in situ Ni exsolution as a fuel electrode for solid oxide cells (SOCs)," *Journal of Materials Chemistry A,* 10.1039/D0TA07090D 2021, doi: 10.1039/D0TA07090D.

[58] G. Tsekouras, D. Neagu, and J. T. S. Irvine, "Step-change in high temperature steam electrolysis performance of perovskite oxide cathodes with exsolution of B-site

dopants," *Energy Environ. Sci.,* vol. 6, no. 1, pp. 256-266, 2013, doi: 10.1039/c2ee22547f.

[59] V. Kyriakou, D. Neagu, E. I. Papaioannou, I. S. Metcalfe, M. C. M. van de Sanden, and M. N. Tsampas, "Co-electrolysis of H2O and CO2 on exsolved Ni nanoparticles for efficient syngas generation at controllable H2/CO ratios," *Applied Catalysis B: Environmental,* vol. 258, p. 117950, 2019/12/05/ 2019, doi: https://doi.org/10.1016/j.apcatb.2019.117950.

[60] J.-h. Myung, D. Neagu, D. N. Miller, and J. T. S. Irvine, "Switching on electrocatalytic activity in solid oxide cells," *Nature,* vol. 537, no. 7621, pp. 528-531, 2016/08/22 2016, doi: 10.1038/nature19090.

[61] D. Neagu *et al.*, "Nano-socketed nickel particles with enhanced coking resistance grown in situ by redox exsolution," (in eng), *Nat Commun,* vol. 6, pp. 8120-8120, 2015, doi: 10.1038/ncomms9120.

[62] D. Neagu *et al.*, "In Situ Observation of Nanoparticle Exsolution from Perovskite Oxides: From Atomic Scale Mechanistic Insight to Nanostructure Tailoring," *ACS Nano,* vol. 13, no. 11, pp. 12996-13005, 2019/10/21 2019, doi: 10.1021/acsnano.9b05652.

[63] N. Q. Minh, "Ceramic Fuel Cells," vol. 76, no. 3, pp. 563-588, 1993, doi: https://doi.org/10.1111/j.1151-2916.1993.tb03645.x.

[64] J. Sfeir, "LaCrO3-based anodes: stability considerations," *Journal of Power Sources,* vol. 118, no. 1, pp. 276-285, 2003/05/25/ 2003, doi: https://doi.org/10.1016/S0378-7753(03)00099-5.

[65] J. Sfeir *et al.*, "Lanthanum Chromite Based Catalysts for Oxidation of Methane Directly on SOFC Anodes," *Journal of Catalysis,* vol. 202, no. 2, pp. 229-244, 2001/09/10/ 2001, doi: https://doi.org/10.1006/jcat.2001.3286.

[66] X. Zhang, Y. Song, G. Wang, and X. Bao, "Co-electrolysis of CO2 and H2O in high-temperature solid oxide electrolysis cells: Recent advance in cathodes," *Journal of Energy Chemistry,* vol. 26, no. 5, pp. 839-853, 2017/09 2017, doi: 10.1016/j.jechem.2017.07.003.

[67] A. K. Opitz *et al.*, "Surface Chemistry of Perovskite-Type Electrodes During High Temperature CO2 Electrolysis Investigated by Operando Photoelectron Spectroscopy," *ACS Appl Mater Interfaces,* vol. 9, no. 41, pp. 35847-35860, Oct 18 2017, doi: 10.1021/acsami.7b10673.

[68] F. M. Sapountzi, S. Brosda, K. M. Papazisi, S. P. Balomenou, and D. Tsiplakides, "Electrochemical performance of La0.75Sr0.25Cr0.9M0.1O3 perovskites as SOFC anodes in CO/CO2 mixtures," *Journal of Applied Electrochemistry,* vol. 42, no. 9, pp. 727-735, 2012/08/08 2012, doi: 10.1007/s10800-012-0459-4.

[69] W. Kobsiriphat, B. D. Madsen, Y. Wang, M. Shah, L. D. Marks, and S. A. Barnett, "Nickel- and Ruthenium-Doped Lanthanum Chromite Anodes: Effects of Nanoscale Metal Precipitation on Solid Oxide Fuel Cell Performance," *Journal of The Electrochemical Society,* vol. 157, no. 2, p. B279, 2010, doi: 10.1149/1.3269993.

[70] Y. Sun *et al.*, "A-site deficient perovskite: the parent for in situ exsolution of highly active, regenerable nano-particles as SOFC anodes," *Journal of Materials Chemistry A,* vol. 3, no. 20, pp. 11048-11056, 2015, doi: 10.1039/c5ta01733e.

[71] I. E. Agency, "The Role of Critical World Energy Outlook Special Report Minerals in Clean Energy Transitions," International Energy Agency, 2021. [Online]. Available: www.iea.org

[72] A. L. Sauvet and J. T. S. Irvine, "Catalytic activity for steam methane reforming and physical characterisation of La1−xSrxCr1−yNiyO3−δ," *Solid State Ionics,* vol. 167, no. 1, pp. 1-8, 2004/02/12/ 2004, doi: https://doi.org/10.1016/j.ssi.2003.11.021.

[73] P. Sujatha Devi and M. Subba Rao, "Preparation, structure, and properties of strontium-doped lanthanum chromites: La1−xSrxCrO3," *Journal of Solid State Chemistry,* vol. 98, no. 2, pp. 237-244, 1992/06/01/ 1992, doi: https://doi.org/10.1016/S0022-4596(05)80231-2.

[74] D. M. Amaya-Dueñas, M. Riegraf, A. Nenning, A. K. Opitz, R. Costa, and K. A. Friedrich, "Operational Aspects of a Perovskite Chromite-Based Fuel Electrode in Solid Oxide Electrolysis Cells (SOEC)," *ACS Applied Energy Materials,* 2022/07/08 2022, doi: 10.1021/acsaem.2c00680.

[75] D. M. Amaya Dueñas *et al.*, "Synthesis and Evaluation of the A-Site Deficient Perovskite La0.65Sr0.3Cr0.85Ni0.15O3-δ as Fuel Electrode for High Temperature Co-Electrolysis Enhanced by In Situ Exsolution of Ni Nanoparticles," *ECS Transactions,* vol. 91, no. 1, pp. 1751-1760, 2019/07/10 2019, doi: 10.1149/09101.1751ecst.

[76] A. Nenning and J. Fleig, "Electrochemical XPS investigation of metal exsolution on SOFC electrodes: Controlling the electrode oxygen partial pressure in ultra-high-vacuum," *Surface Science,* vol. 680, pp. 43-51, 2019/02 2019, doi: 10.1016/j.susc.2018.10.006.

[77] J. I. Goldstein, D. E. Newbury, J. R. Michael, N. W. M. Ritchie, J. H. J. Scott, and D. C. Joy, *Scanning Electron Microscopy and X-Ray Microanalysis*. Springer, 2018.

[78] P. W. Hawkes and J. C. H. S. (Eds.), *Springer Handbook of Microscopy*. Springer, 2019.

[79] Y. Leng, "Scanning Electron Microscopy," in *Materials Characterization*, 2013, pp. 127-161.

[80] C. Scheu and W. D. Kaplan, "Introduction to Scanning Electron Microscopy," in *In-Situ Electron Microscopy*, ch. 1, pp. 1-37.

[81] N. D. Lisgarten, "Practical Methods in Electron Microscopy Vol 1," *Materials Science Physics Bulletin,* vol. 24, pp. 299-299, 1973, doi: 10.1088/0031-9112/24/5/025.

[82] Y. Leng, "Thermal Analysis," in *Materials Characterization*, 2013, pp. 333-365.

[83] C. Pirola, F. Galli, and G. S. Patience, "Experimental methods in chemical engineering: Temperature programmed reduction—TPR," vol. 96, no. 11, pp. 2317-2320, 2018, doi: https://doi.org/10.1002/cjce.23317.

[84] Y. Leng, "X-Ray Diffraction Methods," in *Materials Characterization*, 2013, pp. 47-82.

[85] J. Epp, "X-ray diffraction (XRD) techniques for materials characterization," in *Materials Characterization Using Nondestructive Evaluation (NDE) Methods*, G. Hübschen, I. Altpeter, R. Tschuncky, and H.-G. Herrmann Eds.: Woodhead Publishing, 2016, ch. 4, pp. 81-124.

[86] Y. Leng, "X-Ray Spectroscopy for Elemental Analysis," in *Materials Characterization*, 2013, pp. 191-219.

[87] J. F. Moulder, W. F. Stickle, P. E.'Sobol, and K. D. Bomben, *Handbook of X-ray Photoelectron Spectroscopy*. Perkin-Elmer Corporation, 1992.

[88] M. D. o. I. C. Atomistic Simulation Group. "Database of Ionic Radii." http://abulafia.mt.ic.ac.uk/shannon/ptable.php (accessed.

[89] I. Yasuda and M. Hishinuma, "Electrical conductivity and chemical diffusion coefficient of Sr-doped lanthanum chromites," *Solid State Ionics,* vol. 80, no. 1, pp. 141-150, 1995/08/01/ 1995, doi: https://doi.org/10.1016/0167-2738(95)00136-T.

[90] D. M. Amaya Dueñas, M. Riegraf, A. Nenning, A. K. Opitz, R. Costa, and A. K. Friedrich, "$La_{0.65}Sr_{0.3}Cr_{0.85}Ni_{0.15}O_{3-\delta}$ perovskite electrocatalyst for high temperature steam and dry CO_2 electrolysis," in *EFCF 2020 14th European SOFC & SOE Forum*, October 20 - 23 2020 2020.

[91] D. Klotz, "Characterization and Modeling of Electrochemical Energy Conversion Systems by Impedance Techniques," PhD, Elektrotechnik und Informationstechnik des Karlsruher Instituts für Technologie (KIT), Karlsruher Instituts für Technologie (KIT), Karlsruhe, 2012.

[92] A. Leonide, *SOFC modelling and parameter identification by means of impedance spectroscopy*. Karlsruhe: KIT Scientific Publishing, 2010.

[93] E. Ivers-Tiffée and A. V. Virkar, "Chapter 9 - Electrode Polarisations," in *High Temperature and Solid Oxide Fuel Cells,* S. C. Singhal and K. Kendall Eds. Amsterdam: Elsevier Science, 2003, pp. 229-260.

[94] *ZView Electrochemical Impedance Software*. (2000). Scribner Associates, Inc.

[95] D. Klotz, A. Weber, and E. Ivers-Tiffée, "Practical Guidelines for Reliable Electrochemical Characterization of Solid Oxide Fuel Cells," *Electrochimica Acta,* vol. 227, pp. 110-126, 2017/02/10/ 2017, doi: https://doi.org/10.1016/j.electacta.2016.12.148.

[96] E. Ivers-Tiffée and A. Weber, "Evaluation of electrochemical impedance spectra by the distribution of relaxation times," *Journal of the Ceramic Society of Japan,* vol. 125, no. 4, pp. 193-201, 2017, doi: 10.2109/jcersj2.16267.

[97] M. Riegraf, "Investigation of sulfur poisoning of Ni-based anodes in solid oxide fuel cells," PhD PhD, 04 Fakultät Energie-, Verfahrens- und Biotechnik, Universität Stuttgart, 2019.

[98] M. Hahn, S. Schindler, L.-C. Triebs, and M. A. Danzer, "Optimized Process Parameters for a Reproducible Distribution of Relaxation Times Analysis of Electrochemical Systems," *Batteries,* vol. 5, no. 2, 2019, doi: 10.3390/batteries5020043.

[99] T. W. Napporn *et al.*, "Chapter 9 - Electrochemical Measurement Methods and Characterization on the Cell Level," in *Fuel Cells and Hydrogen,* V. Hacker and S. Mitsushima Eds.: Elsevier, 2018, pp. 175-214.

[100] A. Weber, "Impedance analysis of porous electrode structures in batteries and fuel cells," *tm - Technisches Messen,* vol. 88, no. 1, pp. 1-16, 2020, doi: 10.1515/teme-2020-0084.

[101] M. Razeghi, "Non-equilibrium Electrical Properties of Semiconductors," in *Fundamentals of Solid State Engineering*. Cham: Springer International Publishing, 2019, pp. 275-318.

[102] L. J. Van Der Pauw, "A Method of Measuring the Resistivity and Hall Coefficient on Lamellae of Arbitrary Shape," *Philips Technical Review,* vol. 20, pp. 220-224, 1958.

[103] L. Volgger, *Elektrochemische Eigenschaften von Fe-dotiertem SrTiO3 Modellanoden für Festoxidzellen* (Electrochemical properties of Fe-doped SrTiO3 model electrodes for solix oxide cells). Wien: Wien, 2015, pp. 114 Seiten, Illustrationen, Diagramme.

[104] M. Gerstl, A. Hutterer, J. Fleig, M. Bram, and A. K. Opitz, "Model composite microelectrodes as a pathfinder for fully oxidic SOFC anodes," *Solid State Ionics,* vol. 298, pp. 1-8, 2016/12/15/ 2016, doi: https://doi.org/10.1016/j.ssi.2016.10.013.

[105] A. B. Stambouli and E. Traversa, "Solid oxide fuel cells (SOFCs): a review of an environmentally clean and efficient source of energy," *Renewable and Sustainable Energy Reviews,* vol. 6, no. 5, pp. 433-455, 2002/10/01/ 2002, doi: https://doi.org/10.1016/S1364-0321(02)00014-X.

[106] S. C. Singhal, "Solid Oxide Fuel Cells: Past, Present and Future," in *Solid Oxide Fuels Cells: Facts and Figures: Past Present and Future Perspectives for SOFC Technologies*, J. T. S. Irvine and P. Connor Eds. London: Springer London, 2013, pp. 1-23.

[107] C. Spiegel, *Designing and building fuel cells*. Citeseer, 2007.

[108] L. Blum, W. A. Meulenberg, H. Nabielek, and R. Steinberger-Wilckens, "Worldwide SOFC Technology Overview and Benchmark," vol. 2, no. 6, pp. 482-492, 2005, doi: https://doi.org/10.1111/j.1744-7402.2005.02049.x.

[109] J. B. Hansen, "Solid oxide electrolysis – a key enabling technology for sustainable energy scenarios," *Faraday Discussions,* 10.1039/C5FD90071A vol. 182, no. 0, pp. 9-48, 2015, doi: 10.1039/C5FD90071A.

[110] W. Dönitz, G. Dietrich, E. Erdle, and R. Streicher, "Electrochemical high temperature technology for hydrogen production or direct electricity generation," *International Journal of Hydrogen Energy,* vol. 13, no. 5, pp. 283-287, 1988/01/01/ 1988, doi: https://doi.org/10.1016/0360-3199(88)90052-3.

[111] W. Dönitz and E. Erdle, "High-temperature electrolysis of water vapor—status of development and perspectives for application," *International Journal of Hydrogen Energy,* vol. 10, no. 5, pp. 291-295, 1985/01/01/ 1985, doi: https://doi.org/10.1016/0360-3199(85)90181-8.

[112] E. Erdle, W. Dönitz, R. Schamm, and A. Koch, "Reversibility and polarization behaviour of high temperature solid oxide electrochemical cells," *International Journal of Hydrogen Energy,* vol. 17, no. 10, pp. 817-819, 1992/10/01/ 1992, doi: https://doi.org/10.1016/0360-3199(92)90026-S.

[113] A. Atkinson *et al.*, "Advanced anodes for high-temperature fuel cells," *Nature Materials,* vol. 3, no. 1, pp. 17-27, 2004/01/01 2004, doi: 10.1038/nmat1040.

[114] H. S. Spacil, "Electrical device including nickel-containing stabilized zirconia electrode," United States, 1970.

[115] M. Mogensen and J. J. Bentzen, "Oxidation of Methane on Oxide Electrodes at 800-1000°C," *Proceedings of The Electrochemical Society,* vol. PV 1989-19, pp. 99-110, 1989, doi: 10.1149/198911.0099PV.

[116] I. S. Metcalfe, P. H. Middleton, P. Petrolekas, and B. C. H. Steele, "Hydrocarbon activation in solid state electrochemical cells," *Solid State Ionics,* vol. 57, no. 3, pp. 259-264, 1992/10/01/ 1992, doi: https://doi.org/10.1016/0167-2738(92)90156-J.

[117] K. M. Liddicott, "High temperature materials chemistry of doped cerium oxide ceramics.," Doctor of Philosophy (PhD) PhD, Imperial College London (University of London), 1994. [Online]. Available: http://hdl.handle.net/10044/1/8619

[118] M. Jabbar, J. Hogh, and N. Bonanos, "High performance fuel electrode for a solid oxide electrochemical cell," Denmark Patent Appl. PCT/EP2012/07095 1, 2013.

[119] Y. Matsuzaki, "Method for preparing anode for solid oxde fuel cells," Japan Patent 5,474,800 Patent Appl. 136,213, 1995.

[120] C. Kleinlogel, M. Gödickemeier, K. Honegger, and L. J. Gauckler, "Solid oxide fuel cells operating with cathode supported thin film electrolyte," in *Ionic and Mixed Conducting Ceramics III’*, Paris, W.L. Worrell, H.L. Tuller, A.C. Khandkar, M.

Mogensen, and W. Gopel, Eds., 1997, vol. PV 97-24,: The Electrochemical Society Inc., pp. 97-105.

[121] R. Doshi, V. L. Richards, J. D. Carter, X. Wang, and M. Krumpelt, "Development of Solid-Oxide Fuel Cells That Operate at 500°C," *Journal of The Electrochemical Society,* vol. 146, no. 4, pp. 1273-1278, 1999/04/01 1999, doi: 10.1149/1.1391758.

[122] K. Honegger, "Performance of SOFC Stacks Operated with CH4 at Reduced Temperatures (600°–800°C)," *ECS Proceedings Volumes,* vol. 1999-19, no. 1, pp. 1019-1026, 1999/01 1999, doi: 10.1149/199919.1019pv.

[123] S. J. A. Livermore, J. W. Cotton, and R. M. Ormerod, "Fuel reforming and electrical performance studies in intermediate temperature ceria–gadolinia-based SOFCs," *Journal of Power Sources,* vol. 86, no. 1, pp. 411-416, 2000/03/01/ 2000, doi: https://doi.org/10.1016/S0378-7753(99)00493-0.

[124] "SOLIDpower acquires business of Ceramic Fuel Cells GmbH," *Fuel Cells Bulletin,* vol. 2015, no. 8, p. 10, 2015/08/01/ 2015, doi: https://doi.org/10.1016/S1464-2859(15)30228-5.

[125] T. d. A. Ferreira, Z. Wuillemin, A. G. Marchetti, and D. Bonvin, "Fast RTO Applied to a Commercial SOFC System," *IFAC-PapersOnLine,* vol. 52, no. 1, pp. 40-45, 2019/01/01/ 2019, doi: https://doi.org/10.1016/j.ifacol.2019.06.034.

[126] M. Hauth *et al.*, "Production and Reliability Oriented SOFC Cell and Stack Design," *ECS Transactions,* vol. 78, no. 1, pp. 2231-2249, 2017/05/30 2017, doi: 10.1149/07801.2231ecst.

[127] FuelCellsWorks. "Ceres and Bosch Scale up for Mass Solid Oxide Fuel Cell (SOFC) Production." https://fuelcellsworks.com/news/ceres-and-bosch-scale-up-for-mass-solid-oxide-fuel-cell-sofc-production/ (accessed.

[128] M. Andersson and B. Sundèn. "Technology review – Solid Oxide Fuel Cell." Energiforsk AB. (accessed.

[129] J. Kupecki, J. Milewski, A. Szczesniak, R. Bernat, and K. Motylinski, "Dynamic numerical analysis of cross-, co-, and counter-current flow configuration of a 1 kW-class solid oxide fuel cell stack," *International Journal of Hydrogen Energy,* vol. 40, no. 45, pp. 15834-15844, 2015/12/07/ 2015, doi: https://doi.org/10.1016/j.ijhydene.2015.07.008.

[130] R. Steinberger-Wilckens, "European SOFC R&D - Status and Trends," *ECS Transactions,* vol. 25, no. 2, pp. 3-10, 2019/12/17 2019, doi: 10.1149/1.3205502.

[131] B. E. Mai, T. Heller, D. Schimanke, J. Lawrence, and C. Wunderlich, "Influence of Operating Conditions on the Reliable Performance of Stacks and Integrated Stack Modules," *ECS Transactions,* vol. 25, no. 2, pp. 187-194, 2009, doi: 10.1149/1.3205524.

[132] S. GmbH. "About Sunfire Renewables everywhere." https://www.sunfire.de/en/about-us

[133] "GrInHy2.0 - Green Industrial Hydrogen " https://www.green-industrial-hydrogen.com/

[134] F. R. Bianchi and B. Bosio, "Operating Principles, Performance and Technology Readiness Level of Reversible Solid Oxide Cells," *Sustainability,* vol. 13, no. 9, p. 4777, 2021. [Online]. Available: https://www.mdpi.com/2071-1050/13/9/4777.

[135] M. C. Verbraeken *et al.*, "Short Stack and Full System Test Using a Ceramic A-Site Deficient Strontium Titanate Anode," vol. 15, no. 5, pp. 682-688, 2015, doi: https://doi.org/10.1002/fuce.201400183.

[136] R. Price *et al.*, "Upscaling of Co-Impregnated La0.20Sr0.25Ca0.45TiO3 Anodes for Solid Oxide Fuel Cells: A Progress Report on a Decade of Academic-Industrial Collaboration," *Advanced Energy Materials,* vol. 11, no. 15, p. 2003951, 2021, doi: https://doi.org/10.1002/aenm.202003951.

[137] A. Hauch, S. Jensen, S. Ramousse, and M. B. Mogensen, "Performance and Durability of Solid Oxide Electrolysis Cells," *Journal of The Electrochemical Society,* vol. 153, 2006.

[138] J. Zhang, C. Lenser, N. H. Menzler, and O. Guillon, "Comparison of solid oxide fuel cell (SOFC) electrolyte materials for operation at 500 °C," *Solid State Ionics,* vol. 344, p. 115138, 2020/01/01/ 2020, doi: https://doi.org/10.1016/j.ssi.2019.115138.

[139] H. Qi *et al.*, "Positive Effects of H2O on the Hydrogen Oxidation Reaction on Sr2Fe1.5Mo0.5O6−δ-Based Perovskite Anodes for Solid Oxide Fuel Cells," *ACS Catalysis,* vol. 10, no. 10, pp. 5567-5578, 2020, doi: 10.1021/acscatal.9b05458.

[140] J. Schefold, A. Brisse, A. Surrey, and C. Walter, "80,000 current on/off cycles in a one year long steam electrolysis test with a solid oxide cell," *International Journal of Hydrogen Energy,* vol. 45, no. 8, pp. 5143-5154, 2020/02 2020, doi: 10.1016/j.ijhydene.2019.05.124.

[141] N. H. Behling, *Fuel Cells: Current Technology Challenges and Future Research Needs*. Elsevier Science, 2012.

[142] J. Laurencin, G. Delette, F. Lefebvre-Joud, and M. Dupeux, "A numerical tool to estimate SOFC mechanical degradation: Case of the planar cell configuration," *Journal of the European Ceramic Society,* vol. 28, no. 9, pp. 1857-1869, 2008/01/01/ 2008, doi: https://doi.org/10.1016/j.jeurceramsoc.2007.12.025.

[143] J. Malzbender and R. W. Steinbrech, "Fracture test of thin sheet electrolytes for solid oxide fuel cells," *Journal of the European Ceramic Society,* vol. 27, no. 7, pp. 2597-2603, 2007/01/01/ 2007, doi: https://doi.org/10.1016/j.jeurceramsoc.2006.11.071.

[144] A. Atkinson and A. Selçuk, "Mechanical behaviour of ceramic oxygen ion-conducting membranes," *Solid State Ionics,* vol. 134, no. 1, pp. 59-66, 2000/10/01/ 2000, doi: https://doi.org/10.1016/S0167-2738(00)00714-1.

[145] A. K. Kushwaha, M. John, M. Misra, and P. L. Menezes, "Nanocrystalline Materials: Synthesis, Characterization, Properties, and Applications," *Crystals,* vol. 11, no. 11, p. 1317, 2021. [Online]. Available: https://www.mdpi.com/2073-4352/11/11/1317.

[146] S. N. Naik and S. M. Walley, "The Hall–Petch and inverse Hall–Petch relations and the hardness of nanocrystalline metals," *Journal of Materials Science,* vol. 55, no. 7, pp. 2661-2681, 2020/03/01 2020, doi: 10.1007/s10853-019-04160-w.

[147] Z. Gong *et al.*, "Influence of grain boundary and grain size on the mechanical properties of polycrystalline ceramics: Grain-scale simulations," vol. 103, no. 10, pp. 5900-5913, 2020, doi: https://doi.org/10.1111/jace.17286.

[148] H. Ryou *et al.*, "Below the Hall–Petch Limit in Nanocrystalline Ceramics," *ACS Nano,* vol. 12, no. 4, pp. 3083-3094, 2018/04/24 2018, doi: 10.1021/acsnano.7b07380.

[149] D. A. Osinkin *et al.*, "Thermal expansion, gas permeability, and conductivity of Ni-YSZ anodes produced by different techniques," *Journal of Solid State Electrochemistry,* vol. 18, no. 1, pp. 149-156, 2014/01/01 2014, doi: 10.1007/s10008-013-2239-4.

[150] C. S. Montross, "Elastic modulus versus bond length in lanthanum chromite ceramics," *Journal of the European Ceramic Society,* vol. 18, no. 4, pp. 353-358, 1998/04/01/ 1998, doi: https://doi.org/10.1016/S0955-2219(97)00143-X.

[151] C. Geipel *et al.*, "Stack Development and Industrial Scale-Up," *ECS Transactions,* vol. 91, no. 1, pp. 123-132, 2019/07/10 2019, doi: 10.1149/09101.0123ecst.

[152] IRENA, "Green Hydrogen Cost Reduction: Scaling up Electrolysers to Meet the 1.5ºC Climate Goal," Abu Dhabi, 2020.

[153] IEA, "How to make sure critical minerals are an enabler, not a bottleneck, for clean energy transitions," IEA, Paris, 2021. [Online]. Available: https://www.iea.org/commentaries/how-to-make-sure-critical-minerals-are-an-enabler-not-a-bottleneck-for-clean-energy-transitions

[154] M. Keersemaker, "Critical Raw Materials," in *Suriname Revisited: Economic Potential of its Mineral Resources*, M. Keersemaker Ed. Cham: Springer International Publishing, 2020, pp. 69-82.

[155] E. Commission, "Critical Raw Materials for Strategic Technologies and Sectors in the EU - A Foresight Study," 2020. [Online]. Available: https://ec.europa.eu/docsroom/documents/42881

[156] E. Commission, "Critical Raw Materials Resilience: Charting a Path towards greater Security and Sustainability," 2020. [Online]. Available: https://eur-lex.europa.eu/legal-content/EN/TXT/?uri=CELEX:52020DC0474

[157] J. Schefold, A. Brisse, and H. Poepke, "23,000 h steam electrolysis with an electrolyte supported solid oxide cell," *International Journal of Hydrogen Energy,* vol. 42, no. 19, pp. 13415-13426, 2017, doi: 10.1016/j.ijhydene.2017.01.072.

[158] "3. Roadmap des Kopernikus-Projektes P2X Phase II - Optionen für ein Nachhaltiges Energiesystem mit Power-to-X Technologien," Dechema, 2021. [Online]. Available: https://dechema.de/studien.html%20

[159] N. Salmon and R. Bañares-Alcántara, "Green ammonia as a spatial energy vector: a review," *Sustainable Energy & Fuels,* 10.1039/D1SE00345C vol. 5, no. 11, pp. 2814-2839, 2021, doi: 10.1039/D1SE00345C.

[160] R. Abbasi *et al.*, "A Roadmap to Low-Cost Hydrogen with Hydroxide Exchange Membrane Electrolyzers," *Advanced Materials,* vol. 31, no. 31, p. 1805876, 2019, doi: https://doi.org/10.1002/adma.201805876.

[161] D. Li *et al.*, "Durability of anion exchange membrane water electrolyzers," *Energy & Environmental Science,* 10.1039/D0EE04086J vol. 14, no. 6, pp. 3393-3419, 2021, doi: 10.1039/D0EE04086J.

10 List of figures

11 Additional publications

11.1 Conference proceedings

- **Conference proceedings: ECS Transactions, 2019:** D. M. Amaya Dueñas, Guoxing Chen, Anke Weidenkaff, Noriko Sata, Feng Han, Rémi Costa and K. Andreas Friedrich "Synthesis and Evaluation of the A-Site Deficient Perovskite La0.65Sr0.3Cr0.85Ni0.15O3-δ as Fuel Electrode for High Temperature Co-Electrolysis Enhanced by In Situ Exsolution of Ni Nanoparticles," *ECS Transactions*, vol. 91, no. 1, pp. 1751-1760, 2019/07/10 2019.
- **Lucerne Proceedings14th European SOFC & SOE Forum 2020:** D. M. Amaya Dueñas, M. Riegraf, A. Nenning, A. K. Opitz, R. Costa, and A. K. Friedrich, "La0.65Sr0.3Cr0.85Ni0.15O3-δ perovskite electrocatalyst for high temperature steam and dry CO2 electrolysis," *in EFCF 2020 14th European SOFC & SOE Forum*, 2020.

11.2 Talks at conferences and colloquia

First author = presenting author

09.07.2018	Amaya Dueñas D.M., Sata N., Han F., Schiller G., Costa R., Friedrich K.A. *Formulations of* $(La_{0.6-x}Sr_{0.4})(Fe_{0.8}Ni_{0.2})O_{3-\delta}$ *and* $(La_{0.7-y}Sr_{0.3})(Cr_{0.85}Ni_{0.15})O_{3-\delta}$ *as fuel electrode materials for high temperature co – electrolysis cells.* Electroceramics XVI Conference in Hasselt, Belgium. July 9 – 12, 2018.
12.09.2019	Amaya Dueñas D.M., Chen G., Weidenkaff A., Sata N., Han F., Schiller G., Costa R., Friedrich K. A. *Synthesis and Evaluation of the A-site Deficient Perovskite* $La_{0.65}Sr_{0.3}Cr_{0.85}Ni_{0.15}O_{3-\delta}$ *as Fuel Electrode for High Temperature Co-electrolysis Enhanced by In Situ Exsolution of Ni Nanoparticles* 16th International Symposium on Solid Oxide Fuel Cells in Kyoto, Japan. September 8 – 13, 2019.
21.10.2020	Amaya Dueñas D.M., Riegraf M., Nenning A., Opitz A.K., Costa R., Friedrich K. A. $La_{0.65}Sr_{0.3}Cr_{0.85}Ni_{0.15}O_{3-\delta}$ *Perovskite Electrocatalyst for High Temperature Steam and Dry* CO_2 *Eelectrolysis.* 14th European SOFC & SOE FORUM Virtual in Lucerne, Switzerland. October 20 – 23, 2020.

10.02 &14.10.2021	Amaya Dueñas D.M., *Perovskite fuel electrode for solid oxide cells (SOC) in Power-to-X applications*. CHEMAmpere research initiative colloquium of the University of Stuttgart.
15.11.2018	Amaya Dueñas D.M., *Assessment of fuel electrode materials for high temperature co–electrolysis in solid oxide electrolysis cells (SOEC)*. TT Institute Colloquium of the Institute of Engineering Thermodynamics, German Aerospace Center (DLR), Stuttgart.

11.3 Posters

24.09.2020	Amaya Dueñas D.M., Riegraf M., Costa R., Friedrich K. A. *High temperature solid oxide cells for Power-to-X applications:status, materials, challenges and prospects*. 10. ProcessNet-Jahrestagung und 34. DECHEMA-Jahrestagung der Biotechnologen 2020 Virtual in Aachen, Germany. September 21 – 24, 2020.

12 Scientific articles – original texts

Article I: Diana-María Amaya-Dueñas, Guoxing Chen, Anke Weidenkaff, Noriko Sata, Feng Han, Indro Biswas, Rémi Costa and K. Andreas Friedrich, "A-site deficient chromite with in situ Ni exsolution as a fuel electrode for solid oxide cells (SOCs)" *J. Mater. Chem. A*, vol. 9, pp. 5685-5701, 2021.

Article II: Matthias Riegraf, Diana M. Amaya-Dueñas, Noriko Sata, K. Andreas Friedrich and R. Costa, "Performance and Limitations of Nickel-Doped Chromite Anodes in Electrolyte-Supported Solid Oxide Fuel Cells" *ChemSusChem,* vol. 14, pp. 2401-2413, 2021.

Article III: D. M. Amaya-Dueñas, M. Riegraf, A. Nenning, A. K. Opitz, R. Costa, and K. A. Friedrich, "Operational Aspects of a Perovskite Chromite-Based Fuel Electrode in Solid Oxide Electrolysis Cells (SOEC)," *ACS Applied Energy Materials,* 2022/07/08 2022, doi: 10.1021/acsaem.2c00680.

Additional Article (not part of the cumulative dissertation): D.-M. Amaya-Dueñas, M. Riedel, M. Riegraf, R. Costa, and K. A. Friedrich, "High Temperature Co-electrolysis for Power-to-X," *Chemie Ingenieur Technik*, vol. 92, no. 1-2, pp. 45-52, 2020/01 2020.

Article I

Journal of
Materials Chemistry A

ROYAL SOCIETY
OF CHEMISTRY

PAPER

View Article Online
View Journal

Check for updates

Cite this: DOI: 10.1039/d0ta07090d

A-site deficient chromite with *in situ* Ni exsolution as a fuel electrode for solid oxide cells (SOCs)†

Diana-María Amaya-Dueñas, *[a] Guoxing Chen, [b] Anke Weidenkaff, [bc] Noriko Sata, [a] Feng Han, [a] Indro Biswas, [a] Rémi Costa *[a] and Kaspar Andreas Friedrich [ad]

A-site deficient lanthanum strontium chromite perovskite $La_{0.65}Sr_{0.3}Cr_{0.85}Ni_{0.15}O_{3-\delta}$ (L65SCrN) decorated by *in situ* exsolution of Ni nanoparticles was synthesized and implemented as a fuel electrode on a 5 cm × 5 cm electrolyte-supported cell (ESC) for solid oxide cells (SOCs) with an active surface of 16 cm^2. The stoichiometric formulation $La_{0.70}Sr_{0.3}Cr_{0.85}Ni_{0.15}O_{3-\delta}$ (L70SCrN) was also prepared in order to evaluate the reducibility and behavior towards Ni exsolution with respect to L65SCrN. This comparison was assessed by means of X-ray diffraction (XRD) and thermogravimetric analysis (TGA) in a reducing atmosphere. Metallic Ni was successfully detected using XRD on the *A*-site deficient formulation after TGA treatment. Surface analysis by means of X-ray photoemission spectroscopy (XPS) revealed a relative enrichment in Cr^{3+}. Ni exsolution was investigated on the L65SCrN formulation by annealing in a reducing atmosphere at 500 °C and 900 °C for 3 hours. The Ni nanoparticle size (from ~8 up to 100 nm) and morphology were characterized by means of scanning electron microscopy (SEM). Furthermore, L65SCrN was screen printed onto a 90 μm thick CGO20-3YSZ-CGO20 electrolyte on which the oxygen electrode $La_{0.58}Sr_{0.4}Fe_{0.8}Co_{0.2}O_{3-\delta}$ (LSCF) was printed on the other side. With ideal contacting, the electrochemical cell performance of the L65SCrN fuel electrode was demonstrated to be comparable to those of the state-of-the-art Ni-based cermets: ASR_{DC_Total} at −0.3 A cm^{-2} was calculated to be 0.676 Ω cm^2 in co-electrolysis operation. Reversible operation (rSOC) at 860 °C with a H_2O/H_2 ratio of 1 could be shown and co-electrolysis operation ($H_2O/CO_2 = 2$) at −0.45 A cm^{-2} and 860 °C with a voltage degradation of less than 3.5 mV/1000 hours could be demonstrated for 950 hours. Even though L65SCrN showed promising results for SOC operation, further investigations of Ni exsolution in doped chromites by varying temperature, time and pO_2 are proposed for a detailed understanding and optimization of the Ni nanoparticle size.

Received 20th July 2020
Accepted 11th January 2021

DOI: 10.1039/d0ta07090d

rsc.li/materials-a

Introduction

Since the industrial revolution, carbon-rich fossil feedstocks have played an important role in our daily life in order to fulfil our needs for energy demand and for a broad range of household and commercial products. Nowadays, the chemical industry relies on crude oil, coal and natural gas to produce the key building blocks such as olefins and aromatics. Nevertheless, the improvement of the corresponding synthesis processes in terms of selectivity and energy consumption or the development of alternative routes has become a major priority for the modern industry due to limited recoverable natural oil reserves and growing environmental considerations regarding greenhouse gas emissions.[1]

CO_2 is emitted in increasing amounts due to the growing need for power generation (coal-based plants) and industrial products, such as steel and chemicals, *e.g.* ethylene production by oxidative coupling of methane (OCM).[1] This greenhouse gas is also an essential feedstock for numerous chemical synthesis processes in combination with hydrogen. In some processes, CO_2 is pre-reduced at high temperature with hydrogen through the reverse water gas shift (RWGS) reaction yielding CO – a more reactive molecule – as an essential building block for downstream chemical synthesis. Methanol, which is an important multipurpose intermediate commonly used for the production of various chemicals, is currently produced from syngas (H_2 + CO) which can also be

---

[a] *German Aerospace Center (DLR), Institute of Engineering Thermodynamics, Pfaffenwaldring 38-40, D-70569 Stuttgart, Germany. E-mail: diana.amayaduenas@dlr.de; remi.costa@dlr.de*

[b] *Institute of Materials and Earth Sciences, Technische Universität Darmstadt, Alarich-Weiss-Str. 2, D-64287 Darmstadt, Germany*

[c] *Fraunhofer IWKS, Materials Recycling and Resource Strategies, Brentanostraße 2a, D-63755 Alzenau, Germany*

[d] *Institute of Building Energetics, Thermal Engineering and Energy Storage (IGTE), University of Stuttgart, Pfaffenwaldring 31, D-70569 Stuttgart, Germany*

† Electronic supplementary information (ESI) available: Additional SEM images of the exsolved Ni nanoparticles. See DOI: 10.1039/d0ta07090d

generated *via* catalytic steam or autothermal reforming of methane.[1]

In the light of syngas production and methanol synthesis, there are significant economic and environmental interest in valorizing renewable carbon sources. For this reason, since the last 10 years, the conversion of plant-derived materials (biomass) and CO_2 has attracted attention from industry and academia with the aim of producing fuels and bulk chemicals using direct electrosynthesis routes with a reduced CO_2 footprint.[2]

Power-to-X concepts intend to convert excess renewable power into diverse fuels and chemicals that can be used for large capacity energy storage.[3,4] Among the various concepts, the technologies based on Solid Oxide Cells (SOCs) operating at temperatures typically around 750–850 °C enable conversion of electricity at a high efficiency into valuable fuels (hydrogen or hydrocarbons) by means of high temperature electrolysis (HTE) without the need of precious catalysts. Interestingly, due to fast kinetics SOCs enable the simultaneous electrolysis of H_2O–CO_2 at high temperature into syngas, which can be further used for large-scale production of methanol and other green fuels and chemicals through the Fischer–Tropsch (F–T) synthesis.[1,5,6] Moreover, SOCs offer the unique advantage of enabling reversible operation. *i.e.* either energy storage or electricity production. In the energy storage mode, electrical energy from renewable sources is converted to valuable fuels (hydrogen or hydrocarbons) by means of HTE, while in discharge mode these fuels could be used for power production through fuel cell operation.[4] A reversible Solid Oxide Cell (rSOC) system could effectively ensure large storage capacity and grid balancing.

State-of-the-art SOCs rely on Ni-based cermet components, owing to the excellent electrical conductivity and high catalytic activity of Ni towards H_2O–CO_2 splitting and hydrogen dissociation reactions at high temperatures. Ni–$Zr_{0.85}Y_{0.15}O_{2-\delta}$ (Ni–YSZ) cermet fuel electrodes – typically used in the so-called Anode-Supported Cells (ASCs) – have been largely investigated in either operating modes. When operated in fuel cell mode, the electrodes are susceptible to poisoning with different fuel gas impurities such as sulfur species that have deleterious effects on performance, especially in reformate gases, and long-term stability.[7,8] Moreover, they suffer from irreversible degradation when exposed to re-oxidation reactions.[9] These cermet electrodes are prone to Ni agglomeration leading to loss of electrical percolation and diminution of the triple-phase-boundary (TPB) length.[10] When operated in electrolysis, they suffer from irreversible microstructural alterations, especially at high temperatures, high current densities and high pH_2O.[11] In co-electrolysis operation, carbon formation has been observed at the electrode–electrolyte interface with a reactant conversion of ~67% at 875 °C, causing microstructural alterations accompanied by a deactivation of the active sites.[12] By contrast, Ni–$Ce_{1-x}Gd_xO_{2-\delta}$ (Ni–CGO) based fuel electrodes – typically used in the Electrolyte-Supported Cells (ESCs) – have also been investigated as fuel electrode materials because of their catalytic properties and CGO phase enhanced tolerance against carbon formation.[13] Nevertheless, due to the large content of metallic Ni, such Ni–CGO cermet electrodes are also vulnerable to dimensional alterations caused by grain coarsening upon redox cycling *i.e.* repeated alternation of oxidizing and reducing atmospheres, which adversely affects the apparent electronic conductivity leading to an increase of the ohmic resistance (R_{ohm}) and the gas transport properties of the electrode.[14]

The wide operating range of SOC-based electrochemical reactors requires robust and durable fuel electrodes with high performance in either operating mode: fuel cell or electrolysis operation. This implies performance and durability in a broad range of partial pressures (pH_2, pH_2O, pO_2, pCO and pCO_2) and a given dimensional stability nearly independent of the atmosphere.

Perovskite-based oxides (ABO_3) have been proposed as alternative materials to the Ni cermets as fuel electrodes for SOCs because of their outstanding stability in both reducing and oxidizing atmospheres and their flexibility in terms of composition, that enables a wide variety of doping elements on their *A*- and *B*-sites to tune their electrocatalytic properties. As a fuel electrode, high catalytic activity can be achieved when the *A*-site is a lanthanide and/or alkaline-earth cation and the *B*-site a transition metal cation such as Mn, Co, Fe, Ni, Cr and Ti.[15]

Strontium titanates have been widely studied and have shown remarkable performance as fuel electrodes in steam electrolysis on the laboratory scale, where the perovskite's surface has been decorated with catalytically active Ni and Fe nanoparticles.[16] It has been reported that surface decoration with catalytically active nanoparticles can be achieved using redox exsolution methods, where a catalytically active metal (*i.e.* Ni or Fe) is incorporated into the crystal lattice of the perovskite backbone under oxidizing conditions and is released (exsolved) on the surface as metal nanoparticles, either by exposure to a reducing atmosphere or by applying a large cathodic overpotential.[17,18] It is generally admitted that exsolution is favoured upon *A*-site deficiency: when the oxygen vacancy concentration is high enough to partially destabilize the perovskite lattice due to the high deficiency on *A*- and *O*-sites, metal particles from the *B*-site exsolve while charge balance of the lattice is maintained.[19] A recent study by Neagu *et al.* about Ni exsolution on lanthanum–calcium doped titanates and lanthanum–cerium doped titanates by *in situ* observation with environmental transmission microscopy (ETEM) showed that the exsolution phenomena and thus the shape of the resulting nanoparticles are significantly affected by the temperature and the oxygen partial pressure (pO_2),[20] being important operating parameters for the rSOC reactors.

Lanthanum chromites present an alternative towards strontium titanates as another perovskite family that can also host *B* cations to be exsolved *in situ* on their surface to enhance the electrocatalytic activity. (La,Sr)(Cr,M)O_3 perovskites (M = Mn, Fe, Co and Ni) have been recently investigated for H_2O electrolysis, CO_2 electrolysis and H_2O–CO_2 co-electrolysis: mostly in stoichiometric formulations[21] and a few with *A*-site deficiency.[17,22] However, the Ni exsolution phenomena on lanthanum chromites upon temperature and atmosphere variation remain unclear, and the performance of such perovskite electrodes still needs to be improved in order to achieve comparable results with the typical Ni-cermet fuel electrodes.

Given the operating conditions of rSOC reactors with a focus on Solid Oxide Electrolysis Cell (SOEC) applications, the lack of Ni exsolution research on chromites arouses the interest to investigate the performance of Ni-decorated chromites as fuel electrodes for SOCs, raising as well the importance to evaluate their durability and performance in either mode on rSOC reactors.

In this paper, we focus on the exploration of the *A*-site deficient chromite $La_{0.65}Sr_{0.3}Cr_{0.85}Ni_{0.15}O_{3-\delta}$ (L65SCrN) fuel electrode decorated with Ni nanoparticles for SOC applications with the aim: (i) of evaluating the Ni exsolution as a function of temperature in $La_{0.65}Sr_{0.3}Cr_{0.85}Ni_{0.15}O_{3-\delta}$ and (ii) of characterizing the electrochemical performance of the screen printed $La_{0.65}Sr_{0.3}Cr_{0.85}Ni_{0.15}O_{3-\delta}$ fuel electrode on a 5 cm × 5 cm ESC in fuel cell operation (SOFC), in H_2O electrolysis and H_2O–CO_2 co-electrolysis operation (SOEC) at high temperature.

Experimental procedures

LSCrN synthesis

$La_{0.65}Sr_{0.3}Cr_{0.85}Ni_{0.15}O_{3-\delta}$ (L65SCrN) and $La_{0.70}Sr_{0.3}Cr_{0.85}Ni_{0.15}O_{3-\delta}$ (L70SCrN) ceramic powders were prepared using the glycine nitrate combustion method described in Sun *et al.*[23] According to these two formulations, stoichiometric amounts of $La(NO_3)_2\cdot 6H_2O$ (99.9% REO Alfa Aesar), $Sr(NO_3)_2$ (98% Alfa Aesar), $Ni(NO_3)_2\cdot 6H_2O$ (98% Alfa Aesar) and $Cr(NO_3)_2\cdot 9H_2O$ (98.5% Alfa Aesar) were dissolved in deionized water and mixed with glycine (J.T.Baker™). The glycine molar ratio for the total content of metal cations was 2 : 1. Next, these solutions were stirred and heated on a hot plate until a dark green-colored gel was formed. Previous thermogravimetric measurements in synthetic air performed on these gels indicated that the solvent evaporation takes place at ~91 °C followed by an exothermic self-combustion reaction at ~220 °C.[21] Therefore, in this study, the gels were heated up to ~220 °C where self-combustion occurred. Finally, the resulting ceramic precursors were calcined in air at a rate of 3 °C min^{-1} up to 1400 °C for one hour since it was the minimal firing temperature at which a perovskite phase could be achieved,[24] which is consistent with previous studies on lanthanum chromites.[25]

Characterization of LSCrN powders

Crystalline structure was investigated using X-ray diffraction (XRD) with a RIGAKU diffractometer operating at 40 kV and 30 mA with a Cu-K$\alpha_{1,2}$ radiation source and a Bragg–Brentano configuration in the range of 2θ from 20–80° with a scanning rate of 0.4° min^{-1}. Crystalline phases were identified from the ICDD database. A different scanning rate of 0.1° min^{-1} was used for the as-prepared and reduced L65SCrN samples, where phases were identified and quantified by Rietveld analyses using the FullProf.2k program suite.

Morphology and microstructure were observed with a scanning electron microscope Zeiss ULTRA PLUS SEM (Carl Zeiss AG, Germany) in combination with energy-dispersive X-ray spectroscopy (EDX) for elemental analysis, where a Bruker XFlash 5010 detector was operated at 125 eV with the Quantax 400 Software. The spatial resolution was ~100 nm and elements with atomic numbers higher than 4 (Boron) could be detected.

Surface chemistry investigations with X-ray photoemission spectroscopy (XPS) were carried out using a system with a base pressure of 2 × 10^{-10} mbar, with a hemispherical analyzer (ESCALAB250, ThermoFisher Scientific) and a monochromated Al Kα source with an X-ray energy of 1486.74 eV (XM1000, ScientaOmicron). The peak shape analysis was carried out with Unifit 2013, applying convoluted Gaussian/Lorentzian profiles and a Shirley background function.[26–28] The surface stoichiometry of the occurring atoms/signals was calculated using the numerically fitted peak areas, photoionization cross sections reported by Yeh and Lindau[29] and instrumental transmission functions given by the manufacturer.

The reducibility of the as-prepared L65SCrN and L70SCrN powders was characterized by means of thermogravimetric analysis (TGA) in a reducing atmosphere (5% H_2–Ar) with the analyzer Netzsch Jupiter 449C at a heating rate of 3 °C min^{-1} from 25 °C to 1200 °C. Such reducibility analysis by TGA was accompanied by a temperature-programmed reduction (TPR) performed on the flow-through quartz reactor TPDRO 1100 (Thermo Scientific, Italy), in which L65SCrN and L70SCrN powder specimens were introduced using quartz glass wool as a support. A thermocouple (type K) was placed in a thin quartz glass tube next to the specimen to monitor the temperature. The oven temperature was monitored and controlled by another thermocouple. The specimens were pretreated in the reactor tube with flowing Ar gas at a flow rate of 20 mL min^{-1} and by heating at a rate of 10 °C min^{-1} from 30 °C to 150 °C with a holding time of 60 min. After cooling the specimen back to 30 °C, the TPR process was initiated with a reducing gas mixture of 5% H_2–Ar at a constant flow rate of 20 mL min^{-1} and a heating rate of 5 °C min^{-1} from 30 °C to 1000 °C with a holding time of 60 min at 1000 °C. Under these conditions, the sample temperature was ~1000 °C while the oven temperature was 1100 °C. The exhaust gas from the reactor was analyzed using a Thermal Conductivity Detector (TCD).

Cell manufacturing

The L65SCrN electrocatalyst was implemented as fuel electrode into an electrolyte-supported cell (ESC) by screen printing, using a commercial square substrate (5 cm × 5 cm and 90 µm of thickness) of 3 mol% Y_2O_3-doped ZrO_2 electrolytes double-side coated with *ca.* 5 µm of $Ce_{0.8}Gd_{0.2}O_{2-\delta}$ (CGO20-3YSZ-CGO20) from Kerafol GmbH, Germany. The fuel electrode ink was prepared by dispersing the L65SCrN powder in a solution (94 wt% α-Terpineol and 6 wt% ethyl cellulose) with a powder to solution ratio of 2 : 1, followed by mixing with the 3-roll milling machine EXAKT 80E EL. The prepared ink was printed on the electrolyte using the screen printer Aurel model 900 (Aurel automation s.p.a, Italy). The half-cell was fired at 1200 °C for 1 hour in air with a heating rate of 3 °C min^{-1}. Afterwards, the oxygen electrode was printed on the other half of the cell with a commercial ink of $La_{0.58}Sr_{0.4}Fe_{0.8}Co_{0.2}O_{3-\delta}$ (LSCF). The printed area for both electrodes was 16 cm^2 (4 cm × 4 cm). Platinum paste was brushed on the sintered fuel electrode surface for current collection. Finally, the cell was fired at a rate of 3 °C min^{-1} to 1050 °C in air and held for one hour.

Electrochemical characterization

The electrochemical performance of the L65SCrN fuel electrode in the ESC architecture was studied on the test bench described elsewhere.[24] The fuel electrode was contacted with a platinum mesh and the oxygen electrode with a gold mesh. A gold frame was used as a sealant between the fuel and the air side. For commissioning, the cells were heated (3 °C min^{-1}) to 900 °C with N_2 (1 SLPM) and air (1 SLPM) for sealing purposes and subsequently reduced with H_2 (1 SLPM) for 1 hour on the fuel side. Afterwards, the operating temperature was adjusted to 860 °C. Electrochemical experiments were carried out in different fuel gas mixtures shown in Table 1. The equilibrium gas phase compositions and the theoretical OCV according to the Nernst voltage were calculated with the software CANTERA.[30]

Electrochemical Impedance Spectroscopy (EIS) was performed in galvanostatic mode with the workstation Zahner PP-240 in a frequency range from 50 mHz to 100 kHz. The amplitude of the current stimulus was 500 mA. Distribution of relaxation times (DRT) calculations were carried out with the impedance analysis and modelling software ec-idea[31] and the equivalent circuit model-fit of the impedance data with the commercially available program ZView®.[32]

In fuel cell (FC) mode, the polarization curves (*i*–*V*) were measured from OCV to 0.8 A cm^{-2} at a rate of 0.012 A s^{-1} and in electrolysis (EC) and co-electrolysis (co-EC) modes from OCV to −1.0 A cm^{-2} at a rate of −0.012 A s^{-1}. For all operating modes the total fuel gas flow was maintained at 1 SLPM, except for co-EC, which was kept at 0.8 SLPM.

Results and discussion

A comparative assessment towards LSCrN reducibility and Ni exsolution was performed between stoichiometric L70SCrN and *A*-site deficient L65SCrN perovskite powder samples. Furthermore, the temperature effect on the Ni exsolution was investigated on the L65SCrN and the electrochemical performance was evaluated in a full cell assembly with an ESC architecture, in which the L65SCrN perovskite was implemented as fuel electrode.

Nickel exsolution assessment on LSCrN powders

Phase identifications of both the as-prepared ceramic powders L70SCrN and L65SCrN, as well as in reduced conditions (with 5% H_2–Ar at 3 °C min^{-1} from 25 °C to 1200 °C) were performed by XRD in order to verify that the perovskite phase was stable after the reduction treatment. X-ray diffractograms of the L70SCrN before and after reduction are shown in Fig. 1. No NiO secondary phase or other impurities could be identified. Interestingly, no metallic Ni could be detected on the reduced L70SCrN sample as one may have expected upon reduction. However, a few nanoparticles could be observed in the SEM image of the reduced L70SCrN powder in Fig. S1† in the ESI. This suggests that the total amount of metallic Ni in the reduced L70SCrN (originating from the reduction of a possible NiO secondary phase as well as from the likely to occur exsolution of metallic Ni upon reduction of the host perovskite) remained below the detection level of the XRD analysis, *i.e.* a phase content of less than 1 wt%.

Table 1 Molar composition at the inlet of the fuel gas for the different operating modes

Operation mode	% H_2	% H_2O	% CO_2
FC	90	10	—
FC-EC	50	50	—
EC	20	80	—
Co-EC	5	63.7	31.3

In contrast, secondary phases could be identified for L65SCrN in both the as-prepared and reduced samples (Fig. 2a and b). Therefore, Rietveld analyses were performed with the aim of quantifying those secondary phases. An orthorhombic lattice (space group 62, Laue class mmm) was calculated for the as-prepared L65SCrN sample with parameters to be $a = 5.496$ Å, $b = 5.450$ Å, $c = 7.737$ Å and $V = 231.762$ Å^3. A secondary phase was identified as nickel oxide (NiO) with cubic lattice (space group 225, Laue class *m*3*m*) and lattice parameters $a = 4.176$ Å and $V = 72.851$ Å^3. Although the NiO content was 4.22 mol%, it was not considered to be a detrimental impurity since it would be reduced *operando* into metallic Ni, being also catalytically active and electronically conductive.

For the reduced L65SCrN sample, an expanded orthorhombic lattice (also space group 62, Laue class mmm) was calculated ($a = 5.465$ Å, $b = 7.758$ Å, $c = 5.506$ Å and $V = 233.409$ Å^3). A secondary phase of metallic Ni was calculated to be 4.83 mol% with a cubic lattice (space group 225, Laue class *m*3*m*) with $a = 3.524$ Å and $V = 43.761$ Å^3, from which the metallic Ni characteristic peak (111) was identified at 44.4°. This corroborates that metallic Ni can be achieved upon exposure of L65SCrN to a reducing atmosphere at high temperatures. It is pertinent to note that the amount of metallic Ni after reduction

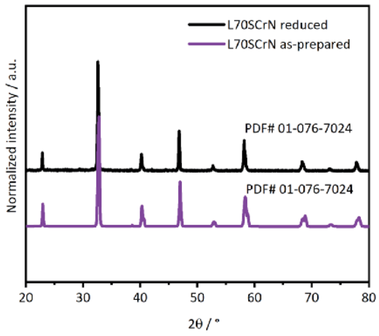

Fig. 1 XRD patterns of the as-prepared L70SCrN powder and reduced in 5% H_2–Ar up to 1200 °C at 3 °C min^{-1}. Crystal systems were identified with ICCD as the perovskite chromite phase: PDF# 01-076-7024.

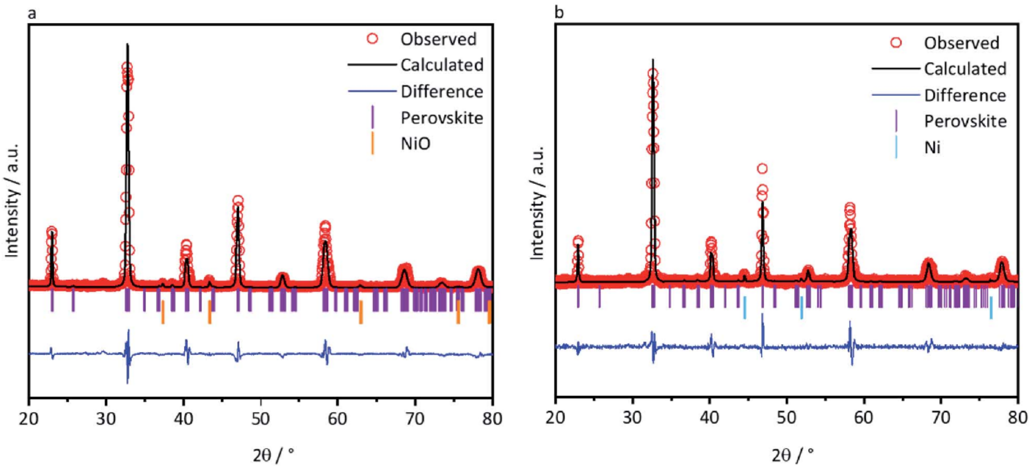

Fig. 2 XRD patterns of the as-prepared L65SCrN powder (a) and reduced (b) in 5% H_2–Ar up to 1200 °C at 3 °C min^{-1}. Crystallographic parameters and the concentration of secondary phases were calculated from Rietveld refinement.

(4.83 mol%) is greater than the content of NiO (4.22 mol%) in the as-prepared sample, indicating that the metallic Ni has been effectively exsolved from the L65SCrN matrix under these reducing conditions. The characteristic peak of the perovskite at 47.2° shifted slightly to a lower diffraction angle (46.9°), which corresponds to an expansion of the perovskite orthorhombic lattice (from 231.762 Å^3 to 233.409 Å^3). This expansion could be due to the loss of Ni^{2+} cations from the lattice that are reduced to Ni^0 and exsolved on the surface in correlation with the consumption of vacancies on the *A*-site, but also due to the oxygen loss.[33,34] A change in the Cr^{4+}/Cr^{3+} ratio in the host perovskite matrix could also contribute to this expansion, taking into account that the ionic radius in an octahedral environment for Cr^{4+} is 0.55 Å and for Cr^{3+} is 0.615 Å.[35] To better assess this, the as-prepared and reduced L65SCrN powders were also investigated by means of XPS.

At first, the XPS studies could not conclusively confirm the presence of a metallic nickel phase in the reduced L65SCrN sample. As the typically used signal of the Ni2p electrons overlaps with the very distinct 3d signals of Lanthanum of an unusual quadruplet shape, the deconvolution of the traces of metallic nickel was not possible this way. Similar to Nenning and Fleig,[25] the Ni3p region was used (Fig. 3a), which also partially overlaps with the Cr3s signal, but the chemical structure of the surface chromium could be evaluated by means of the Cr2p signal (Fig. 3b) and added as boundary to the numerical model for the nickel 3p region, with its low cross section. While it was possible to identify two occurring Ni species in both the as-prepared and reduced L65SCrN samples, which are attributed to oxidic Ni^{2+} (~67.2 eV) and surface $Ni(OH)_2$ (~69.6 eV),[36] the clear evidence for a Ni^0 species is lost in the signal noise. However, the signal deconvolution, which was performed using the aforementioned chromium signature and a fixed Lorentzian peak width for the as-prepared sample, converged to a result with Gaussian line widths of 2.2 eV (Ni^{2+}) and 2.6 eV ($Ni(OH)_2$), which correspond to the overall findings of broader signals for the latter. For the reduced sample, it converged to Gaussian linewidths of 3.0 eV (Ni^{2+}) and 2.2 eV ($Ni(OH)_2$) – which has to be considered a false solution, due to the resulting linewidths. The deconvolution with three components, Ni^{2+}, $Ni(OH)_2$ and Ni^0, however, could not be calculated successfully. The accuracy of the peak fit, which relies on the data quality, may be argued, but the indirect indicator supports the findings from the XRD evaluation.

It has to be noted that the high surface sensitivity of this method might misguide the interpretation if not considered. The information depth, *i.e.* 3λ, where λ is the escape depth of the relevant electrons, is below 10 nm,[37] which means that only the topmost surface of the crystallites is visible to this method. This surface sensitivity may also explain the presence of $Ni(OH)_2$ that can easily form on top of the nickel exsolved surface particles.[38]

The nickel ratio was calculated with the Ni3p signal for the as-prepared and reduced samples. The concentration of nickel on the surface was 11.2 at% for the as-prepared sample and 3.8 at% for the reduced sample (Table 2). These results, which may seem surprising at first, could be explained by an agglomeration of surface nickel in nanoparticles upon reduction. Since their typical particle size (Fig. 3d) is larger than the information depth, that is less than 10 nm, they may not be fully probed by XPS. This is an important finding because this suggests that nickel on the surface of the L65SCrN sample changes its distribution, one can expect homogeneous on the surface of the as-prepared perovskite, to a more heterogeneous distribution where nickel is agglomerated and likely concentrated into nanoparticles during reduction. This indicates that the top surface of the perovskite after reduction tends to be depleted in nickel, yielding an overall reduction of the nickel concentration on the surface of the material analyzed by XPS.

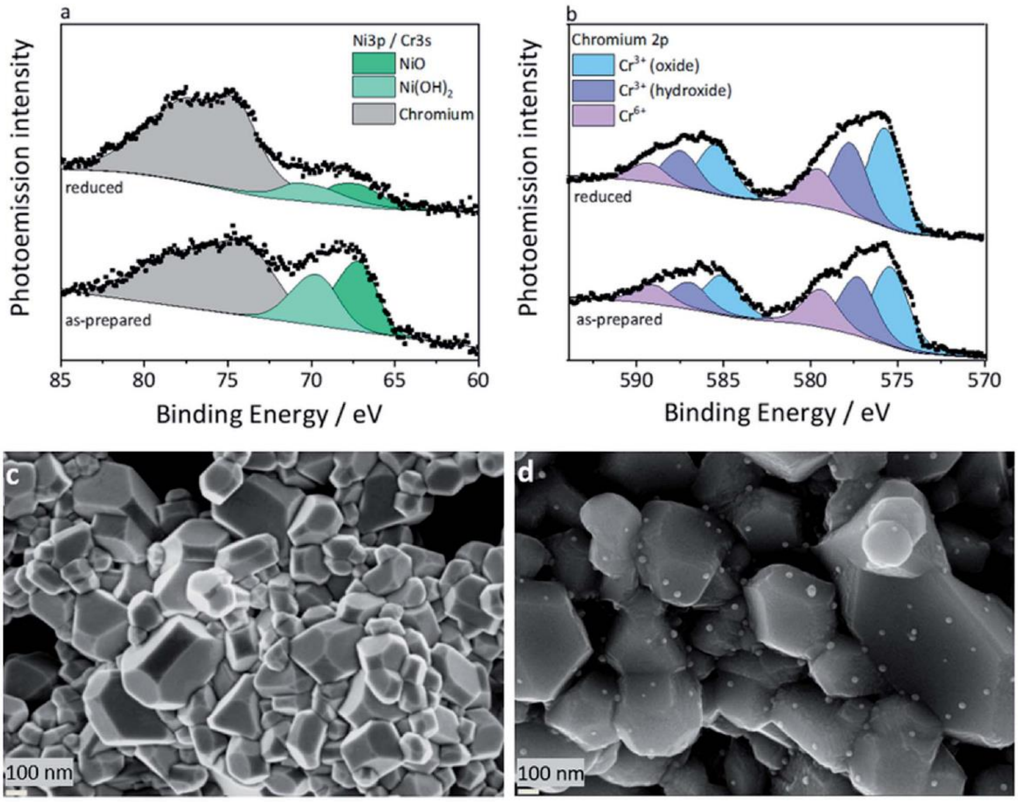

Fig. 3 (a) Photoemission (XPS) spectra of the overlapping nickel 3p and chromium 3s region. The chromium signature was fed into the model based on the data obtained from more distinct chromium 2p signals shown in (b). The linewidth of the NiO peak fit of the reduced sample reveals that an additional (metallic) nickel component at ~65 eV on the surface of the reduced sample may be hidden, but could not be resolved. (b) Photoemission spectra of the chromium 2p region. Possible Cr^{4+} cannot be distinguished from the predominant oxidic Cr^{3+}. (c) SEM image of the as-prepared L65SCrN powder sample and (d) reduced L65SCrN powder sample (subjected to a thermal treatment with 5% H_2–Ar at a ramp of 3 °C·min^{-1} from 25 °C to 1200 °C). Both (c) and (d) powder samples were analyzed by XRD and XPS.

Table 2 Atomic percentages of surface species, calculated from the photoemission spectra

Surface species	As-prepared	Reduced
Cr^{3+} (oxide)	10.7 at%	14.2 at%
Cr^{3+} (hydroxide)	7.8 at%	10.3 at%
Cr^{6+}	5.2 at%	5.4 at%
Ni3p (total)	11.2 at%	3.8 at%

The ratio between the surface states of chromium was determined by a peak fit of the Cr3p region. The separated components were identified, according to systematic studies by Biesinger *et al.*,[39] to be Cr^{3+} (oxide) at ~575.7 eV, Cr^{3+} (hydroxide) at ~577.6 eV, and Cr^{6+} at 579.5 eV. A Cr^{4+} state, as a possible cause for the observed change in lattice parameters, has been discussed in earlier works on LSCr perovskites,[40] but cannot be distinguished with this method due to the very close binding energies of Cr^{3+} and the anomalous Cr^{4+}.[41,42] Considering the inherent surface sensitivity of photoemission spectroscopy, the bulk properties of the investigated perovskite crystallites are not accessible anyway, and the surface states of chromium are not relevant to the lattice parameters. However, the surface stoichiometry (Table 2) of these chromium species can give indirect insight. The reduced L65SCrN sample shows an abundance of surface Cr^{3+} (both oxidic and hydroxide), which would be consistent with the mentioned lattice expansion observed by XRD (Fig. 2).

In order to better understand and highlight the role of the *A*-site deficiency in the Ni exsolution, TGA and TPR were performed in a reducing atmosphere (5% H_2–Ar) on the as-prepared L70SCrN and L65SCrN powders. Since no other volatile species or compounds are expected to be formed during such thermal treatments, the net weight loss measurement by TGA is attributed to the net loss of oxygen, assuming that the oxygen from the perovskite lattice (and from the NiO secondary phase) reacted with hydrogen to form H_2O.[34] The TGA and TPR profiles are shown in Fig. 4a and b, respectively. In Fig. 4a, the maximum onset for weight loss, corresponding to the maximum value of the derivate ($\mathrm{DTG_{Max}}$), occurs at 442 °C for L65SCrN and at 472 °C for L70SCrN.

The main peaks in the TPR profiles (Fig. 4b) occur at 431 °C and 474 °C for L65SCrN and L70SCrN, respectively. These values are in good agreement with the maxima of the TGA derivatives considering the difference of these measurements such as temperature increment. One should point out that these maxima are in the temperature range where phase transitions are expected to take place during the reduction of the perovskite.[43] Along the temperature range of the TGA measurement (until 1200 °C), the total weight losses were 1.94 wt% for L70SCrN and 2.72 wt% for L65SCrN. Assuming that the NiO secondary phase (4.22 mol%) of the L65SCrN powder was fully reduced over the thermal treatment, it accounts for 0.04 wt% losses in the TGA experiment, yielding a net weight loss of 2.68 wt% for L65SCrN. Interestingly, both perovskites showed a continuous weight loss above 600 °C at a comparable rate, since the gap between the corresponding signals of the two phases remained at ~0.78 wt%. For the specific case of L70SCrN, this evolution contrasts with the observation reported by Sun *et al.*[44] This suggests a continuous evolution of the exsolution process upon temperature increase under reducing conditions. Considering SOC operation, this observation is of particular interest if temperature variations during operation are considered. From the TGA results, the oxygen deficiencies (δ), which are related to the oxygen vacancy concentration, were calculated using the method described by Myung *et al.*[18] Upon reduction, an ABO_3 perovskite loses oxygen turning to the $ABO_{3-\delta}$ form with a corresponding change of mass from m_{ABO_3} to $m_{ABO_{3-\delta}}$. Since the quantity of perovskite moles is conserved, it is possible to assume the following relation:

$$n_{\text{total}} = \frac{m_{ABO_3}}{\mathrm{MW}_{ABO_3}} = \frac{m_{ABO_{3-\delta}}}{\mathrm{MW}_{ABO_{3-\delta}}} \tag{1}$$

where MW_{ABO3} and $\mathrm{MW}_{ABO3-\delta}$ are the molecular weights of the as-prepared and reduced perovskite samples, respectively. This expression can also be written in terms of the atomic weight of oxygen A_{O} as:

$$n_{\text{total}} = \frac{m_{ABO_3}}{\mathrm{MW}_{ABO_3}} = \frac{m_{ABO_{3-\delta}}}{\mathrm{MW}_{ABO_3} - (\delta A_{\mathrm{O}})} \tag{2}$$

Knowing that the weight loss measured by TGA is given by:

$$\Delta m = \frac{m_{ABO_3} - m_{ABO_{3-\delta}}}{m_{ABO_3}} \tag{3}$$

Eqn (2) and (3) could be arranged in terms of the net oxygen mass loss, *i.e.* oxygen deficiency δ (mol O/mol ABO_3) generated upon reduction such as:[18]

$$\delta = \frac{\mathrm{MW}_{ABO_3}}{A_{\mathrm{O}}} \Delta m \tag{4}$$

For the cases of L65SCrN and L70SCrN, *i.e.* with Ni cations on the *B*-site that can be reduced and forced out of the lattice, the reduction and exsolution processes of nickel will result in a consumption of the oxygen vacancies, so that it is not possible to relate directly net oxygen mass loss to oxygen deficiency. Nonetheless, though the initial oxygen stoichiometry was not determined in each of the compounds, a net specific oxygen consumption δ_{O} can be calculated in analogy with eqn (4). Therefore, by considering the net weight losses of 1.94 wt% and 2.68 wt%, the net oxygen consumption for each perovskite was calculated to be $\delta_{\mathrm{O}}(\text{L70SCrN}) = 0.27$ (mol O/mol L70SCrN) and

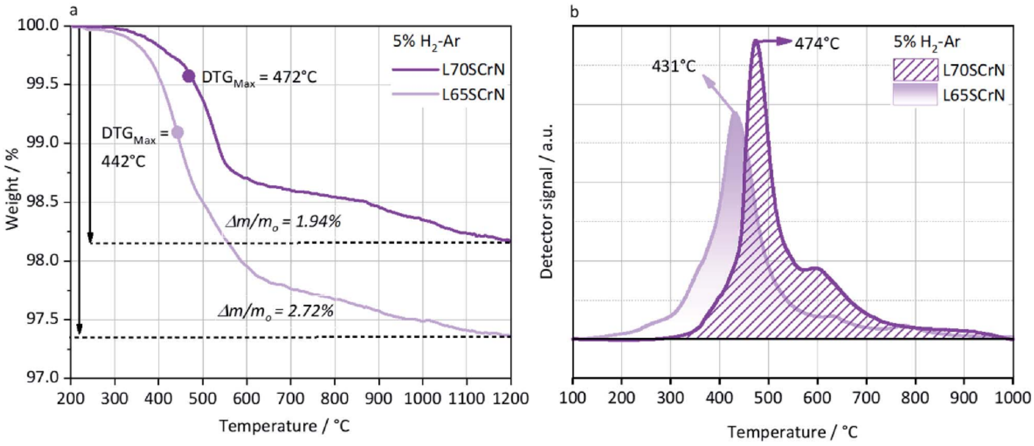

Fig. 4 (a) TGA of L65SCrN and L70SCrN in 5% H_2–Ar up to 1200 °C at 3 °C min^{-1}. The maximum of the derivative function, *i.e.* where the mass loss kinetics is the fastest was calculated and is indicated by the DTGMax. (b) TPR of L65SCrN and L70SCrN in 5% H_2–Ar up to 1000 °C at 5 °C min^{-1}.

δ_O(L65SCrN) = 0.36 (mol O/mol L65SCrN) for L70SCrN and L65SCrN, respectively. The significant difference in the net specific oxygen consumption upon reduction between L65SCrN and L70SCrN suggests that the *A*-site deficiency enhances the reducibility of the LSCrN, which seems to favor the exsolution of metallic Ni. To better understand the influence of the temperature and time on the formation of metallic nickel, the Ni nanoparticles' morphology was investigated in two isothermal reducing treatments: below and above 600 °C. These treatments were performed on L65SCrN since it showed superior reducibility and are explained and detailed in the following section.

Influence of the temperature on the Ni exsolution on L65SCrN

L65SCrN powder samples were exposed to pure hydrogen at different temperatures. For comparison, powder samples were annealed in hydrogen at either 500 °C or 900 °C for an annealing time of 3 hours. After reduction, the presence of the metallic Ni concomitant with the perovskite phase was confirmed in the XRD patterns (Fig. 5). However, the presence of impurity traces such as SrO_2 and La_2O_3 could also be noted for the reduced samples and traces of $Sr_3(CrO_4)_2$ for the as-prepared sample. SEM imaging of the two powder samples, *i.e.* L65SCrN reduced at 500 °C for 3 hours and L65SCrN reduced at 900 °C for 3 hours, revealed different morphologies (Fig. 6). For the L65SCrN sample reduced at 500 °C for 3 hours, one can observe spherical well-dispersed nanoparticles on the perovskite surface of a diameter of ~8 nm (Fig. 6a, surface type **1**) to ~30 nm (Fig. 6a, surface type **2**). The presence of the nanoparticles is correlated with a local enrichment in nickel which suggests that those nanoparticles are very likely made of metallic nickel. These observations are detailed in the ESI, in Fig. S2 and S3.† The corresponding EDS maps of Ni and Cr are shown in Fig. S4 and S5† respectively. Interestingly, it could be suggested that the exsolution of Ni nanoparticles on the surface of the perovskite grains may depend on the crystallographic orientation: surfaces denoted by type 1 appear to have qualitatively higher Ni nanoparticle density than type 2 surfaces (Fig. 6a). Though it was not possible to determine the specific crystallographic orientations of those surfaces, this strongly suggests that exsolution of nanoparticles is influenced by the surface characteristics of the perovskite grains. This is in agreement with the observations made on titanates by Neagu *et al.* as they found that during exsolution the particles remained socketed in the [110] crystallographic orientation with respect to the perovskite lattice, which is one of the key structural features that provides exsolved nanoparticles their stability.[20] Such an orientation relationship is in accordance with previous reports, whereby the diffusion direction for *B*-site cations in perovskite lattices is along the [110] orientation.[19,20,15] On the L65SCrN sample reduced at 900 °C for 3 hours coarser Ni nanoparticles of an irregular shape of ~30 nm up to 100 nm could be observed (Fig. 6b). Such nanoparticle growth is consistent with the observations made in the corresponding XRD pattern (red pattern in Fig. 5) that reveals a more intense Ni characteristic peak. A closer inspection of the different surfaces could not reveal a variation in nanoparticle density, which appears qualitatively lower than the one on the sample reduced at 500 °C. This lower particle density on the surface of the perovskite and their coarser particle size suggest a growth mechanism of the Ni nanoparticles that takes place upon temperature increase.

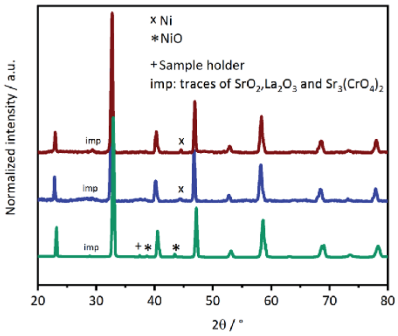

Fig. 5 XRD patterns of the as-prepared L65SCrN powders (green pattern) reduced in H_2 at 500 °C for 3 hours (blue pattern) and reduced in H_2 at 900 °C for 3 hours (red pattern). The host chromite perovskite phase was identified with the PDF #01-076-7024 for all three patterns.

This is in good agreement with the observation made by Jo *et al.* on Co exsolved nanoparticles on strontium titanates, where the average grain size increased while the Co nanoparticle density decreased.[46]

Comparable observation of Ni coarsening on chromites was reported by Sauvet *et al.* after methane reforming experiments on *A*-site stoichiometric $La_{0.70}Sr_{0.3}Cr_{0.95}Ni_{0.05}O_{3-\delta}$ between 750–850 °C.[47] Kobsiriphat *et al.* attempted to explain Ni and ruthenium nucleation in the chromites $La_{0.8}Sr_{0.2}Cr_{0.69}Ni_{0.31}O_{3-\delta}$ and $La_{0.8}Sr_{0.2}Cr_{0.82}Ru_{0.18}O_{3-\delta}$ under reduction in dry hydrogen at 800 °C for different times.[48] They observed that the Ni nanoparticles had coarsened significantly from a particle size of ~10–15 nm (after 3 hours) to an average hemisphere diameter of 50–60 nm after 311 hours of reduction. In contrast, for the Ru-doped chromite after 311 hours of reduction at 800 °C, there was no significant change in the Ru nanoparticles since their size did not exceed 10 nm. From these observations and by analogy to thin-film nucleation, they concluded that particle coarsening may be due to a fast surface diffusion, which would allow nuclei to be fed by adatoms yielding larger and more widely spaced nuclei.[48] Therefore, they suggested that the faster Ni particle coarsening was likely explained by larger Ni surface diffusivities in comparison to Ru on the chromite, although quantitative data on chromites are not available.[48] This would be consistent with the above-mentioned observations made on the nickel concentration determined by XPS on the surface of the as-prepared and reduced L65SCrN samples. Such high surface diffusivity was highlighted by Sakai *et al.*, who investigated the chromium diffusion in lanthanum chromites between ~700–1400 °C by ^{50}Cr tracer diffusion and secondary ion mass spectrometry (SIMS).[19] They estimated that independently of the temperature, the grain boundary diffusion coefficient was 10^5 times larger than the bulk diffusion coefficient.[49] Interestingly,

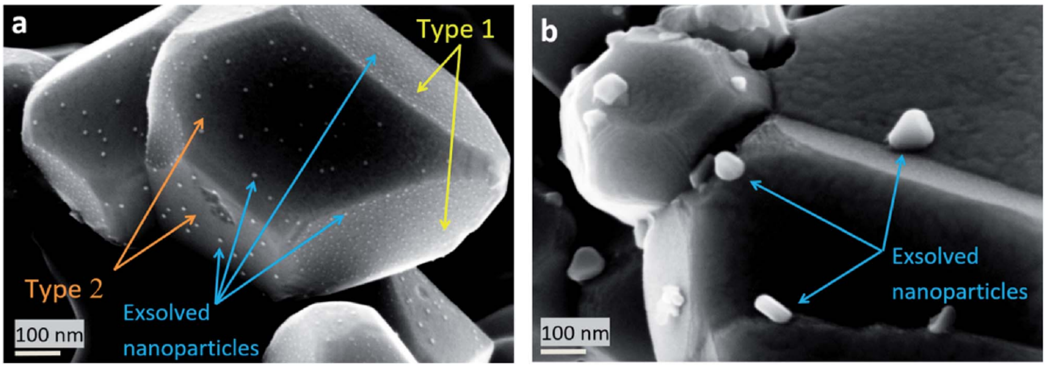

Fig. 6 SEM images of Ni exsolution after 3 hour treatment under a H_2 atmosphere at (a) 500 °C and (b) 900 °C.

this behavior has also been observed in other perovskite families, such as strontium titanates $SrTi_{0.75}Co_{0.25}O_{3-\delta}$, where exsolved Co particles diffuse onto the existing Co nanoparticles rather than nucleating in new locations at the grain boundaries, due to the increment of Co diffusivity at high temperatures (above 700 °C). In this case, the distances between the particles previously nucleated are assumed to be shortened.[46] Another interesting observation was made by Kousi *et al.* on $La_{0.7}Ce_{0.1}Co_{0.3}Ni_{0.1}Ti_{0.6}O_{3-\delta}$ (LCCNT) where they identified different sizes on the exsolved Ni–Co nanoparticles in the bulk as compared to the ones exsolved on the surface: the bulk particles were smaller (~10 nm) than the ones exsolved on the surface ~40 nm, noting as well that on the bulk the nanoparticle population was significantly higher. These conjectures were made based on a SEM cross-section evaluation, where it is possible to identify the surface and the bulk.[50]

Moreover, it is possible to correlate the differences in the observed Ni exsolution morphologies at 500 °C and 900 °C upon reduction (Fig. 6) with the formation of oxygen vacancies, since the exsolution is favored when these vacancies reach a high concentration.[19] The formation of oxygen vacancies upon reduction may take place either in a surface site or in a bulk site.[51] It has been claimed that there is a strong correlation between the bulk and the surface kinetics, which indicates that not only the oxygen vacancy concentration but also pO_2 plays a significant role in the surface exchange processes in mixed ionic and electronic conductors (MIEC) such as chromites.[52]

Another approach was made by Gao *et al.* who investigated Ni exsolution phenomena on a Sc-based *A*-site deficient perovskite $La_{0.4}Sr_{0.4}Sc_{0.9}Ni_{0.1}O_{3-\delta}$ (LSSN) at different temperatures and annealing times. They proposed that Ni exsolution could be considered as a chemically driven heterogeneous phase transformation, being a consequence of four physical processes: diffusion, reduction, nucleation and growth. They found that the nucleation is affected by: mechanical stresses, related strains on the perovskite lattice, metallic Ni wetting angles, and *A*-site and oxygen vacancies. These factors significantly determine where the nucleation would take place. Moreover, parameters such as the atmosphere (*e.g.* pO_2 and pH_2), annealing time and temperature may affect the particle growth.[53]

In the case of *A*-site dopant diffusion, a study carried out on manganite-based perovskite oxides, $LnMnO_3$, demonstrated that the surface oxygen vacancy attracts the dopant (that partially substituted the host on the *A*-site) driving it to the surface on the host sublattice.[33] It has been assessed by DFT (density functional theory) that the elastic and electrostatic interactions of the dopant with the surrounding lattice are driving forces for dopant segregation on perovskite compounds. The factors that may affect these driving forces are the dopant size, the lattice parameter, and the distribution of charged vacancies.[33] However, the diffusion phenomenon from the segregating cations should be carefully studied since the surface composition depends both on thermodynamics and kinetics,[33] which could be also the case for the *B*-site dopant diffusion in other perovskite systems.

Regarding L65SCrN in the present study, it is unclear how the Ni enrichment on the surface originating from the bulk may occur. If we consider the assumption by Gao *et al.* that the mass transport process during the Ni exsolution is critical for the particle growth, it is likely that such growth results from the Ni^{2+} ion diffusion followed by the reduction reaction to metallic Ni, which may be limited by two possible models: mechanical energy effects (as a function of the strain activation energy) or limited Ni supply.[53] They found that the Ni particles preferably nucleate on the surface rather than in the bulk due to their tendency to decrease the strain activation energy.[53] Using DFT calculations, they concluded that these models are likely to represent the actual Ni exsolution mechanism on LSSN. This contrasts with the observations reported on lanthanum titanate-based fuel electrodes for which the particle – substrate interaction prevails and thus stabilizes the Ni exsolved nanoparticles on the surface in the temperature range between ~650–900 °C in reducing atmospheres.[20] For instance, Neagu *et al.* observed directly the Ni exsolution process by ETEM on two different compositions with widely different content of exsolvable Ni: $La_{0.43}Ca_{0.37}Ti_{0.94}Ni_{0.06}O_3$ and $La_{0.8}Ce_{0.1}Ti_{0.6}Ni_{0.4}O_3$. They found that the location of the particle-socket did not change during the timescale of the experiment, indicating that the nanoparticle was locked/socketed in place once it was formed (exsolved).[20] More precisely, they found during the experiment that additional particles formed within the nanoscale proximity of the first ones but neither of them moved nor drifted under the environmental transmission microscope (ETEM) electron beam. This revealed that particle–support interactions are strongly dominant over particle–particle interactions for titanates.[20] Contrary to the case of lanthanum chromites, particle–particle interaction prevails at high temperatures.

Although lanthanum titanates do not seem to exhibit the same behavior as strontium titanates, lanthanum scandates or lanthanum chromites towards Ni particle growth, recent studies highlighted that for perovskite oxide-based electrocatalysts, there is a strong influence of the gas atmosphere, *i.e.* pO_2 in correlation with the temperature, on the shape of the exsolved nanoparticles,[20,25] which is susceptible to affect their electrocatalytic performance.

In this study, the reduction of L65SCrN at low temperatures (~500 °C) yielded the finest and well-dispersed Ni exsolved nanoparticles. Such operating conditions are still far below from the typical operating temperatures ($T > 800$ °C) of ESC in SOC applications. Since it is shown that Ni particle–particle interactions prevail at high temperature in chromites, yielding particle coarsening, it is an important aspect to consider for the implementation of L65SCrN as a fuel electrode into a SOC stack because it may affect the morphological stability of the reactive surfaces. Possibly, the Ni exsolved particle size could be optimized with a rigorous investigation on the Ni exsolution phenomena in these *A*-site deficient chromites. Synthesis and processing parameters may also play a significant role: porous structures may be one key factor for Ni exsolution.[53] For a better understanding, additional investigation of the Ni concentration profiles across the perovskite grains upon reduction as well as the Ni particle size evolution as a function of temperature, annealing time, gas atmosphere, grain size and porosity would be necessary, *e.g.* by TEM and TOF-SIMS, accompanied by DFT modeling.[33,46,53]

Therefore, it is questionable how stable a L65SCrN electrocatalyst may perform at the stack level since pO_2 gradients are usually observed along the gas channels: for instance, high pH_2 at the inlet and high pH_2O at the outlet are characteristic of FC operation, while in EC mode high pH_2O at the inlet and high pH_2 at the outlet are typical (assuming high fuel and steam utilizations for both modes). Moreover, reversible operation (FC-EC) would expose the electrocatalyst alternatively to pO_2 gradients.

In the following section, we focus on the electrochemical performance of cells with the L65SCrN fuel electrode upon variation of the operating conditions.

SOC electrochemical performance with the L65SCrN electrocatalyst as a fuel electrode

The electrochemical performance of a full cell with an ESC architecture and a L65SCrN fuel electrode has been evaluated in FC, FC-EC, EC and co-EC modes as described in Table 1.

Performance evaluation in FC, FC-EC and EC operation

The measured open circuit voltage (OCV) was 1.25 V at 900 °C with pure H_2/air, demonstrating appropriate gas tightness of the sealing. For the three different operating modes, the measured OCV was slightly above (~20 mV) the theoretical Nernst potential E:[54]

$$E = E^0 + \frac{RT}{4F}\ln pO_2 + \frac{RT}{2F}\ln\frac{pH_2}{pH_2O} \tag{5}$$

Such a difference was assigned to a deviation of the inlet gas composition due to inaccuracy of the steam supply mass flow control.

Polarization curves at 860 °C in fuel cell (FC), reversible (FC-EC) and electrolysis (EC) operation are shown in Fig. 7a. In FC mode, *i.e.* with a 90% H_2–10% H_2O fuel gas mixture, the oscillations observed find their origin in pH_2O fluctuations from the steam supply due to marginal operation. In reversible mode FC-EC, *i.e.* with a 50% H_2–50% H_2O fuel gas mixture, the *I–V* characteristics evolve continuously from either side of the OCV which reflects the reversible functionality of the full cell and thus the L65SCrN electrocatalyst in either mode.

In EC mode, with a 20% H_2–80% H_2O fuel gas mixture, the *I–V* characteristics show a nearly linear evolution from OCV until an inflection point which corresponds to the thermoneutral voltage of steam electrolysis (~1.29 V).[3] Above this value, the slope of the polarization curve decreases yielding a curve flattening. This is explained by the exothermal nature of the steam electrolysis at higher cell voltages, causing a net heat production. Since the oven of the test bench was operated isothermally, this heating effect cannot be controlled at the cell level causing a net increment of the temperature and enhancing the electrode reaction kinetics.[3]

EIS data recorded near OCV conditions are shown in the Nyquist Plot of Fig. 7b. The ohmic resistance R_{ohm} is estimated to be 0.47 Ω cm^2 with 10% H_2O, 0.46 Ω cm^2 with 50% H_2O, and 0.45 Ω cm^2 with 80% H_2O, suggesting a sensitivity of this parameter to pH_2 and thus pO_2 in the feed gas. As a p-type conductor, this increment of R_{ohm} upon increase of pH_2 could be explained by a decrease of the conductivity in L65SCrN, since the positively charged oxygen vacancies that are created upon reduction hinder the transportation of electrical holes,[55] and decrease the effect of the alkaline earth doping on the electrical conductivity of lanthanum chromites.[56] However, it is important to note that the ohmic resistance values are comparable with commercial ESC references, since they are slightly lower than that for a state-of-the-art Ni-CGO fuel electrode tested also at 860 °C with an estimated value of 0.55 Ω cm^2.[3]

At low frequencies, *i.e.* below 1 Hz, the EIS data were scattered due to the small voltage variations induced by fluctuations in the steam supply, which made difficult to determine accurately the total area specific resistance from these spectra. Therefore, the total area specific resistance ($\text{ASR}_{\text{DC\_Total}}$) was calculated as the slope from the polarization curves at ±0.3 A cm^{-2} (linear range) where the influences of gas conversion and concentration polarization are expected to be minimal.

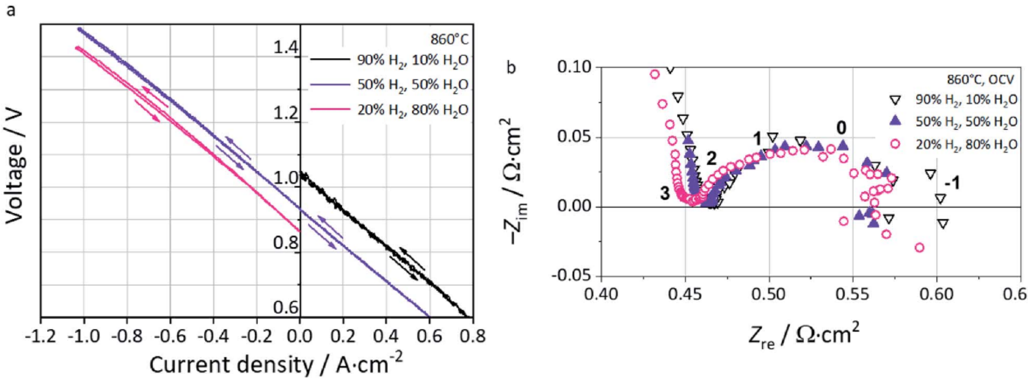

Fig. 7 (a) Polarization curves at 860 °C in FC, FC-EC and EC modes. (b) Nyquist plot at OCV for fuel gas compositions 90% H_2–10% H_2O (black), 50% H_2–50% H_2O (purple) and 20% H_2–80% H_2O (pink) at 860 °C with indication of frequency decades.

These values correspond to 0.58 Ω cm^2 (FC-10% H_2O), 0.54 Ω cm^2 (FC-50% H_2O), 0.56 Ω cm^2 (EC-50% H_2O) and 0.57 Ω cm^2 (EC-80% H_2O). Interestingly, the measured values are in the same order of magnitude than the ones reported by Schefold *et al.* on a commercial ESC: ASR_{DC_Total} = 0.5 Ω cm^2, which consisted of an electrolyte of 3YSZ, a LSCF air electrode, screen-printed CGO layers as the diffusion barrier between the electrolyte and electrodes and a Ni-CGO fuel electrode operated in steam electrolysis (EC-75% H_2O) at 850 °C.[57]

Performance evaluation in co-EC operation

Electrochemical characterization of this cell with the L65SCrN fuel electrode was performed in co-electrolysis mode at 860 °C (co-EC) with the fuel gas composition 5% H_2, 63.7% H_2O and 31.3% CO_2.

ASR_{DC_Total} at −0.3 A cm^{-2} was calculated from the polarization curve (Fig. 8a) to be 0.676 Ω cm^2. This value lies in the same order of magnitude (being lower) as the one reported for an ESC reference with a Ni-CGO fuel electrode tested in co-electrolysis (25% H_2, 25% H_2O, 25% CO_2, 25% CO) at 830 °C which showed an ASR_{DC_Total} of 0.84 Ω cm^2 at −0.3 A cm^{-2}.[58]

Even though these conditions are not directly comparable, this first approach suggests promising performance of the L65SCrN electrocatalyst as a fuel electrode. The polarization curve shows a linear evolution from OCV until the thermoneutral voltage of co-electrolysis that is determined under the tested conditions to ~1.32 V lying between the steam electrolysis value (1.29 V) and CO_2 electrolysis (1.46 V).[3,59] Above this point, the curve flattens due to the decrement in the ASR_{DC_Total} value, probably enhanced by the temperature increment in this exothermal regime.[3]

From the EIS spectra recorded at OCV (Fig. 8c and d), a R_{ohm} of 0.47 Ω cm^2 was identified for L65SCrN (blue pattern). Furthermore, the polarization resistance ASR_{AC_Pol} was estimated to be 0.29 Ω cm^2, which can be directly compared with the estimation by Dueñas *et al.* on an ESC with the Ni-CGO fuel electrode under the same operating conditions (green pattern): 0.23 Ω cm^2.[3]

Regarding the electrode polarization processes, they are dominated by one main contribution which suggests a convolution of the electrode losses with the gas losses (conversion and diffusion processes).

A calculation of the distribution of relaxation times (DRT) was performed with the aim of identifying relevant processes within the L65SCrN fuel electrode-cell. Five contributions or processes could be identified (Fig. 8b), which allowed proposing the equivalent circuit model (ECM) shown in Fig. 8e, with good fitting of the EIS spectra in Fig. 8c and d ($\chi^2 = 1.55 \times 10^{-4}$). The proposed ECM comprised an ohmic resistance R_o of 4.69 × 10^{-1} Ω cm^2 to model the ohmic losses and a series connection of five *RQ*-elements, where *Q* represents a constant-phase element (CPE).

Five different physical and electrochemical processes were identified as shown in Table 3, where the resulting peak frequency (f_{DRT_peak}) and the polarization resistance values (area under the peaks) from the DRT analysis were used to calculate the capacitance of an ideal RC element from the general eqn (6):[60]

$$f_{peak} = \frac{1}{2\pi(RQ)^{1/n}} \tag{6}$$

for $n = 1$. The resulting *R* and *Q* (which has the characteristic of a capacitor *C* for $n = 1$) were used as the initial parameters for the equivalent circuit model fitting in ZView for the five *RQ*-elements. The fitting parameters including *R*, *Q* and *n* (for *n* between 0 and 1) were then iterated until new f_{ECM_peak} matched with f_{DRT_peak}.

For the case of the LSCF charge transfer process (Peak#2) and the LSCF/CGO interfacial double-layer capacitance (Peak#1), characteristic frequencies were identified with comparable values as the ones reported by Yurkiv *et al.*[61] For the electrochemical process on the L65SCrN fuel electrode, there is

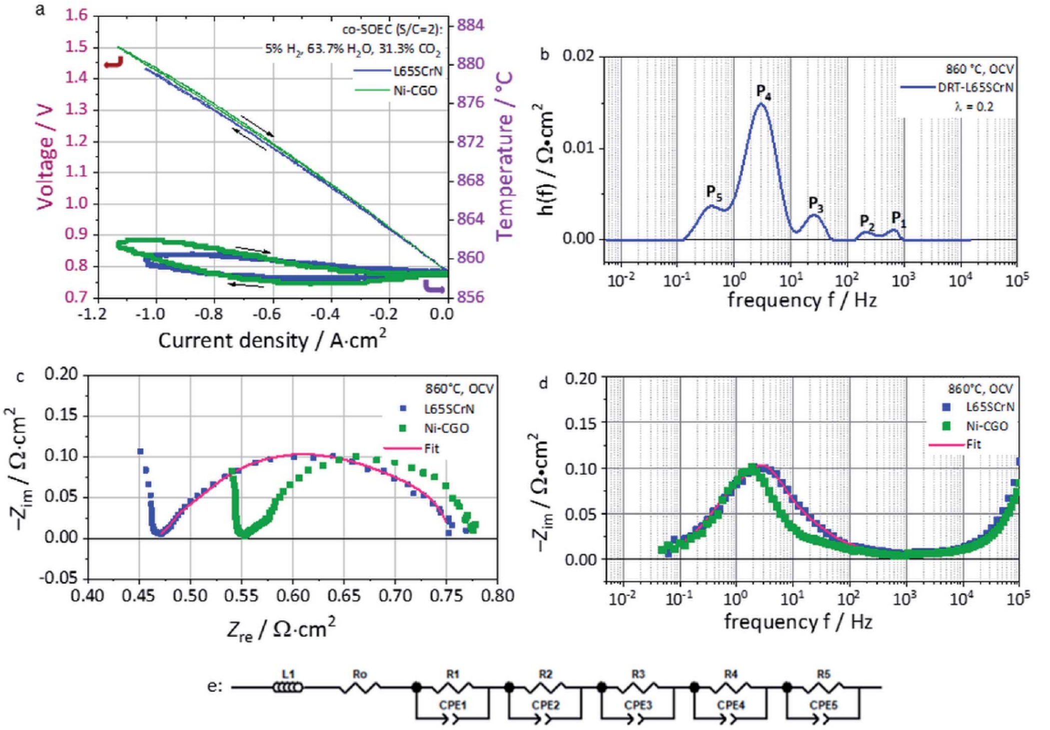

Fig. 8 (a) Polarization curves in co-electrolysis mode (co-EC) with the fuel gas composition of 5% H_2, 63.7% H_2O and 31.3% CO_2 at 860 °C of the L65SCrN fuel electrode ESC (blue pattern) and state-of-the-art Ni-CGO fuel electrode ESC (green pattern). (b) DRT calculation of the L65SCrN impedance spectra using (c) the Nyquist plot and (d) the Imaginary impedance plot at OCV at 860 °C with fuel gas composition 5% H_2, 63.7% H_2O and 31.3% CO_2. (e) ECM proposed with the fitting on the L65SCrN impedance spectra.

a lack of reported EIS data, which makes difficult the precise identification of the processes.

Nonetheless, since no additional high frequency processes are visible in the EIS spectra it is suspected that the L65SCrN charge transfer process is correlated with large chemical capacitance linked to its oxygen non-stoichiometry which overlaps with the gas conversion process. For this impedance feature, the DRT analysis suggests two processes (Peak#3 and Peak#4) at a frequency between ~3–25 Hz that, by analogy with the behavior of MIEC materials reported by Adler *et al.*,[62] are likely to be connected to each other and be characteristic of the response of the L65SCrN. A last process (Peak#5) at low frequencies between 0.1 Hz and 1 Hz was attributed to the gas losses where there is an overlapping of the RWGS reaction (catalytic conversion),[63] the diffusion in the electrodes and the gas conversion processes (within the gas channels). At frequencies above 10^3 Hz, it was not possible to fit the EIS spectrum due to an artifact of the measurement.

Overall, this corresponds to a first approach to model and understand the electrochemical behavior of an ESC with a L65SCrN fuel electrode in co-electrolysis. However, this would need to be confirmed and further investigated to understand in detail the different electrochemical processes that take place within the cell and does not preclude other approach to better reflect the behavior of the electrode materials. Especially, with the proposed model, if two connected processes are reasonable to consider for the impedance feature of L65SCrN, a parametric study varying temperature, current density and gas compositions of the fuel electrode with DRT studies will be needed in order to understand the response of the L65SCrN fuel electrode and make a clear process assignment.[64] After the above described electrochemical tests were performed, the tested ESC was observed by SEM (Fig. 9), where no delamination or mismatch at none of the interfaces platinum current collector-L65SCrN, L65SCrN-CGO20, CGO20-3YSZ and CGO20-LSCF could be observed on the polished cross section, which suggests good thermo-mechanical compatibility between the different cell components. Elemental analysis performed by EDS revealed the presence of silicon, likely in the form of SiO_2 species, within the CGO20 barrier layer (Fig. S6 and Table S1 in the ESI†). Therefore, long-term evaluation in co-electrolysis with ultrapure feed water was performed with a new cell in order to exclude any exogenous sources of degradation and clearly

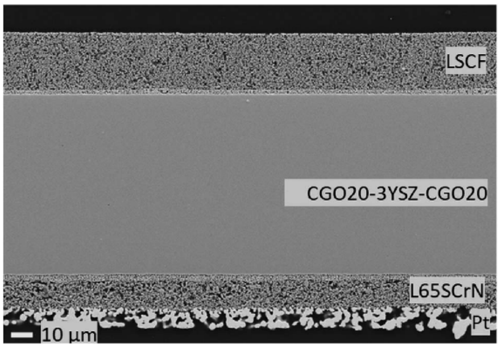

Fig. 9 Cross-sectional view of the ESC implementing the L65SCrN electrocatalyst as the fuel electrode after rSOC operation at 860 °C.

assess the stability of the L65SCrN fuel electrode in operation in view of SOC applications.

Evaluation of the long-term stability in co-EC operation

Long-term steam co-electrolysis was carried out for 950 hours under galvanostatic conditions at a fixed current density of -0.46 A cm^{-2} at 860 °C with an initial voltage of ~1.3 V (Fig. 10a). EIS measurements at OCV (Fig. 10c and d) were performed in order to monitor the evolution upon operation. Compared to the previous cell (Fig. 8), a higher R_{ohm} was measured likely due to a contact issue between the electrodes and the current collectors for this long-term test. However, the polarization resistance (R_{pol}), for testing times above 677 hours, but possible already from the first 100 hours, coincides with the one reported in Fig. 8c, being *ca.* ~0.3 Ω cm^2 for both cases. The same accounts with the imaginary part of the impedance Z_{Im} from Fig. 8d and 10d, which are in the same order of magnitude, *i.e.* close to -0.1 Ω cm^2 in both cases.

The first 100 hours of the test are marked by a decreasing voltage of the cell, meaning an improvement of the cell performance (Fig. 10a and b). This improvement is expressed by a decrease of both R_{ohm} and R_{pol} over time, which could be due to the following factors:

(i) the oxygen electrode needed *ca.* 100 hours to be correctly contacted, due possibly to the gold mesh current collector stabilization.

(ii) A removal of impurities that are present in a trace amount in CO_2 that may have been adsorbed on the surface of the perovskite and poisoned the electrode during the 24 hours of cell operation at OCV, before the start of the galvanostatic durability test.

(iii) An activation process of the L65SCrN fuel electrode to accommodate the defect chemistry under the testing conditions (~100 hours) during which one can speculate further nickel exsolution to occur.

This last feature presents some analogy with the phenomenon reported by Neagu *et al.* on titanates,[20] who reported such evolution in a few minutes time-frame and not in several hours as for this study. As this behavior of titanates was reported in pure hydrogen, it is reasonable to consider the gas composition to play a significant role in this observation. After the first 100 hours of operation, the voltage evolved nearly linearly. Cyclic fluctuations of the water supply resulted in voltage oscillation of about ~1–2 mV. The corresponding voltage increment due to the degradation could be estimated as 3.2 mV/1000 h. This is about ~1.6 times lower than the value reported by Schefold *et al.*, on an ESC cell with a Ni-CGO cermet fuel electrode operated in steam electrolysis (EC-75% H_2O) at 850 °C and -0.7 A cm^{-2} who measured 5.1 mV/1000 h.[57] Despite the difference under operating conditions and the lower applied current density, such a low voltage degradation rate reported for an ESC with a L65SCrN fuel electrode is promising. After cooling, SEM investigation of the non-polished surface of the L65SCrN fuel electrode after 950 hours of co-electrolysis operation was

Table 3 Physical and electrochemical processes identified on the ESC with the L65SCrN fuel electrode operating in co-EC mode at 860 °C with their corresponding ECM elements

Peak #	Cell component	Physical/electrochemical origin	ECM elements[65,66]	Characteristic frequency
1	Oxygen electrode	LSCF/CGO interfacial double-layer capacitance[61]	$R_1 = 4.23 \times 10^{-3}$ Ω cm^2, $Q_1 = 6.09 \times 10^{-2}$ s$^{0.97}$/Ω cm^2, $n = 0.97$	~7.96×10^2 Hz
2		LSCF charge transfer[61]	$R_2 = 6.25 \times 10^{-3}$ Ω cm^2, $Q_2 = 1.28 \times 10^{-1}$ F cm^{-2}, $n = 1$	~1.99×10^2 Hz
3 and 4	Fuel electrode	L65SCrN fuel electrode electrochemical reaction	$R_3 = 3.32 \times 10^{-2}$ Ω cm^2, $Q_3 = 2.06 \times 10^{-1}$ s$^{0.99}$/Ω cm^2, $n = 0.99$	~2.45×10^1 Hz
			$R_4 = 1.71 \times 10^{-1}$ Ω cm^2, $Q_4 = 3.00 \times 10^{-1}$ F cm^{-2}, $n = 1$	~3.11 Hz
5	Fuel electrode (+oxygen electrode)	Gas diffusion (perpendicular to cell) and gas conversion (parallel to the cell in co-flow configuration) including contact mesh and flow field	$R_5 = 6.92 \times 10^{-2}$ Ω cm^2, $Q_5 = 3.69$ F cm^{-2}, $n = 1$	~3.70×10^{-1} to 6.23×10^{-1} Hz

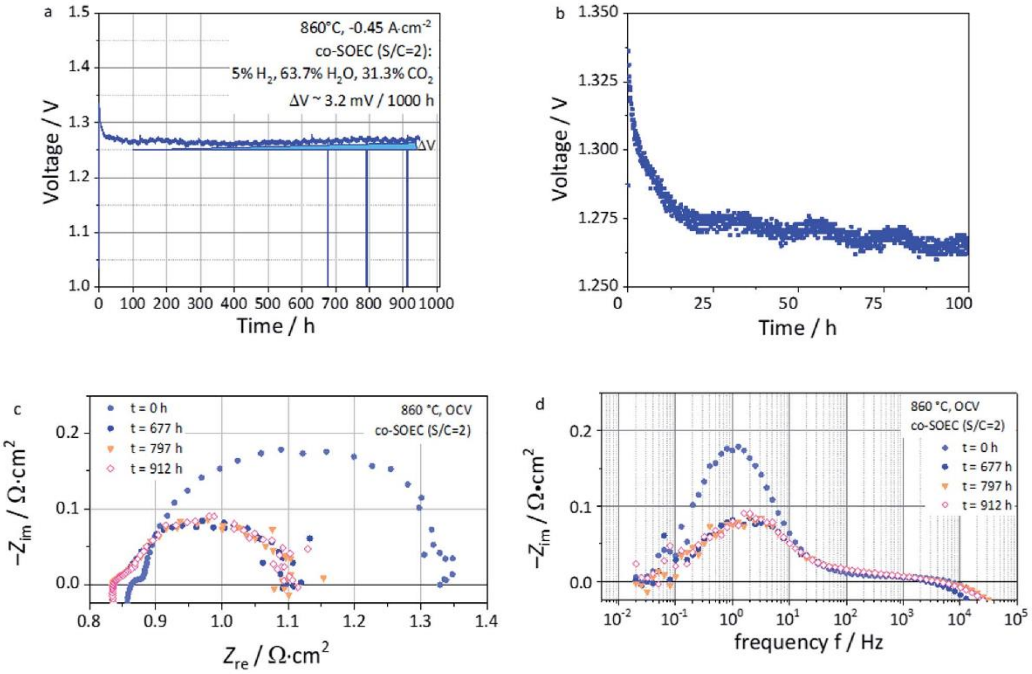

Fig. 10 (a) Voltage *vs.* time during long-term co-electrolysis (co-EC) with the fuel gas composition of 5% H_2, 63.7% H_2O and 31.3% CO_2 at 860 °C and -0.46 A cm^{-2} of the L65SCrN fuel electrode ESC (b) Zoom of (a) until 100 hours of operation. (c) Nyquist plot and (d) imaginary impedance plot at OCV and 860 °C during long-term study (951 hours).

performed (Fig. 11). As expected, the contamination of the electrode by silicon was negligible, suggesting a minimal impact on the transport properties of the L65SCrN fuel electrode (EDS analysis shown in the ESI in Fig. S7 and Table S2†). Investigation of the surface of the L65SCrN perovskite grains revealed the presence of Ni exsolved nanoparticles well distributed over the whole area of the analyzed sample. This is illustrated in a representative manner in Fig. 11 and S8.† The average size of those exsolved nanoparticles was estimated in the range of 10 to 25 nm on this sample, which is significantly lower than the one estimated on the powder sample at 900 °C in pure hydrogen (Fig. 6b). Considering the 950 hour operating

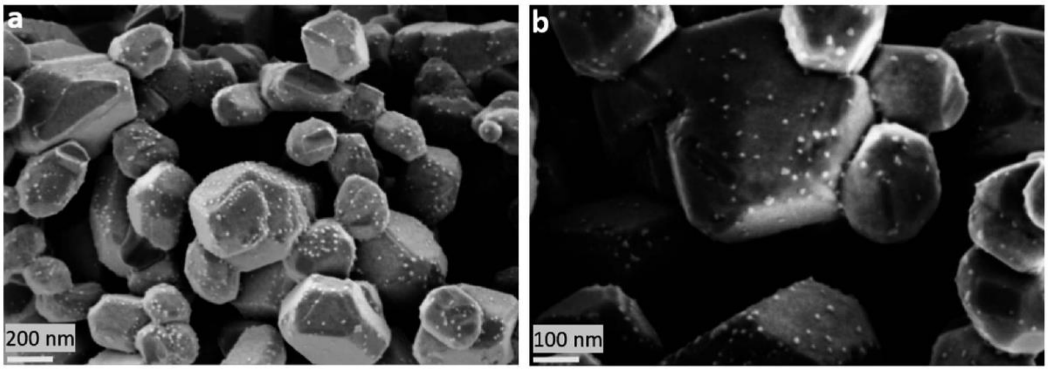

Fig. 11 (a) and (b) SEM images with Ni nanoparticles after 950 hour co-electrolysis operation (co-EC) with the fuel gas composition of 5% H_2, 63.7% H_2O and 31.3% CO_2 at 860 °C and -0.46 A cm^{-2} of the L65SCrN fuel electrode ESC.

time, this observation suggests that particle coarsening was limited and did not occur under the testing conditions. This is consistent with observations reported where the size of the exsolved nanoparticle increases until a critical stable radius, as a function of the temperature and time.[46,53] Knowing that the oxygen partial pressure pO_2 was about $\sim 10^{-24}$ bar in the case of powder sample reduction at 900 °C,[67] and only $\sim 10^{\ 15}$ bar in this case of long-term co-electrolysis,[30] it seems that pO_2 plays the most important role in the morphology of the exsolved nanoparticles. The relative predominance of the parameters that affect the Ni exsolution morphology could be qualitatively ranked as follows: pO_2 > temperature > time. Since electrolysis operation implies reducing conditions to the fuel electrode, it is nonetheless reasonable to expect that the applied current density and thus the overpotential at the L65SCrN fuel electrode is going to have an additional influence on the exsolved nickel nanoparticles. Since *A*-site deficiency and exsolution are intimately correlated, it is difficult to decorrelate the impact of the two phenomena on the cell performance. Working with an *A*-site deficient perovskite is of high interest with perspective of industrialization since it enables to control the impurities (as the *B*-site elements) in the produced materials. ESCs are intrinsically characterized by a high operating temperature to counter-balance the ohmic losses induced by the thickness of the electrolyte. This feature limits the impact of the electrocatalysis on the overall cell performance. However, given the contingencies of the ESC cell configuration, we believe that the observed behavior and performance is to a large extent due to the exsolution of nickel.

Conclusions

Lanthanum strontium chromite perovskites with partial nickel substitution were investigated for the sake of developing an alternative electrocatalyst to traditional cermets as the fuel electrode for SOC applications. These materials have been synthesized and their propensity to exsolve Ni nanoparticles under exposure to a reducing atmosphere has been investigated *ex situ*. Introduction of a deficiency up to 5% on the *A*-site of the perovskite was shown to be effective to enhance the exsolution capability of the synthesized material (L65SCrN), compared to a full stoichiometric perovskite (L70SCrN).

The density and particle shape of the exsolved nanoparticles on the surface of the perovskite were shown to be sensitive to the crystallographic orientations of the surfaces and pO_2. This behavior is consistent with the observations made on other families of perovskites with exsolution of nanoparticles such as titanates. However, in contrast to the titanates, the evolution in the shape, size and coverage ratio of the Ni nanoparticles, upon temperature increase characterized by a particle coarsening, suggests that particle–particle interactions prevail over particle–substrate interactions on the surface of lanthanum chromites. This significant morphological change of the nanoparticles under operating conditions could affect their catalytic activities over time and thus impact the overall performance and durability of an electrode made of these materials.

Tested on ESCs and with optimal contacting solutions, L65SCrN electrodes demonstrated performance levels that are comparable with the ones of state-of-the-art cermet fuel electrodes in fuel cell, electrolysis and co-electrolysis operation: representative conditions for a reversible SOC system. Excellent voltage stability was reported in co-electrolysis operation over 950 hours with a voltage degradation of about 3.2 mV/1000 hours. Qualitatively, it is suggested that pO_2 is the main factor governing the particle size followed by the temperature and then time. This suggests that the nanoparticles can be dimensionally stable when the system is operated isothermally, or when exsolution takes place at a temperature higher than the nominal operating temperature of the cell. Therefore, considering a SOC stack implementing cells with L65SCrN fuel electrodes, one can reasonably expect that the exsolution would take place during the commissioning of the stack, yielding coarsened Ni nanoparticles that are dimensionally stable during operation, fulfilling the durability requirements.

However, as a disadvantage the high temperature thermal treatment that is usually performed for stack commissioning would yield coarsened nanoparticles that may impede further electrode performance optimization. One aspect to consider and being advantageous would be to maintain the exsolved nanoparticles as fine as possible to optimally improve the performance of L65SCrN electrodes by tuning for instance pO_2.

Additional investigation of the exsolution phenomena by varying parameters such as temperature, time and pO_2 would be thus needed in order to better understand the mechanisms of exsolution. Another important aspect to evaluate is how the Ni nanoparticle size impacts the performance of the electrode and how to fine tune the exsolution parameters for maximizing electrocatalytic activity. This would enable improving the presented L65SCrN fuel electrode and developing a durable electrode morphology for rSOC applications.

Conflicts of interest

There are no conflicts to declare.

Note added after first publication

This article replaces the version published on 5th February 2021, in which there was an error in a value of oxygen partial pressure quoted in the text. This has now been corrected, and the Royal Society of Chemistry apologises for this error.

Acknowledgements

We would like to thank the University of Bayreuth, Chair for Electrical Energy Systems, for providing the impedance analysis and modelling software ec-idea (https://www.ec-idea.uni-bayreuth.de). Also, the German Academic Exchange Service (DAAD) is acknowledged for the PhD scholarship of Diana-María Amaya-Dueñas with the award DLR/DAAD Research Fellowships – Doctoral Studies, 2017.

References

1 E. V. Kondratenko and U. Rodemerck, in *Perovskites and Related Mixed Oxides: Concepts and Applications*, ed. P. Granger, V. I. Parvulescu, S. Kaliaguine and W. Preiller, Wiley-VCH Verlag GmbH & Co. KGaA, Weinheim, 1st edn, 2016, pp. 517–537, Recent Progress in Oxidative Conversion of Methane to Value-Added Products.

2 P. De Luna, C. Hahn, D. Higgins, S. A. Jaffer, T. F. Jaramillo and E. H. Sargent, *Science*, 2019, **364**, 350.

3 D. M. Amaya Dueñas, M. Riedel, M. Riegraf, R. Costa and K. A. Friedrich, *Chem. Ing. Tech.*, 2020, **92**, 45–52.

4 S. Santhanam, M. P. Heddrich, M. Riedel and K. A. Friedrich, *Energy*, 2017, **141**, 202–214.

5 Y. Zheng, J. Wang, B. Yu, W. Zhang, J. Chen, J. Qiao and J. Zhang, *Chem. Soc. Rev.*, 2017, **46**, 1427–1463.

6 G. Kasiraman, B. Nagalingam and M. Balakrishnan, *Energy*, 2012, **47**, 116–124.

7 M. Riegraf, M. P. Hoerlein, R. Costa, G. Schiller and K. A. Friedrich, *ACS Catal.*, 2017, 7, 7760–7771.

8 M. Riegraf, A. Zekri, M. Knipper, R. Costa, G. Schiller and K. A. Friedrich, *J. Power Sources*, 2018, **380**, 26–36.

9 R. Costa, F. Han, P. Szabo, V. Yurkiv, R. Semerad, S. K. Cheah and L. Dessemond, *Fuel Cells*, 2018, **18**, 251–259.

10 T. L. Skafte, J. Hjelm, P. Blennow and C. R. Graves, in *Proceedings of 12^{th} European SOFC & SOE Forum 2016*, ed. European Fuel Cell Forum, Lucerne, 2016, pp. 8–27, Quantitative review of degradation and lifetime of solid oxide cells and stacks.

11 M. P. Hoerlein, M. Riegraf, R. Costa, G. Schiller and K. A. Friedrich, *Electrochim. Acta*, 2018, **276**, 162–175.

12 Y. Tao, S. D. Ebbesen and M. B. Mogensen, *J. Electrochem. Soc.*, 2014, **161**, F337–F343.

13 V. Duboviks, R. C. Maher, M. Kishimoto, L. F. Cohen, N. P. Brandon and G. J. Offer, *Phys. Chem. Chem. Phys.*, 2014, **16**, 13063–13068.

14 A. Faes, A. Hessler-Wyser, A. Zryd and J. V. Herle, *Membr*, 2012, **2**, 585–664.

15 H. Zhu, P. Zhang and S. Dai, *ACS Catal.*, 2015, **5**, 6370–6385.

16 G. Tsekouras, D. Neagu and J. T. S. Irvine, *Energy Environ. Sci.*, 2013, **6**, 256–266.

17 V. Kyriakou, D. Neagu, E. I. Papaioannou, I. S. Metcalfe, M. C. M. van de Sanden and M. N. Tsampas, *Appl. Catal., B*, 2019, **258**, 117950.

18 J.-h. Myung, D. Neagu, D. N. Miller and J. T. S. Irvine, *Nature*, 2016, **537**, 528–531.

19 D. Neagu, T.-S. Oh, D. N. Miller, H. Ménard, S. M. Bukhari, S. R. Gamble, R. J. Gorte, J. M. Vohs and J. T. S. Irvine, *Nat. Commun.*, 2015, **6**, 8120.

20 D. Neagu, V. Kyriakou, I.-L. Roiban, M. Aouine, C. Tang, A. Caravaca, K. Kousi, I. Schreur-Piet, I. S. Metcalfe, P. Vernoux, M. C. M. van de Sanden and M. N. Tsampas, *ACS Nano*, 2019, **13**, 12996–13005.

21 F. M. Sapountzi, S. Brosda, K. M. Papazisi, S. P. Balomenou and D. Tsiplakides, *J. Appl. Electrochem.*, 2012, **42**, 727–735.

22 X. Zhang, Y. Song, G. Wang and X. Bao, *J. Energy Chem.*, 2017, **26**, 839–853.

23 Y. Sun, J.-H. Li, M.-N. Wang, B. Hua, J. Li and J.-L. Luo, *J. Mater. Chem. A*, 2015, **3**, 14625–14630.

24 D. M. Amaya Dueñas, G. Chen, A. Weidenkaff, N. Sata, F. Han, G. Schiller, R. Costa and K. A. Friedrich, *ECS Trans.*, 2019, **91**, 1751–1760.

25 A. Nenning and J. Fleig, *Surf. Sci.*, 2019, **680**, 43–51.

26 R. Hesse, T. Chassé and R. Szargan, *Fresenius. J. Anal. Chem.*, 1999, **365**, 48.

27 D. A. Shirley, *Phys. Rev. B: Condens. Matter Mater. Phys.*, 1972, **55**, 4709.

28 A. Proctor and P. M. A. Sherwood, *Anal. Chem.*, 1982, **54**, 13.

29 J. J. Yeh and I. Lindau, *At. Data Nucl. Data Tables*, 1985, **32**, 1–155.

30 D. G. Goodwin, H. K. Moffat and R. L. Speth, *Cantera: An object-oriented software toolkit for chemical kinetics, thermodynamics, and transport processes, Version 2.2.0*, 2015.

31 M. Hahn, S. Schindler, L.-C. Triebs and M. A. Danzer, *Batteries*, 2019, **5**, 43.

32 D. Johnson, *ZView Electrochemical Impedance Software, Version 2.3b*, Scribner Associates, Inc., 2000.

33 W. Lee, J. W. Han, Y. Chen, Z. Cai and B. Yildiz, *J. Am. Chem. Soc.*, 2013, **135**, 7909–7925.

34 A. J. Carrillo, K. J. Kim, Z. D. Hood, A. H. Bork and J. L. M. Rupp, *ACS Appl. Energy Mater.*, 2020, **3**, 4569–4579.

35 Database of Ionic Radii, http://abulafia.mt.ic.ac.uk/shannon/ptable.php, accessed July 2020.

36 A. K. Opitz, A. Nenning, C. Rameshan, M. Kubicek, T. Götsch, R. Blume, M. Hävecker, A. Knop-Gericke, G. Rupprechter, B. Klötzer and J. Fleig, *ACS Appl. Mater. Interfaces*, 2017, **9**(41), 35847–35860.

37 M. P. Seah and W. A. Dench, *Surf. Interface Anal.*, 1979, **1**, 1–11.

38 M. Lorenz and M. Schulze, *Surf. Sci.*, 2000, **454–456**, 234–239.

39 M. C. Biesinger, B. P. Payne, A. P. Grosvenor, L. W. M. Lau, A. R. Gerson and R. S. C. Smart, *Appl. Surf. Sci.*, 2011, **257**, 2717–2730.

40 N. Gunasekaran, N. Bakshi, C. B. Alcock and J. J. Carberry, *Solid State Ionics*, 1996, **83**, 145–150.

41 I. Ikemoto, K. Ishii, S. Kinoshita, H. Kuroda, M. A. Alario Franco and J. M. Thomas, *J. Solid State Chem.*, 1976, **17**, 425–430.

42 F. Garbassi, E. Mello Ceresa, G. Basile and G. C. Boero, *Appl. Surf. Sci.*, 1982-1983, **14**, 330–350.

43 D. Papargyriou, D. N. Miller and J. T. S. Irvine, *J. Mater. Chem. A*, 2019, **7**, 15812.

44 Y. Sun, J. Li, Y. Zeng, B. S. Amirkhiz, M. Wang, Y. Behnamiana and J. Luo, *J. Mater. Chem. A*, 2015, **3**, 11048–11056.

45 R. A. De Souza, M. S. Islam and E. Ivers-Tiffée, *J. Mater. Chem.*, 1999, **9**, 1621–1627.

46 Y.-R. Jo, B. Koo, M.-J. Seo, J. K. Kim, S. Lee, K. Kim, J. W. Han, W. Jung and B.-J. Kim, *J. Am. Chem. Soc.*, 2019, **141**, 6690–6697.

47 A. L. Sauvet and J. T. S. Irvine, *Solid State Ionics*, 2004, **167**, 1–8.

48 W. Kobsiriphat, B. D. Madsen, Y. Wang, M. Shah, L. D. Marks and S. A. Barnett, *J. Electrochem. Soc.*, 2010, **157**, B279–B284.

49 N. Sakai, K. Yamaji, T. Horita, H. Negishi and H. Yokokawa, *Solid State Ionics*, 2000, **135**, 469–474.

50 K. Kousi, D. Neagu, L. Bekris, E. Cali, G. Kerherve, E. I. Papaioannou, D. J. Payne and I. S. Metcalfe, *J. Mater. Chem. A*, 2020, **8**, 12406–12417.

51 A. Ladavos and P. Pomonis, in *Perovskites and Related Mixed Oxides: Concepts and Applications*, ed. P. Granger, V. I. Parvulescu, S. Kaliaguine and W. Preiller, Wiley-VCH Verlag GmbH & Co. KGaA, Weinheim, 1st edn, 2016, pp. 369–387, Methane Combustion on Perovskites.

52 C. Pirovano, A. Rolle and R.-N. Vannier, in *Perovskites and Related Mixed Oxides: Concepts and Applications*, ed. P. Granger, V. I. Parvulescu, S. Kaliaguine and W. Preiller, Wiley-VCH Verlag GmbH & Co. KGaA, Weinheim, 1st edn, 2016, pp. 169–184, Perovskite and Derivative Compounds as Mixed Ionic–Electronic Conductors.

53 Y. Gao, D. Chen, M. Saccoccio, Z. Lu and F. Ciucci, *Nano Energy*, 2016, **27**, 499–508.

54 O. A. Baturina and A. E. Smirnova, in *New and Future Developments in Catalysis: Batteries, Hydrogen Storage and Fuel Cells*, ed. S. L. Suib, Elsevier, 2013, pp. 69–97, Catalytic Processes Using Fuel Cells, Catalytic Batteries, and Hydrogen Storage Materials.

55 Y.-J. Yang, T.-L. Wen, H. nTu, D.-Q. Wang and J. Yang, *Solid State Ionics*, 2000, **135**, 475–479.

56 S. P. Jiang, L. Liu, K. P. Ong, P. Wu, J. Li and J. Pu, *J. Power Sources*, 2008, **176**, 82–89.

57 J. Schefold, A. Brisse, A. Surrey and C. Walter, *Int. J. Hydrogen Energy*, 2019, **45**, 5143–5154.

58 M. Preininger, B. Stoeckl, V. Subotić, F. Mittmann and C. Hochenauer, *Appl. Energy*, 2019, **254**, 113695.

59 X. Sun, M. Chen, S. H. Jensen, S. D. Ebbesen, C. Graves and M. Mogensen, *Int. J. Hydrog. Energy*, 2012, **37**, 17101–17110.

60 A. Leonide, PhD dissertation, Karlsruhe Institute of Technology (KIT), 2010.

61 V. Yurkiv, R. Costa, Z. Ilhan, A. Ansar and W. G. Bessler, *J. Electrochem. Soc.*, 2014, **161**, F480–F492.

62 S. B. Adler, J. A. Lane and B. C. H. Steele, *J. Electrochem. Soc.*, 1996, **143**, 3554–3564.

63 J.-C. Njodzefon, C. R. Graves, M. B. Mogensen, A. Weber and J. Hjelm, *J. Electrochem. Soc.*, 2016, **163**, F1451–F1462.

64 S. Dierickx, A. Weber and E. Ivers-Tiffée, *Electrochim. Acta*, 2020, **355**, 136764.

65 M. R. Shoar Abouzari, F. Berkemeier, G. Schmitz and D. Wilmer, *Solid State Ionics*, 2009, **180**, 922–927.

66 C. H Hsu and F. Mansfeld, *Corrosion*, 2001, **57**, 747–748.

67 M. H. Pihlatie, A. Kaiser, M. Mogensen and M. Chen, *Solid State Ionics*, 2011, **189**, 82–90.

Article I – Supplementary information

Electronic Supplementary Material (ESI) for Journal of Materials Chemistry A.

Electronic supplementary information (ESI)

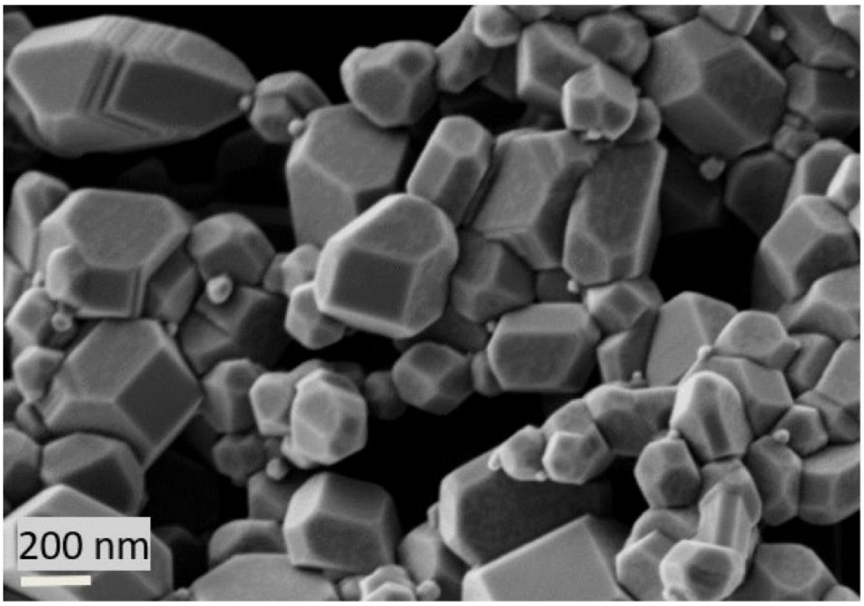

Fig S1. SEM image of L70SCrN after reduction.

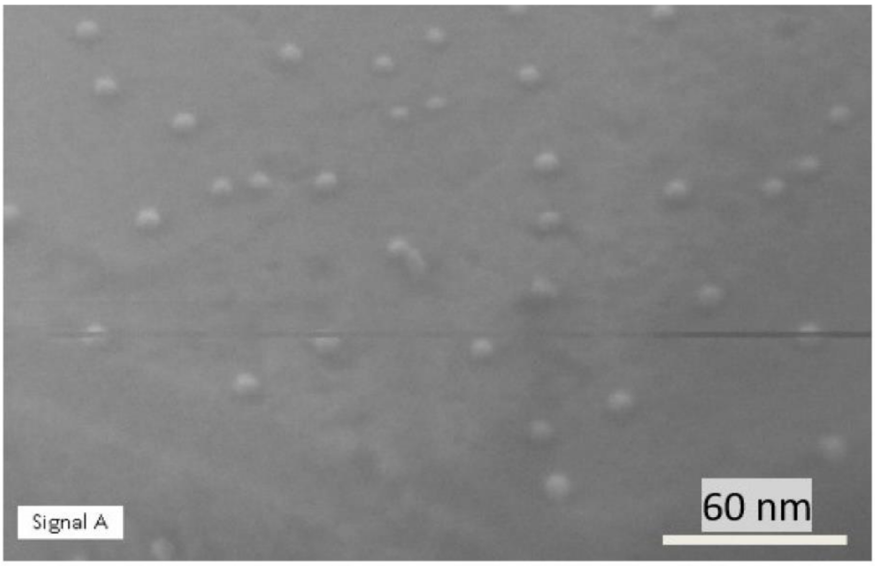

Fig S2. SEM image (magnification 400X, 10 kV). Ni exsolution after 3 hours treatment under H_2 atmosphere at 500 °C on surface Type 1 from Figure 6a.

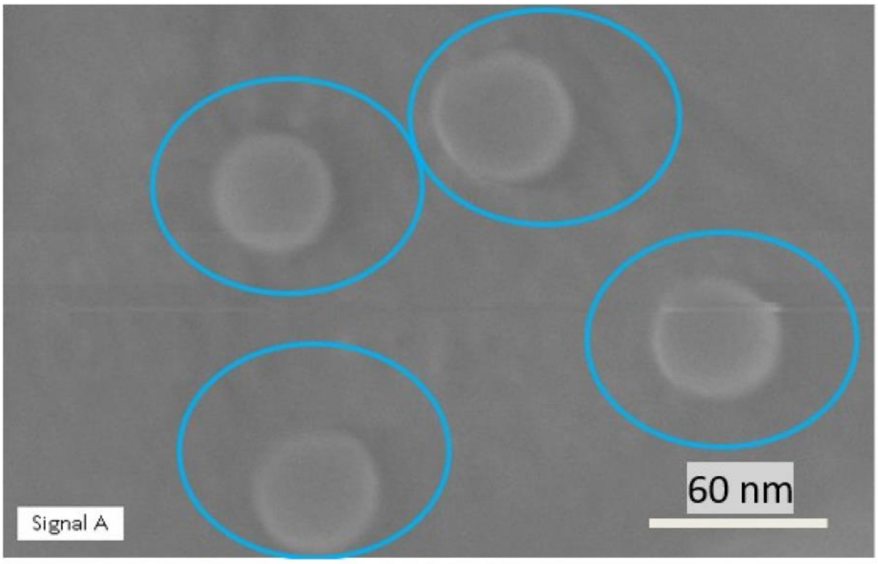

Fig S3. SEM image (magnification 400X, 10 kV). Ni exsolution after 3 hours treatment under H_2 atmosphere at 500 °C on surface Type 2 from Figure 6a.

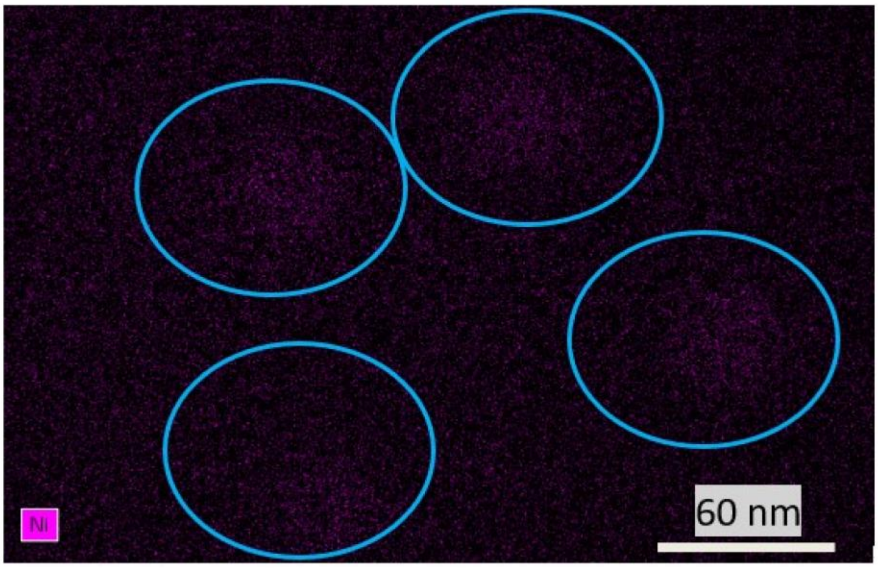

Fig S4. EDS mapping of Ni signal on SEM image shown on Fig. S3, where the area corresponding to the 4 nanoparticles shown on Fig. S3 could be correlated with an enrichment in Ni.

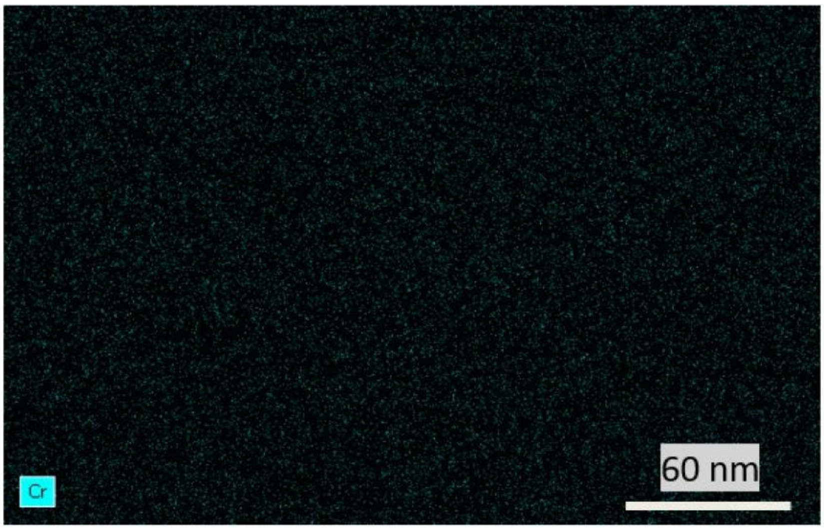

Fig S5. EDS mapping of Cr signal on SEM image shown on Fig. S3, where the area corresponding to the 4 nanoparticles shown on Fig. S3 could not be correlated with an enrichment in Cr.

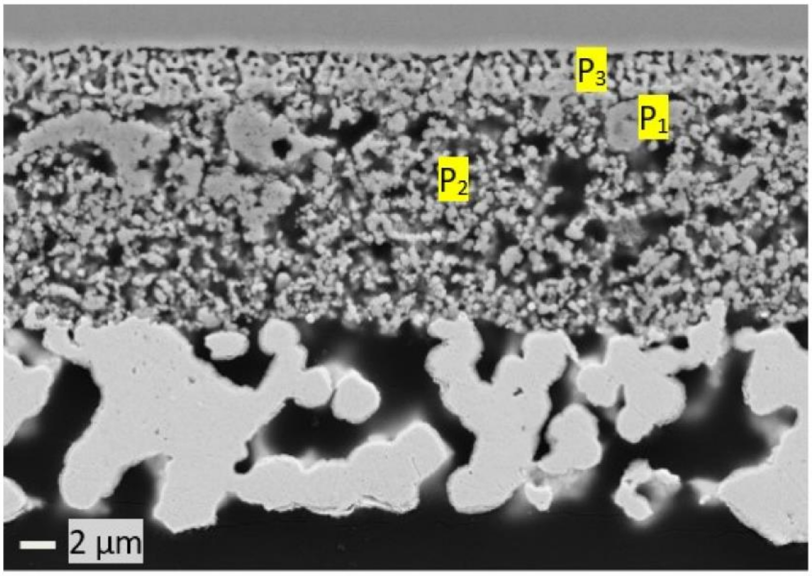

Fig S6 Polished cross-section view of the L65SCrN fuel electrode ESC after FC, FC-EC, EC and co-EC operation at 860 °C with EDX point analysis.

Table S1. EDX with point analysis on Fig. S6 and mass percent content by element.

Element	**La**	**Sr**	**Ni**	**Cr**	**O**	**Zr**	**Gd**	**Ce**	**Si**	**C**	**Pt**
P 1	39.89	16.91	2.23	22.37	18.59	-	-	-	-	-	-
P 2	47.07	11.16	3.12	21.70	16.94	-	-	-	-	-	-
P 3	-	6.62	-	-	13.93	0.93	12.16	61.0	5.37	-	-

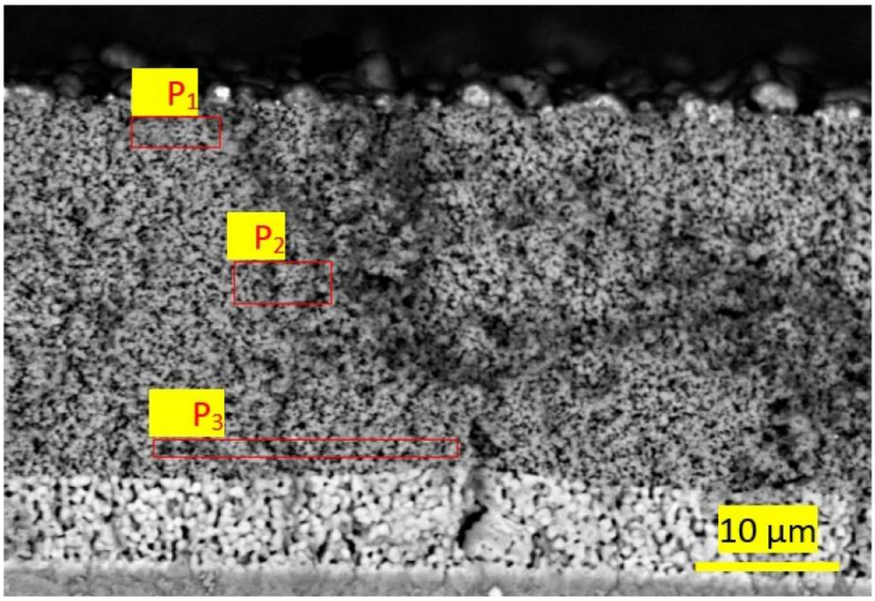

Figure S7. Cross-section view of the L65SCrN fuel electrode ESC after long-term co-EC operation at 860 °C with EDX point analysis

Table S2. EDX with point analysis on Fig. S7 and mass percent content by element.

Element	**C**	**O**	**Al**	**Si**	**Cr**	**Ni**	**Sr**	**Zr**	**La**
P 1	2.82	22.35	0.53	0.14	20.22	2.14	13.38	2.19	36.23
P 2	1.98	18.16	-	0.01	22.03	3.34	9.84	1.18	43.46
P 3	1.51	15.64	-	0.06	23.57	2.93	10.49	0.89	44.90

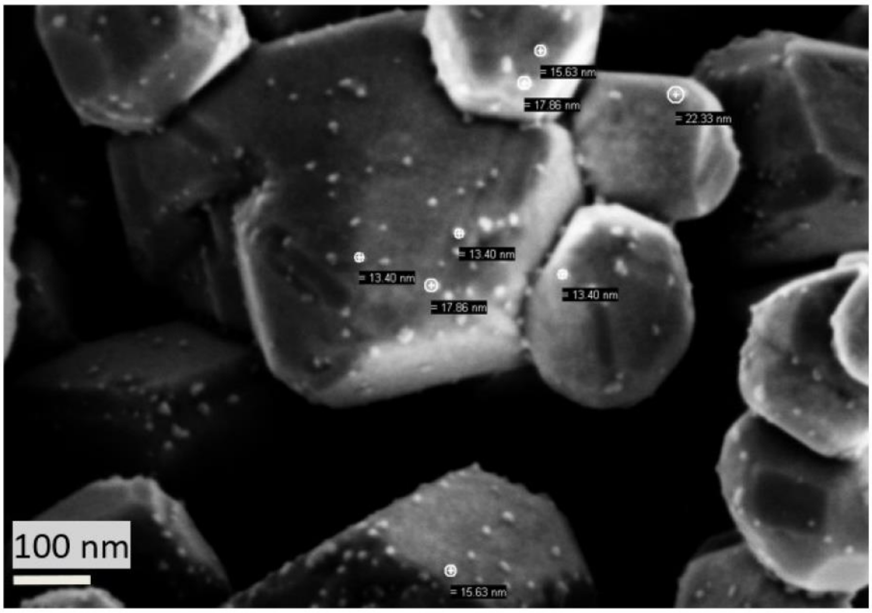

Figure S8. SEM image representative of the electrode surface showing the Ni nanoparticles of typical size after co-electrolysis at 860°C during 950 hours at -0.46 A.cm^{-2}.

Article II

ChemSusChem
Full Papers
doi.org/10.1002/cssc.202100330
Chemistry Europe
European Chemical Societies Publishing

Performance and Limitations of Nickel-Doped Chromite Anodes in Electrolyte-Supported Solid Oxide Fuel Cells

Matthias Riegraf,*[a] Diana M. Amaya-Dueñas,[a] Noriko Sata,[a] K. Andreas Friedrich,[a, b] and Rémi Costa*[a]

Ni-doped chromite anodes were integrated into electrolyte-supported cells (ESC) with 5×5 cm^2 size and investigated in fuel cell mode with H_2/H_2O fuel gas. Both a stoichiometric and a nominally A-site deficient chromite anode material showed promising performance at 860 °C approaching the ones of state-of-the-art Ni/Gd-doped ceria (CGO) anodes. While the difference in polarization resistance was small, an increased ohmic resistance of the perovskite anodes was observed, which is related to their limited electronic conductivity. Increasing the chromite electrode thickness was shown to enhance performance and stability considerably. Degradation increased with current density, suggesting its dependency on the electrode potential, and could be reversed by redox cycling. Sulfur poisoning with 20 ppm hydrogen sulfide led to rapid voltage drops for the chromite anodes. It is discussed that Ni nanoparticle exsolution facilitates hydrogen dissociation to the extent that it is not rate-limiting at the investigated temperature unless an insufficiently thick electrode thickness is employed or sulfur impurities are present in the feed gas.

Introduction

Although their lifetime and performance are continuously improved, solid oxide fuel cells (SOFC) keep on struggling with commercialization. A key factor determining the economic viability of solid oxide fuel cells is their durability, which, despite continuous lifetime and performance increase over the last decades, is currently restricted by degradation of the different cell components, especially the electrode materials.

An ideal SOFC fuel electrode (anode) shows high electronic and ionic conductivity, good thermal and chemical stability with the adjacent layers under reducing conditions and excellent (electro-)catalytic activity towards hydrogen and hydrocarbon oxidation. In addition, high resistivity towards redox cycling, carbon deposition and sulfur poisoning during operation with hydrocarbons or reformates is desirable.

Ni-based cermet anodes such as Ni/Yttria-stabilized zirconia (YSZ) have been developed where the metallic Ni provides the electronic conductivity and the YSZ phase, which is also the electrolyte material, provides the ionic conductivity. Ni/YSZ anodes show excellent performance during hydrogen oxidation, water gas shift reaction and reforming of various fuels such as methane due to the high catalytic activity of the Ni phase. These advantages and the outstanding mechanical stability of YSZ have made Ni/YSZ the historical electrode of choice in commercial applications of the anode-supported cell (ASC) architecture. However, despite its advantages, the electrode also faces degradation problems such as low tolerance towards sulfur impurities in the feed gas, susceptibility towards carbon formation and poor redox stability. Ni/Gadolinium-doped ceria (CGO) electrodes have shown lower short-term performance drops and increased long-term stability upon sulfur exposure, also in reformate fuels.[1] Furthermore, there are reports indicating lower overpotentials and increased tolerance towards carbon formation and increased redox stability.[2] These favorable characteristics are related to the mixed ionic and electronic conductivity (MIEC) properties of CGO at high temperatures and in reducing atmospheres,[3] which extends the active reaction zone from the triple-phase boundary (TPB) to the double-phase boundary between CGO and gas phase.[4] Despite the good inherent (electro-) catalytic activity of CGO and its decent electronic conductivity, both properties are still significantly enhanced by adding a metallic Ni phase to the electrodes. Therefore, redox cycling of conventional sintered Ni/CGO electrodes is still an issue due to the dimensional expansion of Ni upon oxidation, which can lead to Ni grain coarsening and even electrode delamination.[2c] In an attempt to increase dimensional electrode stability, infiltration of Ni nanoparticles into a ceramic backbone has shown to lead to outstanding electrode performance, but rapid grain coarsening at higher temperatures entails high degradation rates.[5] Furthermore, mechanical stability of Ni/CGO is rather poor, which currently restricts their use to electrolyte-supported cell (ESC) and metal-supported cell architectures.[6]

---

[a] Dr. M. Riegraf, D. M. Amaya-Dueñas, Dr. N. Sata, Prof. K. A. Friedrich,
Dr. R. Costa
Institute of Engineering Thermodynamics
German Aerospace Center (DLR)
Pfaffenwaldring 38–40, 70569 Stuttgart (Germany)
E-mail: matthias.riegraf@dlr.de
remi.costa@dlr.de
[b] Prof. K. A. Friedrich
Institute for Building Energetics, Thermotechnology and Energy Storage
University of Stuttgart
Pfaffenwaldring 31, 70569 Stuttgart (Germany)

Supporting information for this article is available on the WWW under https://doi.org/10.1002/cssc.202100330

As alternative fuel electrode materials, a variety of single-phase perovskite materials (ABO_3) that display desirable MIEC properties have been investigated over the last decades. To ensure high phase stability the host B-site cation should remain in an oxidized state at low pO_2 to withstand reduction to its metallic form and the associated decomposition of the perovskite structure when exposed to hydrogen. Most frequently, Cr, Mn, and Ti cations are employed as host B-site cations.[7] Electrical conductivity and electrocatalytic activity can be tuned by partial substitution with a wide variety of multivalent dopants of the A and B cations. For example, (electro-) catalytic activity can be significantly improved by introduction of transition metals such as Ni,[8] Ru,[8a,9] Pd[10] on the B site, which are released (exsolved) on the surface as metal nanoparticles upon reduction. This process occurs since the lattice loses oxygen and gains electrons upon reduction until metal nucleation becomes favorable. The nanoparticles show high stability due to their strong anchorage in the perovskite matrix, and thus, higher resistance against particle agglomeration than infiltrated nanoparticles.[8c] Moreover, such electrodes have shown excellent redox stability with regeneration of nanoparticles through redox cycling.[8a,e,10a]

$LaCrO_3$-based oxides have been investigated as interconnect materials for SOFCs and are considered as potential anode materials due to their high electronic conductivity and stability in both reducing and oxidizing conditions at high temperatures and also due to their low activity toward carbon deposition.[11]

For stoichiometric perovskites, Sr was found to be a particularly good choice as A-site substituent leading to high stability of the perovskite structure and high electrical conductivity.[11b,12] Optimum electrical conductivity can be achieved for 30–40% Sr on the A-site.[13] Furthermore, Sr substitution on the A-site leads to a better match of the coefficient of thermal expansion (CTE) with CGO.[11a] Among a multitude of different B-site substituents, Ni was identified as very promising leading to excellent (electro)catalytic activity.[11b,12a] Additionally, Ni-doped $LaCrO_3$-based oxides also showed lower activity towards carbon formation than Ni/YSZ cermet anodes.[14] Based on such considerations, Kobsiriphat et al. investigated $La_{0.8}Sr_{0.2}Cr_{1-y}X_yO_{3-\delta}$ (X=Ni, Ru) electrodes and observed Ni nanocluster formation of approximately 10 nm in diameter upon reduction but also considerable coarsening to 50 nm after 300 h at 800 °C.[8a]

Recent studies on titanates have revealed that the exsolution process is favored in A-site deficient perovskites, which can lead to a higher concentration of Ni nanoparticles on the perovskite surface since exsolution acts to locally revert the perovskite towards a "defect-free" ABO_3 stoichiometry.[8b,c,15] However, such titanate electrodes with Ni exsolution have mainly been investigated on button cell level (≈1 cm^2 active area) and have not been directly compared to state-of-the-art Ni/cermet electrodes in operation with equivalent boundary conditions.

Furthermore, only one pioneering study in literature has investigated A-site deficient lanthanum chromites and their application in SOFC: Sun et al. observed increased performance of an A-site deficient $La_{0.6}Sr_{0.3}Cr_{0.85}Ni_{0.15}O_{3-\delta}$ anode in comparison to the stoichiometric perovskite electrode ($La_{0.7}Sr_{0.3}Cr_{0.85}Ni_{0.15}O_{3-\delta}$) in small button cells at 800 °C.[8d] Significant performance degradation was observed within 24 h of operation related to Ni particle coarsening, but redox cycling was shown to lead to full recovery. Interestingly, a promoting effect of 5000 ppm H_2S on hydrogen oxidation was reported.

Recently, we have introduced the chromite formulation $La_{0.65}Sr_{0.3}Cr_{0.85}Ni_{0.15}O_{3-\delta}$ (L65SCrN) and demonstrated the successful up-scaling of exsolution-based perovskite electrodes from the commonly used button cell level to 5×5 cm^2 large ESC.[16] The performance of the cell in (co-)electrolysis mode was promising. In the present study, cells with this perovskite electrode are investigated in fuel cell operation. The aim of the study is to assess electrode performance and durability of nominally A-site deficient L65SCrN and stoichiometric L70SCrN electrodes and their comparison with state-of-the-art Ni/CGO electrodes.

Results and Discussion

In the following subsections, an analysis of the crystallographic structure of L65SCrN and L70SCrN is shown. Then, the investigation of ESC with LSCrN electrodes with regards to performance, durability, redox stability, and finally towards their sulfur tolerance will be presented.

Crystallographic structure analysis

The crystalline structures of both commercial L70SCrN and L65SCrN ceramic powders were analyzed by X-ray diffraction (XRD). The as-prepared and the reduced powders were analyzed in order to check the crystalline phases. All X-ray diffractograms are shown in Figure 1. The main phase is identified as an LSCrN perovskite structure, consistent with the ones observed in our previous study (PDF# 01-076-7024).[16]

Furthermore, both powders show a secondary $SrCrO_4$ phase that cannot be detected anymore after reduction. This is consistent with literature studies that reported the formation of $SrCrO_4$ after the annealing of chromites at high temperature in air.[17] Since no $SrCrO_3$ signal was observed after reduction, it is likely that $SrCrO_4$ formation was reversed under reducing conditions and the cations were integrated into the perovskite structure. This can be explained by the partial oxidation of Cr^{3+} species in the perovskite lattice to Cr^{6+} and the segregation of $SrCrO_4$ at the surface. In literature reports, Cr^{6+} disappeared gradually during reduction in H_2/H_2O at 700 °C, and after reduction the surface was dominated by Sr^{2+} and Cr^{3+} cations.[17b] Thus, it is likely that the observed $SrCrO_4$ on the two powders is due to the surface chemistry of the perovskite grains that differs from the bulk in oxidizing conditions.

In both oxidized powders, a NiO secondary phase could be detected. A magnification of the XRD patterns of the relevant angles is depicted in Figure S2 and shows that the NiO signal at the characteristic diffraction angles of approximately 37 and 42° is significantly stronger in the L65SCrN than in the L70SCrN sample.

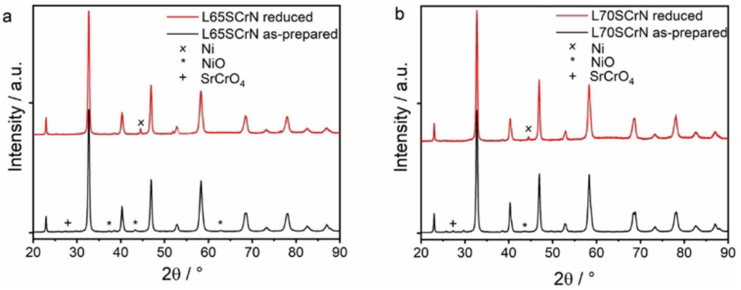

Figure 1. XRD patterns of (a) L65SCrN and (b) L70SCrN powder. Both (a) and (b) show as-prepared and reduced (5% H_2/95% N_2 at 1000 °C for 1 h) samples.

The amount of NiO in the L7SCrN perovskite was determined to be only 0.75% by Rietveld refinement (Supporting Information) and thus, it is assumed that the crystal structure is indeed stoichiometric (or close to). In the L65SCrN powder, the NiO concentration was 4.55%. Based on its nominal perovskite composition and the amount of NiO, the real cationic between A- and B-site of L65SCrN is 0.995. Thus, the composition of the perovskite phase was likely close to a stoichiometric one with an estimated A-site deficiency of <1%. The difference in La content in the supplied powders likely leads to a different La/Sr ratio that influences the electrode properties. In fact, the small shift of the perovskite peak at approximately 40° to a lower diffraction angle for the L65SCrN demonstrates that the chemical compositions of two perovskites are different. In the following, L65SCrN denotes a composite of a perovskite with A-site deficiency and reduced NiO.

After reduction, only metallic nickel could be identified as secondary phase. It is reasonable to consider that the metallic Ni phase in the reduced samples stems from both the initial NiO secondary phase and the exsolved Ni from the perovskite lattice. The observed Ni diffraction peak is rather sharp suggesting relatively large particles sizes over 100 nm. Diffraction peaks of Ni nanoparticles could be hidden in the background in this case when the amount of nanoparticles is not very high. Based on the quantified amount of NiO from the Rietveld refinement, an estimate of the TPB lengths between reduced Ni, perovskite and gas phase for both the reduced NiO and exsolved Ni was carried out and showed that the TPB length can be expected to be about one order of magnitude higher for the exsolved Ni particles due to their small particles size and, thus, dominate the electrocatalytic activity (see the Supporting Information).

Electrochemical performance

Cell performance was assessed by means of current-voltage characteristics (*i-V* curves). An initial *i-V* curve of all the cells tested in the present study is shown in Figure 2. The Ni/CGO-based cell displayed the highest performance with 0.98 A cm^{-2} at 0.6 V, which is consistent with the recently observed performance of a similar cell.[18] The cell with 25 μm thick L65SCrN electrode demonstrated a promising performance of 0.87 A cm^{-2} at 0.6 V approaching the one of the state-of-the-art Ni/CGO-based ESC. The performance of the cell with 19 μm thick electrode L70SCrN was slightly lower showing a current density of 0.81 A cm^{-2} at 0.6 V. The cell with 8 μm thick L65SCrN electrode displayed a significantly lower performance of 0.68 A cm^{-2} at 0.6 V.

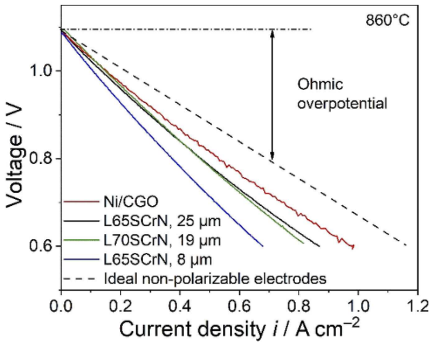

Figure 2. *i–V* curves of the tested cells at 860 °C and in 97% H_2, 3% H_2O fuel gas. The dashed curve denotes a cell with ideal non-polarizable electrodes, that is, without polarization resistance.

Anodes of all cells are depicted in Figure 3. It can be seen that the microstructure of the different L65SCrN (Figure 3a,c) and L70SCrN (Figure 3b) anodes is similar with the same grain size of approximately 300–500 nm. Since the 25 μm thick L65SCrN and the 19 μm thick L70SCrN electrode were applied onto the substrate with the same mesh, the difference in their thickness is likely due to a slightly different viscosity of the prepared inks. The Pt particles in the current collector layers are 5–10 μm large. To investigate a possible effect of Pt on the electrochemical performance, a cell without LSCrN functional fuel electrode and only brushed Pt was investigated. The *i-V* curve of the cell (Figure S1) in pure hydrogen at 860 °C shows a low maximum current density of 0.18 A cm^{-2} at 0.6 V. Thus, it can be assumed that only a small TPB length between LSCrN/Pt/gas phase with limited electro-catalytic performance is created, and the performance differences between the various cells can be ascribed to differences in behavior of the different LSCrN electrodes. The thickness of the Ni/CGO anode

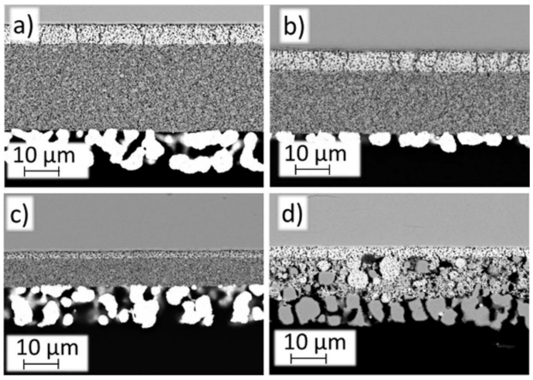

Figure 3. SEM cross-section images of the anodes investigated in the present study: (a) 25 µm thick L65SCrN anode with Pt current collector layer, (b) 19 µm thick L70SCrN anode with Pt current collector layer, (c) 8 µm thick L65SCrN with Pt current collector layer, (d) Ni/CGO anode with Ni current collector layer.

including the Ni current collector is about 25 µm and thus, comparable to Figure 3b.

In Figure 4a,b, initial impedance spectra of all cells are depicted at open circuit voltage (OCV). They show that the main reason for the highest performance of the Ni/CGO-based cell is the ohmic resistance of 0.42 Ω cm^2 which is significantly lower than for the other cells. The cells with 25 µm thick L65SCrN and 19 µm thick L70SCrN anode display similar ohmic resistance values of 0.48 and 0.49 Ω cm^2, respectively. On the contrary, the cell with 8 µm thick L65SCrN shows a considerably higher value of 0.56 Ω cm^2.

The ohmic resistance of SOC is usually assumed to be governed by the electrolyte due to its limited ionic conductivity. However, this cannot explain the different values in the present study because all cells employed the same substrate. Since the cathode is also the same in all cells (or very similar in case of LSCF/CGO), the different ohmic resistance values must be caused by the anodes. It was shown that the ionic resistivity of the ceramic matrix in the porous Ni cermet anode structures leads to losses in the polarization resistance since it is coupled to the charge transfer reaction and porous gas diffusion, and not increased ohmic resistance.[19]

Therefore, it is most likely that the increased ohmic resistance of the LSCrN electrodes in comparison to Ni/CGO is rather related to the comparatively low electronic conductivity of the perovskite. In our previous work, we observed that the p-type electronic conductivity of LSCrN decreased with decreasing pO_2, suggesting that ohmic resistance losses in the electrode are particularly high at low humidity in the fuel gas.[16] In this regard, the perovskite composition can be expected to have a significant influence on the electronic conductivity.[13] However, possible differences between L65SCrN and L7SCrN do not lead to significantly different ohmic resistance values.

Additionally, the 8 µm thick L65SCrN electrode also shows an increased polarization resistance of 0.30 Ω cm^2 in comparison to the other cells with thicker electrodes (0.17–0.2 Ω cm^2, see discussion below). The reason for the increased resistance values is probably the thickness of the electrode being below the optimum electrochemically active thickness d_{opt} as described in Ref. [20]. The electrode polarization resistance as a function of the electrode thickness is illustrated in the middle panel of Figure 5. The resistance evolution with thickness is a complex function of the geometry and material of the current collector, as well as porosity, microstructure, electronic/ionic conductivity, and electro-catalytic activity of the electrode. In addition, the in-plane electrode electronic conductivity and the ratio between electrode thickness and current collector spacing are low when the electrode thickness is low and this leads to the current restriction effect (left panel of Figure 5). $La_{1-x}Sr_xCrO_3$-based electrodes have shown decent electrical conductivity under reducing conditions (0.1–10 S cm^{-1} at 800 °C).[12b,13] Still, the electrical conductivity Ni/YSZ anodes in reducing atmosphere lies significant higher, typically above 1000 S cm^{-1}.[21] Thus, it is very likely that the performance of thin L65SCrN anodes are limited by the perovskite's electronic conductivity. This leads to a bending of the current lines in the electrode and heterogeneous current density distribution in the electrode as sketched in Figure 5 (left panel). In particularly pronounced cases, the current then almost exclusively flows under the current collectors. As a consequence, this can cause a fraction of the electrode and even the electrolyte to become inactive leading to a reduction in effective electrode/electrolyte area. Pouillet's law states the following [Eq. (1)]:

$$R = \frac{1}{\sigma} \frac{d}{A_{eff}} \tag{1}$$

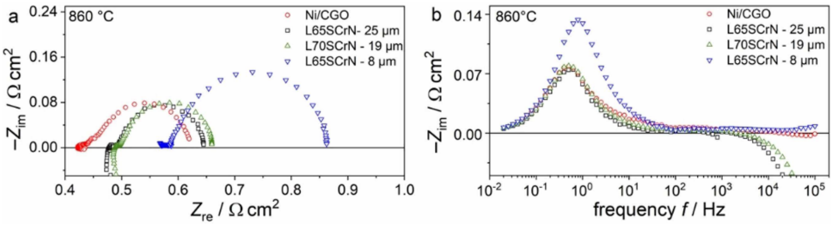

Figure 4. (a) Complex-plane and (b) imaginary impedance plots of the four tested cells at 860 °C, OCV and 97 % H_2, 3 % H_2O.

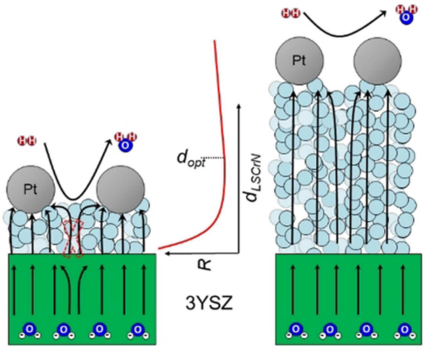

Figure 5. Schematic illustration of the current lines in electrolyte and LSCrN fuel electrode and the resistance R as function of the electrode thickness d_{LSCrN}. d_{opt} denotes the optimum electrode thickness with the lowest resistance value.

with R being the electrical resistance, σ the electrical conductivity, d the electrode thickness, and A_{eff} the effective cross-sectional area, so the ohmic and polarization resistance increase with decreasing effective area. An electrode thickness d_{opt} exists, for which the ratio d_{LSCrN}/A_{eff} is minimal.

A further increase of electrode thickness beyond the electrochemically active electrode thickness also leads to an additional ohmic resistance if the electronic conductivity of the electrode is low (Figure 5, right panel). Therefore, it is likely that further improvements in ohmic resistance can be achieved by optimizing electrode morphology and processing conditions, possibly reducing the cell resistance of the perovskite-based cells closer to the ones of state-of-the-art Ni/CGO cells.

Interestingly, the polarization resistance of the Ni/CGO-based cell (0.2 $\Omega\,cm^2$) is similar or even slightly larger than the ones of the cells with 25 µm thick L65SCrN and 19 µm thick L70SCrN anodes of 0.17 $\Omega\,cm^2$, demonstrating excellent perovskite kinetics. The polarization resistance of all three cells is dominated by a semicircle with a peak frequency of 0.5 Hz. At the peak frequency and below ($<$1 Hz) the curves of all cells coincide, which indicates that it is probably associated with the gas conversion in agreement with what we already suggested in our recent studies.[18,22] However, although the shape of this low frequency contribution is the same for all cells, the gas conversion resistance is generally strongly dependent on variations of the steam content at the present operating conditions ($pH_2O = 0.03$ bar), which could be caused by small deviations in sealing and/or gas flow rates. In addition, the inlet gas is humidified with a water bubbler the exact temperature of which can show small variations depending on the room temperature. Thus, minor differences between the gas conversion resistance values cannot be excluded.

Moreover, for Ni/CGO-based cells of the same type as used in the present study, we have reported the peak frequency of the anode charge transfer process to be between 1–10 Hz.[18,23] The impedance response at these frequencies is also increased in comparison with the cells with 25 µm thick L65SCrN and 19 µm thick L70SCrN anodes and responsible for the difference in polarization resistance between the cells. The increased polarization resistance of the cell with 8 µm thick L65SCrN electrode is mainly caused by an increased impedance response at frequencies of approximately 1 Hz. Therefore, it is concluded that the L65SCrN anode process lies at frequencies of 1–10 Hz similar to the Ni/CGO anode process. However, since anode processes and gas conversion contribution overlap in the impedance spectra, it is difficult to quantify the anode resistance.

Moreover, the cell resistance at OCV at such a high temperature is mainly dominated by the ohmic resistance, which impedes the assessment of the difference in performance of the two perovskite electrodes. Nevertheless, both the ohmic and polarization resistance of the cell with L65SCrN perovskite were shown to be slightly decreased in comparison to the cell with stoichiometric electrode. This is also in accordance with a study observing the same trend by comparing stoichiometric L73SCrNi15 and A-site deficient L63SCrNi15, although in the present study the difference is not as pronounced.[8d] In the cited study, a significant increase in (electro-)catalytic electrode activity of A-site deficient perovskite electrodes was demonstrated at 800 °C. These effects were related to the increased oxygen vacancy formation caused by A-site deficiency which enhanced the mobility of the lattice oxygen and increased Ni nanoparticle density on the surface. The authors reported a sixfold decrease in polarization resistance by employing an A-site deficient perovskite. Although the compositions of the perovskites used in their and in our recent study are different,[16] the behaviors in terms of thermogravimetric analysis (TGA) and XRD measurements were similar, showing 2.5 % oxygen weight loss at 900 °C upon reduction and the characteristic Ni peaks in the A-site deficient perovskite materials. However, we could not observe a performance-enhancing effect of similar magnitude. One reason could be that in the present work, the perovskite phase in L65SCrN is probably close to stoichiometry. An A-site deficiency of less than 1 %, as discussed above is likely not to be sufficient to induce a significant enhancement over the L70SCrN. The difference in La/Sr ratio and in nickel concentration on B-site among the two perovskites as estimated in the Supporting Information may also account for the small performance gain observed in the cell with L65SCrN electrode.

Another reason that not a larger difference between the two-chromite based electrode is observed is the different operating temperatures between the present study (860 °C) and the study by Sun et al (800 °C).[8d] The change of operating temperature could lead to a different role of Ni in the hydrogen oxidation mechanism. Two main effects of the formation of distributed metallic Ni particles on MIEC oxide anodes can be anticipated. First, it may facilitate dissociative adsorption of hydrogen.[24] Second, it can favor the subsequent charge transfer reaction at the TPB that depending on the system, can either occur via hydrogen spillover, oxygen spillover or even via an interstitial bulk hydrogen transfer.[25] For example, it has been indicated that for Ni/YSZ anodes adsorbed surface oxygen shows an intermediate stability on Ni and thus, facilitates the charge transfer kinetics according to the Sabatier principle.[26] However, the latter effect only occurs if Ni-bound intermediates actively take place in the rate-limiting step (often the charge transfer reaction). If the charge transfer reaction occurs on the oxide surface at the perovskite/gas phase double phase boundary (DPB), Ni addition is not expected to have an influence on its kinetics. This was for example shown to be the case for Ni/CGO anodes when the CGO/gas phase DPB is large in comparison to the TPB.[1a,4c] In such electrodes it was suggested that the rate-limiting step occurs on the CGO surface without significant (electro-)catalytic contribution of the Ni phase. Then the role of Ni is only to dissociate hydrogen and to provide electronic conductivity to the electrode. This means that in case of Ni cermet electrodes where hydrogen dissociation on the ceramic phase is sufficiently fast, Ni does not necessarily play an electrocatalytic role during hydrogen oxidation.

The slightly increased performance of the L65SCrN electrode in comparison to L70SCrN could indeed indicate an increased surface area and, thus, increased availability of Ni active sites and their promoting effect on hydrogen oxidation kinetics. The presence of nickel particles originating from the NiO secondary phase likely did not cause the improvement of the polarization resistance because the resulting TPB length is likely far less than the one resulting from surface exsolved nanoparticles (see the Supporting Information). The only limited performance gain indicates that Ni does not actively contribute to the charge transfer step. The small performance gain could then suggest that hydrogen dissociation occurs on Ni but is probably not the rate-limiting step under the investigated conditions. Possibly, this could rather be the charge transfer reaction occurring at the DPB between the perovskite and the gas phase after a hydrogen spillover from Ni. Since the operating temperature of 860 °C is high, it is possible that at lower temperatures they start to lead to more significant kinetic losses.

Since the kinetics are also dependent on the amount of Ni active sites, differences might become more apparent at lower temperatures. The change of rate-limiting step during hydrogen oxidation on perovskites depending on temperature was also suggested by Zhu et al. who observed improved anode performance of $Sr_{0.95}(Ti_{0.3}Fe_{0.63}Ni_{0.07})O_{3-\delta}$ in comparison to the Ni-free $SrTi_{0.3}Fe_{0.7}O_{3-\delta}$ particularly at temperatures below 800 °C and low pH_2.[27] The authors proposed that Ni–Fe nanoparticle exsolution enhances hydrogen dissociative adsorption, which had been identified as key fuel oxidation rate-limiting step at these conditions in a previous study.[28] However, at conditions similar to the ones in the present study (850 °C, 97 % H_2, 3 % H_2O) the performance of both cells was similar.

In addition, it has been shown that in the case of $La_{0.8}Ce_{0.1}Ni_{0.4}Ti_{0.6}O_3$ exsolved nanoparticles can also be submerged in the bulk of the host perovskite which can induce strain in the lattice and enhance oxygen transport.[29] This bulk exsolution process seems to be particularly favored by A-site deficiency and high operating temperatures, where the relatively high energy barriers associated with nucleation and growth within an oxide lattice that arise from strain and oxide lattice reconstruction around the particle can be overcome. Thus, providing that exsolution of nanoparticles may be favored in L65SCrN due to its composition and/or small A-site deficiency it cannot be excluded that bulk and not only surface Ni particles contribute to the performance gain.

Nevertheless, the electro-catalytic activity of both tested chromites reaches the one of a state-of-the-art Ni/CGO anode at 860 °C although it is hard to clearly identify the origin of the small performance enhancement in the L65SCrN electrode.

To further demonstrate the influence of the different electrodes on cell performance, the ohmic overpotential of the Ni/CGO-based cell was calculated by multiplying the ohmic resistance with the current density (Figure 2). The ohmic resistance was obtained from the Nyquist plot in Figure 4a and assumed to be constant over the whole investigated potential range. By subtracting the obtained values from the OCV, the *i-V* curve of an ideal non-polarizable electrode can be calculated. This has been done for the Ni/CGO-based cell since metallic nickel is an excellent electronic conductor and thus, Ni/cermet electrodes are usually assumed to not display any losses caused by electronic resistivity. Thus, in Figure 2 the *i-V* curve of a cell with two ideal non-polarizable electrodes, that is, no anode/cathode resistance and also no mass transport resistance, is depicted. The difference between this hypothetical curve and the actually measured *i-V* curves can then be ascribed to the polarization resistance of the cell. The graph clearly demonstrates that all cells' performance behavior is strongly dominated by the ohmic overpotential. Considering the favorable electrochemical performance of the 25 μm thick L65SCrN and 19 μm thick L70SCrN perovskite electrodes (based on electrochemical impedance spectra), the difference between their *i-V* curves and the one of Ni/CGO can almost exclusively be attributed to their larger ohmic losses and thus, to their limited electronic conductivity.

The comparatively small difference of 0.18 A cm^{-2} at 0.6 V between the polarization curve of the Ni/CGO-based ESC (0.98 A cm ^{2}) and the hypothetical curve with two ideal non-polarizable electrodes (1.16 A cm^{-2}) illustrate the potential improvement in cell performance by further optimizing the electrode kinetics of the anode. If electrocatalytic activity of the LSCrN based electrode is already sufficient under the given conditions (860 °C), improvement of current collection in the LSCrN based electrode represent the key challenge to match performance of state-of-the-art Ni/CGO anodes.

Sulfur poisoning effect

As a next step, the performance of two cells with 25 μm thick L65SCrN and 19 μm thick L70SCrN electrode was assessed at 0.5 A cm^{-2} with and without the addition of 20 ppm H_2S in the fuel gases. The evolution of the voltage over time during the poisoning tests is depicted in Figure 6.

Consistent with the *i-V* curves in Figure 2, the initial voltage of 0.777 V of the cell with L65SCrN electrode is slightly higher than the 0.769 V observed for the L70SCrN electrode. After 1 h of voltage stabilization, 20 ppm H_2S were introduced into the fuel gas. This led to the nearly same rapid voltage drop of 35 and 34 mV for the L65SCrN and the L70SCrN electrode, respectively. After 1.5 h of poisoning, the cells were recovered by switching off the sulfur supply. This led to a nearly full regeneration of the initial voltage after 15 h. The effect of the

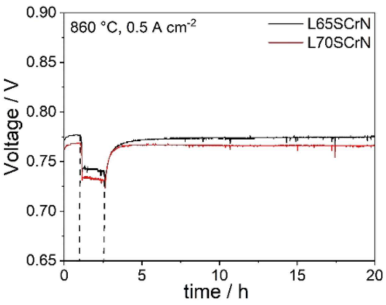

Figure 6. Transient sulfur poisoning test at 860 °C and 0.5 A cm−2 for cells with 25 μm thick L65SCrN and 19 μm thick L70SCrN electrode. After 1 h in sulfur-free conditions, 20 ppm H_2S were introduced. After 1.5 h, the sulfur supply was switched off again.

sulfur poisoning on the impedance spectra at 0.5 A cm−2 is shown for the cells with L65SCrN and the L70SCrN electrode in Figure 7. Both cells show the same behavior of a pronounced increase in polarization resistance related to the anode contribution at approximately 1 Hz with no change of the ohmic resistance.

The observed pronounced sensitivity of the electrode to sulfur poisoning is in agreement with our recent observations about Ni/CGO and Ni/YSZ anodes, where we could correlate the rapid voltage drop with Ni surface blockage by adsorbed sulfur atoms.[1,30] Therefore, it is reasonable to assume a comparable phenomenon for the exsolved Ni nanoparticles on the perovskite surface. The voltage drops of approximately 35 mV at 860 °C in the present study are significantly lower than the values of more than 150 mV observed for Ni/YSZ at 850 °C at the same current density and gas phase conditions, which demonstrates the superior tolerance of LSCrN electrodes compared to Ni/YSZ cermets. However, this is still 3.5 times higher than the values we observed for Ni/CGO cermets.[1a] Therefore, considering the above-mentioned anode materials in ESC configuration, the ranking regarding their tolerance towards sulfur poisoning is Ni/CGO > LSCrN ≫ Ni/YSZ.

Although we suggested the hydrogen dissociation not to be rate-limiting at 860 °C in sulfur-free hydrogen, this might change upon addition of 20 ppm H_2S which will lead to an estimated sulfur coverage of 0.83 on Ni according to the Temkin-like isotherm derived by Alstrup et al.[31] This will block the Ni surface to a large extent for hydrogen adsorption and dissociation and, thus, lead to an increase of the anode polarization resistance.

Interestingly, Sun et al. observed a promoting effect of 5000 ppm H_2S on hydrogen oxidation at 800 °C.[8d] They suggested that the hydrogen sulfide may adsorb on the surface oxygen site of the perovskite to form a H_2–S–O bond that is an effective carrier for H_2 to react with oxygen ions since the H–S bond might be easier to break than the H–H bond. Such a promoting effect could not be observed in our study. At the significantly lower H_2S content that we have used, it is likely that the observed performance drop is mostly due to the deleterious effect of the formation of the Ni–S bond on the surface of the exsolved nickel particles. Thus, the different behavior would be due to a different nature of the sulfur-electrode interaction that might become favorable at higher sulfur concentrations and/or lower temperature. Indeed, at typical SOFC operating temperatures and low H_2S concentrations sulfur does not only adsorb on the Ni surface but reacts to Ni sulfide compounds at concentrations of 1000 ppm or higher.[8d]

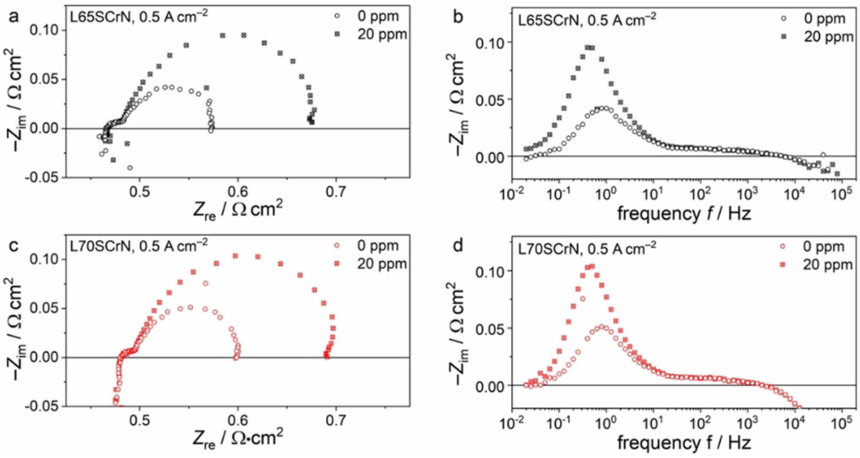

Figure 7. Complex-plane and imaginary impedance plot of the electrochemical impedance spectra of the cells with 25 μm thick (a,b) L65SCrN and (c,d) 19 μm thick L70SCrN electrode with and without the addition of 20 ppm H_2S.

ChemSusChem
Full Papers
doi.org/10.1002/cssc.202100330
Chemistry Europe
European Chemical Societies Publishing

Durability and redox stability of L65SCrN

Durability and redox stability were investigated with the L65SCrN anode that reached a higher cell performance than L70SCrN (see Figure 2). Cells with 8 µm and 25 µm thick LSCr65N anodes were compared in order to further understand their behavior (Figure 2).

Cell with 8 µm thick anode

Figure 8a shows the voltage evolution of two nominally equal cells with 8 µm thick anode that were operated at 0.5 A cm^{-2} exposed to several redox cycles (RC) by purging the anode chamber with air for 45 min. The testing protocol of the cells is reported in Table 1. In the protocol, cell 2 went through four redox cycles, whereas cell 1 only through one. For both cells, the time under polarization led to a severe voltage degradation that has been recovered after each redox cycle.

The effect of a redox cycle on the cell impedance spectra is exemplified in Figure 9 for cell 2. After the second redox cycle impedance spectra show both a reduced ohmic and polarization resistance. In the polarization resistance the peak frequency of the affected process lies at approximately 1 Hz confirming the assignment of this frequency region to an anode process as suggested in the previous subsection. A breakdown of the cell resistance before and after each redox cycle into ohmic and polarization losses for both cells is depicted in Figure 10.

Table 1. Protocol of redox cycling test of the two cells with 8 µm thick L65SCN electrodes.

Time period [h]	Testing conditions Cell 1	Cell 2
<0	18 h reduction in H_2	
0–94	Constant current density of 0.5 A cm^{-2}	
94–97	OCV (current cycle)	
97–116	Constant current density of 0.5 A cm^{-2}	
117	**Redox cycle 1**	
120–188	Constant current density of 0.5 A cm^{-2}	
189	OCV, 5% H_2, 95% N_2	**Redox cycle 2**
192–196	Constant current density of 0.5 A cm^{-2}	
197–259	OCV, 5% H_2, 95% N_2	
260–264	Constant current density of 0.5 A cm^{-2}	
265	OCV, 5% H_2, 95% N_2	**Redox cycle 3**
266–231	Constant current density of 0.5 A cm^{-2}	
332	OCV, 5% H_2, 95% N_2	**Redox cycle 4**
333	Cool-down, 5% H_2, 95% N_2	

Between the initial reduction and the first redox cycle after 117 h, both cells showed significant degradation. In this period, the cell voltages decreased by 128 and 50 mV for cell 1 and cell 2, respectively. Nevertheless, the observed voltage drops may have different origins. For cell 1 this was nearly equally due to an increase of the ohmic and the polarization resistances. Both contributions were entirely recovered to their initial values after redox cycle 1. For cell 2, on the contrary, the voltage decrease was almost entirely attributed to a significant increase in polarization resistance, while the ohmic resistance even

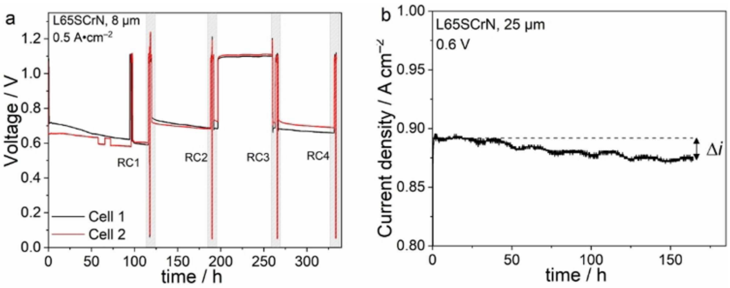

Figure 8. (a) Life cycle of the cell with 8 µm thick L65SCrN anode with indication of the RC. (b) Durability test of the cell with 25 µm thick L65SCrNat 0.6 V. All measurements were performed at 860 °C.

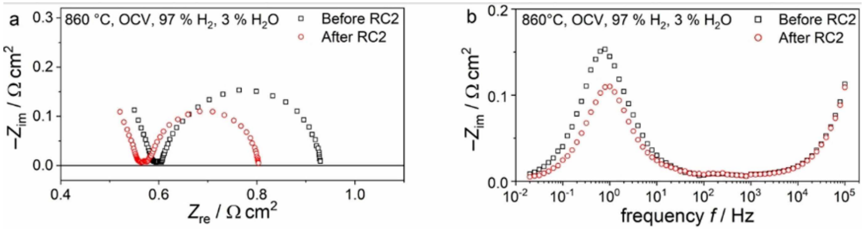

Figure 9. (a) Complex-plane and (b) imaginary impedance plots of the electrochemical impedance spectra of the cells with 8 µm thick L65SCrN before and after RC 2.

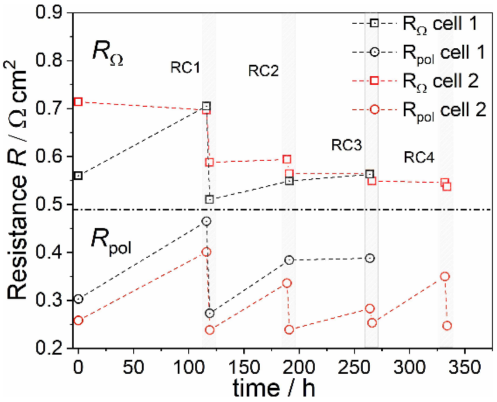

Figure 10. Evolution of ohmic and polarization resistance of the cells with 8 µm thick L65SCrN electrodes during 4 RC.

decreased slightly in the first 117 h. Despite different initial values of R_{ohm} for cell 1 and cell 2, they converged to a comparable value of approximately 0.7 Ω cm^2 after 117 h, and the performance of both cells was comparable with a voltage of 0.741 and 0.716 V at 0.5 A cm^{-2} for cell 1 and cell 2, respectively. Beyond this time, the ohmic resistance evolved differently for the two cells. Cell 1 achieved the lowest R_{ohm} value after RC1, while the value continuously deteriorated with time afterwards. For cell 2 on the contrary, the R_{ohm} value improved with each occurrence of a redox cycle, so that the lowest value was measured after RC4. This difference in behavior could be assigned to a specific evolution of the contacting at the oxygen electrode and its interface with the gold mesh due to creeping at high temperature as we already observed in previous experiments in our testing set up. This effect led to a better contacting of the cells over time and thus, a decrease in ohmic resistance. The effect was more pronounced for cell 2 explaining its lower initial performance and smaller initial degradation rate. Thus, it is likely that a faulty contacting of cell 2 accounted for the difference in evolution of the R_{ohm} between the two samples.

Redox cycles 2, 3, and 4 were only carried out for cell 2. In between each cycle the cell operation mainly led to an increase in polarization resistance and an only minor increase in ohmic resistance. After each new redox cycle, the degradation was fully recovered. The degradation rate of the polarization resistance in each step was similar when the cell was operated at 0.5 A cm^{-2} ($\Delta R_{pol0,1} = 0.123$ Ω cm^2/100 h; $\Delta R_{pol1,2} = 0.14$ Ω cm^2/100 h; $\Delta R_{pol3,4} = 0.147$ Ω cm^2/100 h). However, it significantly reduced when the cell was left at OCV between redox cycle 2 and 3 ($\Delta R_{pol2,3} = 0.06$ Ω cm^2/100 h). Since the fuel utilization at 0.5 A cm^{-2} was only 6 % and thus, the change in steam content in the fuel gas compartment was low, these findings suggest the anodic bias to be the reason for the increased degradation rate under current.

In order to correlate the influence of redox cycling on cell performance with changes in the L65SCrN electrode material, cell 2 was recovered by exposure to RC4 before cooling down, while cell 1 had been operated for more than 200 h after the last redox cycle and was cooled down without redox cycling. Both cells were cooled down in forming gas with 5 % H_2 and 95 % N_2. Figure 11 shows a comparison of the two fracture surfaces.

The degraded cell 1 (Figure 11a) shows a few nanoparticles of approximately 50 nm diameter on top of the perovskite surface (orange circles). However, the recovered cell 2 (Figure 11b) depicts a significantly greater amount of Ni nanoparticles of approximately 10–20 nm particle size.

The presence of fewer nanoparticles may indicate a change in the oxidation state of the perovskite due to the anodic bias in SOFC operation, which probably leads to changes in the defect chemistry of the perovskite. This could have a significant effect on the perovskite's transport properties and surface chemistry, including the presence of Ni nanoparticles. Ni exsolution occurs via the reduction of Ni from the (+II or +III) state to a neutral charge [Eq. (2)]:

$$\mathrm{Ni}^{n+} + ne \rightleftharpoons \mathrm{Ni}^0;\ n = 2, 3 \qquad (2)$$

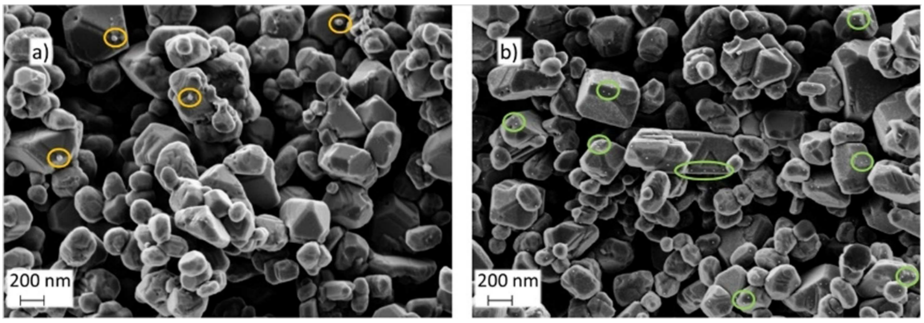

Figure 11. SEM images of the fractured 8 µm thick L65SCrN electrodes of the (a) degraded cell (b) and the cell that was exposed to a redox cycle before cooldown. (a) Orange and (b) green circles are shown to highlight the nanoparticles.

where the electrons e are supplied by the oxygen contained in the perovskite upon the reaction with hydrogen. Thus, the electron loss may counteract the chemical reduction of the anode at OCV (860 °C with 3 % H_2O/H_2) and favor the formation of Ni^{2+}/Ni^{3+} with a subsequent re-incorporation of Ni nanoparticles into the perovskite lattice as Ni cations.

Similarly fast degradation as for the 8 µm thick L65SCrN electrode has been reported in literature for stoichiometric LSCrN perovskite anodes and was correlated with Ni agglomeration.[8a,13] Exsolved Ni particles agglomerated on a chromite anode at 800 °C and OCV over 300 h, while Ru particles were more stable. This behavior was suggested to be caused by the high surface diffusivity of Ni in comparison to Ru metal particles on chromite surfaces. The nanoparticle size was also reported to increase with reduction time for other parent perovskites.[32] The presence of larger nanoparticles on the degraded electrode in Figure 11a is consistent with this proposed particle growth mechanism. It is even possible that particle agglomeration and incorporation under anodic bias occur simultaneously.

The presence of numerous small nanoparticles in Figure 11b indicates their regeneration by redox cycling, which correlates well with the performance recovery observed after each redox cycle. This is also in agreement with previous studies, that suggested Ni reincorporation into the chromite lattice upon oxidation and exsolution back to the surface as small, well-dispersed metallic particles after every reduction step.[8d,e,10a] Such fully reversible exsolution and dissolution after redox cycling has recently been observed by transmission electron microscopy (TEM), energy-dispersive X-ray spectroscopy (EDX), and XRD for CoFe alloy nanoparticles in $La_{0.4}Sr_{0.6}Co_{0.2}Fe_{0.7}Mo_{0.1}O_{3-\delta}$ and Co-doped $Sr_2Fe_{1.5}Mo_{0.5}O_{6-\delta}$.[32,33] In a few publications, it was suggested that exsolved particles do not necessarily dissolve back into the bulk, and are still present on the surface in their oxidized state.[34] However, this was mainly observed between 500–700 °C and probably related to the sluggish kinetics at such low temperatures. Furthermore, the oxidized particles could still be observed by scanning electron microscopy (SEM). Based on the SEM analysis in Figure 11 we report that it is likely that Ni nanoparticles in the present work can be re-incorporated into the lattice.

However, compared to what we observed recently on L65SCrN powders reduced at 900 °C,[16] the sample exposed to a redox cycle before cooling showed a significantly reduced population density of Ni nanoparticles. The phase transformation of Ni exsolution has been shown to proceed with prolonging time,[8b,32] and since the redox-cycled electrode was only operated in hydrogen for 1 h before cooling down, it is possible that equilibrium had not been reached.

In any case, the observed increased degradation under anodic bias contrasts to the operation of electrodes with extensive Ni exsolution in electrolysis mode, where Ni exsolution was shown to be favored since the equilibrium of Equation (2) is shifted to the right side.

In addition to SEM/EDX analysis, the two electrodes were characterized by XRD. For this purpose, the Pt current collectors were scratched off and the samples were analyzed from a top view perspective (Figure 12). All the layers down to the 3YSZ electrolyte were identified by XRD with only minor unknown peaks (marked with X around 31 and 55°). A possible candidate of this minor phase is the $La_2Sr_2PtO_7$ perovskite, however, it is not yet clearly identified.[35] No significant differences could be observed in the diffraction patterns of the two samples. Therefore, it can be excluded that large-scale phase transformations of the L65SCrN electrode occur during SOFC degradation that are reversed by redox cycling. The observed perovskite phase corresponds to the one observed in the powder in Figure 1 and metallic Ni was detected in both samples, which is an overlap of the Ni that stems from the initial NiO secondary phase and the nanoparticles formed on the surface and in the bulk. Since the intensity and width of these peaks in both samples are similar, no quantitative

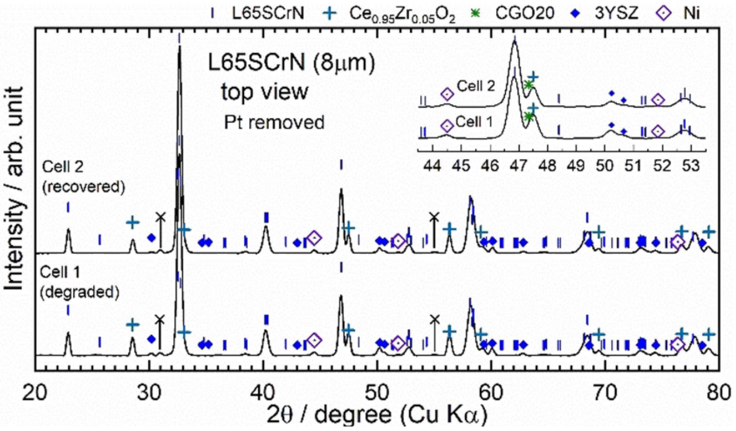

Figure 12. XRD patterns of the 8 µm thick L65SCrN electrodes of the degraded cell, and the cell that was exposed to a redox cycle before cool-down.

difference can be reported. The characteristic peaks of two fluorite phases were observed, which correspond to the 3YSZ and CGO20 layers. The peaks of the CGO20 layers are shifted to slightly higher angles than the cubic fluorite CGO20 phase (PDF#01-080-5535). This lattice shrinkage can be explained by the formation of an interdiffusion zone between CGO and YSZ that results in a solid solution phase of ceria and zirconia.[36]

In any case, the large differences in morphology from our recent study suggests that based on a post mortem analysis of the perovskite surfaces by SEM, their in situ state cannot be inferred.[16] Thus, no detailed information about possible microstructure-related degradation phenomena such as Ni coarsening or Ni re-integration into the lattice can be given. More detailed experiments will be carried out in the future to further explore the observed effect.

Cell with 25 μm thick anode

Figure 8b shows a potentiostatic durability test at 0.6 V over 175 h for a cell with the 25 μm thick electrode. The cell only shows a current density decrease of 19 mA cm^{-2} from 0.893 to 0.874 V over the entire course of the experiment. Although the operating conditions were different from the test of the cells with 8 μm thick anodes, this 2% voltage decrease over 175 h represents a significantly lower performance loss than the ones observed for the cells with thinner electrodes. After the 175 h, the cell was exposed to a redox cycle and then cooled down. The cell did not show a recovery effect upon redox cycling which suggests a different origin of its degradation that seems to be irreversible in contrast to the one observed for the cells with 8 μm thick anodes.

Based on the observed influence of anode overpotential on performance degradation for the 8 μm thick electrode and the impact of the current restriction on L65SCrN electrode performance, it is likely that the combination of these effects is responsible for the increased stability of the 25 μm thick electrode.

We showed L65SCrN degradation in the 8 μm thick electrode to be strongly potential-dependent with more severe degradation at lower cell potential. However, as discussed above the 8 μm thick electrode is operated at significantly larger anode overpotential due to the current restriction effect. Therefore, the 8 μm thick electrode shows a reduced effective electrochemically active surface area and a larger current density per effective electrochemically active surface area. This leads to a reduced local potential step (i.e., increased local overpotential) in the electrochemically active area which entails increased degradation. According to this hypothesis, it is likely that the decreased stability of the 8 μm thick L65SCrN electrode can be explained by a less homogeneous current distribution along the cell. According to Equation (2) metallic Ni is less stable if the electrode is operated at a low cell potential, that is, high anode overpotential, and it is possible that at such conditions the exsolved Ni is re-incorporated into the perovskite lattice as Ni^{2+}/Ni^{3+}. Alternatively, the strongly potential-dependent degradation behavior could possibly be due to enhanced Ni particle coarsening at high anode overpotentials.

Conclusions

Ni-doped chromite anodes were successfully integrated into electrolyte-supported cells (ESC) with 5×5 cm^2 size and their performance, durability, redox stability, and sulfur tolerance was investigated in solid oxide fuel cell (SOFC) operation with H_2/H_2O fuel gas. In comparison to infiltration techniques that lead to rapid performance losses due to fast particle agglomeration, the present study uses an industrially more viable approach to incorporate Ni nanoparticles into the anode via exsolution. Ni nanoparticles are formed on the perovskite surface in situ upon reduction. In comparison to the stoichiometric $La_{0.7}Sr_{0.3}Cr_{0.85}Ni_{0.15}O_{3-\delta}$ (L70SCrN) electrode, a nominal $La_{0.65}Sr_{0.3}Cr_{0.85}Ni_{0.15}O_{3-\delta}$ (L65SCrN)-based cell showed slightly better performance due to previously observed, enhanced Ni exsolution. Cells with both chromite anodes showed promising performance approaching the ones of state-of-the-art Ni/gadolinium-doped ceria (Ni/CGO) anode-based cells. The difference was shown to originate from an increased ohmic resistance of the chromite electrodes, while similar polarization resistance values were observed. 25 μm thick L65SCrN electrodes exhibited both superior performance and stability in comparison to 8 μm thick electrodes. The difference can be explained by the current restriction effect in the thinner anode. The chromite-based anodes showed a strongly potential-dependent degradation behavior that is likely related to Ni nanoparticle coarsening on the perovskite surface, or Ni re-integration into the lattice. Redox cycling led to recovery of the anode degradation due to re-integration of the Ni particles into the perovskite lattice. Sulfur poisoning with 20 ppm hydrogen sulfide led to rapid voltage drops of 35 mV at 0.5 A cm^{-2}. Discussion of the mechanism leads to the conclusion that Ni nanoparticles facilitate hydrogen dissociation to the extent that it is not rate-limiting at the investigated temperature unless an insufficiently thick electrode thickness is employed or sulfur impurities are present in the feed gas. Hence, approaches for future research could be the increase of the electronic conductivity of Ni-based chromite anodes by tuning the phase composition or by adding a highly electronically conductive second phase. At the high operating temperatures of 860 °C used in this study, the electrocatalytic activity of LSCrN anodes with Ni exsolution is sufficient to compete with state-of-the-art Ni/CGO electrodes. However, if lower operating temperatures are targeted, the performance of the perovskite anodes should be re-evaluated.

Experimental Section

LSCrN powder crystallographic characterization

$La_{0.65}Sr_{0.3}Cr_{0.85}Ni_{0.15}O_{3-\delta}$ (L65SCrN) and $La_{0.7}Sr_{0.3}Cr_{0.85}Ni_{0.15}O_{3-\delta}$ (L70SCrN) powders were supplied by Marion Technologies (Verniolle, France) with particle size diameters of approximately 300–500 nm. To ensure compatibility with our previous study,[16] the crystalline structure of both commercial powders were analyzed (before and after reduction) by XRD using a D8 ADVANCE (BRUKER AXS GmbH, Germany) diffractometer with a CuK_α radiation source operating at 40 kV and 40 mA in Bragg-Brentano geometry. A variable divergence slit (12 mm) was used for the primary optics and soller slits (2.5°) were used for both the primary and secondary sides. Diffraction signal was collected by the LYNXEYE XE-T in 2θ

range of 10–135° with a scanning rate of 0.4 s per step and an increment step of 0.02°. High energy resolution mode was used on the LYNXEYE XE-T to filter the fluorescent emission from Ni.

Cell manufacturing

L65SCrN and L70SCrN inks were prepared by dispersing the perovskite powder in a 94 wt% α-terpineol and 6 wt% ethyl cellulose solution with a powder/solution ratio of 2:1 and then mixing in a 3-roll mill. Subsequently, different ESC were manufactured by using a commercial square substrate (5×5 cm^2 and 90 μm thickness) of 3 mol% Y_2O_3-doped ZrO_2 electrolytes coated on both sides with $Ce_{0.8}Gd_{0.2}O_{2-\delta}$ (CGO20) from Kerafol GmbH (Eschenbach, Germany). As anodes, 4×4 cm^2 L65SCrN and L70SCrN perovskites were implemented via screen-printing. Two different mesh thicknesses were used for the L65SCrN anode to obtain different electrode thicknesses of approximately 8 and 25 μm (after firing). For the L70SCrN anode, only the latter mesh was using during the screen-printing to produce an electrode with a thickness of 19 μm. The resulting half cells were fired at 1200 °C for 1 h in air with a heating rate of 3 Kmin ^{1}. Afterwards, the cathode was screen-printed on the other side of the electrolyte with a commercial ink of $La_{0.58}Sr_{0.4}Fe_{0.8}Co_{0.2}O_{3-\delta}$ (LSCF) supplied by Heraeus GmbH (Hanau, Germany) resulting in a cathode thickness of approximately 20 μm. Pt paste was brushed on the sintered anode surface for current collection. Then, the cell was fired at 1050 °C for 1 h in air with a heating rate of 3 Kmin^{-1}.

Furthermore, state-of-the-art cells supplied by Sunfire GmbH (Dresden, Germany) were used as a reference. They are based on the same CGO20(5 μm)|3YSZ (90 μm)|CGO20 (5 μm) sandwich structure as the cells in the present work. A Ni/CGO20 anode was deposited including a functional layer and a more porous current collector layer with increased Ni content. On the cathode side, a LSCF/CGO composite cathode with a LSCF current collector layer was used.

Electrochemical characterization

The setup for cell testing enables the characterization of up to four cells simultaneously under variation of current density and has been illustrated and described in detail elsewhere.[1a,30] The high reproducibility of measurements between the different positions has been demonstrated in previous studies.[1b,18,37] All cells were operated at 860 °C with 97% H_2 and 3% H_2O at a constant total fuel flow rate of 1 L min^{-1} for every cell. H_2S was taken from a pressurized H_2S/H_2 bottle that contained 200 ppm H_2S. The cathode was operated with air at a constant flow rate of 1 SLPM. The cells were heated (3 K min ^{1}) to 900 °C for sealing and reduction. Proper sealing of all cells was ensured by confirming the OCV to be higher than 1.2 V in pure hydrogen. Pt and Au meshes were used for contacting on the anode and the cathode side, respectively.

Electrochemical impedance spectroscopy (EIS) was performed by means of an electrochemical workstation (Zahner® PP-240 with Thales software) in a frequency range from 20 mHz to 100 kHz with 10 points per decade. The amplitude of the current stimulus was chosen to be 500 mA. SEM images were acquired using a Zeiss Ultra Plus SEM. XRD analysis of the cells was also performed after the test operation using D8 Discover GADDS equipped with a VÅNTEC-2000 area detector (Bruker AXS, Germany). The diffraction pattern was recorded in the Bragg-Brentano geometry with a tuned monochromatic and collimated CuK$_\alpha$ radiation source.

Acknowledgements

The German Academic Exchange Service (DAAD) is acknowledged for the Ph.D. scholarship of D.-M.A.-D. We gratefully acknowledge financial support from the German Ministry for Economic Affairs and Energy (BMWi) within the framework of the project "Kostenoptimierter Stack und verbessertes Offgrid-System (KO-SOS)" via grant number 03ETB005C. Christian Geipel and Christian Walter from Sunfire are acknowledged for the supply of cells. Regis Jardin and Jürgen Domes from Bruker AXS are acknowledged for XRD powder diffraction. Feng Han is acknowledged for advice with regards to cell manufacturing. Open access funding enabled and organized by Projekt DEAL.

Conflict of Interest

The authors declare no conflict of interest.

Keywords: electrocatalysis · exsolution · fuel cell · perovskite · solid oxide cells

[1] a) M. Riegraf, M. P. Hoerlein, R. Costa, G. Schiller, K. A. Friedrich, *ACS Catal.* **2017**, *7*, 7760–7771; b) M. Riegraf, A. Zekri, M. Knipper, R. Costa, G. Schiller, K. A. Friedrich, *J. Power Sources* **2018**, *380*, 26–36.
[2] a) P. Boldrin, E. Ruiz-Trejo, J. Mermelstein, J. M. Bermudez Menendez, T. Ramirez Reina, N. P. Brandon, *Chem. Rev.* **2016**, *116*, 13633–13684; b) J. Mermelstein, M. Millan, N. Brandon, *J. Power Sources* **2010**, *195*, 1657–1666; c) B. Iwanschitz, J. Sfeir, A. Mai, M. Schütze, *J. Electrochem. Soc.* **2009**, *157*, B269–B278.
[3] M. Mogensen, *Solid State Ionics* **2000**, *129*, 63–94.
[4] a) C. Zhang, M. E. Grass, A. H. McDaniel, S. C. Decaluwe, F. E. Gabaly, Z. Liu, K. F. McCarty, R. L. Farrow, M. A. Linne, Z. Hussain, G. S. Jackson, H. Bluhm, B. W. Eichhorn, *Nat. Mater.* **2010**, *9*, 944–949; b) Z. A. Feng, F. El Gabaly, X. Ye, Z. X. Shen, W. C. Chueh, *Nat. Commun.* **2014**, *5*, 1–9; c) W. C. Chueh, Y. Hao, W. Jung, S. M. Haile, *Nat. Mater.* **2012**, *11*, 155–161.
[5] a) M. C. Tucker, *J. Power Sources* **2017**, *369*, 6–12; b) S. P. Jiang, *Int. J. Hydrogen Energy* **2012**, *37*, 449–470.
[6] a) S. Kavurucu Schubert, M. Kusnezoff, A. Michaelis, S. I. Bredikhin, *J. Power Sources* **2012**, *217*, 364–372; b) A. Mai, B. Iwanschitz, U. Weissen, R. Denzler, D. Haberstock, V. Nerlich, A. Schuler, *ECS Trans.* **2011**, *25*, 87–95; c) D. Udomsilp, J. Rechberger, R. Neubauer, C. Bischof, F. Thaler, W. Schafbauer, N. H. Menzler, L. G. J. de Haart, A. Nenning, A. K. Opitz, O. Guillon, M. Bram, *Cell Rep. Phys. Sci.* **2020**, *1*, 100072; d) R. T. Leah, A. Bone, M. Lankin, A. Selcuk, M. Rahman, A. Clare, L. Rees, S. Phillip, S. Mukerjee, M. Selby, *ECS Trans.* **2015**, *68*, 95–107.
[7] L. Shu, J. Sunarso, S. S. Hashim, J. Mao, W. Zhou, F. Liang, *Int. J. Hydrogen Energy* **2019**, *44*, 31275–31304.
[8] a) W. Kobsiriphat, B. D. Madsen, Y. Wang, M. Shah, L. D. Marks, S. A. Barnett, *J. Electrochem. Soc.* **2010**, *157*, B279–B279; b) D. Neagu, G. Tsekouras, D. N. Miller, H. Ménard, J. T. S. Irvine, *Nat. Chem.* **2013**, *5*, 916–923; c) D. Neagu, T. S. Oh, D. N. Miller, H. Ménard, S. M. Bukhari, S. R. Gamble, R. J. Gorte, J. M. Vohs, J. T. S. Irvine, *Nat. Commun.* **2015**, *6*, 1–8; d) Y. Sun, J. Li, Y. Zeng, B. S. Amirkhiz, M. Wang, Y. Behnamian, J. Luo, *J. Mater. Chem. A* **2015**, *3*, 11048–11056; e) V. B. Vert, F. V. Melo, L. Navarrete, J. M. Serra, *Appl. Catal. B* **2012**, *115–116*, 346–356.
[9] W. Kobsiriphat, B. D. Madsen, Y. Wang, L. D. Marks, S. A. Barnett, *Solid State Ionics* **2009**, *180*, 257–264.
[10] a) D. M. Bierschenk, E. Potter-Nelson, C. Hoel, Y. Liao, L. Marks, K. R. Poeppelmeier, S. A. Barnett, *J. Power Sources* **2011**, *196*, 3089–3094; b) Y. Nishihata, J. Mizuki, T. Akao, H. Tanaka, M. Uenishi, M. Kimura, T. Okamoto, N. Hamada, *Nature* **2002**, *418*, 164–167.
[11] a) N. Q. Minh, *J. Am. Ceram. Soc.* **1993**, *76*, 563–588; b) J. Sfeir, *J. Power Sources* **2003**, *118*, 276–285.

[12] a) J. Sfeir, P. A. Buffat, P. Mockli, N. Xanthopoulos, R. Vasquez, H. J. Mathieu, J. Van herle, K. R. Thampi, *J. Catal.* **2001**, *202*, 229–244; b) S. P. Jiang, L. Liu, K. P. Ong, P. Wu, J. Li, J. Pu, *J. Power Sources* **2008**, *176*, 82–89.
[13] A. L. Sauvet, J. T. S. Irvine, *Solid State Ionics* **2004**, *167*, 1–8.
[14] R. T. Baker, I. S. Metcalfe, *Appl. Catal. A* **1995**, *126*, 297–317.
[15] J. T. S. Irvine, D. Neagu, M. C. Verbraeken, C. Chatzichristodoulou, C. Graves, M. B. Mogensen, *Nat. Energy* **2016**, *1*, 1–13.
[16] D.-M. Amaya-Dueñas, G. Chen, A. Weidenkaff, N. Sata, F. Han, R. Costa, K. A. Friedrich, *J. Mater. Chem. A* **2021**, *9*, 5685–5701.
[17] a) A. Nenning, J. Fleig, *Surf. Sci.* **2019**, *680*, 43–51; b) D. Chen, B. Mewafy, F. Paloukis, L. Zhong, V. Papaefthimiou, T. Dintzer, K. M. Papazisi, S. P. Balomenou, D. Tsiplakides, D. Teschner, V. Pérez-Dieste, C. Escudero, S. Zafeiratos, *J. Catal.* **2020**, *381*, 520–529.
[18] M. Riegraf, F. Han, N. Sata, R. Costa, **2021**, unpublished results.
[19] S. Dierickx, J. Joos, A. Weber, E. Ivers-Tiffée, *Electrochim. Acta* **2018**, *265*, 736–750.
[20] A. K. Opitz, M. Gerstl, M. Bram, *Fuel Cells* **2019**, *19*, 417–428.
[21] S. D. Kim, H. Moon, S. H. Hyun, J. Moon, J. Kim, H. W. Lee, *Solid State Ionics* **2006**, *177*, 931–938.
[22] M. Riedel, M. P. Heddrich, K. A. Friedrich, *Int. J. Hydrogen Energy* **2019**, *44*, 4570–4581.
[23] M. Riegraf, R. Costa, G. Schiller, K. A. Friedrich, S. Dierickx, A. Weber, *J. Electrochem. Soc.* **2019**, *166*, F865–F872.
[24] S. Primdahl, M. Mogensen, *Solid State Ionics* **2002**, *152–153*, 597–608.
[25] S. Gewies, W. G. Bessler, *J. Electrochem. Soc.* **2008**, *155*, B937–B937.
[26] J. Rossmeisl, W. G. Bessler, *Solid State Ionics* **2008**, *178*, 1694–1700.
[27] T. Zhu, H. E. Troiani, L. V. Mogni, M. Han, S. A. Barnett, *Joule* **2018**, *2*, 478–496.
[28] T. Zhu, D. E. Fowler, K. R. Poeppelmeier, M. Han, S. A. Barnett, *J. Electrochem. Soc.* **2016**, *163*, F952–F961.
[29] K. Kousi, D. Neagu, L. Bekris, E. Papaioannou, I. Metcalfe, *Angew. Chem. Int. Ed.* **2020**, *59*, 2510–2519; *Angew. Chem.* **2020**, *132*, 2531–2540.
[30] M. Riegraf, V. Yurkiv, R. Costa, G. Schiller, K. A. Friedrich, *ChemSusChem* **2017**, *10*, 587–599.
[31] I. Alstrup, J. R. Rostrup-Nielsen, S. Røen, *J. Appl. Catal.* **1981**, *1*, 303–314.
[32] H. Lv, L. Lin, X. Zhang, Y. Song, H. Matsumoto, C. Zeng, N. Ta, W. Liu, D. Gao, G. Wang, *Adv. Mater.* **2020**, *32*, 1906193.
[33] H. Lv, T. Liu, X. Zhang, Y. Song, H. Matsumoto, N. Ta, C. Zeng, G. Wang, X. Bao, *Angew. Chem.* **2020**, *59*, 15968–15973; *Angew. Chem.* **2020**, *132*, 16102–16107.
[34] a) K.-Y. Lai, A. Manthiram, *Chem. Mater.* **2018**, *30*, 2838–2847; b) D. Neagu, E. I. Papaioannou, W. K. Ramli, D. N. Miller, B. J. Murdoch, H. Ménard, A. Umar, A. J. Barlow, P. J. Cumpson, J. T. Irvine, I. S. Metcalfe, *Nat. Commun.* **2017**, *8*, 1-8.
[35] S. G. Ebbinghaus, C. Erztoument, I. Marozau, *J. Solid State Chem.* **2007**, *180*, 3393–3400.
[36] A. Tsoga, A. Gupta, A. Naoumidis, D. Skarmoutsos, P. Nikolopoulos, *Ionics* **1998**, *4*, 234–240.
[37] M. P. Hoerlein, M. Riegraf, R. Costa, G. Schiller, K. A. Friedrich, *Electrochim. Acta* **2018**, *276*, 162–175.

Manuscript received: February 15, 2021
Revised manuscript received: April 12, 2021
Accepted manuscript online: April 12, 2021
Version of record online: May 7, 2021

Article II – Supplementary information

ChemSusChem

Supporting Information

Performance and Limitations of Nickel-Doped Chromite Anodes in Electrolyte-Supported Solid Oxide Fuel Cells

Matthias Riegraf,* Diana M. Amaya-Dueñas, Noriko Sata, K. Andreas Friedrich, and Rémi Costa*

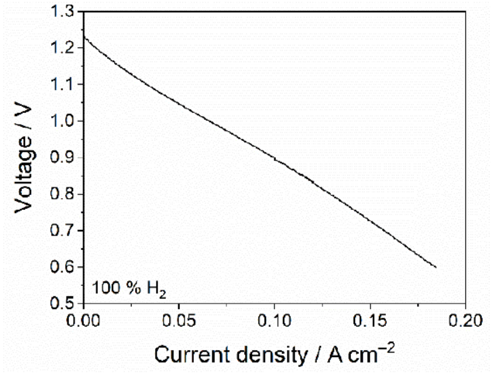

Fig. S1. Current-voltage characteristics of a cell with a brushed Pt layer as functional fuel electrode.

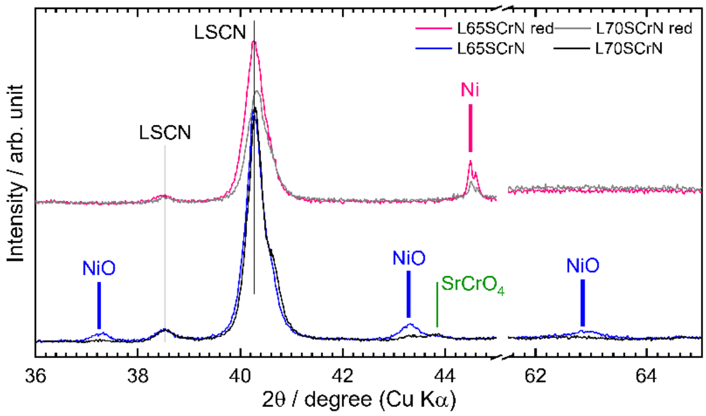

Fig. S2. XRD patterns of the reduced and as-prepared L65SCrN and L7SCrN powder.

Rietveld quantification

A Rietveld refinement was carried out with the TOPAS software using XRD measurements from the Bruker D8 Advance.

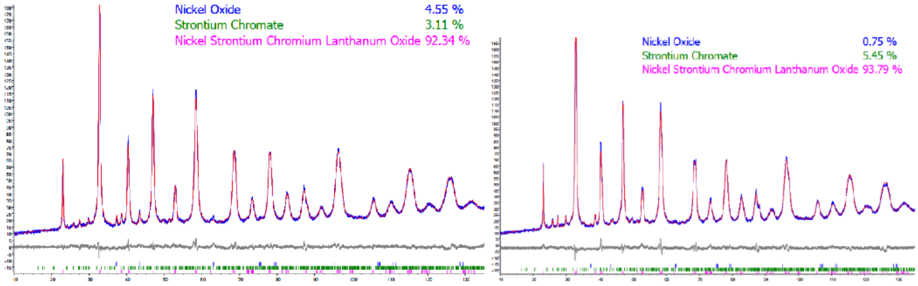

Fig. S3: Rietveld refinement of the raw L65SCrN (left) and L7SCrN (right) powder.

Based on the Rietveld refinement and the quantified phases in the supplementary information, an estimation of the composition (A/B ratio, Sr content on A site, Ni content on B site) of the L65SCrN and L7SCrN perovskites can be made:

L65SCrN:

$La_{0.65}Sr_{0.3-0.031}Cr_{0.85-0.0311}Ni_{0.85-0.0455}O_{3-\delta}$ =

$La_{0.65}Sr_{0.2689}Cr_{0.8189}Ni_{0.1045}O_{3-\delta}$

A/B ratio: 0.995

Sr content on A site: 0.29

Ni content on B site: 0.11

L7SCrN:

$La_{0.7}Sr_{0.3-0.0545}Cr_{0.85-0.0545}Ni_{0.85-0.0075}O_{3-\delta} = La_{0.7}Sr_{0.2455}Cr_{0.7955}Ni_{0.1425}O_{3-\delta}$

A/B ratio: 1.008

Sr content on A site: 0.26

Ni content on B site: 0.15

The ratio between moles on the A-site and the B-site in O L65SCrN is 0.995, corresponding to an estimated A-site deficiency of 0.5 mol%.

Estimation of TPB lengths

The approximate TPB length of the Ni/L65SCrN/gas phase interface can be calculated based on the assumption that all Ni particles are perfect spheres with the mean diameter *d:*

$TPB = \pi * d * N = \pi * d * x_{Ni} * M / (V*\delta) = 6 * x_{Ni} * M / (d^2 * \delta)$,

with *m* being the mass, *V* the volume, *M* the molar mass and δ the density of Ni, and x_{Ni} the molar fraction of Ni.

To determine the TPB length contributions of Ni particles originating from the reduced NiO secondary phase and exsolved Ni particles, the respective values can be estimated. The reduced NiO particles are expected with a size in the sub-µm / µm range. A rather small particle size diameter of 0.25 µm was assumed. The exsolved Ni nanoparticles are much smaller as shown in Fig. 11 and were assumed to have an average diameter of 20 nm. For a molar fraction $x_{Ni,submicron}$ of 0.0455, corresponding to the amount of NiO in the oxidized powder, a TPB length of $2.67\ 10^{13}$ µm/mol is obtained. When only 0.6 mol % of Ni is exsolved, a value taken from our recent study of the same material (Amaya-Dueñas et al., *J. Mat. Chem. A* 2021, 9, 5685), a TPB length of $5.93*10^{14}$ µm/mol is obtained. The more than one order of magnitude larger TPB length corresponding to the exsolved Ni indicates that the influence of exsolved Ni is dominating the electro-catalytic contribution of the Ni phase in the L65SCrN electrode. This contribution is probably even larger for the L7SCrN electrode due to the lower amount of NiO in the raw powder.

Article III

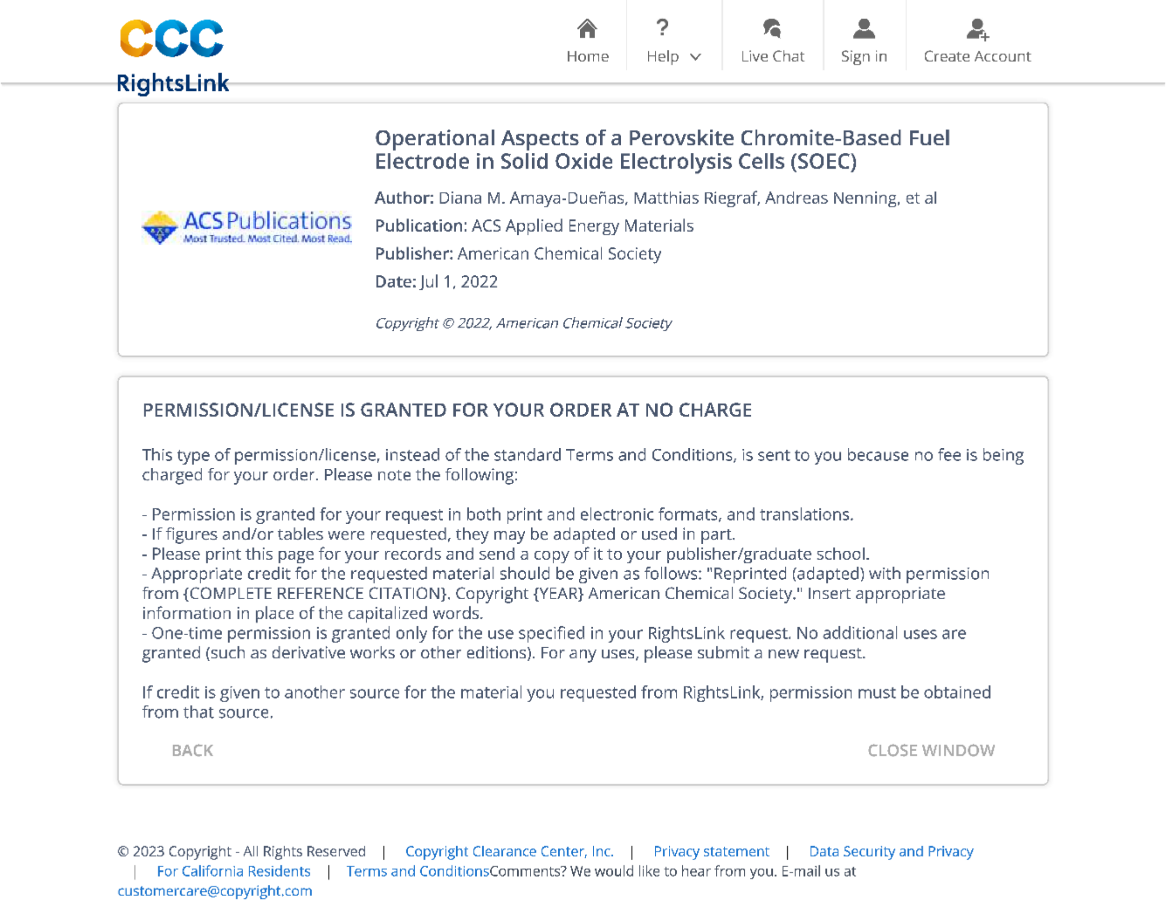

Operational Aspects of a Perovskite Chromite-Based Fuel Electrode in Solid Oxide Electrolysis Cells (SOEC)

Author: Diana M. Amaya-Dueñas, Matthias Riegraf, Andreas Nenning, et al
Publication: ACS Applied Energy Materials
Publisher: American Chemical Society
Date: Jul 1, 2022

Copyright © 2022, American Chemical Society

PERMISSION/LICENSE IS GRANTED FOR YOUR ORDER AT NO CHARGE

This type of permission/license, instead of the standard Terms and Conditions, is sent to you because no fee is being charged for your order. Please note the following:

- Permission is granted for your request in both print and electronic formats, and translations.
- If figures and/or tables were requested, they may be adapted or used in part.
- Please print this page for your records and send a copy of it to your publisher/graduate school.
- Appropriate credit for the requested material should be given as follows: "Reprinted (adapted) with permission from {COMPLETE REFERENCE CITATION}. Copyright {YEAR} American Chemical Society." Insert appropriate information in place of the capitalized words.
- One-time permission is granted only for the use specified in your RightsLink request. No additional uses are granted (such as derivative works or other editions). For any uses, please submit a new request.

If credit is given to another source for the material you requested from RightsLink, permission must be obtained from that source.

© 2023 Copyright - All Rights Reserved | Copyright Clearance Center, Inc. | Privacy statement | Data Security and Privacy | For California Residents | Terms and ConditionsComments? We would like to hear from you. E-mail us at customercare@copyright.com

Reprinted (adapted) with permission from *ACS Appl. Energy Mater.* 2022, 5, 7, 8143–8156. Copyright 2023 American Chemical Society.

ACS APPLIED ENERGY MATERIALS

www.acsaem.org Article

Operational Aspects of a Perovskite Chromite-Based Fuel Electrode in Solid Oxide Electrolysis Cells (SOEC)

Diana M. Amaya-Dueñas,* Matthias Riegraf, Andreas Nenning, Alexander K. Opitz, Rémi Costa,* and K. Andreas Friedrich

Cite This: *ACS Appl. Energy Mater.* 2022, 5, 8143–8156 Read Online

ACCESS | Metrics & More | Article Recommendations | Supporting Information

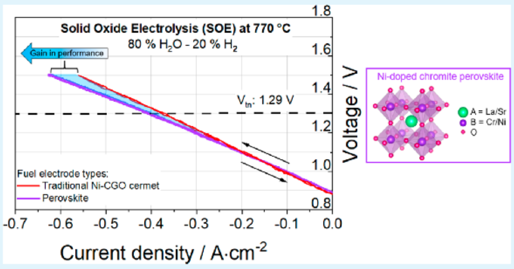

ABSTRACT: The lanthanum strontium chromite perovskite $La_{0.65}Sr_{0.3}Cr_{0.85}Ni_{0.15}O_{3-\delta}$ (L65SCrN) was implemented as fuel electrode in electrolyte-supported cells (ESC). The electrochemical cell performance in steam electrolysis operation with a fuel gas mixture of 80% H_2O–20% H_2 was demonstrated to be comparable to that of Ni-CGO-based state of the art cells at 860 °C. At 830, 800, and 770 °C, the perovskite fuel electrode exhibited a gain in performance. Lower apparent activation energy barrier values were calculated for the L65SCrN in symmetrical and full cell configurations, in contrast to Ni-CGO fuel electrodes. A reaction model is proposed, where the water-splitting reaction mainly occurs on the oxygen vacancy sites on the L65SCrN surface and where the exsolved metallic Ni nanoparticles assist the catalytic activity of the electrode with hydrogen spillover and H_2 desorption. We observed a voltage degradation of ~48 mV/kh during 1000 h of operation under steam electrolysis conditions at 860 °C close to the thermoneutral voltage. van der Pauw conductivity measurements corroborated this degradation with a decrease of the perovskite's p-type conductivity, which appeared to be a diffusion-limited phenomenon. Nevertheless, the lower activation energy of the perovskite-based fuel electrode for solid oxide cells (SOCs) is promising for green hydrogen production via steam electrolysis at a reduced temperature (below 860 °C) and without the need of a hydrogen sweep.

KEYWORDS: *high-temperature electrolysis, solid oxide electrolysis cell, green hydrogen, fuel electrode, perovskite, chromite, p-type, conductivity*

1. INTRODUCTION

Water electrolysis powered with electricity from renewable sources is a promising pathway to green hydrogen production.[1] The various electrolysis processes can be classified into two main categories: (i) the low-temperature technologies (LTE) that include mainly alkaline electrolysis (AE) and proton exchange membrane electrolysis (PEMEL), which both make use of liquid water at an operating temperature below 100 °C, and (ii) the high-temperature technologies (HTE), which operate typically with ceramic cells at temperatures above 600 °C to convert steam into hydrogen. Due to a different state of the water at these operating temperatures, the thermoneutral voltage for these technologies corresponds to 1.47 V for LTE and 1.29 V for HTE.[2] Typically, the operating voltage for the LTE technologies is ~1.8 V, while the HTE can be operated at ~1.3 V. Since a significant amount of the energy required for the water splitting is supplied in the form of heat in HTE, these systems yield a lower specific electrical energy consumption in comparison to the LTE. While AE systems require 47–65 kWh/kg H_2 and PEMEL about 50–76 kWh/kg H_2, HTE systems offer the highest electrical efficiency with a consumption of ca. 40–44 kWh/kg H_2.[3] Moreover, typical high-temperature cells, i.e. solid oxide cells (SOC), are unique due to their reversibility (rSOC). Such systems can be operated either as solid oxide electrolysis cells (SOECs) to convert sustainable electricity into chemical energy (in the form of green hydrogen, fuels, or chemicals) or as solid oxide fuel cells (SOFCs), to directly convert such chemical energy back into electricity.[4] This allows the versatile use of large storage-power generation units, which would require only one type of cell (rSOC) and not separate power-to-fuel (electrolysis mode) and fuel-to-power (fuel cell mode) systems.[4] In solid oxide electrolysis (SOE), the water splitting reaction occurs at the fuel electrode of the SOC, as shown in eq 1:[5]

$$H_2O + 2e^- \rightarrow H_2(g) + O^{2-}(\text{electrolyte}) \quad (1)$$

Received: March 4, 2022
Accepted: June 27, 2022
Published: July 8, 2022

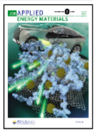

Since the electrode kinetics are enhanced due to the high temperature,[6,7] the PGM (platinum-group metal) catalysts typically used in PEMEL are avoided. State of the art SOC fuel electrode materials are porous nickel-based cermets due to their high electrical conductivity. Their notable catalytic activity of both the metallic nickel phase (toward H_2 dissociation) and the ceramic ceria-based phase (toward H_2O splitting and recombination) enables a reversible operation.[8,9] In cathode-supported cells (CSCs), nickel is traditionally mixed with yttria-stabilized zirconia (YSZ) into Ni-YSZ composite fuel electrodes, while it is more commonly found in combination with gadolinium-doped ceria (CGO), in the form of Ni-CGO cermets in electrolyte-supported cells (ESCs). However, when they are operated in electrolysis, nickel cermet electrodes are prone to irreversible degradation processes. Data from several studies suggest that the main issues correspond to the following:

(i) Nickel agglomeration at high temperature: this may yield a loss of percolation in the cermet and a reduction of the active triple-phase-boundary (TPB) lengths.

(ii) Nickel migration away from the interface between the electrolyte−fuel electrode: this is especially sensitive in CSCs at high temperatures, high overpotentials, and high relative humidity, i.e. high pH_2O.[10−13] Some studies suggest the formation of $Ni(OH)_2$ volatile species in gas mixtures of H_2 and H_2O, which could be transported and reprecipitated in other locations within the fuel electrode.[14−16] Moreover, others also explain this microstructure evolution under electrolysis conditions by a polarization-dependent interfacial energy between Ni and the oxide ion conducting phase, thus for example affecting the Ni wettability on the oxide surface.[17−19]

(iii) Structural damage of the cell—especially in CSCs—during redox cycles: such an event may affect the nickel percolation and even lead to cell failure by electrolyte fracture.[20] As a consequence, once the nickel cermet electrodes are activated, i.e. when the NiO has been reduced into metallic nickel, there is the need to keep the electrode chemically reduced. Therefore, small amounts of hydrogen are added to the steam feed.

(iv) Carbon deposition in H_2O + CO_2 co-electrolysis and dry CO_2 electrolysis operation: this is especially critical in CSCs with Ni-YSZ electrodes. In contrast, the mixed ionic and electronic transport properties of ceria-based materials grant a superior tolerance against carbon formation to Ni-CGO composites in ESCs.[21]

Such contingencies in electrolysis operation with high pH_2O are inherent to the use of metallic nickel as the electrocatalyst, current collector, and in the case of CSCs, as part of the structural component. In addition to these technical drivers, the International Energy Agency (IEA) recently classified nickel as a critical raw material for the energy transition,[22] because of the increased demand in other technologies such as batteries and AE, among others. Hence, such a classification represents an additional driver for finding nickel substitutes. In regard to the HTE technologies, these issues drive the development of alternative fuel electrodes that could compete with the Ni cermets on SOECs. Among the most important requirements on the use and implementation of such alternative fuel electrodes are (i) promising catalytic activity, (ii) good electric conductivity, and (ii) high dimensional and chemical stability in dual atmospheres with high steam and high hydrogen contents.

As alternative, mixed ionic and electronic conductors (MIECs) such as the perovskite-based oxides (ABO_3) have attracted considerable interest due to their remarkable stability under reducing and oxidizing conditions. Despite their limited mechanical properties in comparison to nickel cermets, perovskite-based electrodes are well-suited for ESC designs.[23] Their electrocatalytic properties can be tuned by a wide range of element combination on the A-site with lanthanides and alkaline-earth metals and also on the B-site with transition metals such as Mn, Co, Fe, Ni, Cr, and Ti.[24] Particularly promising performance in steam electrolysis at 800 °C (−0.9 A cm^{-2} at 1.3 V) has been shown with strontium titanate fuel electrodes with precipitation of metallic nanoparticles of Ni and Fe on the perovskite surface.[25] Such precipitation of catalytically active metals, which are embedded in the perovskite lattice under oxidizing conditions and then are exsolved as metallic nanoparticles on the perovskite surface under cathodic polarization and/or chemical reduction, is often denoted as exsolution.[8,25−27]

Strontium-doped lanthanum chromites, which are p-type conductors, have also been investigated as electrocatalysts since reducible 3d transition metals (M) can be hosted on the B-site, yielding a large family of compounds with the general formula $(La,Sr)(Cr,M)O_3$. Various stoichiometric formulations as well as A-site deficient chromites have been recently investigated in H_2O electrolysis, CO_2 electrolysis, and co-electrolysis.[8,27−29] A-site deficient formulations were demonstrated to be more favorable for metal exsolution due to the high cation and oxygen vacancy concentration that partially destabilizes the perovskite lattice. Under reducing conditions, some of the B-site cations are reduced to metals and exsolved on the surface, maintaining the charge balance of the host perovskite lattice.[30]

In our recent work, we studied a lanthanum chromite $La_{0.65}Sr_{0.3}Cr_{0.85}Ni_{0.15}O_{3-\delta}$ fuel electrode decorated with exsolved Ni nanoparticles for SOC applications. Promising and comparable performance with respect to the typical nickel cermet fuel electrodes in ESCs was achieved.[8] Post-test analysis after 950 h of high-temperature H_2O and CO_2 co-electrolysis operation suggested a remarkable dimensional stability of the Ni exsolved nanoparticles in the tested conditions.[8]

Most of the research and development efforts reported so far have focused on tuning the composition of the chromite electrodes. However, very little is known about the operational aspects and benefits that such fuel electrode materials could provide to high-temperature electrolysis cells over the traditional cermets. Data about the comparative assessment of perovskite-based electrodes with state of the art fuel electrodes are limited. Therefore, the main objective of this work is to identify operational benefits for SOE operation by using perovskite-based fuel electrode cells instead of the traditional state of the art Ni-CGO cermets in ESCs. The performance of $La_{0.65}Sr_{0.3}Cr_{0.85}Ni_{0.15}O_{3-\delta}$ (L65SCrN) and Ni-CGO fuel electrodes are evaluated, as well as the temperature dependence of the electrochemical performance of the L65SCrN-based cells between 770 and 860 °C. For the latter cells, the durability in steam electrolysis operation was investigated for 1000 h.

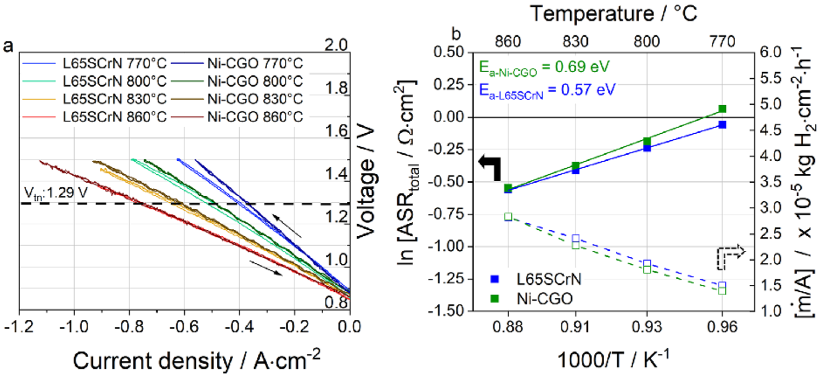

Figure 1. (a) Polarization curves of L65SCrN and Ni-CGO fuel electrodes on full ESCs in electrolysis mode with a fuel gas mixture of 80% H_2O–20% H_2 (0.8 slpm of H_2O and 0.2 slpm of H_2) at 860, 830, 800, and 770 °C. The thermoneutral voltage (1.29 V) of steam electrolysis is depicted. (b) Arrhenius-type plots of ASR_{total} for the L65SCrN and Ni-CGO cells calculated from (a) on a linear interval close to the thermoneutral point. The corresponding normalized hydrogen production rate is shown on the right axis.

2. EXPERIMENTAL METHODS

2.1. Cell Preparation. ESCs were investigated in two different configurations: symmetrical button cells and full square cells, implementing the perovskite fuel electrode L65SCrN.

2.1.1. L65SCrN Symmetrical Button-Cell Manufacturing. A chromite powder with the nominal composition $La_{0.65}Sr_{0.3}Cr_{0.85}Ni_{0.15}O_{3-\delta}$ (L65SCrN) was synthesized by the nitrate combustion method for qualification purposes,[8] for which the powder production capacity was limited to ~10 g. SEM imaging of this powder is shown Figure S1 in the Supporting Information. The fuel electrode ink was prepared by dispersing the L65SCrN powder in a liquid ink vehicle (94 wt % α-terpineol and 6 wt % ethyl cellulose) with a powder to liquid ratio of 2:1 and mixed with an EXAKT 80E EL three-roll mill. An Aurel Model 900 device (Aurel automation s.p.a, Italy) was used for the screen printing of the electrodes.[8] Symmetrical button cells were prepared by screen printing 10 mm diameter circles of the L65SCrN ink on 20 mm diameter commercial electrolytes CGO20 (5 μm)|3YSZ (90 μm)|CGO20 (5 μm) from Kerafol GmbH (Eschenbach, Germany) and after drying, heated at a rate of 3 °C/min to 1200 °C in air and fired for 1 h. Platinum paste was used as the current collector and was hand-brushed on both electrode surfaces. Afterward, the cells were heated at nominal rate to 1050 °C in air and held at that temperature for 1 h. The active electrode area was 0.785 cm^2.

2.1.2. Full-Cell Manufacturing. For these cells, the L65SCrN ceramic powder was supplied by Marion Technologies[31] (Verniolle, France) as shown in Figure S2. For the transposition on a larger scale, the same formulation as that used for the symmetrical cells was produced in the kilogram range, in order to obtain a sufficient amount of powder with the same characteristics for a further study and up-scaling. With this commercial powder, a L65SCrN ink was prepared as described above. Full cells were prepared by screen printing an area of 40 mm × 40 mm of the L65SCrN fuel electrode ink on 50 mm × 50 mm commercial electrolytes from Kerafol CGO20 (5 μm)|3YSZ (90 μm)|CGO20 (5 μm). Then, those half-cells were fired in air at 1100 °C for 1 h at the nominal heating rate of 3 °C/min. Next, an area of 40 mm × 40 mm of the $La_{0.58}Sr_{0.4}Fe_{0.8}Co_{0.2}O_{3-\delta}$ (LSCF) oxygen electrode (Heraeus commercial reference) was printed on the other side of the electrolytes. The LSCF-printed electrode was co-fired in air with the brushed-platinum paste on the fuel electrode at 1050 °C for 1 h. Moreover, state of the art cells supplied by Sunfire GmbH (Dresden, Germany) with Ni-CGO cermet fuel electrodes were used as reference. Apart from the fuel electrode, the cells had the same architecture and employed the same electrolyte substrate as the L65SCrN-based cells in this work. For the oxygen electrode, a LSCF/CGO composite with a LSCF current collector layer was used.

2.2. Symmetrical Cell Characterization. Symmetrical button cells were tested at open circuit voltage (OCV) in a single-chamber configuration at 860, 830, 800, and 770 °C with humidified H_2 flow. In order to minimize the gas diffusion contribution to the ASR on the symmetrical cells, electrochemical tests were carried out at a reduced pressure of ca. 295 mbar (10% H_2O–90% H_2) and ca. 79 mbar (38% H_2O–62% H_2). The pressure was regulated by pumping the chamber with a continuous feed gas flow rate of 0.02 slpm. The electrodes were contacted with highly porous Ni foams in a testing chamber of fused silica. These measures decrease the gas diffusion ASR to roughly 0.01 Ω cm^2.[32,33] Four button cells were measured at the same time by using a multiplexing setup.[32] Electrochemical impedance spectroscopy (EIS) was performed in a four-wire mode with a Novocontrol Alpha impedance analyzer in a frequency range from 50 mHz to 100 kHz and an amplitude of the voltage stimulus of 50 mV. Equivalent circuit model fitting of the impedance data was performed with the commercially available program Zview®.[34]

2.3. Full Cell Characterization. The electrochemical characterizations of the L65SCrN fuel electrode implemented in a full ESC and the Ni-CGO reference cell were carried out on a high-temperature cell-test bench.[8,11] The L65SCrN fuel electrode was contacted with a platinum mesh and the Ni-CGO with a nickel mesh. For both types of cells, the oxygen electrode was contacted with a gold mesh. A sealing gold frame was applied, and the cells were heated at a rate of 3 °C/min to 900 °C (to ensure gas tightness with the gold seal) with N_2 (1 slpm) on the fuel side and with air (1 slpm) on the oxygen side, respectively, Then, the fuel electrodes were reduced with H_2 (1 slpm) for 1 h at 900 °C. Afterward, the operating cell temperatures were adjusted to 860, 830, 800, and 770 °C. For each temperature, the fuel gas composition was set to 80% H_2O–20% H_2 (0.8 slpm of H_2O and 0.2 slpm of H_2) and polarization curves (i–V) were measured from the OCV to 1.5 V at a rate of −0.012 A s^{-1}. Galvanostatic EIS measurements were performed at the OCV with an SP-200 electrochemical workstation from BioLogic Science Instruments, at a frequency range from 50 mHz to 100 kHz and an AC amplitude of 500 mA. To avoid the scattering of the EIS data at low frequencies caused by fluctuations from the steam supply, the fuel gas was diluted with 0.5 slpm of N_2 during the impedance measurements. Subsequently, a galvanostatic durability test of ~1000 h on the L65SCrN fuel electrode cell with a fuel gas composition of 80% H_2O–20% H_2 (0.8 slpm of H_2O and 0.2 slpm of H_2) at 860 °C was carried out. The current density was fixed to −0.67 A cm^{-2}. EIS measurements at the OCV were carried out in a specific time interval. Equivalent circuit model fitting of these data was performed with Zview®.[34] After such a long-term SOE operation, the L65SCrN fuel electrode cell's morphology was observed with a Zeiss ULTRA PLUS

SEM (Carl Zeiss AG, Germany) scanning electron microscope (SEM) in combination with energy-dispersive X-ray spectroscopy (EDS) for elemental analysis, with a Bruker Xflash 5010 detector supported with Quantax 400 software. The crystalline structure was investigated by X-ray diffraction (XRD) using a D8 Discover GADDS diffractometer, equipped with a VÅNTEC-2000 area detector (Bruker AXS, Germany) and a microfocused Cu Kα radiation source operated at 50 kV and 0.6 mA with a Bragg–Brentano geometry. Crystalline phases were identified with the ICDD database.

2.4. Conductivity Measurements. The electrical conductivity was measured on porous L65SCrN films (from ink prepared with commercial L65SCrN powder) that were screen-printed on inert, insulating 1 × 1 cm^2 Al_2O_3 substrates and subsequently fired in air at 1100 °C for 1 h at a ramp rate of 3 °C/min. On these, four-wire Van der Pauw measurements[35] were performed to determine the sheet resistance and effective conductivity in varying gas mixtures and temperatures in a high-temperature measurement chamber consisting of a fused silica tube inside a tubular furnace. As feed gases, humidified argon (pH_2O ~25 mbar; 2.4% H_2–97.6% Ar) and oxygen were mixed in a 4:1 ratio at a total flow rate of 50 sccm. Although the partial pressures of H_2 and H_2O were much smaller during the Van der Pauw measurements, the resulting pO_2 (which is a function of the mixing ratio) was equal to that in the SOE full-cell tests (~10^{-16} bar). Therefore, the defect chemistry and Ni exsolution kinetics were comparable to those of the full-cell electrolysis measurements (80% H_2O–20% H_2).

3. RESULTS AND DISCUSSION

3.1. Temperature Dependence of the Steam Electrolysis with L65SCrN and Ni-CGO Fuel Electrodes in ESCs.

Polarization curves of full cells with L65SCrN and Ni-CGO fuel electrodes in SOE operation are shown in Figure 1a. The fuel gas mixture was 80% H_2O–20% H_2, and the operating temperature was varied from 860 to 770 °C. At the typical SOE operating temperatures, the thermoneutral voltage for steam electrolysis remained relatively constant at 1.29 V. For both types of cells, the specific electrical energy requirement,[36] close to the thermoneutral voltage (1.29 V), was calculated to be ~35 kWh/kg H_2. This calculation was estimated as the ratio between the consumed power and the produced hydrogen mass flow, assuming a Faraday efficiency of ~1. For stacks the values are typically slightly higher, in the range between 37 and 44 kWh/kg H_2.[3,37] Regardless of the fuel electrode and the temperature, the cell voltage U_{cell} showed a nearly linear evolution without an indication of mass transport limitations in the investigated range. At 860 °C, the comparable performance of the two cells was appreciable. However, at lower temperatures, a significant performance difference was observed: at the thermoneutral voltage of ~1.29 V, the L65SCrN-based cells displayed higher electrolysis current densities, i.e. 0.65, 0.52, and 0.40 A cm^{-2}. In contrast, those values were 0.61, 0.48, and 0.37 A cm^{-2} for the Ni-CGO cells at 830, 800, and 770 °C, respectively. Above 1.29 V, the curves flatten slightly, likely due to improved electrode kinetics and electrode/electrolyte transport characteristics due to the local heating on entering the exothermal regime.[38] Nonetheless, to a first approximation, U_{cell} can be described by Ohm's law in eq 2 as a function of the following:

(i) the OCV (U_{OCV}).

(ii) the applied electrolysis current density J.

(iii) the area-specific resistance of the cell ($\text{ASR}_{\text{total}}$), which is the slope of the polarization curves in the linear range, and which is a function of the operating temperature. The temperature dependence of ASR_{total} can be described by an Arrhenius-type expression as shown in eq 3.

$$U_{\text{cell}} = U_{\text{OCV}} + \text{ASR}_{\text{total}} \times J \tag{2}$$

$$\text{ASR}_{\text{total}} = B\,\exp\!\left(\frac{E_a}{RT}\right) \tag{3}$$

Figure 1b shows the Arrhenius-type plot of $\text{ASR}_{\text{total}}$. The exponential fits were shown to be suitable to describe the temperature dependence, and thus it was possible to determine an apparent activation energy barrier E_a of the $\text{ASR}_{\text{total}}$ for the two types of cells: E_a = 0.57 eV for the cells with the L65SCrN fuel electrode (R^2 > 0.999) and E_a = 0.69 eV for the cells with the Ni-CGO cermet fuel electrode (R^2 > 0.996). The normalized hydrogen production rate $\frac{\dot{m}}{A}$ is also reported as complementary indicator of the performance (Figure 1b, right axis), with $\dot{m}$ being the calculated mass flow rate of produced hydrogen and A being the active area of the cell. At 860 °C both types of cells produced similar amounts of hydrogen. However, at lower temperatures the hydrogen production rate calculated for the L65SCrN-based cell was systemically higher than that for the Ni-CGO-based cell. This observation correlates well with the lower apparent E_a calculated for the L65SCrN-based cell, which reflects lower $\text{ASR}_{\text{total}}$ values at lower temperatures. To elucidate the different temperature dependences of the two types of cells, it is thus necessary to further resolve the specific contributions of the $\text{ASR}_{\text{total}}$, which can be described as the sum of the Ohmic and polarization resistance terms:[39]

$$\text{ASR}_{\text{total}} = \text{ASR}_{\text{Ohmic}} + \text{ASR}_{\text{polarization}} \tag{4}$$

On consideration of the contribution of the electrolyte, the current collection, and interfacial resistances (CCI) to the Ohmic term, as well as the contributions to the polarization term from the fuel and oxygen electrode processes and the gas transport losses, eq 4 can be detailed as

$$\begin{aligned}\text{ASR}_{\text{total}} = {} & (\text{ASR}_{\text{electrolyte}} + \text{ASR}_{\text{CCI}}) \\ & + (\text{ASR}_{\text{fuel electrode}} + \text{ASR}_{\text{oxygen electrode}} \\ & + \text{ASR}_{\text{gas}})\end{aligned} \tag{5}$$

The term corresponding to the gas transport losses mainly accounts for the gas conversion polarization along the gas channels of the cell housing and also due to the fuel utilization of 25% at −1 A cm^{-2}. The gas diffusion limitation (gas flow perpendicular to the fuel electrode) is expected to be minimal in the ESC architecture. Since the electrolyte and the oxygen electrode were similar for both type of cells, the difference in $\text{ASR}_{\text{total}}$ can be attributed to the different fuel electrodes and the corresponding interfacial resistances. The thicknesses of both fuel electrodes were on the same order of magnitude, L65SCrN ~13 μm and Ni-CGO ~10–13 μm,[40] which are most likely thicker than the characteristic electrochemically active thickness. Hence, the kinetics are co-limited by ion conduction and electrochemical reactions within the porous fuel electrode and do not change with a variation in thickness.[32,41,42]

The specific response of each cell upon temperature variation was systematically investigated by EIS at the OCV, with the aim of identifying the different impedance processes. Figure 2 shows imaginary impedance spectra for the (a)

https://doi.org/10.1021/acsaem.2c00680
ACS Appl. Energy Mater. 2022, 5, 8143–8156

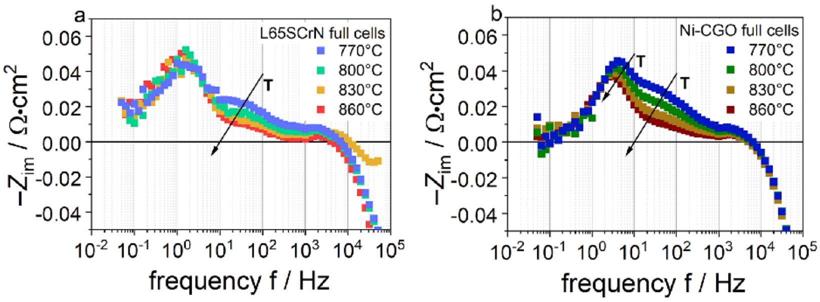

Figure 2. Imaginary impedance spectra recorded at the OCV of (a) L65SCrN- and (b) Ni-CGO-based full ESCs in electrolysis mode with a fuel gas mixture of 80% H_2O−20% H_2 (0.4 slpm of H_2O, 0.1 slpm of H_2, and 0.5 slpm of N_2) at 860, 830, 800, and 770 °C.

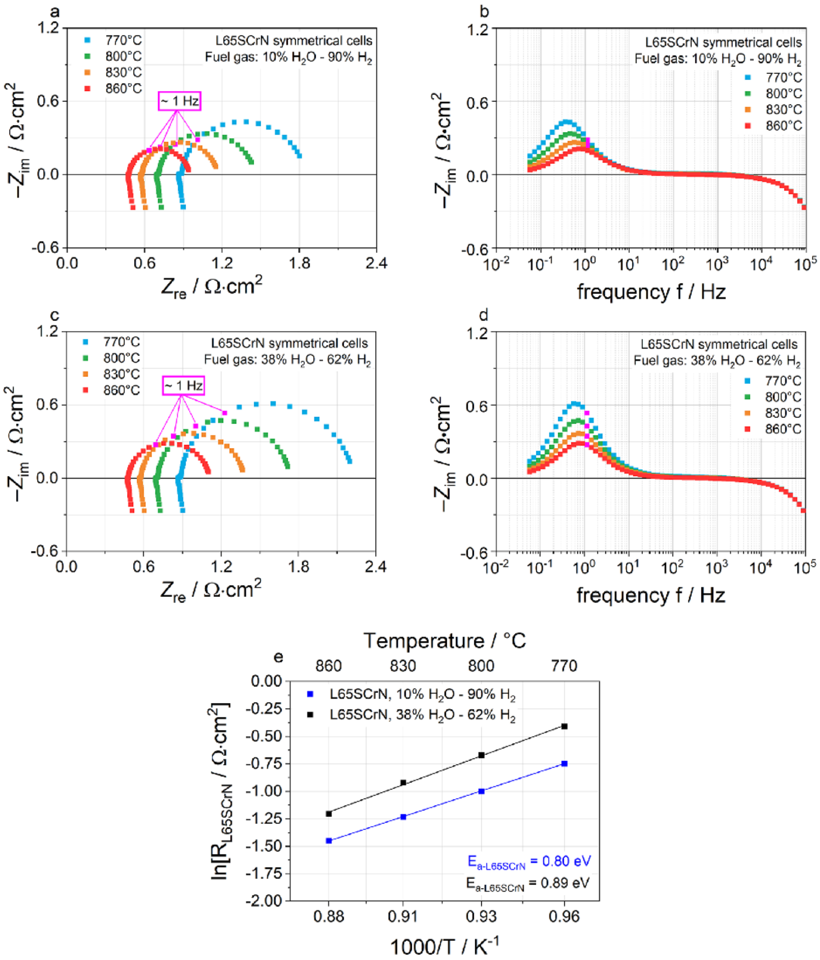

Figure 3. EIS spectra recorded at OCV of L65SCrN symmetrical cells at 860, 830, 800, and 770 °C: (a) Nyquist and (b) imaginary impedance plots for the fuel gas mixture of 10% H_2O−90% H_2; (c) Nyquist and (d) imaginary impedance plots for the fuel gas mixture of 38% H_2O−62% H_2. (e) Arrhenius-type plots of L65SCrN symmetrical cells calculated from ECMs at the OCV with fuel gas mixtures of 10% H_2O−90% H_2 (blue pattern) and 38% H_2O−62% H_2 (black pattern).

L65SCrN- and (b) Ni-CGO-based full cells at different temperatures. The characteristic frequencies of the charge transfer process on the LSCF oxygen electrode and the LSCF/CGO interfacial double-layer capacitance were identified to be between 100 Hz and 1 kHz.[8,43,44] A low-frequency peak, which is generally associated with the gas conversion in our setup,[11] was identified at ~3 Hz. A slightly lower frequency (~1−3 Hz) of the gas conversion was observed for the L65SCrN electrodes, which is in agreement with our previous work with similar L65SCrN fuel electrodes.[8] The gas conversion resistance can be expected to slightly increase with higher temperature,[45] which is in accordance with the observed behavior for the L65SCrN-based cell at frequencies ~1 Hz (Figure 2a).

However, the Ni-CGO-based cell showed an opposite temperature dependence of the impedance at frequencies of ~1 Hz, where the resistance decreased with increasing temperature (Figure 2b). This behavior was possibly caused by an increased convolution of the gas conversion process and the Ni-CGO fuel electrode process at low temperatures. Moreover, the temperature variation showed a strong dependence of a process between 3 and 100 Hz for both cells, characterized by a decrement of the imaginary impedance upon a temperature increase. These processes are likely linked to electrochemical polarization and surface oxygen exchange processes for both fuel electrode types, which is consistent with previous studies of L65SCrN[8] and Ni-CGO fuel electrodes.[46,47] Nevertheless, these processes could overlap with the gas conversion at ~1 Hz.[40,44,48] Additionally, on porous electrodes, ion conduction, stoichiometry changes (chemical capacitance), and surface redox kinetics cannot be deconvoluted by individual frequencies. All of these phenomena make very difficult to precisely quantify the $ASR_{\text{fuel electrode}}$ term. What stands out from these spectra is the response of the imaginary impedance of the L65SCrN-based cell in the frequency range between 1 and 100 Hz upon changes in temperature, which was less pronounced than that of the Ni-CGO-based cell, thus being in accordance with the trend observed on the polarization curves in Figure 1. In the Nyquist plots of these EIS spectra (Figure S3), a slight difference in the Ohmic resistance between the L65SCrN and Ni-CGO-based cells can be observed for all temperatures. For each temperature, the perovskite-based cell exhibited a systematically higher Ohmic resistance, with an increment of ~0.08 Ω cm^2 with respect to the Ni-CGO cells. As an example, at 860 °C an ASR_{Ohmic} of 0.46 Ω cm^2 was identified for Ni-CGO, while it was 0.54 Ω cm^2 for the L65SCrN cells. For the case at 770 °C, the ASR_{Ohmic} for Ni-CGO was identified at 0.86 Ω cm^2 and for L65SCrN at 0.94 Ω cm^2. Such a systematic difference in the Ohmic resistance could be attributed to a lower electronic conductivity of the perovskite electrodes. A minor contribution to this difference might also originate from slightly different contact resistances between electrodes and current collectors. However, this cannot explain by far the entire observed difference in the Ohmic resistance. In order to better assess the processes on the L65SCrN fuel electrodes, the temperature dependence was evaluated in a symmetrical cell configuration in H_2−H_2O atmospheres as follows.

3.2. Temperature and Gas Composition Dependence of the Polarization Resistance of L65SCrN Fuel Electrodes.

EIS measurements at the OCV of L65SCrN symmetrical button cells are shown in Figure 3a−d, in which the Nyquist plots showed two semicircle-like features for all four temperatures and both gas compositions (Figure 3a,c). The low-frequency process at peak frequencies of ~0.1−1 Hz was likely related to a L65SCrN surface process.[8] In the symmetrical-cell test setup, H_2 and H_2O partial pressures were lower and the atmosphere was more reducing, in comparison to the full-cell setup. Therefore, due to the different oxygen stoichiometry in the symmetrical setup, the CGO buffer layer and the L65SCrN exhibit higher chemical capacitances, which could be modeled in a parallel connection. Moreover, the surface kinetics are lower due to the lower H_2 and H_2O partial pressures, which leads to a decrement of the characteristic frequency, also due to the larger ASR and chemical capacitance. Consequently, for the symmetrical cells studied in this work, the characteristic frequency shifted to lower values, identified at ~0.4−0.6 Hz (Figure 3b.d). Equivalent circuit model (ECM) fitting was performed in order to estimate the resistance values of the different thermally activated contributions. Details of the ECM for each temperature are described in Figures S4 and S5 and Tables S1−S10. The fitted resistance values of the L65SCrN electrode polarization process as a function of temperature are shown in the Arrhenius-type plot in Figure 3e.

Apparent activation energy barrier values E_a for the L65SCrN electrochemical processes were calculated from the Arrhenius-type relation, as shown in eq 3.[49] The exponential fits were calculated with a single apparent activation energy barrier. These Arrhenius-type plots yielded E_a = 0.80 eV ($R^2 >$ 0.999) for the gas composition 10% H_2O−90% H_2 and E_a = 0.89 eV ($R^2 >$ 0.997) for 38% H_2O−62% H_2. These similar values suggest that the mechanistic pathway is the same for both gas-phase compositions with no significant influence of pH_2 on the nature of the rate-determining step between 90% and 62% H_2. Furthermore, these values are within the range of other perovskite-type MIEC fuel electrode materials (tested in H_2−H_2O mixtures), such as $Sr(Ti,Fe)O_{3-\delta}$ (STF),[50] as well as for CGO thin-film electrodes.[51,52] The calculated E_a values for the L65SCrN surface process are within the relatively broad range reported for Ni-CGO cermets of ~0.51−1.16 eV in H_2−H_2O mixtures.[32,48,49,53] Due to the similarity with the electrolyte substrates, the most suitable reference data for comparison are the results from the symmetrical cells Ni-CGO|CGO-3YSZ-CGO|Ni-CGO reported by Riegraf et al.[49] In their work, the authors calculated an apparent activation energy of ~1.16 eV for symmetrical Ni-CGO cells tested in 20% H_2O−80% H_2 between 600 and 900 °C.[49]

Overall, the calculated apparent activation energy depends not only on the energy barrier of the rate-limiting step but also on the temperature-dependent concentrations of surface adsorbates, oxygen vacancies, and polarons. Because of the complexity of the deconvolution of these steps, a quantification of such activation energies would be very challenging and would require density functional theory (DFT) modeling, which goes beyond the scope of this work. Instead, one could assume that the calculated apparent E_a is probably related to a rate-limiting step, which has a different activation energy barrier for L65SCrN than for Ni-CGO. One important difference between the Ni-CGO cermet and the perovskite L65SCrN electrodes is the Ni dispersion. In Ni-CGO the Ni particles are percolating in the electrode and are much coarser than the exsolved Ni nanoparticles on the L65SCrN. Another relevant difference is the ceramic phase: different intermediate steps could take place on the CGO surface in contrast to the L65SCrN surface.

Hence, it is reasonable to assume that the kinetics of the intermediate reaction steps are likely to be different. Nevertheless, what can be drawn from these results in correlation with the full-cell measurements is that the kinetics of both electrodes are similar at 860 °C due to the comparable good cell performances. Below 860 °C the perovskite-based fuel electrodes show a gain in performance, which could possibly indicate that the reaction kinetics at these temperatures are more favorable on the L65SCrN than on the Ni-CGO fuel electrodes. With regard to perovskite electrodes, the reaction kinetics might be enhanced by metallic nanoparticles exsolved on the perovskite's surface. Such performance improvements have been reported on ferrite perovskites with exsolution of Fe[54,55] and Ni.[56]

In our previous work,[31] we observed that sulfur species poisoned the metallic Ni on the L65SCrN surface in SOFC operation, for which we speculated that Ni is likely involved in the H_2 dissociation and perhaps also in a possible charge-transfer reaction at the TPB for the gas phase/exsolved metallic Ni phase/perovskite phase.

Analogously to this, it was proposed on ferrite perovskites in SOFC operation that water recombination occurs on the perovskite surface and that hydrogen spills over the metal (Fe or Ni) exsolutions.[54] The authors also assumed that the dissociation of H_2 is much faster on the metal particles in comparison to the perovskite surface.[54]

For the reverse case, it has been reported that on CGO and ferrite perovskites the H_2O dissociation is much faster than the H_2 desorption.[57,58] Since the L65SCrN electrodes decorated with Ni exsolutions are very similar systems to a transition metal supported by an acceptor-doped oxide, we consider that also here the Ni is assisting the electrode kinetics. This assumption is also in line with the results of a DFT study by Hansen and Wolverton, who investigated the kinetics and thermodynamics of H_2O dissociation on thin films of $CeO_{2-x}(111)$ deposited on close-packed noble-metal surfaces. They found that H_2 desorption exhibited a higher kinetic energy barrier on the ceria surface and therefore H_2 desorption was taking place via hydrogen spillover on the noble-metal particles.[59] Therefore, we also suppose for L65SCrN with Ni exsolutions that hydrogen spillover from the L65SCrN surface to the metallic Ni particles facilitates hydrogen recombination and desorption in SOE operation.

As sketched in the mechanism in Figure 4, we propose that the adsorbed H_2O dissociates into the proton H^+ and the hydroxyl group OH^- on the perovskite surface, where the positively charged proton H^+ attaches to the lattice oxygen $O_O^\times$ to form $OH_O^\bullet$ and the negatively charged hydroxyl group OH^- fills the positively charged oxygen vacancy $V_O^{\bullet\bullet}$ to form another $OH_O^\bullet$.[5] By means of an electron transfer, these two $2OH_O^\bullet$ groups are then electrochemically reduced to $2O_O^\times$ and $2H_{ad}$. Then, hydrogen adatoms spill over from the perovskite surface to the exsolved metallic Ni, where finally $2H_{ad}$ desorbs as $H_2(g)$ away from the electrode. The electroneutrality of the perovskite lattice is maintained with one lattice oxygen $O_O^\times$ filling the oxygen vacancy $V_O^{\bullet\bullet}$ on the electrolyte, which is transported in the form of O^{2-} to the oxygen electrode,[5,60] as suggested in eq 1.

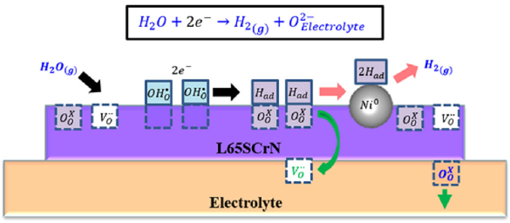

Figure 4. Sketch of the proposed model for the water-splitting reaction with the oxygen vacancies on the L65SCrN fuel electrode. The hydrogen spillover, recombination, and desorption take place on the metallic Ni nanoparticles exsolved on the perovskite surface.

3.3. Long-Term Stability of L65SCrN Fuel Electrodes in SOE.

The long-term behavior was evaluated over 1000 h under galvanostatic conditions at 860 °C with a fixed electrolysis current density of −0.67 A cm^{-2}, corresponding to the initial thermoneutral voltage of 1.29 V. Impedance measurements were carried out roughly each 100 h at the OCV (Figure 5). During the first 36 h there was a performance improvement, where the cell voltage decreased to 1.27 V. This improvement correlated with a strong shrinkage of the low-frequency fuel electrode arc in the impedance spectra in Figure 5c,d. During this time, very likely the surface chemistry of the L65SCrN electrode changed due to the electrolysis operation. The most obvious candidate for this process is Ni exsolution ($Ni^{2+/0}$),[8] creating metallic surface particles that are catalytically more active for H_2 formation in comparison to the bare oxide surface. Also, the increment of the oxygen vacancy concentration may modify the hydration properties of the perovskite surface,[5] as well as the Cr species reduction ($Cr^{6+/4+}$ and $Cr^{4+/3+}$) and Sr migration. Altogether, these phenomena that depend on the gas composition, cathodic overpotential, and temperature possibly led to an activation of the fuel electrode.

After this period, the voltage increase rate was estimated close to 48 mV/1000 h, which corresponds to a relative voltage increment $\Delta U/U_0$ of about 3.6%. These results represent a degradation twice as high as that from Schefold et al., who reported 25 mV/1000 h corresponding to $\Delta U/U_0$ of 1.7%. Their results were measured in the first 1000 h of operation of an ESC with a Ni-CGO fuel electrode operated in steam electrolysis (75% H_2O) at 850 °C and −0.7 A cm^{-2}. Over 8000 h, they reported an average voltage drift of 5.1 mV/1000 h.[40]

ECM fitting was performed in order to quantify the evolution of both the Ohmic and polarization resistances, as depicted in Figure 5b (those ECMs are detailed in Table S11 and Figure S6). From the plot in Figure 5b and the Nyquist plot in Figure 5c, it is noticeable that the Ohmic resistance shifted to higher values with time. Until an operation time of ca. 833 h this value strongly increased by 9.4%, but then seemed to stabilize at 0.58 Ω cm^2 (see Figure 5b). EIS recorded after 67 h confirmed that the polarization resistance remained constant along the duration of the test at ca. 0.1 Ω cm^2 (Figure 5b,c), which is in good agreement with our previous study, thus also ratifying the reproducibility of these results.[8] After 400 h of operation, in an attempt to recover the Ohmic resistance, a redox cycle was applied to the cell by flushing 0.1 slpm of oxygen for 1 h on the fuel side. However, the Ohmic resistance degraded continuously. In summary, the degradation processes mainly affected the Ohmic resistance while the electrochemical electrode kinetics remained rather stable.

https://doi.org/10.1021/acsaem.2c00680
ACS Appl. Energy Mater. 2022, 5, 8143−8156

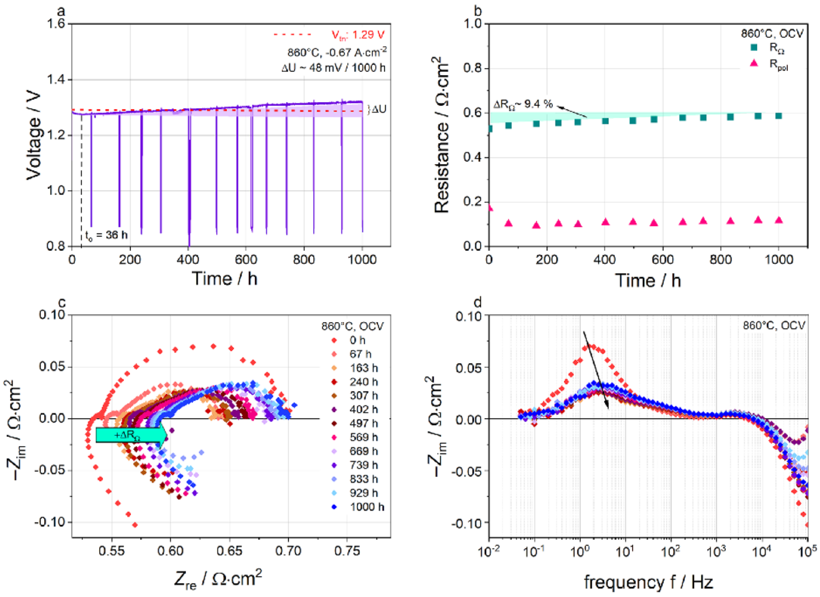

Figure 5. (a) Voltage vs time during 1000 h long-term SOE with a fuel gas mixture of 80% H_2O−20% H_2 (0.8 slpm of H_2O and 0.2 slpm of H_2) at 860 °C and −0.67 A cm^{-2} of the L65SCrN fuel electrode in a full ESC. (b) Fitted values of the evolution of the Ohmic and polarization resistances during the long-term study. (c) Nyquist plot and (d) imaginary impedance plot at the OCV and 860 °C during the long-term study of 1000 h in SOE with the fuel gas mixture 80% H_2O−20% H_2 (0.8 slpm of H_2O and 0.2 slpm of H_2).

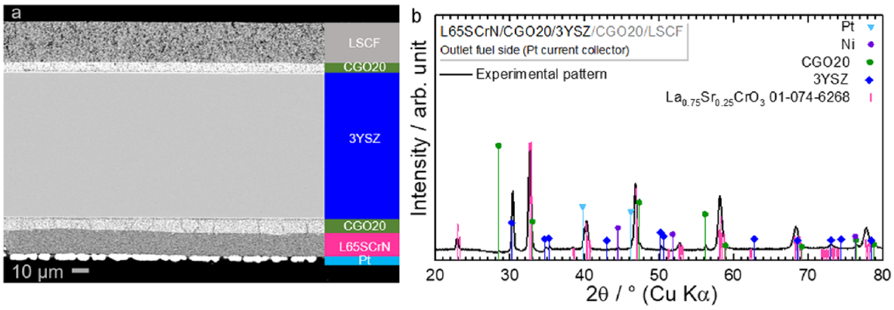

Figure 6. (a) Cross-section view of outlet side of the ESC implementing the L65SCrN fuel electrode after SOE operation at 860 °C for ca. 1000 h. (b) XRD pattern of outlet side from the ESC, performed on the fuel electrode side Pt/L65SCrN/CGO/3YSZ after SOE operation at 860 °C for ca. 1000 h.

To identify any significant chemical changes in the L65SCrN electrode after the long-term test, microstructural investigations were performed. The SEM image in Figure 6a shows that there was no delamination at any of the interfaces, suggesting a good thermal and mechanical compatibility between the different cell components. However, tiny cracks are visible on the CGO barrier layer on the fuel electrode side, for which an artifact from sample cleavage during the metallographic preparation may not be excluded. Nevertheless, in the case that those cracks were generated under SOE operation, they would imply a decrease of the active cell area for the electrochemical reaction, which would increase both the Ohmic and polarization resistances. In such a case, since the Ohmic resistance represents most of the overall cell resistance, the expected changes in the polarization resistance would be hard to observe and resolve.

Elemental analysis performed by EDS revealed the presence of Sr and Zr within the CGO barrier layer, as well as distinctive morphologies within the L65SCrN layer correlating with the presence of Ce and also Gd (Figures S7 and S9 and Tables S12 and S13 in the Supporting Information). These results could suggest the presence of a zirconate phase in the CGO barrier layer. Complementary to this, XRD characterizations were performed at both the inlet and the outlet of the fuel electrode. In Figure 6b, the X-ray diffraction pattern at the outlet shows the identified characteristic peaks of the different components of the fuel electrode (L65SCrN, CGO20, 3YSZ, and Pt). Nonetheless, these results did not reveal pertinent secondary

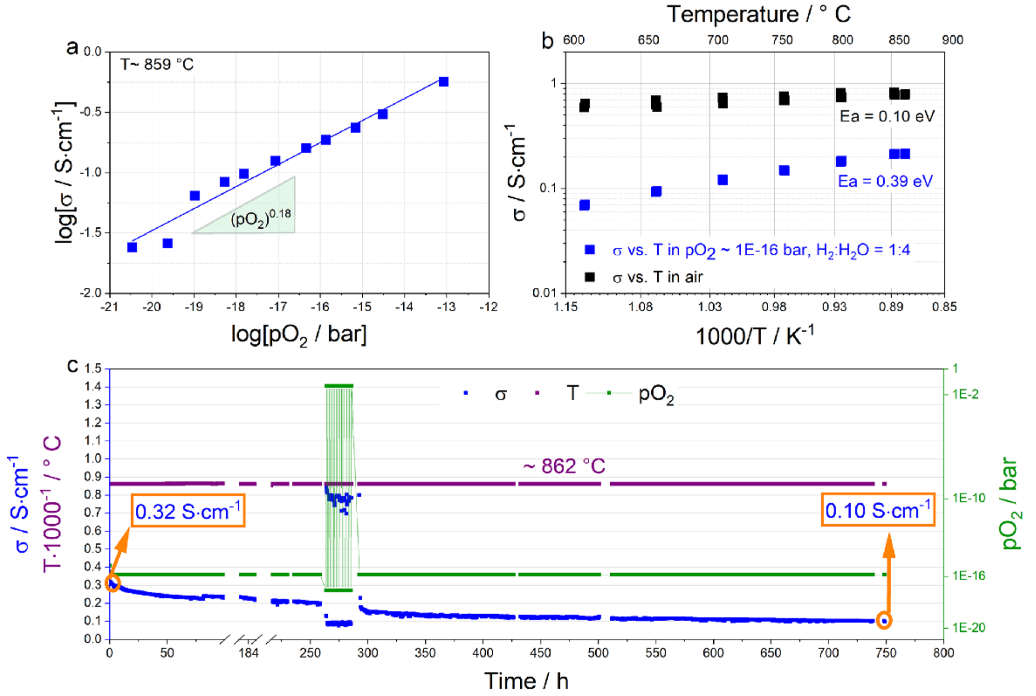

Figure 7. (a) Van der Pauw conductivity measurement of the L65SCrN conductivity vs oxygen partial pressure at 859 °C. (b) L65SCrN conductivity vs temperature in air (black dots) and also at a constant oxygen partial pressure of ~10^{-16} bar (blue dots). (c) L65SCrN conductivity (blue dots), sample temperature (violet dots), and oxygen partial pressure (green dots) vs time during a 750 h durability test.

phases or phase decomposition, suggesting that a zirconate phase was likely not relevant to explain the measured degradation.

With respect to the strong Ohmic degradation, the effect of the cathodic overpotential on the L65SCrN transport properties should be considered cautiously. In electrolysis operation, the hydrogen partial pressure increases at high current densities while the oxygen potential in the perovskite is decreased, creating more oxygen vacancies. In p-type conductors, such as L65SCrN, the positively charged oxygen vacancies that are created under strongly reducing conditions would decrease the concentration of electron holes along the B−O−B chains in the perovskite lattice.[61,62] Therefore, a possible decrease in the (electronic) conductivity could explain the observed increment of the Ohmic resistance. Because of this observation, Van der Pauw conductivity measurements were performed on porous L65SCrN samples, as shown in Figure 7.

3.4. L65SCrN Conductivity Assessment under SOE Operating Conditions. The pO_2 dependence of the conductivity was evaluated at ~860 °C for different oxygen partial pressures (Figure 7a). A $(pO_2)^{0.18}$ dependence was identified for the range between ~10^{-20} and 10^{-13} bar. This dependence is reasonably close to $(pO_2)^{0.17}$, which was measured on LSCrN formulations by Sauvet and Irvine[63] and by Yasuda and Hishinuma.[64] Meadowcroft reported $(pO_2)^{0.19}$ on undoped lanthanum chromites.[65] This behavior is compatible with the hole conduction in p-type conductors.

The temperature dependence in air (Figure 7b, black dots) yielded E_a = 0.10 eV, which agrees with the values between 0.11 and 0.14 eV reported in previous studies.[63,64] For a better comparison with the cell test in Figure 5, the conductivity measurement under reducing atmospheres was performed at a constant pO_2 of ~10^{-16} bar (H_2:H_2O mixing ratio of 1:4) between ~600 and 860 °C (Figure 7b, blue dots). The measured in-plane conductivity was as low as ~0.2−0.3 S cm^{-1} at 860 °C, which was ~2 orders of magnitude lower in contrast to the reported values for a densely sintered bulk perovskite,[64] due to its tortuosity and lower volume fraction.[66] Also, the much smaller particle interface area (sintering neck) in a porous ceramic likely leads to a higher grain boundary resistance, which further decreases the conductivity.

Under these reducing conditions, an apparent activation energy value of E_a = 0.39 eV was calculated. In constrast to the E_a estimation in air, this higher activation energy value could possibly give an insight into how the conductivity is affected under reducing atmospheres. In this p-type conductor, it is assumed that the holes (charge carriers $h^•$) are present on the Cr sites, such as $Cr^{4+} = Cr_{Cr}^{•} = h^{•}$,[63,64] with polaron hopping taking place on the B−O−B chains along corner-sharing octahedra in the perovskite lattice.

In the Sr-doped lanthanum chromite $La_{1-x}Sr_xCrO_{3-\delta}$, the concentration of Cr^{4+} and thus the hole concentration is governed by the concentration of Sr^{2+} at high pO_2.[65] Zhang et al. reported that on lanthanum chromites the Ni doping on the B-site has an enhancing effect on the conductivity by promoting Cr^{4+}. They demonstrated that the electric conductivity is directly proportional to the concentration of Cr^{4+}, which was enhanced for the doped-chromite $\mathrm{La_{0.9}Ca_{0.1}Cr_{0.5}Ni_{0.5}O_3}$ in contrast to $\mathrm{La_{0.9}Ca_{0.1}CrO_3}$,[67] due to charge disproportionation of B-site cations according to:

$$\mathrm{Ni}_{\mathrm{Cr}}^{\times} + \mathrm{Cr}_{\mathrm{Cr}}^{\times} \rightarrow \mathrm{Ni}_{\mathrm{Cr}}' + \mathrm{Cr}_{\mathrm{Cr}}^{\bullet} \tag{6}$$

In L65SCrN, the following reactions may take place upon exposure to low $\mathrm{pO_2}$:

$$2\mathrm{Cr}_{\mathrm{Cr}}^{\bullet} + \mathrm{O}_{\mathrm{O}}^{\times} \rightarrow 2\mathrm{Cr}_{\mathrm{Cr}}^{\times} + \frac{1}{2}\mathrm{O}_2 + \mathrm{V}_{\mathrm{O}}^{\bullet\bullet} \tag{7}$$

$$2\mathrm{Ni}_{\mathrm{Cr}}^{\times} + \mathrm{O}_{\mathrm{O}}^{\times} \rightarrow 2\mathrm{Ni}_{\mathrm{Cr}}' + \frac{1}{2}\mathrm{O}_2 + \mathrm{V}_{\mathrm{O}}^{\bullet\bullet} \tag{8}$$

However, the nickel cation undergoes reduction to its metallic state:[8]

$$\mathrm{Ni}_{\mathrm{Cr}}' + \mathrm{O}_{\mathrm{O}}^{\times} \rightarrow \mathrm{Ni}^{0} + \frac{1}{2}\mathrm{O}_2 + \mathrm{V}_{\mathrm{Cr}}''' + \mathrm{V}_{\mathrm{O}}^{\bullet\bullet} \tag{9}$$

This phenomenon of Ni exsolution and thus Ni depletion of the perovskite lattice creates B-site vacancies that are not thermodynamically stable due to the nominally A-site deficient initial composition. Thereby, A- and B-site vacancies may recombine at the perovskite surface through the annihilation of $\mathrm{ABO_3}$ unit cells, reducing the understoichiometry on the A-site, such as

$$\mathrm{V}_{\mathrm{La}}''' + \mathrm{V}_{\mathrm{Cr}}''' + 3\mathrm{V}_{\mathrm{O}}^{\bullet\bullet} \rightarrow \mathrm{nil} \tag{10}$$

On consideration of the nominal A-site deficiency of L65SCrN, the electroneutrality of the lattice is written as

$$3[\mathrm{V}_{\mathrm{La}}'''] + [\mathrm{Sr}_{\mathrm{La}}'] + [\mathrm{Ni}_{\mathrm{Cr}}'] + 3[\mathrm{V}_{\mathrm{Cr}}'''] = [\mathrm{Cr}_{\mathrm{Cr}}^{\bullet}] + 2[\mathrm{V}_{\mathrm{O}}^{\bullet\bullet}] \tag{11}$$

$$[\mathrm{Cr}_{\mathrm{Cr}}^{\bullet}] = 3[\mathrm{V}_{\mathrm{La}}'''] + [\mathrm{Sr}_{\mathrm{La}}'] + [\mathrm{Ni}_{\mathrm{Cr}}'] + 3[\mathrm{V}_{\mathrm{Cr}}'''] - 2[\mathrm{V}_{\mathrm{O}}^{\bullet\bullet}] \tag{12}$$

Therefore, qualitatively, upon exsolution the decrement of Ni^{2+} ($\mathrm{Ni}_{\mathrm{Cr}}'$) cations and A-site vacancies ($\mathrm{V}_{\mathrm{La}}'''$) will reduce the concentration of $\mathrm{Cr}_{\mathrm{Cr}}^{\bullet}$, which may thus be detrimental for the conductivity. However, a detailed investigation of the point defect chemistry of L65SCrN goes beyond the scope of this work.

With regard to the role of the exsolved metallic nickel nanoparticles on the conductivity of L65SCrN, it is possible to assume that, since they are isolated from each other, they cannot form a Ni-percolating network, leading to a marginal effect on the electronic conductivity. This may be explained by the discrete distributon of the Ni nanoparticles on the perovskite surface as shown in our previous work.[8] Therefore, it is likely that the exsolved Ni nanoparticles on the L65SCrN perovskite are not decisive for the conductivity, but rather that their role is mainly catalytical, by assisting the reaction kinectics with the hydrogen spillover process and $\mathrm{H_2}$ desorption in SOE operation.

The extent of the conductivity change over time was evaluated by performing Van der Pauw measurements of the electronic in-plane conductivity of porous L65SCrN films on insulating substrates under humid $\mathrm{H_2}$ atmospheres for ∼750 h, as shown in Figure 7c. Once the temperature was stabilized at ∼860 °C and the $\mathrm{pO_2}$ at $\sim 10^{-16}$ bar, the initial conductivity was measured to be ca. 0.32 S $\mathrm{cm^{-1}}$, which served as the initial value for this durability test. During the first ∼257 h, the conductivity decreased to a value of ca. 0.24 S $\mathrm{cm^{-1}}$. Shortly after that, 10 redox cycles were performed (each lasting about 1 h; see hours ∼263−285 in Figure 7c) in order to evaluate if the conductivity recovered. Nevertheless, a slow conductivity degradation to a value of ∼0.10 S $\mathrm{cm^{-1}}$ for the total testing time of ∼750 h was observed, for which the redox cycles did not recover the initial conductivity.

Similar to the redox cycle performed in the 1000 h full-cell test, the conductivity of L65SCrN did neither recovered nor severely deteriorated after redox cycling. The overall rather slow trend toward lower effective conductivity and increased Ohmic resistance indicates that the underlying reaction mechanism must involve a kinetically slow process, which includes cation diffusion. During an oxidation cycle, oxygen ion diffusion into the lattice can possibly be much faster. This was observed by Yasuda and Hishinuma, who reported the fractional conductivity change versus time by abruptly changing $\mathrm{pO_2}$ on $\mathrm{La_{0.65}Sr_{0.35}CrO_{3-\delta}}$ samples at 1000 °C.[64] They modeled this behavior as a non-steady-state diffusion process, for which the driving force was considered as the oxygen exchange between the sample and the surroundings. After 2500 s, they observed that the conductivity stabilized at a constant value.[64] Based on their observations, it is possible to assume that, for the L65SCrN perovskite, the durations of the redox cycles (each with a time of 3600 s) were long enough to fill the oxygen vacancies, but very likely were not long enough to enable the Ni cation diffusion within the lattice, which would take possibly longer times at temperatures lower than 1000 °C.

Hence, we suspect that the degradation is likely to be influenced by the modification of the L65SCrN lattice chemistry, likely due to the exsolution of Ni, leading to changes in the charge carrier concentration. When they are taken together, these results suggest that the observed Ohmic degradation at the cell level possibly originates from a degradation of the electronic conductivity of L65SCrN. The various phenomena mentioned before are likely to act in synergy, causing this long-term degradation.

However, we cannot unambiguously estimate in this work which is indeed the most relevant effect. In general, we could assume that, upon the reduction of L65SCrN, there is a trade-off between the amount of Ni on the B-site, which enhances the catalytic activity, and the deterioration of the bulk transport properties. The oxygen vacancy formation would promote Ni exsolution, but from a certain amount of exsolved Ni and therefore Ni depletion from the perovskite lattice, the electronic conductivity of the perovskite would be decreased. Therefore, in general for MIEC electrocatalysts with exsolution of metallic nanoparticles, it is challenging to estimate to what extent the reduction of the B-site cations affects the long-term stability of the electronic conductivity, which may be unveiled by the Ohmic degradation evolution over time. Notwithstanding, an additional contribution to the Ohmic degradation observed in this study from the electrolyte and the barrier layers may not be excluded (eq 5).

3.5. Toward Steam SOE Operation without Hydrogen in the Feed Gas. In this work, it was also investigated whether L65SCrN fuel electrodes are suitable for steam electrolysis without a hydrogen sweep feed, not only at 860 °C but also at lower temperatures: i.e., 800 °C. Therefore, we performed tests on the same cell from section 3.3 at 860 and 800 °C with a fuel gas composition of 50% $\mathrm{H_2O}$−50% $\mathrm{N_2}$ at −0.25 A $\mathrm{cm^{-2}}$. Polarization curves and 70 h durability tests are shown in Figure 8. Analogously to Figure 5, during the first 10

https://doi.org/10.1021/acsaem.2c00680
ACS Appl. Energy Mater. 2022, 5, 8143−8156

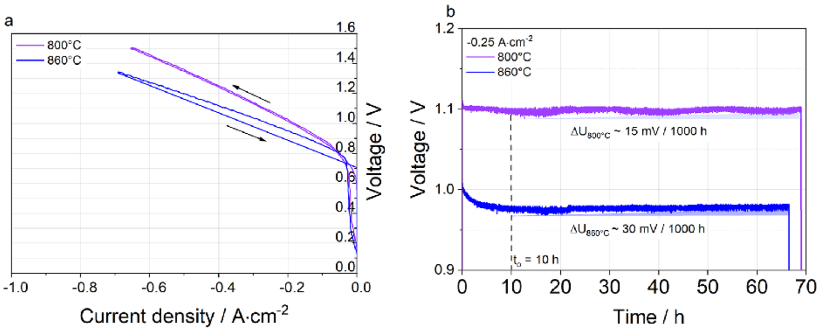

Figure 8. (a) Polarization curves at 860 and 800 °C in SOE of a full ESC with a L65SCrN fuel electrode with the fuel gas mixture of 50% H_2O–50% N_2 (0.5 slpm of H_2O and 0.5 slpm of N_2). (b) Voltage vs time during a 70 h durability test in steam electrolysis with a fuel gas mixture of and a fixed current density of -0.25 A cm^{-2} at 860 °C (blue data) and 800 °C (purple data).

h of operation an activation of the fuel electrode was observed, which was more pronounced at 860 °C. A voltage drift of 30 mV/1000 h was determined at 860 °C, while at 800 °C the drift was 15 mV/1000 h. In this case, it is reasonable to estimate a possible degradation in terms of an Ohmic drift, since the applied electrolysis current density was constant for both operating temperatures. With the observed voltage drift and Ohm's law expressed as $\Delta U = J \times \Delta \mathrm{ASR}_{\mathrm{total}}$, the degradation could be calculated as

$$\Delta \mathrm{ASR}_{\mathrm{total},860^{\circ}\mathrm{C}} = \frac{\Delta U_{860^{\circ}\mathrm{C}}}{J} = \frac{0.03\ \mathrm{V}}{0.25\ \mathrm{A\ cm}^{-2}} = 0.12\ \Omega\ \mathrm{cm}^2 \tag{13}$$

$$\Delta \mathrm{ASR}_{\mathrm{total},800^{\circ}\mathrm{C}} = \frac{\Delta U_{800^{\circ}\mathrm{C}}}{J} = \frac{0.015\ \mathrm{V}}{0.25\ \mathrm{A\ cm}^{-2}} = 0.06\ \Omega\ \mathrm{cm}^2 \tag{14}$$

What stands out from these results is the advantage of operating below 860 °C in terms of the $\mathrm{ASR}_{\mathrm{total}}$ degradation. Figure 8b reveals that there has been a slight increase in the measured voltage for the test at 800 °C, in contrast to the drift observed at 860 °C, which is greater by a factor of 2. These results indicate that operation at lower temperatures would reduce the $\mathrm{ASR}_{\mathrm{total}}$ degradation and therefore would also reduce the drift in voltage on durability test in SOE operation. This is also consistent with a diffusion-limited degradation process.

As an opening to steam electrolysis without hydrogen on the feed gas, the L65SCrN perovskite could be considered a promising fuel electrode for the production of green hydrogen at ~800 °C. This operation mode would avoid the need of a reducing gas in the fuel feed in order to keep the fuel electrode chemically reduced. Even so, further long-term investigations at different temperatures (lower than 860 °C), testing times and also different electrolysis current densities would be required in order to better evaluate the durability of these perovskite fuel electrodes.

4. CONCLUSIONS

L65SCrN and Ni-CGO fuel electrodes were investigated for SOE operation at different temperatures in an ESC architecture. Estimations of the specific energy consumption and the produced hydrogen rate normalized by the active area of the cells confirmed similar performances at 860 °C. However, L65SCrN-based cells showed a performance gain at lower temperatures. The temperature dependence of $\mathrm{ASR}_{\mathrm{total}}$ and the specific resistance of the perovskite fuel electrode surface process, in full- and symmetrical-cell configurations, respectively, demonstrated lower apparent activation energy barrier values E_a in contrast to the Ni-CGO cermets. This possibly finds its origin in the superior catalytic behavior of L65SCrN over Ni-CGO below 860 °C. With the proposed reaction model for water splitting and hydrogen formation, it was possible to assume that the role of the exsolved Ni nanoparticles is mainly catalytic. We suppose that the metallic Ni assists the hydrogen spillover and H_2 desorption on the L65SCrN perovskite surface for the production of green hydrogen from water electrolysis at high temperatures.

During a 1000 h test at 860 °C in SOE operation, the L65SCrN-based cell showed a significant degradation of 48 mV/1000 h, for which an increment by 9.4% of the Ohmic resistance over time was identified. This degradation was possibly related to cation diffusion, which may affect the transport properties of the perovskite electrode. These outcomes may raise the question of how stable this perovskite electrode is in SOE operation and if other operation modes, such as co-electrolysis, would be less detrimental for the transport properties. Also, lowering the operating temperature from 860 to 800 °C could be a suitable approach to mitigate degradation issues.

From an operational point of view, L65SCrN electrodes could also be operated in pure steam electrolysis, which can avoid the requirement of sweeping steam with hydrogen on the feed gas. This may facilitate the system design and operation, as well as decrease operational costs. The performance gain observed with a temperature decrement for the perovskite electrode could be beneficial for operation at larger scales. At the stack level, where temperature gradients are significant, the use of perovskite fuel electrodes may yield a more homogeneous performance between the different repeating units. This effect could be particularly favorable in cell architectures with a lower Ohmic contribution of the electrolyte. For instance, in CSC- or metal-supported cell architectures in terms of dynamic operation. Nevertheless, a key challenge remains in the development and identification of MIEC materials that are more stable for SOE operation on the long-term.

Beyond the specific case of this chromite, further experiments using other perovskite compositions that are more stable over time, as well as different cell architectures, could shed more light on the benefit of their implementation into cells and stacks for applications in SOE systems.

■ ASSOCIATED CONTENT

Ⓢ Supporting Information

The Supporting Information is available free of charge at https://pubs.acs.org/doi/10.1021/acsaem.2c00680.

> Additional SEM images of ceramic powders, Nyquist plots of full ESCs tested in SOE operation, equivalent circuit model (ECM) fittings, EDS analyses, and XRD spectra (PDF)

■ AUTHOR INFORMATION

Corresponding Authors

Diana M. Amaya-Dueñas − *German Aerospace Center (DLR), Institute of Engineering Thermodynamics, D-70569 Stuttgart, Germany;* orcid.org/0000-0002-4188-0062; Email: diana.amayaduenas@dlr.de

Rémi Costa − *German Aerospace Center (DLR), Institute of Engineering Thermodynamics, D-70569 Stuttgart, Germany;* orcid.org/0000-0002-3534-1935; Email: remi.costa@dlr.de

Authors

Matthias Riegraf − *Institute of Chemical Technologies and Analytics, TU Wien, A-1060 Vienna, Austria;* orcid.org/0000-0002-0383-2545

Andreas Nenning − *Institute of Chemical Technologies and Analytics, TU Wien, A-1060 Vienna, Austria;* orcid.org/0000-0001-9313-3731

Alexander K. Opitz − *Institute of Chemical Technologies and Analytics, TU Wien, A-1060 Vienna, Austria;* orcid.org/0000-0002-2567-1885

K. Andreas Friedrich − *German Aerospace Center (DLR), Institute of Engineering Thermodynamics, D-70569 Stuttgart, Germany; Institute of Building Energetics, Thermal Engineering and Energy Storage (IGTE), University of Stuttgart, D-70569 Stuttgart, Germany;* orcid.org/0000-0002-2968-5029

Complete contact information is available at:
https://pubs.acs.org/10.1021/acsaem.2c00680

Author Contributions

The manuscript was written through contributions of all authors. All authors have given approval to the final version of the manuscript.

Notes

The authors declare no competing financial interest.

■ ACKNOWLEDGMENTS

The German Academic Exchange Service (DAAD) is acknowledged for the Ph.D. scholarship of D.-M.A.-D. with the award DLR/DAAD Research Fellowships−Doctoral Studies, 2017. Günter Roth and Dr. Robert Ruckdäschel are acknowledged for the SEM sample preparation and analyses, as are Dr. Noriko Sata for the XRD measurements and Dr. Feng Han for his support on the sample cutting and preparation for the conductivity measurements. We are grateful to Prof. Dr. Jürgen Fleig from the Institute of Chemical Technologies and Analytics at TU Wien for the support with this collaboration. Part of this work received funding from the German Federal Ministry of Education and Research (BMBF) within the Kopernikus Project P2X (Grant n03SFKE20).

■ REFERENCES

(1) *The National Hydrogen Strategy*; Federal Ministry for Economic Affairs and Energy Berlin: June 2020.

(2) Hauch, A.; Kungas, R.; Blennow, P.; Hansen, A. B.; Hansen, J. B.; Mathiesen, B. V.; Mogensen, M. B. Recent advances in solid oxide cell technology for electrolysis. *Science* **2020**, *370* (6513), 1.

(3) Andreas, F.; Marcelo, C.; Müller, M.; Smolinka, T.; Weber, A.; Harnisch, F.; Brinner, A.; Löffler, M. S.; Jörissen, L. In *Von der Elektrolyse zur Brenntoffzelle*; FVEE - Jahrestagung 2019: Energy Research for Future - Forschung für die Herausforderungen der Energiewende, 2019.

(4) Mogensen, M. B.; Chen, M.; Frandsen, H. L.; Graves, C.; Hansen, J. B.; Hansen, K. V.; Hauch, A.; Jacobsen, T.; Jensen, S. H.; Skafte, T. L.; Sun, X. Reversible solid-oxide cells for clean and sustainable energy. *Clean Energy* **2019**, *3* (3), 175−201.

(5) Qi, H.; Lee, Y.-L.; Yang, T.; Li, W.; Li, W.; Ma, L.; Hu, S.; Duan, Y.; Hackett, G. A.; Liu, X. Positive Effects of H2O on the Hydrogen Oxidation Reaction on Sr2Fe1.5Mo0.5O6-δ-Based Perovskite Anodes for Solid Oxide Fuel Cells. *ACS Catal.* **2020**, *10* (10), 5567−5578.

(6) Ebbesen, S. D.; Mogensen, M. Electrolysis of carbon dioxide in Solid Oxide Electrolysis Cells. *J. Power Sources* **2009**, *193* (1), 349−358.

(7) Peters, R.; Deja, R.; Blum, L.; Nguyen, V. N.; Fang, Q.; Stolten, D. Influence of operating parameters on overall system efficiencies using solid oxide electrolysis technology. *Int. J. Hydrogen Energy* **2015**, *40* (22), 7103−7113.

(8) Amaya-Dueñas, D.-M.; Chen, G.; Weidenkaff, A.; Sata, N.; Han, F.; Biswas, I.; Costa, R.; Friedrich, K. A. A-site Deficient Chromite with In Situ Ni Exsolution as Fuel Electrode for Solid Oxide Cells (SOC). *Journal of Materials Chemistry A* **2021**, *9*, 5685−5701.

(9) Riegraf, M.; Zekri, A.; Knipper, M.; Costa, R.; Schiller, G.; Friedrich, K. A. Sulfur poisoning of Ni/Gadolinium-doped ceria anodes: A long-term study outlining stable solid oxide fuel cell operation. *J. Power Sources* **2018**, *380*, 26−36.

(10) Knibbe, R.; Wang, H.-J.; Blennow, P.; Thydén, K.; Persson, Å. H.; Mikkelsen, L.; Klemensø, T. Oxidation in ceria infiltrated metal supported SOFCs - A TEM investigation. *J. Power Sources* **2013**, *228*, 75−82.

(11) Hoerlein, M. P.; Riegraf, M.; Costa, R.; Schiller, G.; Friedrich, K. A. A parameter study of solid oxide electrolysis cell degradation: Microstructural changes of the fuel electrode. *Electrochim. Acta* **2018**, *276*, 162−175.

(12) Tietz, F.; Sebold, D.; Brisse, A.; Schefold, J. Degradation phenomena in a solid oxide electrolysis cell after 9000 h of operation. *J. Power Sources* **2013**, *223*, 129−135.

(13) Chen, J.; Ouyang, M.; Boldrin, P.; Atkinson, A.; Brandon, N. P. Understanding the Coarsening and Degradation in a Nanoscale Nickel Gadolinia-Doped-Ceria Electrode for High-Temperature Applications. *ACS Appl. Mater. Interfaces* **2020**, *12* (42), 47564−47573.

(14) Holzer, L.; Iwanschitz, B.; Hocker, T.; Münch, B.; Prestat, M.; Wiedenmann, D.; Vogt, U.; Holtappels, P.; Sfeir, J.; Mai, A.; Graule, T. Microstructure degradation of cermet anodes for solid oxide fuel cells: Quantification of nickel grain growth in dry and in humid atmospheres. *J. Power Sources* **2011**, *196* (3), 1279−1294.

(15) Chen, G.; Guan, G.; Kasai, Y.; Abudula, A. Nickel volatilization phenomenon on the Ni-CGO anode in a cathode-supported SOFC operated at low concentrations of H2. *Int. J. Hydrogen Energy* **2012**, *37* (1), 477−483.

(16) Mogensen, M. B.; Hauch, A.; Sun, X.; Chen, M.; Tao, Y.; Ebbesen, S. D.; Hansen, K. V.; Hendriksen, P. V. Relation Between Ni Particle Shape Change and Ni Migration in Ni-YSZ. Electrodes - a Hypothesis. *Fuel Cells* **2017**, *17* (4), 434−441.

(17) Jiao, Z.; Busso, E. P.; Shikazono, N. Influence of Polarization on the Morphological Changes of Nickel in Fuel Electrodes of Solid Oxide Cells. *J. Electrochem. Soc.* **2020**, *167* (2), 024516.

(18) Nakajo, A.; Rinaldi, G.; Caliandro, P.; Jeanmonod, G.; Navratilova, L.; Cantoni, M.; Van herle, J. Evolution of the Morphology Near Triple-Phase Boundaries in Ni-Yttria Stabilized Zirconia Electrodes Upon Cathodic Polarization. *Journal of Electrochemical Energy Conversion and Storage* **2020**, *17* (4), 041004.

(19) Song, B.; Bertei, A.; Wang, X.; Cooper, S. J.; Ruiz-Trejo, E.; Chowdhury, R.; Podor, R.; Brandon, N. P. Unveiling the mechanisms of solid-state dewetting in Solid Oxide Cells with novel 2D electrodes. *J. Power Sources* **2019**, *420*, 124−133.

(20) Faes, A.; Hessler-Wyser, A.; Zryd, A.; Van Herle, J. A Review of RedOx Cycling of Solid Oxide Fuel Cells Anode. *Membranes (Basel)* **2012**, *2* (3), 585−664.

(21) Duboviks, V.; Maher, R. C.; Kishimoto, M.; Cohen, L. F.; Brandon, N. P.; Offer, G. J. A Raman spectroscopic study of the carbon deposition mechanism on Ni/CGO electrodes during CO/CO2 electrolysis. *Phys. Chem. Chem. Phys.* **2014**, *16* (26), 13063−13068.

(22) Agency, I. E. *The Role of Critical World Energy Outlook Special Report Minerals in Clean Energy Transitions*; International Energy Agency: 2021.

(23) Holtappels, P.; Ramos, T.; Tietz, F.; Malzbender, J.; Mai, A.; Hansen, J. R.-.; Irvine, J. T. S. *Sulphur, Carbon, and re-Oxidation Tolerant Anodes and Anode Supports for Solid Oxide Fuel Cells*; European Commision: 2015.

(24) Zhu, H.; Zhang, P.; Dai, S. Recent Advances of Lanthanum-Based Perovskite Oxides for Catalysis. *ACS Catal.* **2015**, *5* (11), 6370−6385.

(25) Myung, J.-h.; Neagu, D.; Miller, D. N.; Irvine, J. T. S. Switching on electrocatalytic activity in solid oxide cells. *Nature* **2016**, *537* (7621), 528−531.

(26) Tsekouras, G.; Neagu, D.; Irvine, J. T. S. Step-change in high temperature steam electrolysis performance of perovskite oxide cathodes with exsolution of B-site dopants. *Energy Environ. Sci.* **2013**, *6* (1), 256−266.

(27) Kyriakou, V.; Neagu, D.; Papaioannou, E. I.; Metcalfe, I. S.; van de Sanden, M. C. M.; Tsampas, M. N. Co-electrolysis of H2O and CO2 on exsolved Ni nanoparticles for efficient syngas generation at controllable H2/CO ratios. *Applied Catalysis B: Environmental* **2019**, *258*, 117950.

(28) Opitz, A. K.; Nenning, A.; Rameshan, C.; Kubicek, M.; Gotsch, T.; Blume, R.; Havecker, M.; Knop-Gericke, A.; Rupprechter, G.; Klotzer, B.; Fleig, J. Surface Chemistry of Perovskite-Type Electrodes During High Temperature CO2 Electrolysis Investigated by Operando Photoelectron Spectroscopy. *ACS Appl. Mater. Interfaces* **2017**, *9* (41), 35847−35860.

(29) Sapountzi, F. M.; Brosda, S.; Papazisi, K. M.; Balomenou, S. P.; Tsiplakides, D. Electrochemical performance of La0.75Sr0.25Cr0.9-M0.1O3 perovskites as SOFC anodes in CO/CO2 mixtures. *J. Appl. Electrochem.* **2012**, *42* (9), 727−735.

(30) Neagu, D.; Kyriakou, V.; Roiban, I.-L.; Aouine, M.; Tang, C.; Caravaca, A.; Kousi, K.; Schreur-Piet, I.; Metcalfe, I. S.; Vernoux, P.; van de Sanden, M. C. M.; Tsampas, M. N. In Situ Observation of Nanoparticle Exsolution from Perovskite Oxides: From Atomic Scale Mechanistic Insight to Nanostructure Tailoring. *ACS Nano* **2019**, *13* (11), 12996−13005.

(31) Riegraf, M.; Amaya-Duenas, D. M.; Sata, N.; Friedrich, K. A.; Costa, R. Performance and Limitations of Nickel-Doped Chromite Anodes in Electrolyte-Supported Solid Oxide Fuel Cells. *ChemSusChem* **2021**, *14*, 2401−2413.

(32) Nenning, A.; Bischof, C.; Fleig, J.; Bram, M.; Opitz, A. K. The Relation of Microstructure, Materials Properties and Impedance of SOFC Electrodes: A Case Study of Ni/GDC Anodes. *Energies* **2020**, *13* (4), 987.

(33) Nenning, A.; Holzmann, M.; Fleig, J.; Opitz, A. K. Excellent kinetics of single-phase Gd-doped ceria fuel electrodes in solid oxide cells. *Materials Advances* **2021**, *2* (16), 5422−5431.

(34) Johnson, D. *ZView Electrochemical Impedance Software, 2.3b*; Scribner Associates, Inc.: 2000.

(35) Van Der Pauw, L. J. A Method of Measuring the Resistivity and Hall Coefficient on Lamellae of Arbitrary Shape. *Philips Technical Review* **1958**, *20*, 220−224.

(36) Perry, S. C.; Ponce de León, C.; Walsh, F. C. Review—The Design, Performance and Continuing Development of Electrochemical Reactors for Clean Electrosynthesis. *J. Electrochem. Soc.* **2020**, *167*, 155525.

(37) SUNFIRE-HYLINK HL40.

(38) Amaya-Dueñas, D.-M.; Riedel, M.; Riegraf, M.; Costa, R.; Friedrich, K. A. High Temperature Co-electrolysis for Power-to-X. *Chemie Ingenieur Technik* **2020**, *92* (1−2), 45−52.

(39) Klotz, D. *Characterization and Modeling of Electrochemical Energy Conversion Systems by Impedance Techniques*; Karlsruher Institute für Technologie (KIT): 2012.

(40) Schefold, J.; Brisse, A.; Surrey, A.; Walter, C. 80,000 current on/off cycles in a one year long steam electrolysis test with a solid oxide cell. *Int. J. Hydrogen Energy* **2020**, *45* (8), 5143−5154.

(41) Opitz, A. K.; Gerstl, M.; Bram, M. Model System Supported Impedance Simulation of Composite Electrodes. *Fuel Cells* **2019**, *19* (4), 417−428.

(42) Adler, S. B. L. J. A.; Steele, B. C. H. Electrode Kinetics of Porous Mixed-Conducting Oxygen Electrodes. *J. Electrochem. Soc.* **1996**, *143*, 3554−3564.

(43) Yurkiv, V.; Costa, R.; Ilhan, Z.; Ansar, A.; Bessler, W. G. Impedance of the Surface Double Layer of LSCF/CGO Composite Cathodes: An Elementary Kinetic Model. *J. Electrochem. Soc.* **2014**, *161* (4), F480−F492.

(44) Njodzefon, J.-C.; Graves, C. R.; Mogensen, M. B.; Weber, A.; Hjelm, J. Kinetic Studies on State of the Art Solid Oxide Cells: A Comparison between Hydrogen/Steam and Reformate Fuels. *J. Electrochem. Soc.* **2016**, *163* (13), F1451−F1462.

(45) Bessler, W. G.; Gewies, S. Gas Concentration Impedance of Solid Oxide Fuel Cell Anodes II. Channel Geometry. *J. Electrochem. Soc.* **2007**, *154*, B548−B559.

(46) Schefold, J.; Brisse, A.; Poepke, H. Long-term Steam Electrolysis with Electrolyte-Supported Solid Oxide Cells. *Electrochim. Acta* **2015**, *179*, 161−168.

(47) Riegraf, M.; Yurkiv, V.; Costa, R.; Schiller, G.; Friedrich, K. A. Evaluation of the Effect of Sulfur on the Performance of Nickel/Gadolinium-Doped Ceria Based Solid Oxide Fuel Cell Anodes. *ChemSusChem* **2017**, *10* (3), 587−599.

(48) Nielsen, J.; Klemensø, T.; Blennow, P. Detailed impedance characterization of a well performing and durable Ni:CGO infiltrated cermet anode for metal-supported solid oxide fuel cells. *J. Power Sources* **2012**, *219*, 305−316.

(49) Riegraf, M.; Costa, R.; Schiller, G.; Friedrich, K. A.; Dierickx, S.; Weber, A. Electrochemical Impedance Analysis of Symmetrical Ni/Gadolinium-Doped Ceria (CGO10) Electrodes in Electrolyte-Supported Solid Oxide Cells. *J. Electrochem. Soc.* **2019**, *166* (13), F865−F872.

(50) Nenning, A.; Volgger, L.; Miller, E.; Mogni, L. V.; Barnett, S.; Fleig, J. The Electrochemical Properties of Sr(Ti,Fe)O3-δfor Anodes in Solid Oxide Fuel Cells. *J. Electrochem. Soc.* **2017**, *164* (4), F364−F371.

(51) Velicsanyi, P.; Gerstl, M.; Nenning, A.; Hutter, H.; Fleig, J.; Opitz, A. K. The Effect of Mn Co-doping on the Electrochemical Properties of Gd$_{0.2}$Ce$_{0.8}$O$_{1.9-\delta}$/Pt Model-composite Electrodes. *ECS Trans.* **2015**, *68*, 1509−1516.

(52) Jung, W.; Dereux, J. O.; Chueh, W. C.; Hao, Y.; Haile, S. M. High electrode activity of nanostructured, columnar ceria films for solid oxide fuel cells. *Energy Environ. Sci.* **2012**, *5* (9), 8682−8689.

(53) Liu, L.; Kim, G.-Y.; Chandra, A. Modeling of Ni-CGO anode in a solid oxide fuel cell deposited by spray pyrolysis. *J. Power Sources* **2012**, *210*, 129−137.

(54) Opitz, A. K.; Nenning, A.; Vonk, V.; Volkov, S.; Bertram, F.; Summerer, H.; Schwarz, S.; Steiger-Thirsfeld, A.; Bernardi, J.; Stierle,

A.; Fleig, J. Understanding electrochemical switchability of perovskite-type exsolution catalysts. *Nat. Commun.* **2020**, *11* (1), 4801.

(55) Opitz, A. K.; Nenning, A.; Rameshan, C.; Rameshan, R.; Blume, R.; Havecker, M.; Knop-Gericke, A.; Rupprechter, G.; Fleig, J.; Klotzer, B. Enhancing electrochemical water-splitting kinetics by polarization-driven formation of near-surface iron(0): an in situ XPS study on perovskite-type electrodes. *Angew. Chem., Int. Ed. Engl.* **2015**, *54* (9), 2628–32.

(56) Zhu, T.; Troiani, H. E.; Mogni, L. V.; Han, M.; Barnett, S. A. Ni-Substituted Sr(Ti,Fe)O3 SOFC Anodes: Achieving High Performance via Metal Alloy Nanoparticle Exsolution. *Joule* **2018**, 2 (3), 478–496.

(57) Feng, Z. A.; El Gabaly, F.; Ye, X.; Shen, Z. X.; Chueh, W. C. Fast vacancy-mediated oxygen ion incorporation across the ceria-gas electrochemical interface. *Nat. Commun.* **2014**, *5*, 4374.

(58) Nenning, A.; Navickas, E.; Hutter, H.; Fleig, J. Water-Induced Decoupling of Tracer and Electrochemical Oxygen Exchange Kinetics on Mixed Conducting Electrodes. *J. Phys. Chem. Lett.* **2016**, *7* (14), 2826–31.

(59) Hansen, H. A.; Wolverton, C. Kinetics and Thermodynamics of H2O Dissociation on Reduced CeO2(111). *J. Phys. Chem. C* **2014**, *118* (47), 27402–27414.

(60) Gu, X.-K.; Nikolla, E. Fundamental Insights into High-Temperature Water Electrolysis Using Ni-Based Electrocatalysts. *J. Phys. Chem. C* **2015**, *119* (48), 26980–26988.

(61) Mizusaki, J.; Yonemura, Y.; Kamata, H.; Ohyama, K.; Mori, N.; Takai, H.; Tagawa, H.; Dokiya, M.; Naraya, K.; Sasamoto, T.; Inaba, H.; Hashimoto, T. Electronic conductivity, Seebeck coefficient, defect and electronic structure of nonstoichiometric La1-xSrxMnO3. *Solid State Ionics* **2000**, *132* (3), 167–180.

(62) Jiang, S. P.; Liu, L.; Ong, K. P.; Wu, P.; Li, J.; Pu, J. Electrical conductivity and performance of doped LaCrO3 perovskite oxides for solid oxide fuel cells. *J. Power Sources* **2008**, *176* (1), 82–89.

(63) Sauvet, A. L.; Irvine, J. T. S. Catalytic activity for steam methane reforming and physical characterisation of La1-xSrxCr1-yNiyO3-δ. *Solid State Ionics* **2004**, *167* (1), 1–8.

(64) Yasuda, I.; Hishinuma, M. Electrical conductivity and chemical diffusion coefficient of Sr-doped lanthanum chromites. *Solid State Ionics* **1995**, *80* (1), 141–150.

(65) Meadowcroft, D. B. Some properties of strontium-doped lanthanum chromite. *J. Phys. D: Appl. Phys.* **1969**, 2 (9), 1225–1233.

(66) Tjaden, B.; Brett, D. J. L.; Shearing, P. R. Tortuosity in electrochemical devices: a review of calculation approaches. *International Materials Reviews* **2018**, 63 (2), 47–67.

(67) Zhang, G. J.; Song, Y. W.; Xiong, H.; Zheng, J. Y.; Jia, Y. Q. Synthesis and crystal structure of La0.9Ca0.1Cr1-xNixO3 (x = 0.0–1.0) and electric conductivity of La0.9Ca0.1Cr0.5Ni0.5O3. *Mater. Chem. Phys.* **2002**, *73* (1), 101–105.

■ NOTE ADDED AFTER ASAP PUBLICATION

After this paper was published ASAP on July 8, 2022 a change was made to the TOC and abstract graphics. The corrected version was reposted July 25, 2022.

Article III – Supplementary information

Reprinted (adapted) with permission from *ACS Appl. Energy Mater.* 2022, 5, 7, 8143–8156.

Supplementary information for:

Operational Aspects of a Perovskite Chromite-Based Fuel Electrode in Solid Oxide Electrolysis Cells (SOEC)

Diana M. Amaya-Dueñas[a], Matthias Riegraf[a], Andreas Nenning[b], Alexander K. Opitz[b], Rémi Costa[a*],*
and K. Andreas Friedrich[a,c]

[a] German Aerospace Center (DLR), Institute of Engineering Thermodynamics, Pfaffenwaldring 38-40, D-70569 Stuttgart, Germany

[b] Institute of Chemical Technologies and Analytics, TU Wien, Getreidemarkt 9, A-1060 Vienna, Austria

[c] Institute of Building Energetics, Thermal Engineering and Energy Storage (IGTE), University of Stuttgart, Pfaffenwaldring 31, D-70569 Stuttgart, Germany

[*] E-mail: diana.amayaduenas@dlr.de ; remi.costa@dlr.de

Cell preparation.

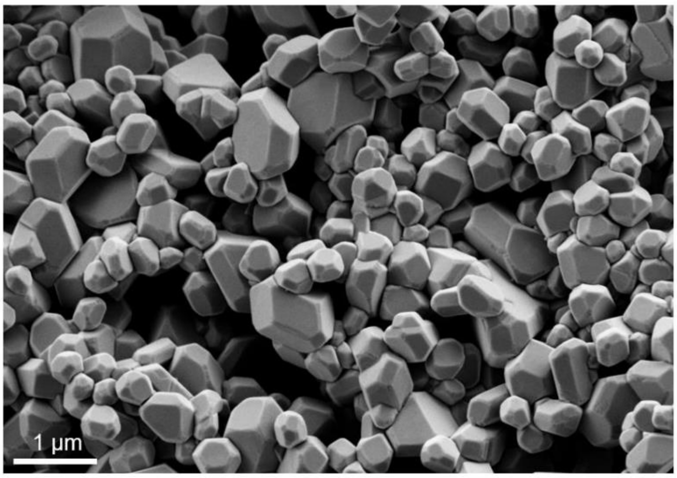

Figure S1. SEM imaging of synthetized L65SCrN ceramic powder by the nitrate-combustion method. Powder was used for the fuel electrode ceramic ink for the symmetrical button cells manufacturing.

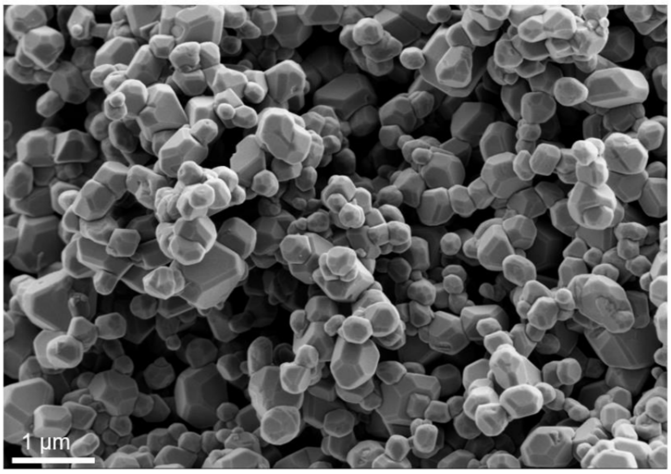

Figure S2. SEM imaging of commercial L65SCrN ceramic powder supplied by Marion Technologies (Verniolle, France). Powder was used for the fuel electrode ceramic ink for the full cells manufacturing process.

Temperature Dependence of the Steam Electrolysis with L65SCrN and Ni-CGO Fuel Electrodes in ESCs.

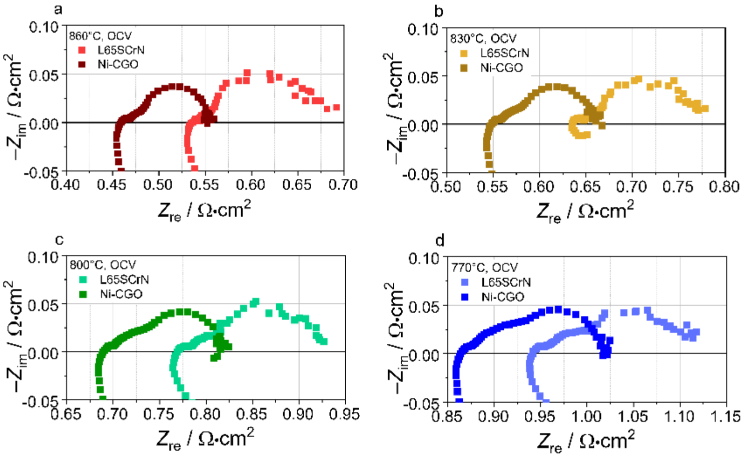

Figure S3. Nyquist plots of impedance spectra recorded at OCV of L65SCrN and Ni-CGO-based full ESCs in electrolysis mode with a fuel gas mixture of 80% H_2O - 20% H_2 (0.4 slpm of H_2O, 0.1 slpm of H_2 and 0.5 slpm N_2) at (a) 860 °C, (b) 830 °C, (c) 800 °C and (d) 770 °C.

Temperature and Gas Composition Dependence of the Polarization Resistance of L65SCrN Fuel Electrodes.

Equivalent circuit model (ECM) fittings on EIS spectra of L65SCrN symmetrical button cells were performed in order to estimate the polarization resistance values of such thermally-activated contributions. Details of the ECM for each temperature are detailed as following:

Composition 10% H_2O - 90% H_2.

Table S1. ECM fitting parameters in ZView of L65SCrN symmetrical cells with fuel gas composition 10% H_2O - 90% H_2 at 860°C

L65SCrN Symmetrical cell	
10% H_2O - 90% H_2	
860°C	
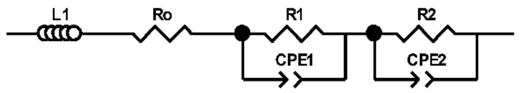	
Possible Process	**ECM elements**
CGO20/ 3YSZ interface	$R_1 = 8.33 \times 10^{-3}\ \Omega$
	$CPE_1 = 4.53 \times 10^{-2}\ s^{0.99}/\Omega$
	$n = 0.99$
Related to L65SCrN processes	$R_2 = 5.98 \times 10^{-1}\ \Omega$
	$CPE_2 = 3.86 \times 10^{-1}\ s^{0.94}/\Omega$
	$n = 0.94$
Fit $\lambda^2 = 2.07 \times 10^{-5}$	

Table S2. ECM fitting parameters in ZView of L65SCrN symmetrical cells with fuel gas composition 10% H_2O - 90% H_2 at 830°C

L65SCrN Symmetrical cell	
10% H_2O - 90% H_2	
830°C	
Possible Process	**ECM elements**
CGO20/ 3YSZ interface	$R_1 = 1.31 \times 10^{-2}\ \Omega$
	$CPE_1 = 5.17 \times 10^{-2}\ s^{0.91}/\Omega$
	$n = 0.91$
Related to L65SCrN processes	$R_2 = 7.44 \times 10^{-1}\ \Omega$
	$CPE_2 = 3.96 \times 10^{-1}\ s^{0.94}/\Omega$
	$n = 0.94$
Fit $\lambda^2 = 4.73 \times 10^{-5}$	

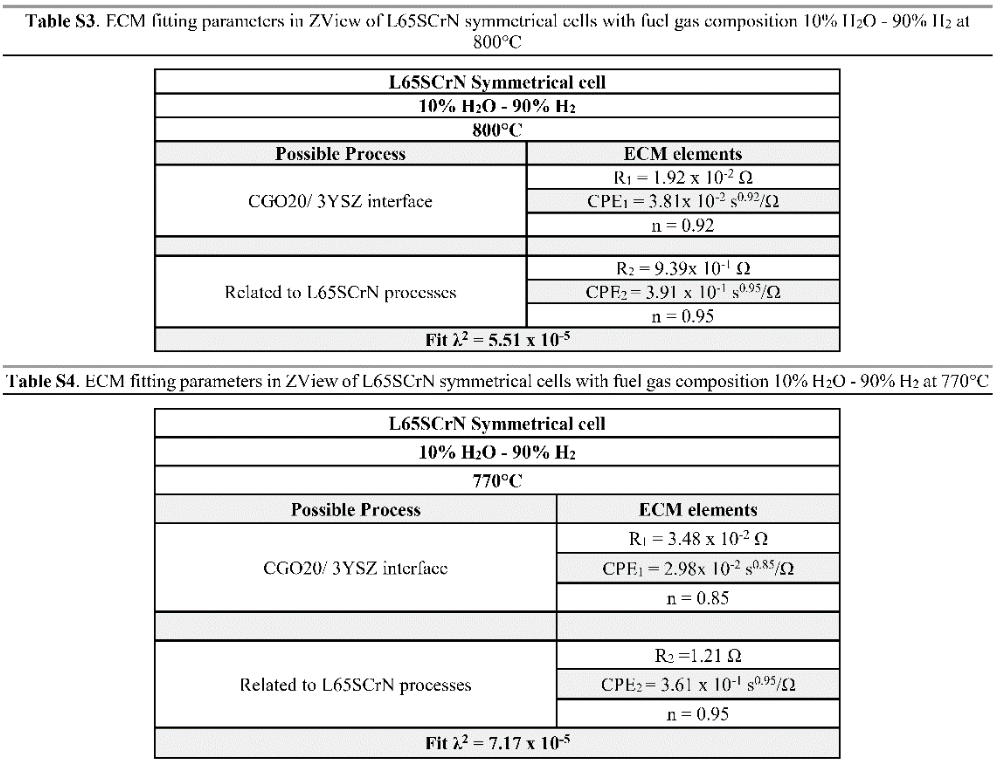

Table S3. ECM fitting parameters in ZView of L65SCrN symmetrical cells with fuel gas composition 10% H_2O - 90% H_2 at 800°C

L65SCrN Symmetrical cell	
10% H_2O - 90% H_2	
800°C	
Possible Process	**ECM elements**
CGO20/ 3YSZ interface	$R_1 = 1.92 \times 10^{-2}\ \Omega$
	$CPE_1 = 3.81 \times 10^{-2}\ s^{0.92}/\Omega$
	n = 0.92
Related to L65SCrN processes	$R_2 = 9.39 \times 10^{-1}\ \Omega$
	$CPE_2 = 3.91 \times 10^{-1}\ s^{0.95}/\Omega$
	n = 0.95
Fit $\lambda^2 = 5.51 \times 10^{-5}$	

Table S4. ECM fitting parameters in ZView of L65SCrN symmetrical cells with fuel gas composition 10% H_2O - 90% H_2 at 770°C

L65SCrN Symmetrical cell	
10% H_2O - 90% H_2	
770°C	
Possible Process	**ECM elements**
CGO20/ 3YSZ interface	$R_1 = 3.48 \times 10^{-2}\ \Omega$
	$CPE_1 = 2.98 \times 10^{-2}\ s^{0.85}/\Omega$
	n = 0.85
Related to L65SCrN processes	$R_2 = 1.21\ \Omega$
	$CPE_2 = 3.61 \times 10^{-1}\ s^{0.95}/\Omega$
	n = 0.95
Fit $\lambda^2 = 7.17 \times 10^{-5}$	

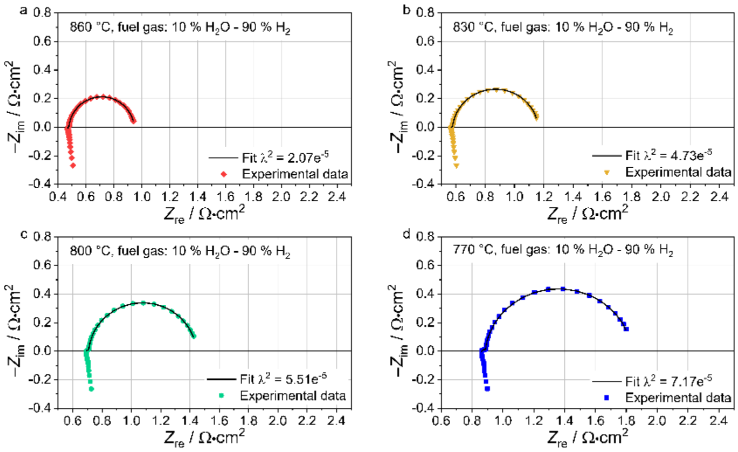

Figure S4. Nyquist plots of experimental data (scatter) and fitting data (line) at OCV of L65SCrN symmetrical button cells with fuel gas mixture of 10% H_2O - 90% H_2 at (a) 860 °C, (b) 830 °C, (c) 800 °C and (d) 770 °C.

Table S5. Arrhenius-type data of L65SCrN symmetrical cells with fuel gas composition 10% H_2O - 90% H_2

T (°C)	1000/T (K^{-1})	R_2 after Zview fitting (Ω)	R_{pol} (Ω•cm²)	R_{pol} for each electrode (Ω•cm²)	Ln [R_{pol}]
860	0.88	0.60	0.47	0.23	-1.45
830	0.91	0.74	0.58	0.29	-1.23
800	0.93	0.94	0.74	0.37	-1.00
770	0.96	1.21	0.95	0.47	-0.75

Composition 38% H_2O – 62% H_2.

Table S6. ECM fitting parameters in Zview of L65SCrN symmetrical cells with fuel gas composition 38% H_2O – 62% H_2 at 860°C

L65SCrN Symmetrical cell **38% H_2O – 62% H_2** **860°C** 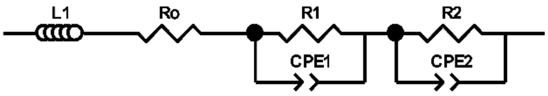	
Possible Process	**ECM elements**
CGO20/ 3YSZ interface	$R_1 = 7.87 \times 10^{-3}$ Ω
	$CPE_1 = 4.35 \times 10^{-2}$ F
	n = 1
Related to L65SCrN processes	$R_2 = 7.64 \times 10^{-1}$ Ω
	$CPE_2 = 3.52 \times 10^{-1}$ $s^{0.95}$/Ω
	n = 0.95
Fit $\lambda^2 = 4.75 \times 10^{-5}$	

Table S7. ECM fitting parameters in Zview of L65SCrN symmetrical cells with fuel gas composition 38% H_2O – 62% H_2 at 830°C

L65SCrN Symmetrical cell	
38% H_2O – 62% H_2	
830°C	
Possible Process	**ECM elements**
CGO20/ 3YSZ interface	$R_1 = 1.20 \times 10^{-2}$ Ω
	$CPE_1 = 2.78 \times 10^{-2}$ F
	n = 1
Related to L65SCrN processes	$R_2 = 1.02$ Ω
	$CPE_2 = 2.28 \times 10^{-1}$ $s^{0.95}$/Ω
	n = 0.95
Fit $\lambda^2 = 3.73 \times 10^{-5}$	

Table S8. ECM fitting parameters in Zview of L65SCrN symmetrical cells with fuel gas composition 38% H_2O – 62% H_2 at 800°C

L65SCrN Symmetrical cell	
38% H_2O - 62% H_2	
800°C	
Possible Process	**ECM elements**
CGO20/ 3YSZ interface	$R_1 = 2.06 \times 10^{-2}$ Ω
	$CPE_1 = 2.67 \times 10^{-2}$ $s^{0.92}$/Ω
	n = 0.92
Related to L65SCrN processes	$R_2 = 1.30$ Ω
	$CPE_2 = 1.92 \times 10^{-1}$ $s^{0.95}$/Ω
	n = 0.95
Fit $\lambda^2 = 4.40 \times 10^{-5}$	

Table S9. ECM fitting parameters in ZView of L65SCrN symmetrical cells with fuel gas composition 38% H_2O - 62% H_2 at 770°C

L65SCrN Symmetrical cell	
38% H_2O - 62% H_2	
770°C	
Possible Process	**ECM elements**
CGO20/ 3YSZ interface	$R_1 = 3.07 \times 10^{-2}$ Ω
	$CPE_1 = 1.97 \times 10^{-2}$ $s^{0.92}$/Ω
	n = 0.92
Related to L65SCrN processes	$R_2 = 1.69$ Ω
	$CPE_2 = 1.62 \times 10^{-1}$ $s^{0.95}$/Ω
	n = 0.95
Fit $\lambda^2 = 5.45 \times 10^{-5}$	

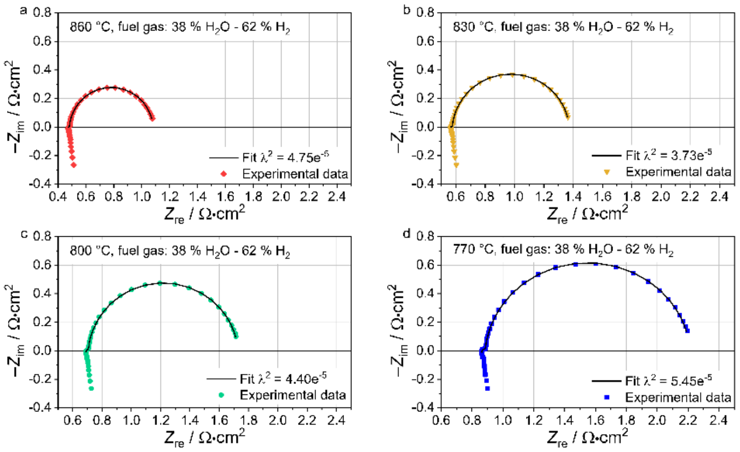

Figure S5. Nyquist plots of experimental data (scatter) and fitting data (line) at OCV of L65SCrN symmetrical button cells with fuel gas mixture of 38% H_2O - 62% H_2 at (a) 860 °C, (b) 830 °C, (c) 800 °C and (d) 770 °C.

Table S10. Arrhenius-type data of L65SCrN symmetrical cells with fuel gas composition 38% H_2O - 62% H_2

T (°C)	1000/T (K^{-1})	R_2 after Zview fitting (Ω)	R_{pol} (Ω•cm^2)	R_{pol} for each electrode (Ω•cm^2)	Ln [R_{pol}]
860	0.88	0.76	0.60	0.30	-1.20
830	0.91	1.02	0.80	0.40	-0.92
800	0.93	1.30	1.02	0.51	-0.67
770	0.96	1.69	1.33	0.66	-0.41

Long-Term Stability of L65SCrN Fuel Electrodes in SOE.

ECM fittings were performed in order to quantify the evolution of the ohmic and polarization resistance from the plots shown on the manuscript in Figure 5 c and d. Those ECMs are detailed as following:

Table S11. ECM fitting parameters in ZView of L65SCrN-based full ESC in steam electrolysis operation for 1000 h long-term with fuel gas composition 80% H_2O - 20% H_2 at 860 °C and -0.67 A•cm^{-2}.

<table>
<tr><td colspan="6">ECM for 1000 h long-term with 80% H_2O - 20% H_2 at 860 °C and -0.67 A•cm^{-2}
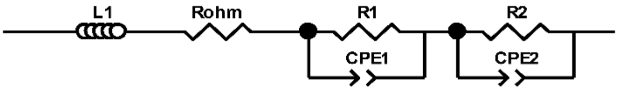 </td></tr>
<tr><th>time (h)</th><th>R_Ω (Ω•cm^2)</th><th>R_1 (Ω•cm^2)</th><th>R_2 (Ω•cm^2)</th><th>R_{pol} (Ω•cm^2)</th><th>Fit λ^2</th></tr>
<tr><td>**0**</td><td>0.53</td><td>0.01</td><td>0.16</td><td>0.17</td><td>2.22 x 10^{-4}</td></tr>
<tr><td>**67**</td><td>0.54</td><td>0.01</td><td>0.09</td><td>0.10</td><td>3.89 x 10^{-4}</td></tr>
<tr><td>**163**</td><td>0.55</td><td>0.02</td><td>0.08</td><td>0.09</td><td>5.80 x 10^{-4}</td></tr>
<tr><td>**240**</td><td>0.56</td><td>0.02</td><td>0.08</td><td>0.10</td><td>5.48 x 10^{-4}</td></tr>
<tr><td>**307**</td><td>0.56</td><td>0.02</td><td>0.08</td><td>0.10</td><td>5.14 x 10^{-4}</td></tr>
<tr><td>**402**</td><td>0.56</td><td>0.01</td><td>0.09</td><td>0.11</td><td>2.69 x 10^{-4}</td></tr>
<tr><td>**497**</td><td>0.57</td><td>0.01</td><td>0.09</td><td>0.11</td><td>2.84 x 10^{-4}</td></tr>
<tr><td>**569**</td><td>0.57</td><td>0.01</td><td>0.09</td><td>0.10</td><td>4.43 x 10^{-4}</td></tr>
<tr><td>**669**</td><td>0.58</td><td>0.02</td><td>0.09</td><td>0.11</td><td>7.39 x 10^{-4}</td></tr>
<tr><td>**739**</td><td>0.58</td><td>0.01</td><td>0.10</td><td>0.11</td><td>4.47 x 10^{-4}</td></tr>
<tr><td>**833**</td><td>0.58</td><td>0.01</td><td>0.10</td><td>0.11</td><td>3.55 x 10^{-4}</td></tr>
<tr><td>**929**</td><td>0.59</td><td>0.01</td><td>0.10</td><td>0.12</td><td>3.93 x 10^{-4}</td></tr>
<tr><td>**1000**</td><td>0.59</td><td>0.01</td><td>0.10</td><td>0.12</td><td>6.48 x 10^{-4}</td></tr>
</table>

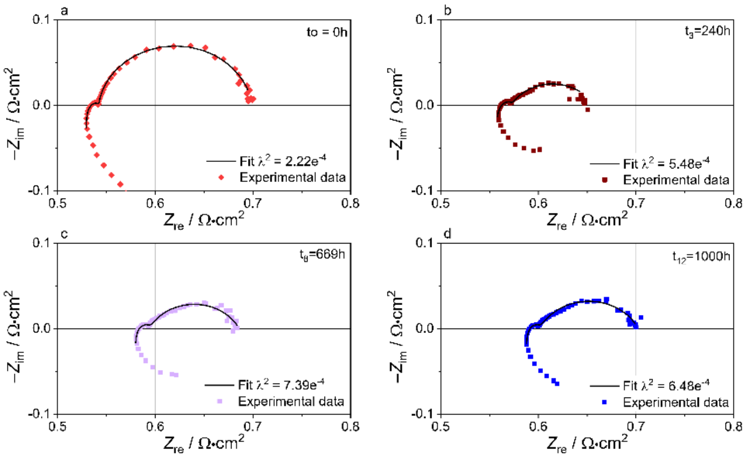

Figure S6. Nyquist plots of experimental data (scatter) and fitting data (line) at OCV of L65SCrN fuel electrode in full ESC with fuel gas mixture of 80% H_2O - 20% H_2 at 860 °C and -0.67 A•cm^{-2} at (a) initial time, (b) 240 hours, (c) 669 hours and (d) 1000 hours of test.

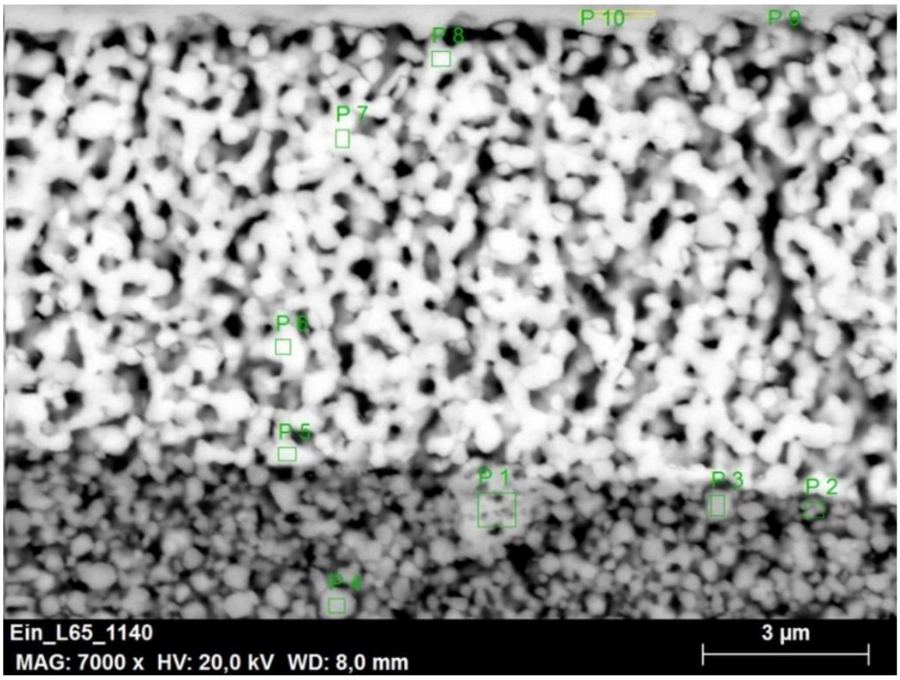

Figure S7. Polished cross-section view of the L65SCrN fuel electrode (inlet side) ESC after 1000h-SOEC operation at 860 °C with EDS point analysis.

Table S12. EDS with point analysis on Figure S7 and atom percent content by element.

Point	La	Sr	Cr	Ni	O	Zr	Gd	Ce
P 1	13.10	6.88	22.10	1.50	45.56	0.56	2.96	7.34
P 2	13.12	4.70	18.88	1.70	31.63	0.27	5.36	24.34
P 3	12.20	6.44	16.73	1.33	51.60	0.61	2.05	9.04
P 4	14.66	5.87	19.28	1.46	57.88	0.85		
P 5	3.63	1.88	5.09	1.38	50.87	0.32	6.59	30.24
P 6		0.62			56.51		8.24	34.62
P 7		0.67			55.83	0.61	7.59	35.31
P 8		2.20			49.63	6.30	8.01	33.86
P 9					20.37	24.11	11.83	43.69
P 10					17.60	42.39	13.04	26.97

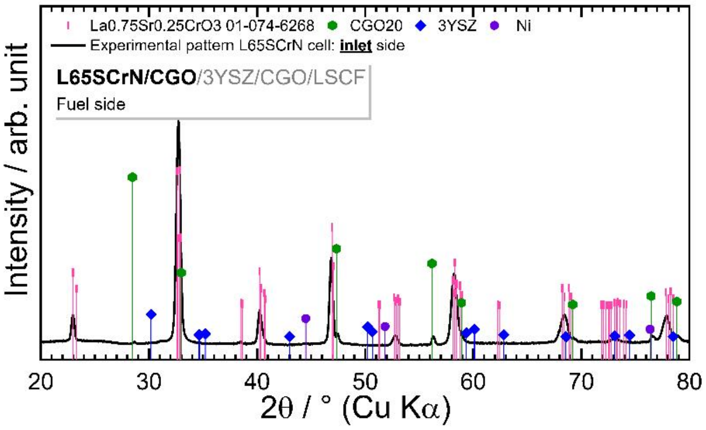

Figure S8. XRD pattern of inlet side from L65SCrN-based ESC performed on the fuel electrode side Pt/L65SCrN/CGO20/3YSZ after SOEC operation at 860 °C for 1000h.

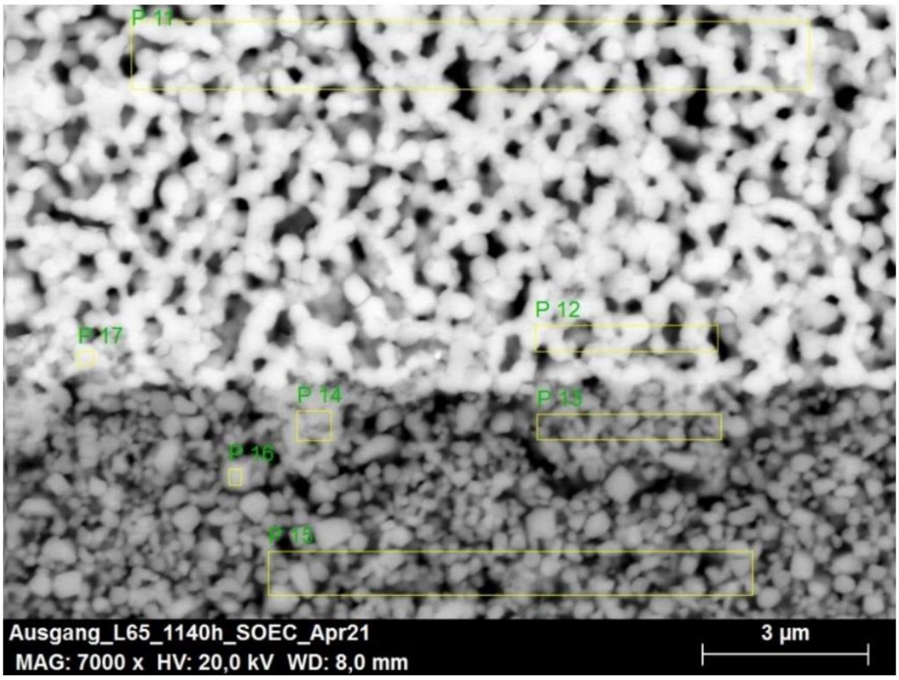

Figure S9. Polished cross-section view of the L65SCrN fuel electrode (outlet side) ESC after 1000h-SOEC operation at 860 °C with EDS point analysis.

Table S13. EDS with point analysis on Figure S9 and atom percent content by element.

Point	La	Sr	Cr	Ni	O	Zr	Gd	Ce
P 11					11.36	0.38	17.01	71.24
P 12		0.73			8.89		16.74	73.64
P 13	37.24	10.61	20.61	1.79	11.46		4.73	13.55
P 14	29.73	11.01	19.68	2.38	12.62		7.71	16.87
P 15	44.82	12.21	22.32	3.92	14.76	1.97		
P 16	42.48	12.24	21.09	1.52	21.23	1.45		
P 17	4.85	4.52	4.82	1.32	14.74	0.72	14.41	54.63

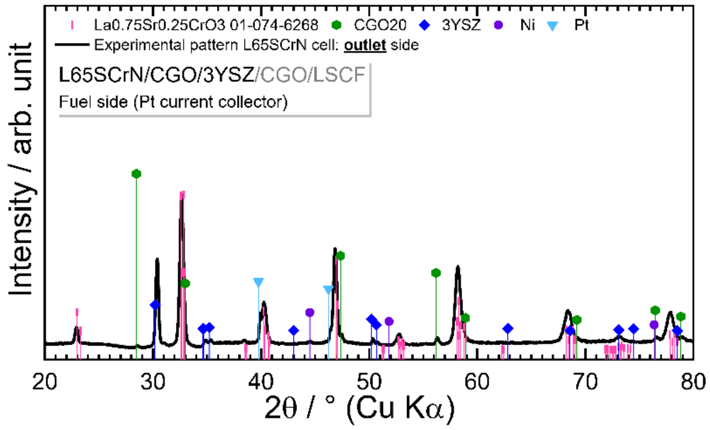

Figure S10. XRD pattern of outlet side from L65SCrN-based ESC performed on the fuel electrode side Pt/L65SCrN/CGO20/3YSZ after SOEC operation at 860 °C for 1000h.

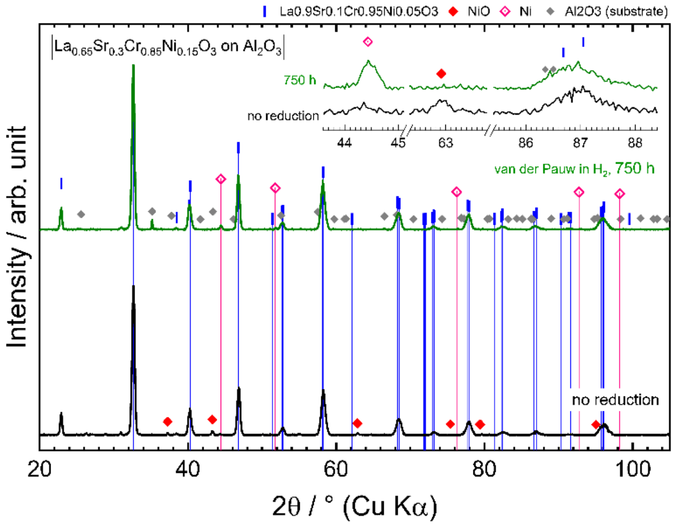

Figure S11. XRD pattern of the L65SCrN sample that was used for the Van-der-Pauw conductivity measurement before and after ca. 750 hours-durability test at ~ 860 °C and pO2 ~ 1E-16.

Additional Article (not part of the cumulative dissertation)

High Temperature Co-electrolysis for Power-to-X

Diana María Amaya Dueñas[1], Marc Riedel[1], Matthias Riegraf[1], Rémi Costa[1,*],
and Kaspar Andreas Friedrich[1,2]

DOI: 10.1002/cite.201900119

High temperature solid oxide cells are attractive electrochemical reactors to perform simultaneous reduction of steam and CO_2 into syngas with the possibility of delivering a tailored composition to downstream processes. The main thermodynamic considerations, performance and impedance curves of electrolyte supported cells in co-electrolysis are shown as a function of temperature and pressure. In dynamic operation, the thermal changes that the reactor undergoes appear stronger in co-electrolysis mode than in steam electrolysis and should be considered in the development of operating strategies.

Keywords: Co-electrolysis, CO_2 reduction, Pressurized operation, Solid oxide cell, Syngas

Received: August 15, 2019; *accepted:* November 20, 2019

1 Introduction

The global growth of energy demand results in an increase of CO_2 emissions and net concentration in the atmosphere with the consequence of fast and considerable impacts on our environment. The necessary reduction of anthropogenic CO_2 emissions has called for the development of technologies to decarbonize our CO_2 intensive societies. With increasing penetration of renewables from wind and solar energies a major contribution to CO_2 reduction in the energy sector is possible; however this only addresses a segment of decarbonization of human society. Beyond the energy system, our modern society makes use of a wide variety of products such as bulk chemicals and derivatives in the form of specialty polymers, plastics, or fuels used for heating or transportation, whose production strongly relies on fossil resources such as oil or natural gas. Unless recycled, the use of these products contributes to a significant extent to the net increase of CO_2 emissions. To address this challenge, Power-to-X technologies aim at converting renewable power into diverse valuable molecules in our economies. High temperature solid oxide cells (SOC) operating typically above 700 °C, are electrochemical reactors that are especially attractive for directly converting chemical energy into electricity owing to the fast reaction kinetics. Moreover, they have been proven to operate efficiently in reversible mode, meaning that the same electrochemical cell is capable of operation either in fuel cell mode generating power, or in steam electrolysis mode converting energy into hydrogen. Among all existing water electrolysis technologies, high temperature steam electrolysis allows the lowest energy consumption with a specific electricity below 3.5 $kWh\,m^{-3}$ of hydrogen. This is an attractive option to produce green hydrogen especially if a renewable steam source is available. Moreover, owing to their high operating temperature SOC present the unique benefit to allow co-electrolysis of CO_2 and H_2O directly into a synthetic gas consisting of a mixture of CO and H_2 whose precise ratio can be tuned depending on the client downstream process. This may be used for producing a wide variety of bulk chemicals and molecules. A general overview of the co-electrolysis process for Power-to-X application is given in Fig. 1.

The SOC that are being used for co-electrolysis are typically state-of-the-art cells that were primarily developed for fuel cell operation as they showed reversible operational capacity. In this work we present an overview of operational aspects and the typical dynamic behavior of SOC employed in co-electrolysis operation.

2 Thermodynamics of Co-electrolysis

Both water splitting (Eq. (1)) and CO_2 electrolysis (Eq. (2)) reactions are endothermic reactions and thus require energy input to occur.

$$H_2O \longrightarrow H_2 + 1/2O_2 \quad \Delta_r H(860\,^\circ C) = 249\ kJ\,mol^{-1} \tag{1}$$

$$CO_2 \longrightarrow CO + 1/2O_2 \quad \Delta_r H(860\,^\circ C) = 283\ kJ\,mol^{-1} \tag{2}$$

$$H_2 + CO_2 \longrightarrow H_2O + CO \quad \Delta_r H(860\,^\circ C) = 34\ kJ\,mol^{-1} \tag{3}$$

---

[1] Diana María Amaya Dueñas, Marc Riedel, Dr.-Ing. Matthias Riegraf, Dr. Rémi Costa, Prof. Kaspar Andreas Friedrich
remi.costa@dlr.de
German Aerospace Center, Institute of Engineering Thermodynamics, Electrochemical Energy Technology, Pfaffenwaldring 38–40, 70569 Stuttgart, Germany.

[2] Prof. Kaspar Andreas Friedrich
University of Stuttgart, Institute of Building Energetics, Thermal Engineering and Energy Storage (IGTE), Pfaffenwaldring 31, 70569 Stuttgart, Germany.

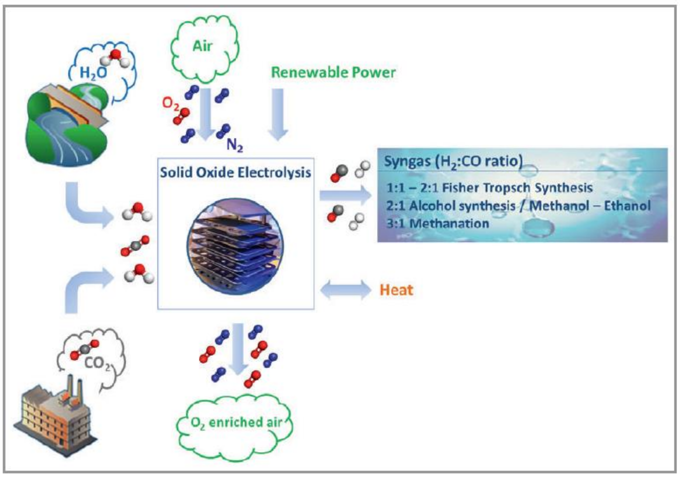

Figure 1. Primary principle of solid oxide electrolysis (SOE) applied for Power-to-X. Downstream conversion processes are exemplified for different syngas compositions.

In co-electrolysis both reactions split into two electrochemical redox half reactions that are responsible for the total electrical power consumption.

In SOC, H_2O and CO_2 reduction occur at the fuel electrode, producing oxygen ions that are transported through the electrolyte to the air electrode where they form molecular oxygen. The two electrochemical reduction reactions are related via the reverse water gas shift (rWGS) reaction (Eq. (3)), which is endothermic and becomes favorable at about 800 °C (Gibbs free reaction enthalpy $\Delta G < 0$). An overview of the reactions occurring in a SOC during co-electrolysis is given in Fig. 2.

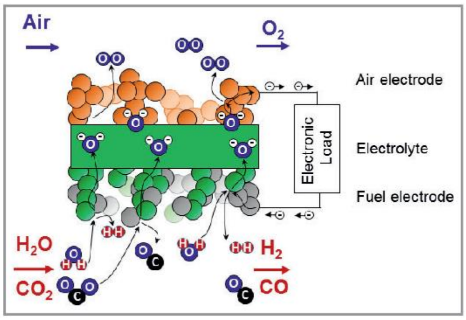

Figure 2. Co-electrolysis process schematic overview within a SOC, regardless the cell architecture. Steam and CO_2 are reduced at the fuel electrode (cathode) while oxygen ions are pumped through the electrolyte to form oxygen at the air electrode (anode).

One of the main reasons of the high efficiency of steam and CO_2 co-electrolysis can be identified based on the fundamental thermodynamics of the system. While increasing the temperature the total energy demand is almost constant; however, the heat demand increases while the electricity demand decreases (Fig. 3).

Solid oxide electrolysis (SOE) can use both electricity and heat effectively, enabling low specific electrical consumption while allowing efficient heat integration. For example, the heat could be provided from an external source such as solar heat or industrial waste heat [2], or just simply from the Joule heat that is generated due to internal losses of the stack. If the Joule heat generation balances the endothermic heat demand, the stack is operated at the thermoneutral voltage. This is a favorable voltage since isothermal operation minimizes local temperature gradients and the corresponding mechanical stress [3], simplifying the system layout. For co-electrolysis at 800 °C, the thermoneutral voltage is ca. 1.32 V, lying between the one for steam electrolysis (1.29 V) and CO_2 electrolysis (1.46 V) [4, 5]. In the present work, the operating temperature of most interest is 860 °C. At this temperature, the thermoneutral voltage still remains on the mentioned values for steam and CO_2 electrolysis, as well as for co-electrolysis [4].

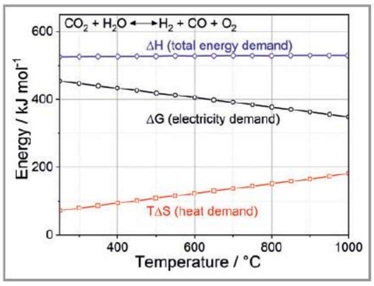

Figure 3. Energy demand of the whole co-electrolysis process depicting the total energy (reaction enthalpy ΔH) demand, the electricity demand (Gibbs free reaction energy ΔG) and the heat demand ($\Delta Q = T\Delta S$, with T being temperature and ΔS the entropy change). Data were taken from Ref. [1].

In contrast to steam electrolysis, co-electrolysis implies carbonaceous species, where the specific challenge is given by the risk of carbon deposition that can occur at the fuel electrode via the Boudouard equilibrium reaction Eq. (4).

$$2CO \rightleftarrows CO_2 + C \quad \Delta_r H(860\,°C) = -169\ \text{kJ mol}^{-1} \qquad (4)$$

3 Solid Oxide Cell Technology and Materials

SOC exist in multiple cell architectures. Planar cell architecture has so far received most of the attention since it is used in most commercial applications for fuel cell operation. Two different cells are used: the electrolyte-supported cells (ESC) or the fuel electrode-supported cells known as anode-supported cells (ASC) in fuel cell applications (Fig. 4) [6–9].

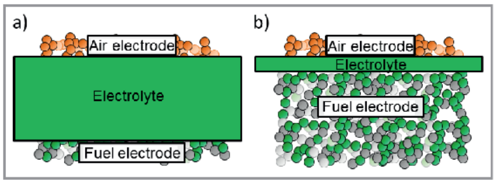

Figure 4. Schematic illustration of an ESC (a) and an ASC (b).

ESC (Fig. 4a) employ typically a thick zirconia-based electrolyte (65–200 µm), which provides mechanical strength to the cell. ESC are operated at high temperature (typically above 800 °C) in order to obtain sufficiently high ionic conductivity and to reduce the ohmic losses related to the large electrolyte thickness. As electrocatalyst for the fuel electrode, the cermet Ni/Ce$_{1-x}$Gd$_x$O$_{2-\alpha}$ (CGO) has attracted attention due to increased redox stability, coking resistance and high tolerance towards potential sulfur-containing impurities in CO$_2$ sources [10–15]. The reason is believed to be that the electro-catalytic activity of CGO shifts the reaction zone of the cermet electrode away from the triple phase boundary (TPB) between metal/ceramic/gas phase to the double phase boundary between CGO surface and gas phase [15–18]. Thus, Ni/CGO shows the potential to alleviate the issues of carbon deposition.

In the ASC design (Fig. 4b), a thin zirconia-based electrolyte (5–15 µm) is supported by a thick porous cermet substrate. This substrate which is about 300 to 500 µm thick is typically made of a nickel/yttria-stabilized-zirconia (Ni/YSZ) cermet providing the mechanical stability to the cell. Compared to ESC, the thin electrolyte allows reduced ohmic losses which improves the overall performance at lower operating temperatures (700–800 °C). For these reasons, the use of the ASC architecture is considered very promising in co-electrolysis and was widely investigated [19–22]. However, the ASC design faces critical challenges due to the thick porous support layer (in SOFC mode the anode, in SOE the cathode), in particular a low tolerance towards redox and thermal cycling. Moreover, it has recently been shown that the possible high operating current densities and corresponding large fuel electrode overpotentials can lead to Ni migration away from the electrode/electrolyte interface in Ni/YSZ fuel electrodes causing severe degradation [23–25].

Another issue relates to the Boudouard reaction (Eq. (4)), which is thermodynamically favored at lower operating temperature and is readily catalyzed by the nickel from the cermet electrode. As all reforming reactions are characterized by fast reaction rates, it is assumed that the carbon formation regime is governed by the thermodynamic equilibrium of the C–H–O mixtures as a function of the composition, pressure and temperature. Diffusion limitations within the thick Ni/YSZ support may cause carbon deposition due to the formation of local non-equilibrium gas phase compositions [20]. This can lead to the formation of carbon nanotubes or whiskers on the Ni surface causing fatal failure of the SOC [19, 20]. The implementation of Ni/CGO cermet with superior tolerance towards carbon deposition into the ASC cell design has not yet been demonstrated. This is mostly due to the lower mechanical properties of the CGO compared to YSZ materials [26], which limits their use to ESC architectures. Therefore, careful selection of the operating conditions is essential to avoid operando carbon deposition in the functional electrode.

4 Operational Aspects

This section focuses on the operational aspects of the co-electrolysis on state-of-the-art ESC in oven environments, in which both cells and stacks were investigated. The ESC consisted of a ~90 µm 3-YSZ electrolyte coated with a CGO layer of about 5 to 10 µm in thickness on both sides. The thin fuel electrode consisted of a 15 µm thick Ni/CGO cermet contacted with a ~10 µm nickel-rich contact layer. The air electrode was made of a 20 to 25 µm thick porous La$_{0.6}$Sr$_{0.4}$Co$_{0.2}$Fe$_{0.8}$O$_{3-\delta}$ (LSCF) layer. These cells with an active surface area of 16 cm^2, were tested at ambient pressure. The fuel gas humidification was implemented with a direct evaporator: the steam was mixed at 120 °C to the feed gas and then heated at nominal operating temperature in the oven. The test bench for cell testing was already illustrated and described in a similar configuration in detail elsewhere [11, 27]. A commercially available stack with ESC was used for operation in pressurized conditions (1.4, 4.0, and 8.0 bar). The stack consisted of 10 cells each with an active area of 127.8 cm^2. In order to have the possibility to record the temperatures during operation, an overall number of five thermocouples were implemented directly on the air electrodes of the cells 1, 5 and 10. The experimental test setup offered the possibility to characterize short stacks in SOFC as well as in SOE. Nevertheless, there was the challenge of maintaining the pressure differences constantly very low (< 20 mbar) between both electrodes and the surrounding furnace gas compartment, especially during operation of SOC stacks at elevated pressure (8 bar). Since larger pressure differences likely damage the whole stack, all pressures were controlled by a sensitive pressure control unit of the test bench. A detailed description of the design and the capabilities of the test setup are published elsewhere [28].

4.1 Operation under Variable Steam to Carbon Ratio at 1 bar

State-of-the-art cells were investigated in co-electrolysis operation at 770, 800, 830 and 860 °C. Two steam to carbon (S/C) ratios (2:1 and 3:1) were considered in order to evaluate the influence of the gas composition on the electrochemical behavior of the cell.

The open circuit voltage (OCV) was ~20 mV above the Nernst potential for every temperature. Such difference may be related to a small deviation of the gas composition from the value, due to small leakages in the cell housing. The polarization curves were recorded up to 1.5 V and are shown in Fig. 5.

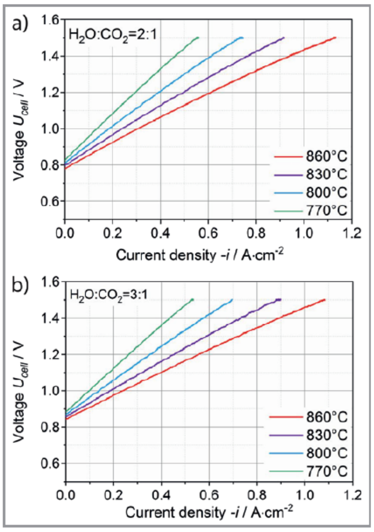

Figure 5. Polarization curves of ESC recorded at different temperatures in co-electrolysis with a (S/C) ratio of 2 (a) and 3 (b).

Electrochemical Impedance Spectroscopy (EIS) spectra were recorded in galvanostatic conditions at OCV and at a direct current (DC) bias of -0.6 A cm^{-2} in both gas mixtures showing comparable characteristics. For S/C of 2:1 at 860 °C (Fig. 6), the ohmic area-specific resistance (ASR), determined as the high frequency intercept of the curve with the Z_{re} axis, could be measured as ASR_{Ω} = 0.55 Ω cm^2 with or without applied current. Comparison of the two spectra shows that the applied current density mostly influences the middle and low frequency region (< 100 Hz). The polarization resistance is measured to be 0.23 and 0.1 Ω cm^2 at OCV and under a DC bias of −0.6 A cm^{-2} respectively. This yields a total ASR_{tot} of 0.78 Ω cm^2 at OCV and 0.65 Ω cm^2 at −0.6 A cm^{-2}. Upon an increase of temperature, a clearly distinguishable flattening of the polarization curves at high current densities is observed. This phenomenon is possibly related to a more predominant contribution of the resistances at fuel and air electrodes to the total cell resistance at high temperature. This effect will be discussed more in detail in Sect. 4.2.

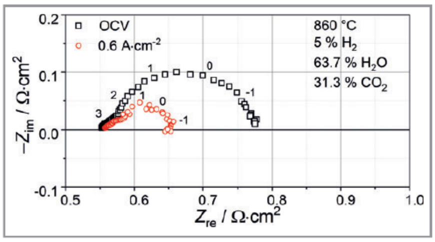

Figure 6. Nyquist plot of galvanostatic EIS measurements recorded at different current densities at 860°C in co-electrolysis operation with S/C = 2. Digits indicate the frequency decades.

To ensure safe operating conditions free of carbon deposition in the fuel electrode, for either tested gas mixtures, the equilibrium compositions (H_2, H_2O, CO_2, and CO) at the outlet at 860 °C are given in Tab. 1.

Table 1. Equilibrium molar fractions at inlet and outlet for the different tested mixtures. Data were calculated at 860 °C with a reactant conversion of 20 %.

Mixture	M1		M2	
S/C	2		3	
Molar fraction at equilibrium	inlet	outlet	inlet	outlet
H_2	0.033	0.163	0.116	0.251
H_2O	0.654	0.524	0.672	0.537
CO_2	0.296	0.232	0.177	0.139
CO	0.017	0.081	0.035	0.073

Both outlet mixtures, denoted by the points M1 and M2, are safely located outside the carbon deposition regime at operating temperature in the ternary C–H–O diagram (Fig. 7).

4.2 Thermal Effects under Dynamic Operation

To investigate the thermal effects of dynamic operation on the SOC, polarization curves in steam and co-electrolysis at 860 °C were recorded while cell temperature was carefully monitored. The results are reported in Fig. 8.

The polarization curves show a nearly linear evolution in both electrolysis and co-electrolysis operation up to an inflection point that corresponds to a change in the measured temperature evolution profile. Above the inflection

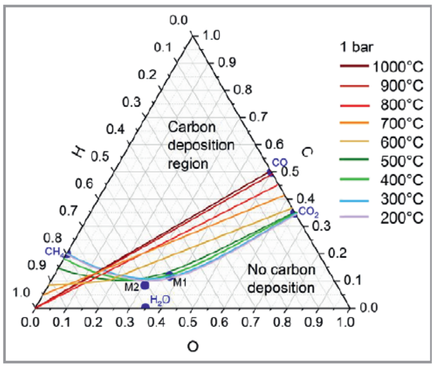

Figure 7. C-H-O ternary diagram with equilibrium compositions of mixtures M1 and M2 at the outlet at 860°C (see Tab. 1). Temperature profiles were adapted from Ref [5].

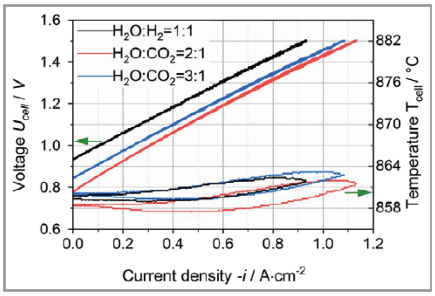

Figure 8. Cell temperature evolution (right axis) and polarization curves (left axis) for ESC in steam electrolysis and co-electrolysis at 860 °C.

point, the slope of the polarization curve, corresponding to the total cell ASR, decreases yielding a flattening of the curve at high current densities. At low current densities the endothermal nature of the electrolysis reactions Eqs. (1) and (2) is not balanced by Joule heat production. Therefore, the cell temperature decreases. This cooling effect lowers both the ionic conductivity of the electrolyte and both the chemical and electrochemical reaction kinetics. Above the thermoneutral voltage the cell is heated continuously due to the exothermal operation. Owing to the isothermal oven operation, this heating cannot be regulated at the cell level leading to a net increase in temperature and acceleration of the electrochemical kinetics. This explains why the total cell resistance decreases above the thermoneutral voltage [29].

A comparison of the temperature evolution profiles shows a more pronounced cooling effect at low current densities for the co-electrolysis experiment at S/C = 2, which also results in a lower slope of the corresponding polarization curve. The reason for this effect is very likely related to the thermodynamics of CO_2 and steam electrolysis. The experiment with S/C ratio of 2 contains the highest ratio of CO_2. Since CO_2 electrolysis is more endothermic than steam electrolysis (see Eqs. (1) and (2)), this results in a more pronounced cooling effect. As a consequence, it can be anticipated that dynamic operation of a SOC stack in co-electrolysis mode will generate stronger thermo-mechanical stress gradients within the stack compared to operation in steam electrolysis. Ergo, the mechanical robustness of cell and stack is of the outmost importance. Additional investigations are required to identify limiting operating conditions in terms of load-cycling and transient ramps that a SOC stack can endure without mechanical failure and to develop safe operating strategies.

4.3 Pressurized Co-electrolysis Operation

Pressurized SOE can be beneficial since many downstream processes, such as the Fischer–Tropsch, require pressurized operation and hence, additional compression work can be significantly reduced or omitted. At the cell level, the OCV increases while increasing operating pressure according to the Nernst equation. Moreover, mass transport limitations are shifted to higher current densities. Furthermore, activation overvoltages in steam electrolysis were shown to be reduced with increasing pressure [30], which can be expected to display similar behavior in co-electrolysis.

Dynamic polarization curves recorded with a 10 layer ESC stack are reported in Fig. 9. Additionally, the core temperature as the characteristic stack temperature is plotted over the current density. The theoretical Nernst voltage based on the gas composition of the feed and the stack

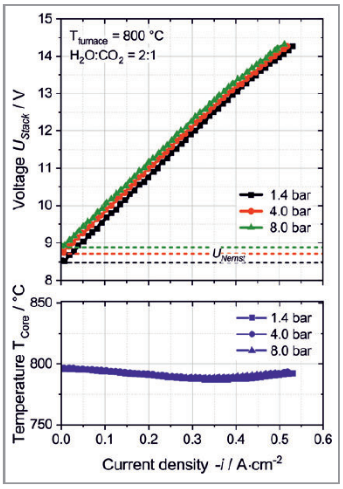

Figure 9. Polarization curves recorded at 800 °C. Inlet gas composition was 60/30/10 $H_2O/CO_2/H_2$ and three different operating pressures of 1.4, 4, and 8 bar were tested. The gas flows were defined for a reactant conversion of 60 % at 0.8 A cm^{-2}. 10 slpm of air was supplied to the air side of the stack.

temperature at OCV is shown as a dotted line for all operating pressures. At OCV, the measured cell voltages are in good agreement with the theoretical values, indicating an accurate media dosage and hardly any leakage in the stack. With increasing current density, the voltage shows an almost linear behavior up to the defined maximum single cell voltage of 1.45 V. Nonetheless, a slight flattening is observed, in which the inflection point is situated at the change in the temperature evolution profile; that is when the stack temperature increases again after the cooling effect due to endothermal operation, which is compensated by the internal Joule heating. This is consistent with observations made at cell level (Sect. 4.2).

Upon pressure increase, the slope is slightly decreased, indicating a positive pressure effect on the reaction kinetics and mass transport in the cells. However, a significant influence of the operating pressure on the achievable current density cannot be observed for the studied stack. This could be explained by the predominant contribution of ohmic resistance (ASR_{Ω}) to the ASR_{tot} of the stack and the corresponding relatively small contribution of the polarization resistance (ASR_{pol}). A detailed theoretical and experimental study of the ohmic resistance and an analysis of the overall ASR can be found in [28].

5 On the Quality of Feed Gas Streams

Respect to the fuel electrode, impurities in the feed gases may adsorb on the electrocatalytically active sites and hinder the reduction reaction. In the long term, similarly to what is observed with sulfur species in fuel cell operation, this may lead to accelerated and irreversible cell degradation that this detrimental for the durability of the system.

In the electrolysis process, steam may originate from different sources. It could be from fresh water direct evaporation or from industrial steam sources and may be of different quality. SiO_2 in feed water is known to be easily transported in the vapor stream and can readily be deposited on the active sites for the co-electrolysis yielding, an accelerated degradation on the electrochemical performance of the reactor. In addition, since cell voltage is a direct function of gas concentration, it is necessary to maintain a constant flow of steam free of any liquid water to avoid unwanted voltage oscillation. Therefore for the benefit of the durability of the electrochemical reactor, it is recommended to provide high quality steam with the lowest amount of impurities.

In the co-electrolysis process, CO_2 represents a non-negligible potential source of impurities. This holds true especially for CO_2 streams originating from industrial or combustion processes of heavy fuels. Independently from the nature of impurities that may contaminate CO_2 streams, further investigation regarding the sensitivity of co-electrolysis process towards CO_2 impurities is required in order to identify purity grades, allowing economically viable exploitation of the electrochemical reactor in co-electrolysis operation.

6 Conclusion

ESC cell architecture has been evaluated for co-electrolysis operation enabling syngas production out of steam and CO_2. From an operational point of view, a major aspect with respect to the coupling of the SOC reactor with a client downstream process is the flexibility in operation that enables production of syngas with tailored composition. Even though the high operating temperature of ESC, together with the use of CGO in the electro-catalytic layer, are favorable to avoid carbon deposition (Eq. (4)) at operating conditions, an important challenge remains to be the processing of the produced hot syngas since carbon deposition is thermodynamically favored at low temperature (Fig.7).

The cells in the SOC reactor undergo larger thermal effects in co-electrolysis operation than in steam electrolysis (Fig. 8) which can be related to the specific thermodynamics of CO_2 reduction and its interplay with the steam reduction through the reverse water gas shift reaction (Eq. (3)). This may result in thermo-mechanical stresses that may adversely affect integrity and durability of the SOC reactor. This is an important aspect to consider for the development of operating strategies in dynamic operation that are safe for the reactor. It is shown that ESC stacks can be operated under pressurized conditions, which may ease process integration by avoiding intermediate compression steps. Stack operation in pressurized conditions is shown up to 8 bar (Fig. 8) with comparable electrochemical behavior as observed on cell level at ambient pressure. The pressure effect may become more favorable on the stack performance once electrode kinetics becomes more significant in the overall stack ASR. This could be achieved at higher temperature with ESC, for which the relative contribution of ohmic losses to the total ASR will be reduced. Regarding durability of the SOC reactor operated in co-electrolysis, it is beneficial to provide high quality steam free of SiO_2. Further investigation regarding the sensitivity of the co-electrolysis process towards CO_2 impurities is mandatory in order to identify purity grades allowing economically viable exploitation of the electrochemical reactor.

The German Academic Exchange Service (DAAD) is gratefully acknowledged for the Ph.D. scholarship of Mrs. Diana M. Amaya Dueñas. Part of this work has received support from the German Federal Ministry of Education and Research (BMBF) within the Kopernikus Project P2X (Grant n°03SFKE20).

Symbols Used

i	[A cm^{-2}]	current density
T	[°C]	temperature
U	[V]	voltage
Z	[Ω cm^2]	impedance
ΔG	[kJ mol^{-1}]	Gibbs free reaction enthalpy
$\Delta_r H$	[kJ mol^{-1}]	enthalpy of reaction

Greek Symbols

α	[–]	oxygen deficiency on cerium-gadolinium oxide
δ	[–]	oxygen deficiency on lanthanum strontium cobalt ferrite

Sub- and Superscripts

re	real part of impedance
im	imaginary part of impedance
pol	polarization resistance
Ω	ohmic resistance
x	gadolinium content on cerium-gadolinium oxide

Abbreviations

ASC	anode-supported cell
ASR	area specific resistance
CGO	cerium-gadolinium oxide $Ce_{1-x}Gd_xO_{2-\alpha}$
DC	direct current
DLR	german aerospace center
EIS	electrochemical impedance spectroscopy
ESC	electrolyte-supported cell
LSCF	lanthanum strontium cobalt ferrite ($La_{0.6}Sr_{0.4}Co_{0.2}Fe_{0.8}O_{3-\delta}$)
OCV	open circuit voltage
rWGS	reverse water gas shift
slpm	standard liter per minute
SOC	solid oxide cell
SOFC	solid oxide fuel cell
SOE	solid oxide electrolysis
TPB	triple phase boundary
YSZ	yttria stabilized zirconia
3-YSZ	3 mol % yttria stabilized zirconia

References

[1] Y. Zheng, J. Wang, B. Yu, W. Zhang, J. Chen, J. Qiao, J. Zhang, *Chem. Soc. Rev.* **2017**, *46 (5)*, 1427–1463. DOI: https://doi.org/10.1039/c6cs00403b

[2] G. Schiller, M. Lang, P. Szabo, N. Monnerie, H. von Storch, J. Reinhold, P. Sundarraj, *J. Power Sources* **2019**, *416*, 72–78. DOI: https://doi.org/10.1016/j.jpowsour.2019.01.059

[3] Q. Fu, C. Mabilat, M. Zahid, A. Brisse, L. Gautier, *Energy Environ. Sci.* **2010**, *3 (10)*, 1382–1397. DOI: https://doi.org/10.1039/c0ee00092b

[4] X. Sun, M. Chen, S. H. Jensen, S. D. Ebbesen, C. Graves, M. Mogensen, *Int. J. Hydrogen Energy* **2012**, *37 (22)*, 17101–17110. DOI: https://doi.org/10.1016/j.ijhydene.2012.08.125

[5] Z. Jaworski, B. Zakrzewska, P. Pianko-Oprych, *Rev. Chem. Eng.* **2017**, *33 (3)*, 217–235. DOI: https://doi.org/10.1515/revce-2016-0022

[6] A. Glauche, T. Betz, M. Ise, *ECS Trans.* **2011**, *5*, 157–165. DOI: https://doi.org/10.1149/1.3569990

[7] M. Kusnezoff, N. Trofimenko, M. Müller, A. Michaelis, *Materials* **2016**, *9 (11)*, 906–914. DOI: https://doi.org/10.3390/ma9110906

[8] A. Mai, B. Iwanschitz, U. Weissen, R. Denzler, D. Haberstock, V. Nerlich, A. Schuler, *ECS Trans.* **2011**, *25 (2)*, 87–95. DOI: https://doi.org/10.1149/1.3569982

[9] M. Bertoldi, O. F. Bucheli, A. Ravagni, *ECS Trans.* **2017**, *78 (1)*, 117–123. DOI: https://doi.org/10.1149/07801.0117ecst

[10] M. Riegraf, A. Zekri, M. Knipper, R. Costa, G. Schiller, K. A. Friedrich, *J. Power Sources.* **2018**, *380*, 26–36. DOI: https://doi.org/10.1016/j.jpowsour.2018.01.067

[11] M. Riegraf, M. P. Hoerlein, R. Costa, G. Schiller, K. A. Friedrich, *ACS Catal.* **2017**, *7 (11)*, 7760–7771. DOI: https://doi.org/10.1021/acscatal.7b02177

[12] S. Kavurucu Schubert, M. Kusnezoff, A. Michaelis, S. I. Bredikhin, *J. Power Sources* **2012**, *217*, 364–372. DOI: https://doi.org/10.1016/j.jpowsour.2012.06.020

[13] J. Mermelstein, M. Millan, N. Brandon, *J. Power Sources* **2010**, *195 (6)*, 1657–1666. DOI: https://doi.org/10.1016/j.jpowsour.2009.09.046

[14] B. Iwanschitz, J. Sfeir, A. Mai, M. Schütze, *J. Electrochem. Soc.* **2009**, *157 (2)*, B269–B278. DOI: https://doi.org/10.1149/1.3271101

[15] M. Riegraf, R. Costa, G. Schiller, K. A. Friedrich, S. Dierickx, A. Weber, *J. Electrochem. Soc.* **2019**, *166 (13)*, F865–F872. DOI: https://doi.org/10.1149/2.0051913jes

[16] T. Nakamura, T. Kobayashi, K. Yashiro, A. Kaimai, T. Otake, K. Sato, J. Mizusaki, T. Kawada, *J. Electrochem. Soc.* **2008**, *155 (6)*, B563–B569. DOI: https://doi.org/10.1149/1.2901047

[17] Z. A. Feng, F. El Gabaly, X. Ye, Z. X. Shen, W. C. Chueh, *Nat. Commun.* **2014**, *5*, 1–9. DOI: https://doi.org/10.1038/ncomms5374

[18] W. C. Chueh, Y. Hao, W. Jung, S. M. Haile, *Nat. Mater.* **2012**, *11 (2)*, 155–161. DOI: https://doi.org/10.1038/nmat3184

[19] Y. Tao, S. D. Ebbesen, W. Zhang, M. B. Mogensen, *ChemCatChem* **2014**, *6 (5)*, 1220–1224. DOI: https://doi.org/10.1002/cctc.201300941

[20] Y. Tao, S. D. Ebbesen, M. B. Mogensen, *J. Electrochem. Soc.* **2014**, *161 (3)*, F337–F343. DOI: https://doi.org/10.1149/2.079403jes

[21] S. D. Ebbesen, M. Mogensen, *J. Power Sources* **2009**, *193 (1)*, 349–358. DOI: https://doi.org/10.1016/j.jpowsour.2009.02.093

[22] C. Graves, S. D. Ebbesen, M. Mogensen, *Solid State Ionics* **2011**, *192 (1)*, 398–403. DOI: https://doi.org/10.1016/j.ssi.2010.06.014

[23] M. B. Mogensen, A. Hauch, X. Sun, M. Chen, Y. Tao, S. D. Ebbesen, K. V. Hansen, P. V. Hendriksen, *Fuel Cells* **2017**, *17 (4)*, 434–441. DOI: https://doi.org/10.1002/fuce.201600222

[24] M. P. Hoerlein, M. Riegraf, R. Costa, G. Schiller, K. A. Friedrich, *Electrochim. Acta* **2018**, *276*, 162–175. DOI: https://doi.org/10.1016/j.electacta.2018.04.170

[25] A. Hauch, S. D. Ebbesen, S. H. Jensen, M. Mogensen, *J. Electrochem. Soc.* **2008**, *155 (11)*, B1184–B1193. DOI: https://doi.org/10.1149/1.2967331

[26] M. Mogensen, T. Lindegaard, U. R. Hansen, G. Mogensen, *J. Electrochem. Soc.* **1994**, *141 (8)*, 2122–2128. DOI: https://doi.org/10.1149/1.2055072

[27] M. Riegraf, V. Yurkiv, R. Costa, G. Schiller, K. A. Friedrich, *ChemSusChem* **2017**, *10 (3)*, 587–599. DOI: https://doi.org/10.1002/cssc.201601320

[28] M. Riedel, M. P. Heddrich, K. A. Friedrich, *Int. J. Hydrogen Energy* **2019**, *44 (10)*, 4570–4581. DOI: https://doi.org/10.1016/j.ijhydene.2018.12.168

[29] J. Aicart, *Modeling and Experimental Validation of High Temperature Steam and Carbon Dioxide Co-Electrolysis*, PhD Thesis, Université de Grenoble **2014**.

[30] M. Henke, C. Willich, J. Kallo, K. A. Friedrich, *Int. J. Hydrogen Energy* **2014**, *39 (24)*, 12434–12439. DOI: https://doi.org/10.1016/j.ijhydene.2014.05.185

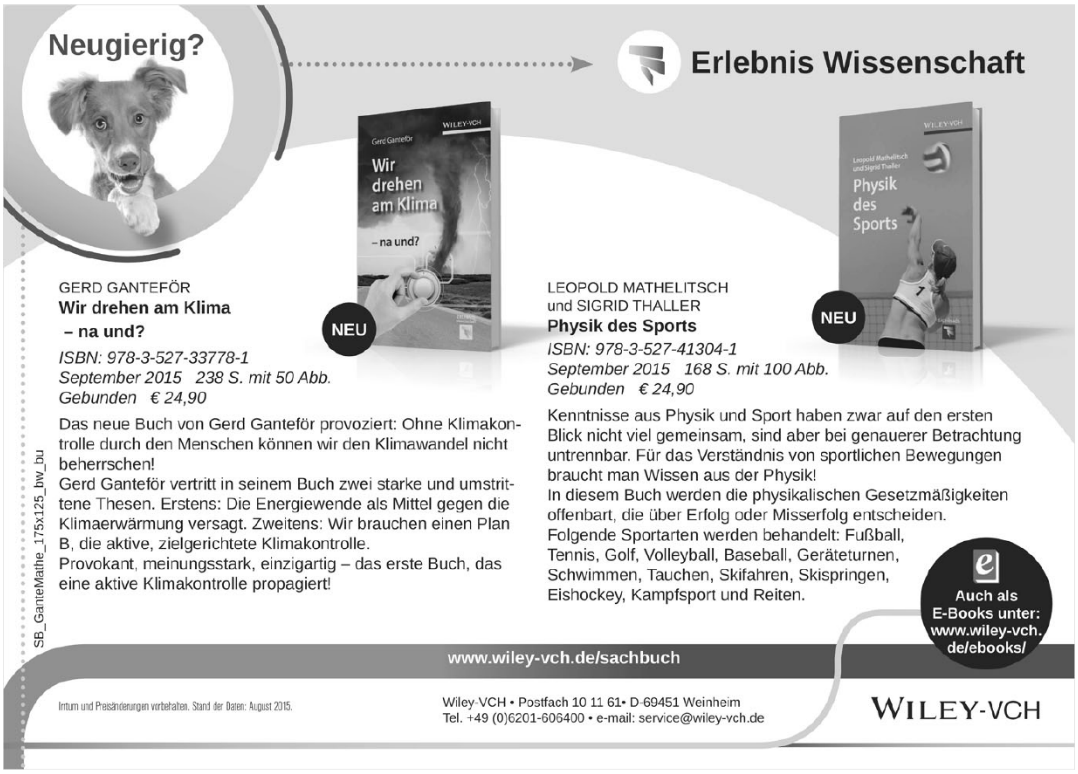

Neugierig?

Erlebnis Wissenschaft

GERD GANTEFÖR
Wir drehen am Klima – na und?
ISBN: 978-3-527-33778-1
September 2015 238 S. mit 50 Abb.
Gebunden € 24,90

NEU

Das neue Buch von Gerd Ganteför provoziert: Ohne Klimakontrolle durch den Menschen können wir den Klimawandel nicht beherrschen!
Gerd Ganteför vertritt in seinem Buch zwei starke und umstrittene Thesen. Erstens: Die Energiewende als Mittel gegen die Klimaerwärmung versagt. Zweitens: Wir brauchen einen Plan B, die aktive, zielgerichtete Klimakontrolle.
Provokant, meinungsstark, einzigartig – das erste Buch, das eine aktive Klimakontrolle propagiert!

LEOPOLD MATHELITSCH
und SIGRID THALLER
Physik des Sports
ISBN: 978-3-527-41304-1
September 2015 168 S. mit 100 Abb.
Gebunden € 24,90

NEU

Kenntnisse aus Physik und Sport haben zwar auf den ersten Blick nicht viel gemeinsam, sind aber bei genauerer Betrachtung untrennbar. Für das Verständnis von sportlichen Bewegungen braucht man Wissen aus der Physik!
In diesem Buch werden die physikalischen Gesetzmäßigkeiten offenbart, die über Erfolg oder Misserfolg entscheiden.
Folgende Sportarten werden behandelt: Fußball, Tennis, Golf, Volleyball, Baseball, Geräteturnen, Schwimmen, Tauchen, Skifahren, Skispringen, Eishockey, Kampfsport und Reiten.

Auch als E-Books unter: www.wiley-vch.de/ebooks/

www.wiley-vch.de/sachbuch

Irrtum und Preisänderungen vorbehalten. Stand der Daten: August 2015.

Wiley-VCH • Postfach 10 11 61• D-69451 Weinheim
Tel. +49 (0)6201-606400 • e-mail: service@wiley-vch.de

WILEY-VCH

SB_GanteMathe_175x125_bw_bu